

ADVERTIMENT. L'accés als continguts d'aquesta tesi queda condicionat a l'acceptació de les condicions d'ús establertes per la següent llicència Creative Commons:  http://cat.creativecommons.org/?page_id=184

ADVERTENCIA. El acceso a los contenidos de esta tesis queda condicionado a la aceptación de las condiciones de uso establecidas por la siguiente licencia Creative Commons:  <http://es.creativecommons.org/blog/licencias/>

WARNING. The access to the contents of this doctoral thesis it is limited to the acceptance of the use conditions set by the following Creative Commons license:  <https://creativecommons.org/licenses/?lang=en>



**Universitat Autònoma
de Barcelona**

Self-Assembly of Colloidal Metal-Organic Framework Particles into Multidimensional Superstructures

Yang Liu

Doctoral Thesis
PhD in Chemistry

Supervisors:

Prof. Dr. Daniel Maspoch

Dr. Inhar Imaz

Tutor:

Dr. Félix Busqué Sánchez

Catalan Institute of Nanoscience and Nanotechnology (ICN2)

Department of Chemistry – Faculty of Sciences

2022

Memoria presentada per aspirar al Grau de Doctor per Yang Liu.

Yang Liu

Vist i plau

Prof. Dr. Daniel Maspoch

ICREA Research Professor & Group Leader

Supramolecular Nanochemistry and Materials Group.

Institut Català de Nanociència i Nanotecnologia (ICN2)

Dr. Inhar Imaz

Senior Researcher & Division Coordinator

Supramolecular Nanochemistry and Materials Group.

Institut Català de Nanociència i Nanotecnologia (ICN2)

Prof. Dr. Félix Busqué

Departament de Química

Universitat Autònoma de Barcelona (UAB)

Bellaterra, 10 de mayo de 2022

The present PhD Thesis has been accomplished at Supramolecular Nanochemistry and Materials Group of the Catalan Institute of Nanoscience and Nanotechnology (ICN2) following the doctoral program in Chemistry of Autonomous University of Barcelona (UAB). According to the decision of the PhD Commission, this PhD Thesis is presented as compendium of publications.

All publications appear in the Thesis in the following order:

Publication 1. “Assembly of Colloidal Clusters Driven by the Polyhedral Shape of Metal–Organic Framework Particles.” Yang Liu, Jiemin Wang, Inhar Imaz, Daniel Maspoch. *J. Am. Chem. Soc.* **2021**, 143 (33), 12943-12947.

Publication 2. “Template-Free, Surfactant-Mediated Orientation of Self-Assembled Supercrystals of Metal-Organic Framework Particles.” Civan Avci, Yang Liu, Jose Angel Pariente, Alvaro Blanco, Cefe Lopez, Inhar Imaz, Daniel Maspoch. *Small* **2019**, 31, 1902520.

Table of Contents

Table of contents	i
Abstract.....	iii
Resumen.....	v
Acknowledgements	vii
Chapter 1 Introduction to Self-Assembly of Colloidal Particles and Metal-Organic Frameworks	1
1. Self-Assembly of Colloidal Particles	3
1.1 Introduction to Self-Assembly of Colloidal Particles	3
1.2 Assembly Forces	5
1.3 Typical Self-Assembly Methods	9
1.4 Self-Assembly of Colloidal Particles into 2D and 3D Superstructures	12
1.4.1 Self-Assembly Symmetries	13
1.4.2 Spherical Particles	13
1.4.3 Polyhedral Particles	16
1.5 Self-Assembly of Colloidal Particles into Supraparticles	21
1.5.1 Supraparticles Made of Spherical Particles	21
1.5.2 Supraparticles Made of Polyhedral Particles	22
1.6 Self-Assembly of Colloidal Particles into Colloidal Molecules and Patchy Particles ...	24
1.6.1 Synthesis Routes of Colloidal Molecules	25
1.6.2 Typical Approaches for the Synthesis of Patchy Particles	28
1.6.3 Self-Assembly of Patchy Particles into the Hierarchical Superstructures.....	30
2. Metal-Organic Frameworks (MOFs)	33
2.1 Introduction to Metal-Organic Frameworks.....	33
2.2 Applications of MOFs	38
2.2.1 Gas Storage.....	38
2.2.2 CO ₂ Sequestration.....	40
2.2.3 Other Gases Storage and Separation	41
2.2.4 Chemical Sensing	42
2.2.5 Catalysis	43
2.3 Colloidal MOFs	44
2.3.1 Synthesis of Colloidal MOF Particles	45

2.3.2 Surface Modification	48
2.3.3 Assembly	52
3. References	55
Chapter 2 Objectives	65
Chapter 3 Summary of Results and Discussion	69
1. Assembly of Colloidal Clusters Driven by the Polyhedral Shape of Metal-Organic Framework Particles	71
2. Template-free, Surfactant-Mediated Orientation of Self-assembled Supercrystals of Metal-Organic Framework Particles	77
3. Coloration in Suparparticles Assembled from Polyhedral Metal-Organic Framework Particles	82
4. References	88
Chapter 4 General Conclusion	89
Chapter 5 Assembly of Colloidal Clusters Driven by the Polyhedral Shape of Metal-Organic Framework Particles	95
Chapter 6 Template-free, Surfactant-Mediated Orientation of Self-assembled Supercrystals of Metal-Organic Framework Particles	123
Appendix Coloration in Suparparticles Assembled from Polyhedral Metal-Organic Framework Particles	143

Abstract

The aim of the present PhD Thesis has been the exploration of Metal-Organic Frameworks (MOFs) as a potential source of polyhedral for the assembly of a new generation of materials. The discovery of thousands of MOFs over the past 25 years has created a huge pool of highly porous, crystalline particles that encompass most known polyhedral shapes. The research presented in this Thesis hopes to dip in this pool, opening up new avenues to synthesize new porous self-assembled materials with original structures that will give access to new photonic properties

The Thesis is organized into two parts. Chapter 1 constitutes the first part where the reader will find an introduction of the self-assembly field, with a brief description of the different interactions that are involved in self-assembly processes, and of different self-assembled systems and synthetic strategies. This Chapter continues with a brief introduction to MOFs, from an historical perspective to their representative applications. We have also pay attention on the few examples in which MOF particles have already been used to generate self-assembled superstructures.

The second part of this Thesis contains a description of the general and specific objectives. Then, in Chapter 3, we will briefly describe and discuss the different results obtained during this Thesis. The detailed results will be found in the three publications reproduced in Chapters 5, 6 and Appendix.

The publication in Chapter 5 focuses on the use of the polyhedral shape of MOF particles to direct the assembly of colloidal clusters through colloidal fusion. Thanks to the geometry of colloidal MOF particles, colloidal clusters with well-defined geometries can be prepared by controlling the attachment of a single polystyrene particle on each face of the polyhedral MOF particle. Following this approach, we show the synthesis of six-coordinated (6-c) octahedral, 8-c cubic, and 12-c cuboctahedral clusters using cubic ZIF-8, octahedral UiO-66, and rhombic dodecahedral ZIF-8 core particles, respectively.

The second publication in Chapter 6 is related to a new template-free method to self-assemble (111)-, (100)-, and (110)-oriented face-centered cubic supercrystals of the ZIF-8 particles by adjusting the amount of surfactant. This publication explains how the orientation of self-assembly of ZIF-8 can be controlled by adjusting the nature and the amount of surfactant.

We also describe that the photonic property of these supercrystals depends on their growth orientation.

The last study found in Appendix presents the assembly of supraparticles using polyhedral MOF particles, which expands the type of self-assemblies made of colloidal MOF particles. This study includes the confinement synthesis of supraparticles of four types of polyhedral MOF particles: cubic, truncated rhombic dodecahedral, and rhombic dodecahedral ZIF-8 particles as well as octahedral UiO-66 particles. We also study the relationship between the ordered structure of the different supraparticles and their structural coloration.

Resumen

La presente Tesis Doctoral ha tenido como objetivo investigar el potencial de los Metal-Organic Frameworks (MOFs) como fuente de partículas poliédricas para ser ensambladas y dar lugar a una nueva generación de materiales auto-ensamblados. Desde su descubrimiento hace unos 25 años, el descubrimiento de miles de MOFs ha generado un amplio catálogo de partículas cristalinas altamente porosas que engloban la mayoría de las formas poliédricas. La investigación presentada en esta Tesis tiene como propósito aprovechar este amplio catálogo de partículas poliédricas para fabricar nuevos materiales auto-ensamblados porosos con estructuras originales y que presenten nuevas propiedades fotónicas.

La Tesis se estructura en dos partes. El Capítulo 1 compone la primera parte, en la cual el lector encontrará una introducción al campo del auto-ensamblado, con una breve descripción de las interacciones involucradas, los diferentes tipos de auto-ensamblado y las diferentes estrategias sintéticas. El capítulo continua con una breve introducción a los MOFs desde sus orígenes hasta sus aplicaciones potenciales. En esta sección, se ha hecho especial énfasis en los pocos ejemplos de la literatura en los cuales partículas de MOFs han sido usadas para generar estructuras auto-ensambladas.

La segunda parte de la Tesis se inicia con el Capítulo 2, donde se definen los objetivos generales y específicos. A continuación, en el Capítulo 3, se describen de una manera concisa los diferentes resultados obtenidos durante esta Tesis. Los resultados detallados se podrán encontrar en las tres publicaciones reproducidas en los Capítulos 5, 6 y Apéndice.

La publicación del Capítulo 5 describe el uso de la forma poliédrica de las partículas de MOF para dirigir el ensamblaje de clústeres coloidales a través de la fusión coloidal. Se ha estudiado como, gracias a esta forma poliédrica, se pueden construir clústeres con diferentes geometrías controlando la interacción de una sola partícula esférica de poliestireno en cada una de caras de los poliedros de MOF. Con esta estrategia, se han podido obtener clústeres octaédricos hexacoordinados (6-c), cúbicos (8-c) y cuboctaédricos (12-c) a partir de partículas de ZIF-8 cúbicas, de UiO-66 octaédricas y de ZIF-8 rombododecaédricas.

En la segunda publicación, incluida en el Capítulo 6, se describe una nueva metodología "sin uso de plantilla" para el auto ensamblado orientado en las direcciones (111)-, (100)-, and (110) de supercristales de partículas de ZIF-8, con simetría cúbica centrada en las

caras. Esta publicación explica como sólo ajustando la naturaleza y la cantidad de surfactante se puede controlar la orientación del auto-ensamblado de partículas de ZIF-8. También se describe la correlación entre las propiedades fotónicas y la orientación del supercristal.

La última estudio, reproducida en el Apéndice, se ha centrado en el ensamblado de suprapartículas esféricas usando las partículas poliédricas de MOF, expandiendo así los tipos de auto-ensamblados de este tipo de partículas. Esta publicación incluye el ensamblaje en esfera confinada de cuatro tipos de partículas de MOF: partículas de ZIF-8 cúbicas, rombododecaédricas truncadas y rombododecaédricas, y partículas de UiO-66 octaédricas. También se ha estudiado la relación entre la estructura ordenada de las diferentes suprapartículas y su coloración estructural.

Acknowledgements

Firstly, I would like to thank my supervisor Prof. Daniel MasPOCH and Dr. Inhar Imaz for their support and guidance during my PhD period. Their patience and tolerance gave me the confidence and motivation to complete my PhD study. I have learned a lot from them. Without their constant help, this dissertation would not be possible.

Secondly, my special thanks to my collaborators Civan, Jiemin Wang, Junwei Wang, and Jose Angel Pariente for their perfect collaborations and generous contributions. I have learned a lot of professional knowledge and gained a friendship from them. I cannot finish this Thesis without their help.

Thirdly, I offer my thanks to our previous group members Luis Carlos, Amirali, Javier Perez, Heng, Jordi, Ceren, Javier Troyano, Jorge, Thais, Vincent, Gerard, Rosa, Najmeh, Hossein, Farnoosh, Asier, Cristina, and Natalia with whom I had a lot of fun working together and learned so much. Among them, I have to mention some people who have impressed me, Luis Carlos, you are a funny and sagacious person, I will not forget your enthusiasm for projects and life and your generous help to me; Heng who is the first Chinese member in Nanoup, thanks to your help and advice when I was a beginner; Ceren, you are a very nice and warm person, I will remember all the happiness we shared each other; Jorge, you are a smart and strong man, I will not forget your confidence for projects; Thais, you are a beautiful and kind person, I will not forget your patience and kindness. It would be boring in the lab without you.

I would like to thank my current group members Laura, Anna, Yunhui, Borja, Akim, Alba, Libni, and postdoc Aranú, Mary, Sonia, Leyre, Cornella, Susana for sharing projects and happiness. Among them, I want to express my admiration for Aranú, I have learned a lot from our discussions; I want to express my gratitude to Laura, I hope our friendship will last forever. Also thanks to our technicians Marta and José for making work easier in the lab for us.

Next, I also thank my flatmates and neighbors Xudong, Ting, Xu, Kaidi, Jiarui, Fei, Zhengwei, Kai, and Junfang who made my life colorful and interesting. Many thanks to my Chinese colleagues in ICN2: Lei Zhao, Qiuyue, Junjie, Liming, Yue Zhang, Zhi Li, Pengyi, Haibing, Zhifu, Peng Xiao, Ying Liu, Junda, and Xin Wen for their help and encouragement. Also thanks to my friends Zhaobin and LiuLiu for their optimistic attitude that gave me confidence. I will not forget your enormous help when I have language problems and many other things.

Meanwhile, I also thank our team of badminton Songbai, Yu Chen, Xiaodong, Huan Tan, Yi Xiao, Hailin, Zheng Ma, Kai Wang, Shun Yao, Yunwei, and Qiaoming with whom I had so much fun playing together. In addition, I would like to express my gratitude to my friends who are in China and other countries. I still remember our pleasant trips and thoughtful conversations. Thank you all guys.

My other special thanks are for the China Scholarship Council (CSC) which provides me the scholarship to finish my PhD study.

Last but not least, I want to express my deepest profound gratitude to my parents and relatives. Thanks to their forever support and love, especially when I miss them and encounter setbacks. None of these could happen without them. I love you!

Chapter 1

Introduction to Self-Assembly of Colloidal Particles and Metal-Organic Frameworks

1. Self-Assembly of Colloidal Particles

1.1. Introduction to Self-Assembly of Colloidal Particles

Self-assembly is the process in which a system's components organize into ordered functional structures or patterns as a consequence of specific, local interactions among the components themselves, without external direction. Self-assembly is a ubiquitous process in nature. For example, Tobacco mosaic virus (TMV) composed of 2130 identical protein subunits, which assemble around the viral ssRNA to form a helical structure with a hollow central cavity of 4 nm diameter, is a perfect illustration that many natural structures find their origin in self-assembly processes.¹ In 1990s, the understanding of self-assembly processes attracted an increased interest among chemists. Inspired by these natural and spontaneous processes, researchers aimed on using non-covalent interactions of different nature to form stable, structurally well-defined aggregates under equilibrium conditions.² Typical examples of molecular self-assembly include the formation of molecular crystals,³ phase-separated polymers,⁴ macromolecular assembly in lipid bilayers,⁵ protein aggregates,^{6,7} and protein folding,⁸ as well as the pairing of nucleotide^{9,10} in DNA nanotechnology.

Based on the self-assembly concept, the 90's represented the advent of colloidal self-assembly. Derived from the Greek word *kolla* (which means glue), the term colloid was first introduced by Thomas Graham in 1861 to describe Francesco Selmi's "pseudosolutions".¹¹ According to Thomas Graham, colloidal systems show slow diffusion rates and no sediments under normal gravity. Colloids can be found everywhere, both in nature and in our daily life; such as in clouds, clay deposits, toothpaste, milk, inks, paints, and even blood. A colloidal suspension can be defined as a mixture of small particles, droplets or bubbles ranging in size from 1 nm to 1 μ m, which are dispersed in a continuous medium that can be solid, liquid or gas. The first studies of colloids can be located in 1827, when the British botanist Brown studied a suspension of pollen grains in water. He observed that minute particles suspended in a liquid experience a permanent motion. In this liquid, each particle equally moved in any direction. This motion, which was termed as 'Brownian motion', appeared due to the irregular collision of colloidal particles with the molecules of the surrounding fluid.¹² In 1905, Albert Einstein and William Sutherland explained the Brownian motion with a quantitative theory. They stated that the Brownian motion of colloidal particles is caused by continuous collisions between solvent molecules with fast-moving. In this motion, two particles move independently

even when they are close to each other within a distance less than their diameter. At higher temperatures, this motion is more active. However, a colloidal suspension is not inherently stable. The particles interact, exerting forces on one another that arise from a variety of physical mechanisms, including van der Waals interactions, steric repulsions, electrostatics, magnetostatics, depletion attractions, hydrodynamic flows, and capillary forces. Thanks to these interactions, colloidal particles can self-assemble into well-ordered and functional superstructures.¹³

Today, self-assembly of colloidal particles provides infinite possibilities for constructing functional materials such as photonic crystals, chemical or biochemical sensors, optical devices, and drug delivery systems. In this introduction, the assembly forces as well as most typical self-assembly methodologies used to create those colloidal superstructures will be introduced. Then, I will cover representative examples of colloidal superstructures, starting from those made of traditional spherical particles. We will also show how polyhedral particles have recently been introduced and are opening new directions in the self-assembly of superstructures field. In this sense, metal-organic frameworks (MOFs) have recently been shown as a promising and rich type of porous polyhedral particles to be used on the self-assembly new architectures.

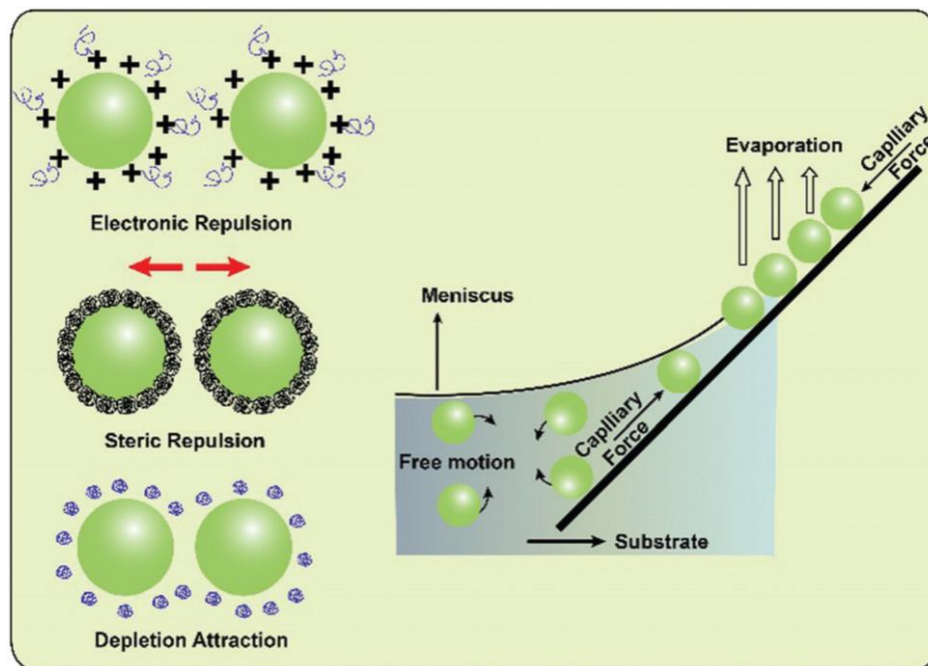


Figure 1. Schematic illustration of some of the typical interactions involved in the self-assembly of colloidal particles. Adapted from ref. 16.

1.2 Assembly Forces

Various forces can play a leading role in the self-assembly of colloidal particles. In general, the forces involved in the assembly of colloidal systems include van der Waals forces, electrostatic effects, steric repulsion, molecular dipole interactions, depletion attraction, capillary and gravitation forces (Figure 1).¹⁴⁻¹⁷

1. van der Waals forces

van der Waals interactions, prevalent in non-covalent interaction between molecules, are fundamental in colloidal systems. They are mainly attractive forces arising from interactions between the partial electric charges. There are three types of van der Waals interactions: the dipole-dipole interaction (Keesom); the Debye interaction between induced dipole and dipole; and the London dispersion forces between two induced dipoles.¹⁸ The relative strength of these interactions is: Keesom forces > Debye forces > London dispersion forces. According to the Hamaker integral approximation,¹⁹ the simplest approach to estimate the van der Waals interaction between two spheres is a pairwise summation of this interaction of atom pairs located within two bodies, which can be presented by the equation :

$$U_{\text{vdw}}(d) = \frac{A}{3} \left[\frac{R_1 R_2}{d^2 - (R_1 + R_2)^2} + \frac{R_1 R_2}{d^2 - (R_1 - R_2)^2} + \frac{1}{2} \ln \left(\frac{d^2 - (R_1 + R_2)^2}{d^2 - (R_1 - R_2)^2} \right) \right]$$

where A is the Hamaker coefficient that depends on the properties of the particles, R_1 and R_2 are the radii of two spheres, and d is the distance between two spheres. Thus, in the self-assembly of monodispersed spherical nanoparticles driven by van der Waals interaction (where the van der Waals interaction acts as a primary attractive component and commonly eliminates electrostatic and steric repulsion), forces normally generate densely packed structures; for instance, hexagonal arrays in two dimensions and hexagonal close-packed or dense *fcc* crystal in three dimensions.²⁰ However, as the Hamaker constant can be affected by multibody effects, retardation and the presence of anisotropic dipolar forces, a real estimation of van der Waals interactions in colloidal polydisperse samples or anisotropic particles is very difficult. For example, in non-spherical nanoparticles, isotropic van der Waals attraction should be balanced with other anisotropic dipolar forces.²¹ For example, nanorod particles prefer to pack densely in a side-by-side configuration rather than an end-to-end arrangement because of the stronger van der Waals between the contact faces.²²

2. Electrostatic effects

Similarly, electrostatic interaction plays an indispensable role in the self-assembly processes. Electrostatic forces are either attractive or repulsive depending if the particles have the same or opposite charged particles. When particles with an identical surface charge approach each other, resulting in an overlap of electrical double layer surrounding the particles, they will be repulsed. On the contrary, oppositely charged particles will be attracted.²³⁻²⁵ Together with van der Waals interactions, electrostatic repulsions are the major forces that govern the stability of a colloidal dispersion. Both interactions are additive, i.e. $W_{\text{total}} = W_{\text{edl}} + W_{\text{vdW}}$ according to Derjaguin, Landau, Verwey, and Overbeek (DLVO) theory. From one side, attractive vdW interactions tend to induce aggregation of colloidal particles, whereas the repulsive forces between particles prevent colloidal particles against aggregation or coagulation.¹⁸ In this respect, Grzybowski *et al.* reported that the random aggregation of nanoplates caused by the strong van der Waals forces can be prevented adding a positively charged surfactant, which lead to their self-assembly nanoplates into ordered mono- and multilayered superlattices induced by solvent evaporation.²⁶ On the other side, the electrostatic attraction among oppositely charged colloidal particles is important to self-assemble binary colloidal particles into nanoclusters, superlattices or supercrystals.¹⁷ Today, it is known that electrostatic interactions can be easily tuned through an external chemical factor (such as pH, size or valence) as well as different solvents and concentrations.¹⁶

3. Steric repulsion

Steric repulsion usually occurs between two colloidal particles coated with polymers or molecules. For instance, if the tails of the long chain molecules are compatible with the continuous phase of the colloid dispersion, they repel one another and cause a repulsion between the particles. This repulsion is due to two effects: an osmotic effect caused by the high concentration of chains in the region of overlap; and a volume restriction effect due to the loss of possible conformations in between the two particles. The effectiveness of the repulsion depends on the length and structure of the chains, the adsorption energy, and the properties of the carrier. Steric repulsive forces can help particles to counteract attractive forces inherently and to maintain colloidal stability.²⁷ For example, the introduction of unsaturated long-chain polymers or tethering end-functionalized polymers enhances an steric stabilization and can promote crystallization of the particles.²⁸

4. Molecular surface interactions

Molecular surface force is an interaction that originates from decorating the surface of nanoscale components with various chemical functions that promote short-range attraction interaction, such as covalent bonds, dipolar interaction, hydrogen bonds, and so on. The specific molecular interactions that functionalize nanoparticles lead to significant and often specific interparticle potentials between themselves, leading to their organization into a variety of ordered structures. The magnitude of these surface forces is approximately equal to the number of single bonds formed multiplied by the effective bond strength of the molecular interactions. Thus, the multivalent interactions consisting of several molecular groups can be very strong between suitably functionalized surfaces. There are three different molecular forces that are widely used in the self-assembly of colloidal particles: the hydrogen bonding, the DNA base-pair interaction and the molecular dipole interaction.²⁹

Hydrogen bonding is intrinsically electrostatic, in which a proton mediates the attraction of two electronegative atoms. It can orient the adjacent molecules, meaning that it is directional and attractive. The density of the surface functional groups (*e.g.*, -OH, -COOH, -NH₂) can usually determine the strength of this interaction. Besides, self-assembly of colloidal particles with hydrogen bonding can be regulated in response to pH values. For example, the carboxylic acid functionalized gold nanorods can be reversibly assembled and disassembled for many cycles by tuning the pH value of the colloidal solution, as the carboxylic acid groups can form hydrogen bonds but the deprotonated acid cannot form them bonds at high pHs.³⁰

DNA base-pair interaction is a special type of hydrogen bonding, which is based on DNA strands binding selectively and strongly with their complementary strands. In addition, the magnitude of this interaction can be modulated by adjusting temperatures below and above the melting temperature. The Mirkin's group first reported the self-assembly of gold nanoparticles coated with DNA strands into macroscopic materials based on the complementary DNA linker.³¹ After that, DNA-based self-assembly has attracted close attention in many aspects and has enabled the formation of complex materials, such as hydrogels, crystal materials, conductive polymer materials, and biomedical materials.^{32,33}

Molecular dipole interaction is very similar to the interaction between magnetic particles. Hence, a molecule with a permanent electric dipole moment interacts with each other through dipole-dipole interactions. A particular example was realized with gold nanoparticles functionalized with azobenzene-terminated thiols and dodecylamine.³⁴ The configuration (*cis* or *trans*) of the azobenzene group can be transformed using UV light. Therefore, when this

group is in its *cis* isomer form, it has an electric dipole moment and therefore, the molecular dipole interactions between the nanoparticles can be switched on.

5. Depletion attraction

The depletion force is an “indirect” attractive force between particles that occurs in colloidal suspensions with more than one species suspended in the continuous phase. The depletion force results from interactions between colloidal particles and so-called depletants, small sized non-absorbing solutes dispersed in a continuous phase and excluded from the volume between the large particles. Asakura and Oosawa firstly demonstrated a model to explain the large hard spheres and small spheres (called depletants) in a dispersion.³⁵ The origin of the phenomenon is this excluded volume that the large disperse phase particles constitute for the depletants due to the repulsion between particles and depletants. So, when the large spheres approach each other, the depletion zones overlap and the depletant cannot enter the gap between spheres. The osmotic pressure of the depletants get unbalanced. The depletants push the particles together because of this unbalanced osmotic pressure. At the same time, the volume available for depletants increases when the depletion zones overlap. The total free energy of the overall system is decreasing because the increment of translational freedom is higher than the loss in entropy from the aggregation of larger spheres. Second parameters, such as the depletant concentration, temperature and the relative size between larger and smaller spheres, leads to changes in the magnitude of the depletion attraction.^{36,37} To date, the depletion attraction has driven the self-assembly of colloidal particles with low curvatures, such as nanocubes and nanorods.³⁸⁻⁴⁰ Additionally, the depletion attraction is also different in smooth or rough particles, with the smooth particles showing preferred depletion attraction.⁴¹

6. Capillary force

Capillary forces are interactions between particles mediated by fluid interfaces. When the suspending liquid enter in contact with a non-miscible mobile phase, it tends to minimize its total surface by appropriately deforming the liquid surface between the solid particles. There are two kinds of capillary forces: the flotation capillary force, and the immersion force.^{23,42} Both of them are governed by the surface tension of the liquid medium, wettability of the particle surface and the particle size. When the particles float at the liquid interface, the deformation can happen in the liquid surface due to gravitational and buoyant force. Then, the liquid surface tension tends to minimize the interface space, thus leading to an effective interaction between the particles. The resulting interaction is called flotation capillary force. If

the particles are located on a solid interface in a liquid film with the thickness less than the particles size, the deformation of the liquid surface is still present. This interaction is called immersion capillary force. This kind of force can be used to produce more complicated ordered assemblies by controlling the solvent evaporation.

7. Gravitation force and Brownian motion

A particle with a size of the colloidal scale (between 1 nm and about 1 μm) undergoes Brownian motion, which is defined as the random motion of particles suspended in a medium. Discovered in 1827 by the British biologist Robert Brown, Brownian motion consists (according to Langevin description) as the combination of essentially two forces acting on a single colloid: the thermal forces induced through collisions with the solvent molecules, and the friction force originated by the solvent viscosity, which damps the particle motion. For colloidal particles, Brownian motion dominates over sedimentation. However, when the colloidal particles have large sizes and high density, gravitational forces can take a predominant role resulting in the particle sedimentation.^{43, 44, 45}

1.3 Typical Self-Assembly Methods

There are several techniques that can be used for the self-assembly of colloidal particles into 2D and 3D superstructures. Below, some of the most typical methods are briefly introduced.

1. Evaporation-induced methods

Surface evaporation-induced self-assembly is the most basic way to self-assemble colloidal particles into ordered superstructures. The technique involves depositing a colloidal suspension on a substrate, followed by allowing the film to evaporate. The key of the process is the formation of the thin film at the liquid meniscus region that creates strong capillary force. Then, temperature, humidity and pressure of colloidal solution play a crucial role during the evaporation process.⁴⁶ Nagayama *et al.* reported a simple way (drop-casting) to study the formation 2D periodic arrays of latex particles.^{47, 48} They proposed a two-stage mechanism. First, attractive capillary forces appearing between particles partially immersed in a liquid layer induced the nucleus formation. Then, crystal growth occurred through convective particle flux caused by the water evaporation from the already ordered array. However, the evaporation of drops of colloidal suspensions and solutions of non-volatile species are not always homogenous

and leave behind ring-like solid residues along the contact line. This coffee-stain effect, named for the characteristic deposit along the perimeter of a spill of coffee, influence negatively the formation of large areas of ordered monolayers. In this case, the use of surfactant or polymer even using anisotropically shaped particles can avoid this effect.⁴⁹⁻⁵¹ Different methods have been explored to make convective assembly sufficiently most robust and reliable. For instance, Nagayama and coworkers introduced an alternative strategy based on vertical deposition to improve the long range order of self-assembled monolayers.⁵² In this case, the direction of substrate movement is opposite to the direction of particle growth front in order to induce the convective assembly. The deposition can be tuned controlling the removing of the substrate slowly. The density and homogeneity of particle films can be also improved by confining the liquid in a Blade-coating-geometry. In this method, the reservoir is held between a substrate and a blade which is moved by a motor against the substrate (Figure 2a).⁵³⁻⁵⁵ The homogeneous monolayer growth relies on the combination of the blade velocity, evaporation rate and concentration of suspension.

2. Spin-coating method

Spin-coating is a thin film production technique that is very common for semiconductor fabrication. It is also a common method for the production of highly uniform colloidal crystal thin films. This technique involves depositing a colloidal dispersion onto an optically flat substrate, which is then rotated at high-speed (1000–10 000 rpm). In this method, several factors dominate the quality and thickness of ordered superstructures, including the rotation and acceleration rates, the particle size, size distribution, dispersant volatility, viscosity and wettability, and the particle concentration (Figure 2c). Moreover, this method can also be combined with other techniques to construct ordered superstructures. For example, Mukherjee and coworkers recently studied the conditions under which perfect colloidal arrays of a variety of particles (PS or PMMA) can form on flat as well as patterned surfaces.⁵⁶

3. External forces-induced methods

External forces such as electric or magnetic fields proved to be powerful tools for the assembly of colloidal particles into ordered structures. However, methods based on these forces require to work with particles that respond to these stimuli. In the case of electric field, the motion of colloidal particles in suspension can be modulated applying constant or alternative voltages. This electric field can regulate the sedimentation velocity or generate lateral attraction of particles to lead to 2D or 3D periodic arrays. For example, Kumacheva *et al.* reported the

electrodeposition of monodispersed charged colloidal spheres onto a substrate patterned with an array of electroconductive grooves.⁵⁷ Other parameters such as voltage, time and particles mobility can also be used to manipulate the growth speed of assemblies. For example, Schope and coworkers found that colloidal monolayers could be better arranged via convective assembly if particles were exposed to an electric field with a vertical position. For the use of magnetic fields, magnetic interactions between magnetic particles are required. In general, substrates are placed between two permanent magnets that generate a magnetic field in parallel or vertical positions.⁵⁸ Magnetic particles can be assembled into an orderly manner according to the magnetic field after evaporating the remaining solvent. In this case, the majority of the self-assembly studies concern ferromagnetic or superparamagnetic particles. As an example, Yin and co-workers reported how magnetic fields can guide the assembly of superparamagnetic colloidal Fe₃O₄-based particles into periodically arranged arrays, and how the photonic properties of the resulting superstructures can be reversibly tuned by manipulating the external magnetic field.⁵⁹

4. Template-assisted methods

Surfaces patterned with two-dimensional arrays can also be used as templates to direct the self-assembly of colloids. These methods consist on confining the colloidal dispersion between two glass substrates. The templates are typically patterned using lithography techniques. By changing the morphology and dimensions of these templates, multiple colloidal particles have been ordered into different structures, clusters, chains, etc.⁵⁸ Template-assisted self-assembly can also be used in combination with other techniques (*e.g.* spin-coating, evaporation-induced methods) to expand the type of superstructures.⁵⁸⁻⁶³

5. Interface-induced methods

Langmuir-Blodgett process is the most studied interface-induced method. As its origin, it was used for the assembly and orientational control of molecular monolayers. The Langmuir-Blodgett process consists on the deposition of amphiphilic compounds at the air-water interface followed by the controlled compression of the generated molecular monolayers to induce ordering and orientation.⁶⁴ Then, a previously immersed substrate is vertically and slowly drawn from solution. The molecules adheres to it leaving a surface that is hydrophobic. In the case of colloidal particles, the process is very similar. A suspension of spherical particles in a solution made of surfactant and water non-miscible solvent mixtures is usually spread onto the water subphase. Then, the solvent is left to evaporate. Finally, the controlled compression of

the layer leads to the formation of ordered superstructures that are easily transferred onto different type of substrates, such as glass or Si-wafer (Figure 2b). Using the Langmuir-Blodgett method, for example, Schoonheydt *et al.* produced 2D opal films by depositing a suspension of ammonium-modified SiO₂ spheres dispersed in a chloroform/ethanol/sodium dodecylsulfate (SDS) mixture on water subphase.⁶⁵ One of problems of the Langmuir-Blodgett method is, however, that it is time consuming and requires special equipment. For this reason, alternative interface-induced methods have also been explored to get long range films without the need of any special equipment. For example, Vogel's group presented a method to produce high quality colloidal monolayers based on direct assembly.⁶⁶ In this method, the particles dispersion is added to the air-water interface via a glass slide tilted with an angle of approximately 45°. The spread dispersion form patches of colloidal monolayers that remained afloat at the interface. The monolayer patches continue to grow in size upon further addition of colloids until the complete interface is covered with a monolayer. Finally, the monolayer is collected immersing a substrate into the water phase and elevating it at a low angle.

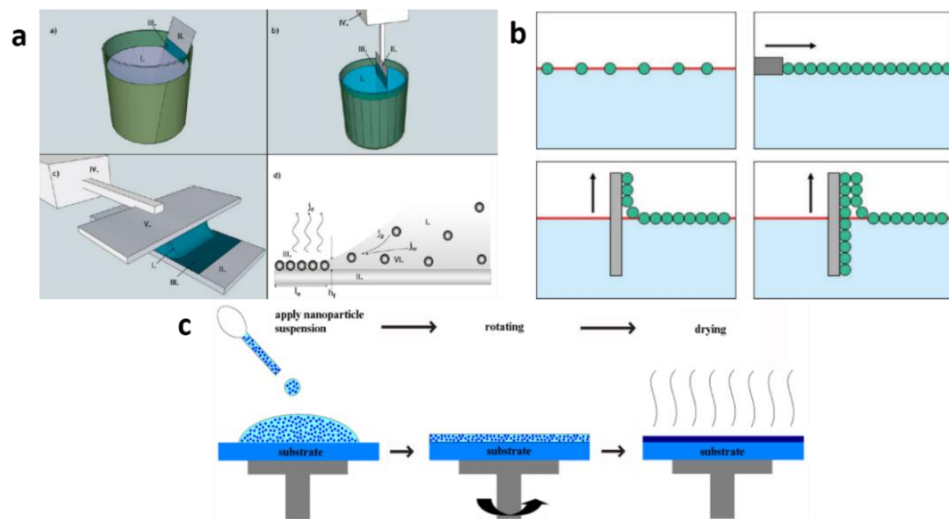


Figure 2. Schematic illustrations of representative self-assembly methods: (a) evaporation-induced methods for convective particle assembly; (b) Langmuir-Blodgett deposition process; and (c) spin-coating. Adapted from ref. 54 and 64.

1.4. Self-Assembly of Colloidal Particles into 2D and 3D Superstructures

Today, the range of colloidal particles that can be self-assembled into ordered superstructures is very vast. Indeed, there are many materials that have been used as colloidal particles, including clays, polymers, porous materials, metals, minerals and semiconductors.¹⁵

In all these materials, the particles shape is a key factor that direct the final self-assembled superstructures.^{67,68} In this section, some representative studies that use different shapes of colloidal particles to assemble different superstructures will be introduced.

1.4.1 Self-Assembly Symmetries

The majority of colloidal systems show either a face center cubic (*fcc*) structure, a hexagonal close packed (*hcp*) structure or a body centered cubic (*bcc*) structure. *Fcc* and *hcp* are considered as close-packed structures because particles cannot be packed any tighter, and each particle touches its neighbor in any direction. In a non-close-packed structures, such as for example *bcc*, the distance between atoms or planes is bigger. The *fcc* structure consists of a particle located at each cube corner and a particle in the center of each cube face. In a *bcc* structure, a particle exists at each cube corner and one particle is at the center of the cube. In this case, there are no close-packed planes, but only close-packed directions. Finally, in a *hcp* structure, a close-packed plane at the bottom and top of the unit cell is separated by three particles in the cell center, which are also part of a close-packed plane (Figure 3).⁶⁹

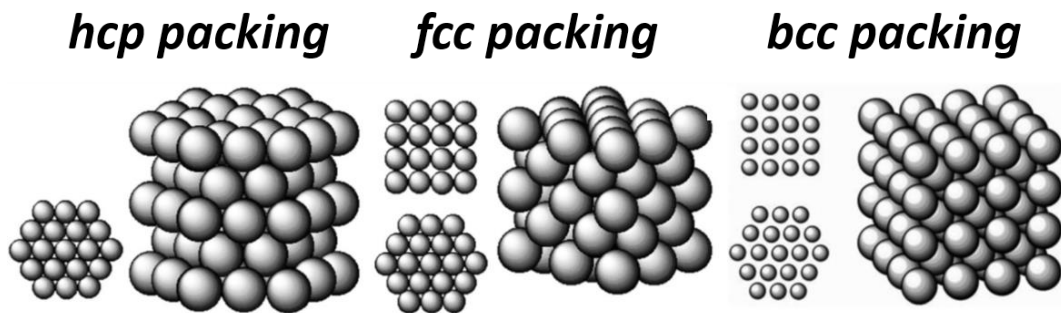


Figure 3. Schematic illustration of the most common structures found in colloidal superstructures. Adapted from ref. 69.

1.4.2 Spherical Particles

In the past decades, self-assembly of colloidal spheres has been regarded as a powerful and effective route to fabricate multidimensional superstructures for myriad applications.^{43,70-74} Sphere serves as the simplest geometrical shape, as it has the lowest surface potential energy and the smallest surface area compared to other shapes. Representative colloidal materials in the form of spherical particles are silica colloids, polystyrene spheres and poly(methyl methacrylate) (PMMA) microspheres. These spherical particles are perfect building blocks to fabricate closed-pack *fcc* and *hcp* structures and open-packed superstructures. For example,

silica spheres with a size large than 0.5 μm self-assembled into a 3D hexagonal *hcp* closed-packed lattice through slowly sedimentation process in cyclohexane.⁷⁵ Takeda and coworkers also reported the formation of highly ordered colloidal crystals by growing two sizes of polystyrene spheres (240 nm and 466 nm) into ordered packing on a glass slide using a fluorinated solvent (Figure 4a).⁷⁶

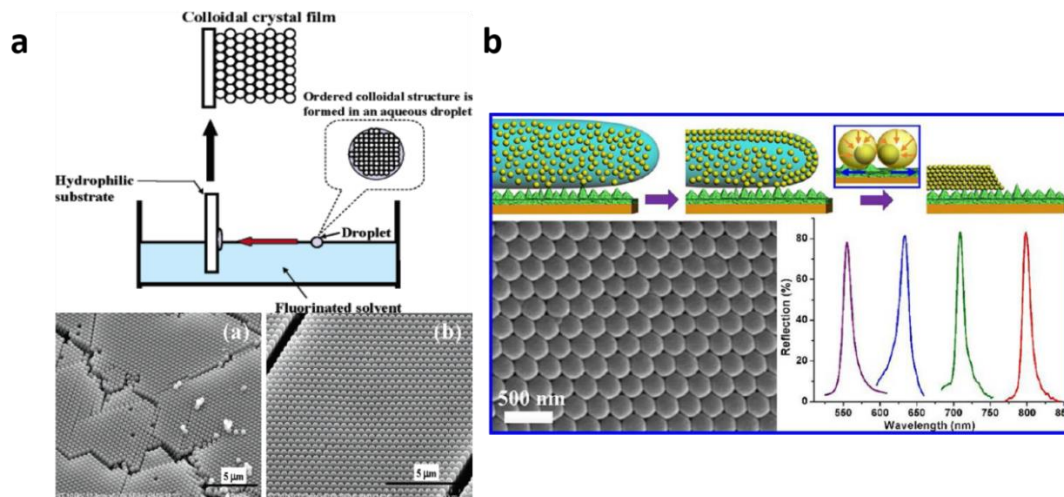


Figure 4. (a) Schematic illustration and SEM images of the formation of highly ordered 3D colloidal polystyrene crystal films. (b) Schematic illustration and SEM images of the formation of colloidal photonic crystals made of latex particles, and their UV-vis reflection spectra. Adapted from ref. 76 and 79.

Another important feature of colloidal particles is that their length scale is comparable to the wavelength of visible light. This makes colloidal self-assembly especially attractive for engineering photonic crystals.^{77,78} For instance, Song's group reported the self-assembly of spherical latex particles into centimeter-scale 3D photonic crystals with a reduced void fraction on low-adhesive superhydrophobic substrates (Figure 4b).⁷⁹ The resulting photonic crystals showed narrow stopbands due to the absence of cracks and void fraction. Also, Cho *et al.* prepared crack-free 3D colloidal silica photonic crystals using a PDMS stamp.⁸⁰ These photonic crystals assembled on curved substrates with various relief patterns via the life-up method. Ozin's group achieved a very high quality colloidal crystal film using isothermal heating evaporation-induced self-assembly procedure, which had a high degree of structural perfection and optical properties.⁸¹

Beyond colloidal crystals made of one type of particles, more complex structures can be designed and fabricated. For example, Jonas's group reported two cases of binary colloidal crystals. Using vertical lifting deposition, these authors transferred a three-component mixture

with colloidal particles of different materials (polystyrene, poly(methylmethacrylate) and silica) in suspension yielding multilayered trimodal colloid crystals. Then, they created inverse opals obtained by pyrolysis.⁸² The same group also reported the formation of binary colloidal crystals by tuning the size and concentration of polystyrene and silica particles (Figure 5a).⁸³ Very recently, in 2020, Sacanna *et al.* made a step forward on controlling of the assembly of spherical colloids.⁸⁴ They could create ionic colloidal crystals isostructural to cesium chloride, sodium chloride, aluminum dibromide and K_4C_{60} by combining different ratios of particles having a different size and nature and using different polymers to control the Columbic forces between particles. Compared to other methods, this approach does not require a previous encoding or engineering of particles to be used as model colloidal ions and primed for crystallization (Figure 5b).

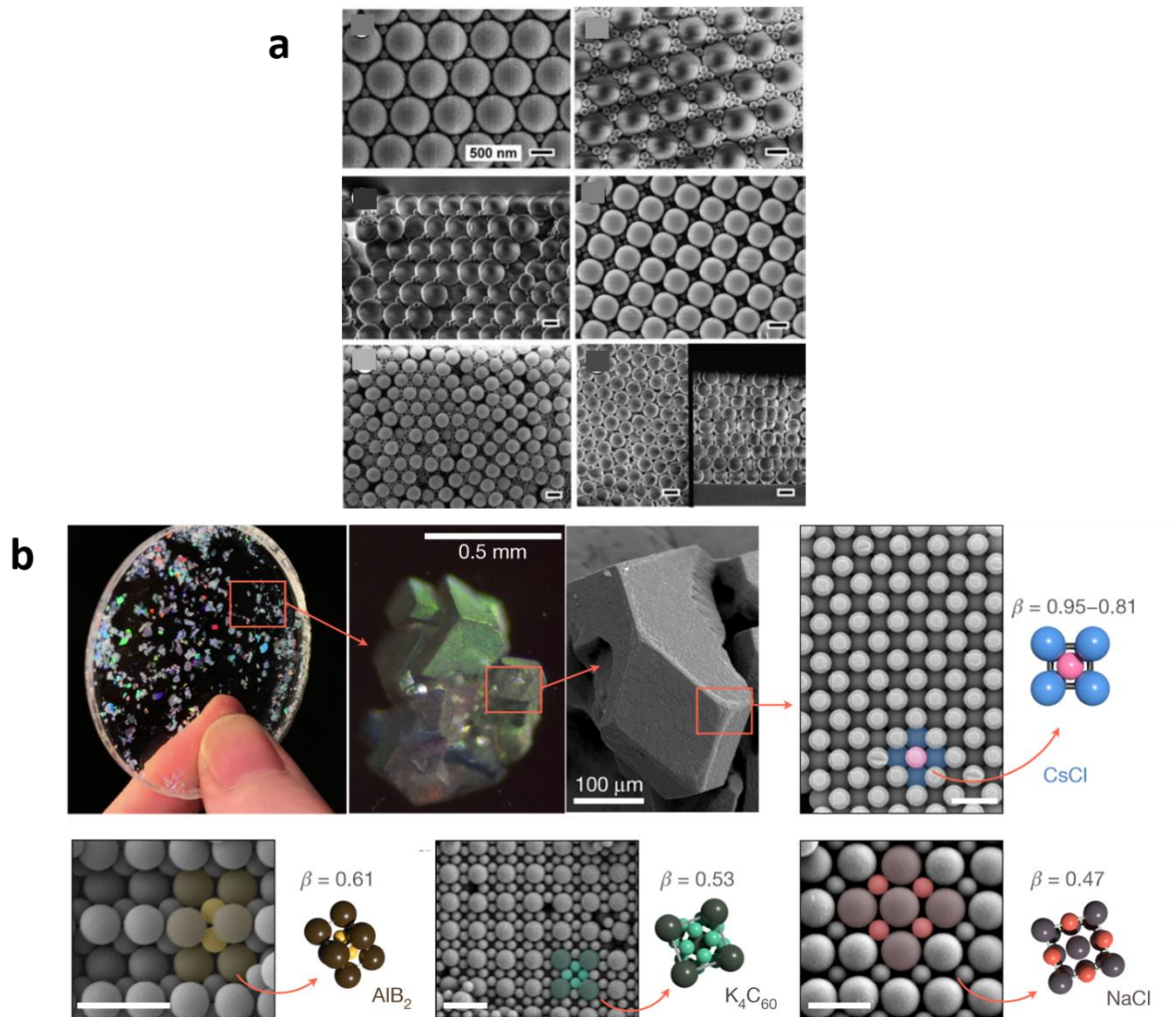


Figure 5. (a) SEM images of the binary colloidal crystals made of polystyrene and silica particles with different lattice geometry. (b) Schematic illustration and SEM images of the different structure of a series of ionic colloidal crystals. Adapted from ref. 83 and 84.

1.4.3 Polyhedral Particles

Well-defined facets and high shape symmetries are the distinct features of polyhedral particles. In order to maximize entropy, polyhedral particles tend to self-assemble and align with each other along their adjacent planes. In this context, Glotzer *et al.* reported 145 convex polyhedra whose assembly arises solely from their anisotropic shape through Monte Carlo simulation. In this study, four types of organizations were investigated, including liquid crystals, plastic crystals, crystals and disordered phases, to help design more complex materials and understand the packing rules of polyhedral particles.⁸⁵ In this section, multidimensional superstructures built with polyhedral particles will be presented in brief. Compared to spherical colloidal particles, the large majority of the self-assembled superstructures composed of polyhedral particles are made with particles which a size is lower than 100 nm.

1.4.3.1 Cubes

Colloidal nanocubes are represented as a regular shape with six $\langle 100 \rangle$ facets.⁸⁶ Typically, nanocube particles prefer to attach face-to-face each other via their $\langle 100 \rangle$ facets and form a square type conformation. Many examples of ordered arrays with simple cubic arrangement have been reported.⁸⁷⁻¹⁰² For example, Wang *et al.* reported the self-assembly of cetrimonium bromide (CTAB)-coated 20 nm Pd nanocubes into well-defined simple cubic supercrystals by slow evaporation of a particle dispersion (Figure 6a).¹⁰¹ The simple cubic arrangements could also be expanded to other arrangements, such as *fcc*, *bcc*, *bct* (body-centered tetragonal), controlling the system condition or particles modification.^{100,103-108} For instance, Gang and Kumar *et al.* revealed that 20 nm Au nanocubes with grafted DNA shells self-assembled into body-centered tetragonal and body-centered cubic arrangements (Figure 6b).¹⁰⁸ Also, Fang and coworkers reported that 20 nm Pt nanocubes can self-assemble into simple-cubic and body-centered tetragonal ordered superstructures via choosing different carrier solvents (hexane and toluene). The authors attributed the different self-assembly to the ligand-solvent interactions.¹⁰⁹

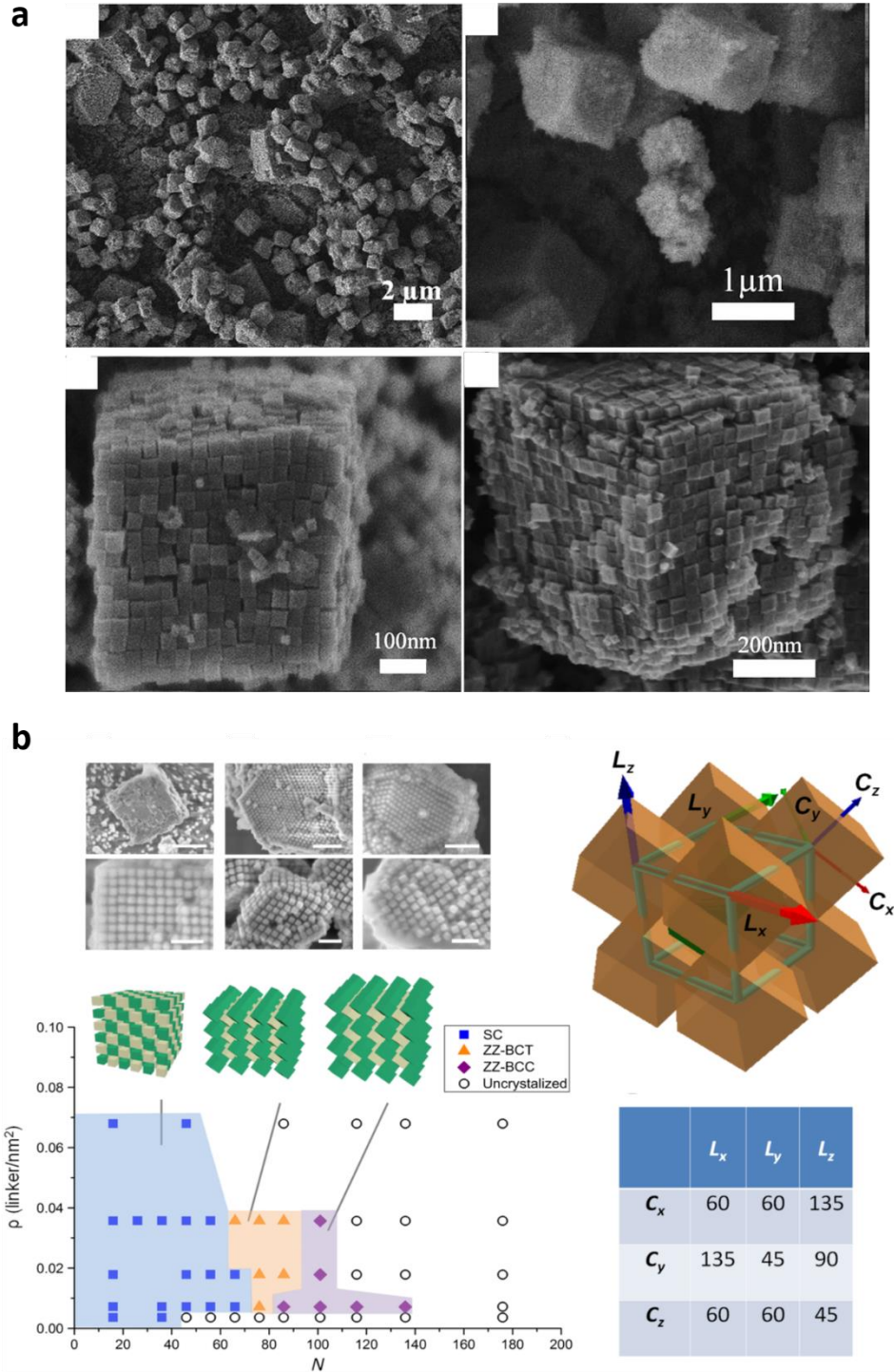


Figure 6. (a) SEM images of simple cubic structures assembled from CTAB-coated Pd nanocubes. (b) SEM images and model explanation of the body-centered tetragonal and body-centered cubic arrangements formed by DNA-grafted Au nanocrystals. Adapted from ref. 101 and 108.

1.4.3.2 Octahedra and truncated octahedra

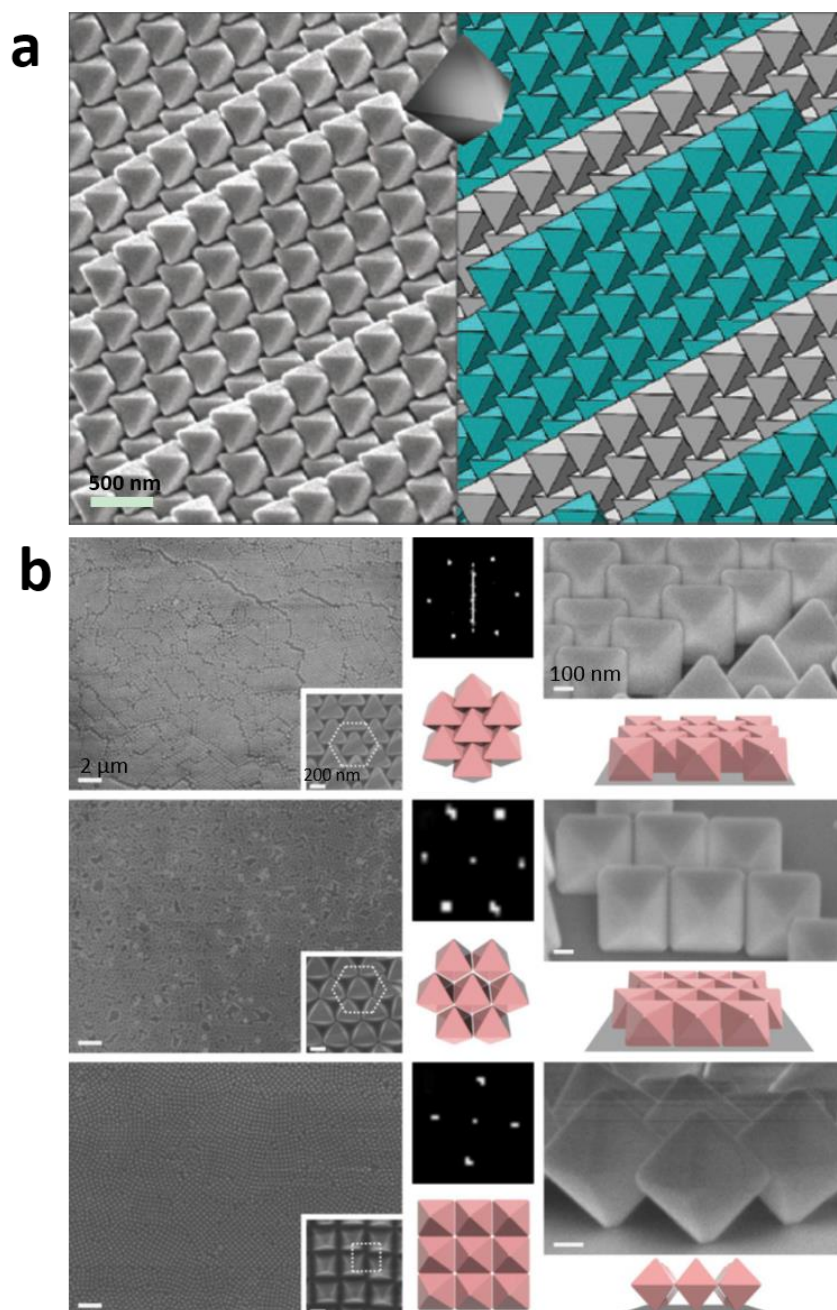


Figure 7. (a) SEM images and the corresponding diagrams of Minkowski superlattice assembled by octahedral Ag particles. (b) SEM images of hexagonal close-packed 2D superlattice, open hexagonal superlattice and square superlattice assembled by tailoring the surface chemistries of octahedral Ag particles. Adapted from ref. 102 and 123.

Octahedron is a Platonic solid that contains 8 triangular faces, 6 vertices and 12 sharp edges. The surface of an octahedron is terminated with eight facets of $\langle 111 \rangle$ direction and twelve edges with $\langle 100 \rangle$ direction. According to theoretical simulations, the densest packing

for hard octahedral particles is the Minkowski lattice.^{110,111} In this time, Yang and coworkers reported that monodisperse polyvinylpyrrolidone (PVP)-coated Ag octahedral particles self-assemble forming a Minkowski dense packing lattice. In this configuration, each octahedral Ag particle is surrounded by six other particles in an incomplete facet-to-facet contact to form dense packing layers (Figure 7a).¹⁰² In addition to this dense packing, small octahedral particles can also assemble in a non-close-packed body-centered cubic (*bcc*) phase.^{112,113} For example, self-assembly of Pt₃Ni nanoparticles into a *bcc* packing structure through drop-casting and solvent evaporation was achieved by Fang and Smilgies. In this *bcc* superstructure, octahedral particles shared their vertices leading to a low packing density assembly.¹¹⁴ Moreover, as the superstructures assembly from octahedral particles can present more than one arrangement, multilayer structures can also be formed.^{99,115-122} In Ling's work, it has been revealed that tuning the surface wettability of octahedral Ag particles can generate three different 2D plasmonic superlattices, including the hexagonal close-packed superlattices; an open hexagonal array via edge-to-edge contact; and a different square superlattice that only the vertices of particles contacting the substrate (Figure 7b).¹²³

1.4.3.3 Tetrahedra

The tetrahedron is a Platonic solid with triangular faces. It has 4 triangular faces, 6 straight edges and 4 vertex corners. To date, only few studies have been published on the self-assembly of tetrahedral particles.¹²⁴⁻¹³⁰ For example, using thermodynamic computer simulations, Glotzer's group revealed that hard tetrahedra undergo a first-order phase transition to a 12-fold symmetry dodecagonal quasicrystal. Applying infinite pressure, their self-assembly reaches a packing fraction of 0.8324.¹²⁶ From the experimental point of view, Talapin's group reported the self-assembly of tetrahedral nanocrystals into an open-structure, which had never been achieved by theoretical simulation (Figure 8a).¹²⁸ In this structure, the spatial proximity of vertices may benefit from the strong ligand-ligand interaction potential on the crystal surface curvature, forming the vertex-to-vertex contact structure. Other two studies are from Chen's group, who used truncated tetrahedral quantum dot nanocrystals as building particles (Figure 8b).^{129,130} These authors demonstrated that three distinct superstructures (1D chiral tetrahelices, 2D quasicrystal-approximant superlattices and 3D cluster-based *bcc* single supercrystals) can be obtained. They also showed the formation of 10-fold quasicrystalline superlattices assembled from truncated tetrahedral quantum dots with anisotropic patchiness.

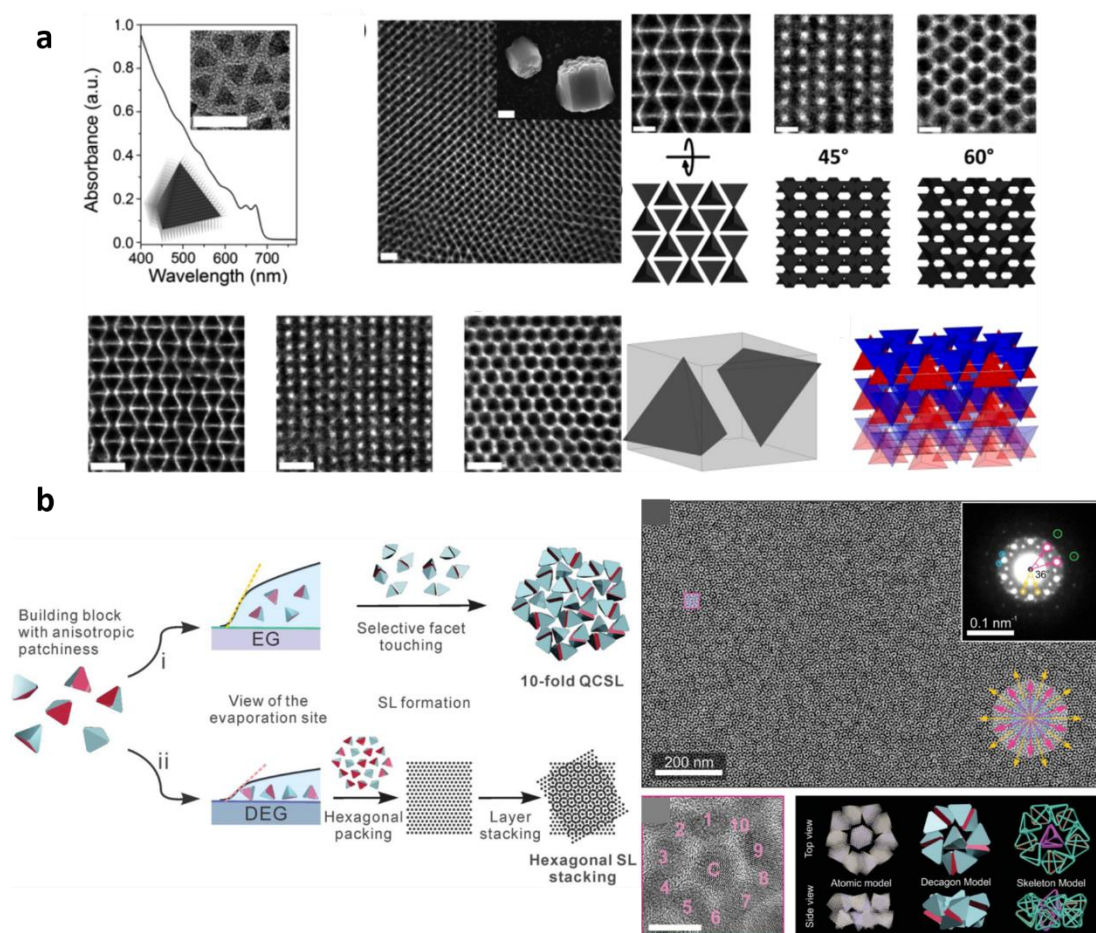


Figure 8. (a) TEM images and model of three projections of the open-structures achieved by Talapin's group. (b) Schematic representation and TEM images of the 10-fold quasicrystalline and hexagonal superlattices stacking from truncated tetrahedral quantum dots. Adapted from ref. 128 and 130.

1.4.3.4 Other shapes

In addition to the most common polyhedral shapes mentioned above, there are other polyhedral shapes particles that can form ordered superstructures. For example, rhombic dodecahedral (RD) nanoparticles can be spontaneously and closely packed into well-defined multilayers of *fcc* or plastic *fcc* structures.¹³¹

Moreover, other more peculiar polyhedral particles including trisoctahedra,¹³² icosidodecahedra,¹³³ rectangular nanoblocks,¹³⁴⁻¹⁴² (hexagonal) bipyramids,^{143,144} and hexagonal bistrustums¹⁴⁵ have been used as building particles to form ordered arrangements. For example, Cheng *et al.* reported that a new type of plasmonic superstructures with four distinct orientational packings (namely, horizontal alignment, circular arrangement, slanted alignment, and vertical alignment) can be self-assembled using bipyramid Au nanoparticles.¹⁴³ Mello Donega and coworkers demonstrated the self-assembly of colloidal hexagonal

bipyramid- and hexagonal bipyramid-shaped 20 nm ZnS nanocrystals into 2D superlattices at the liquid–air interface (Figure 9a).¹⁴⁴ Interestingly, the small truncation at the tip of the hexagonal bipyramid-shaped nanocrystals transformed the resulting superstructures from an hexagonal to a tetragonal arrangement. Also, an exotic structure, a four-leaf clover-like structure, was also created from the self-assembly of Au@Ag right bipyramidal particles driven by a depletion attraction from Zhang’s group (Figure 9b).¹⁴⁵

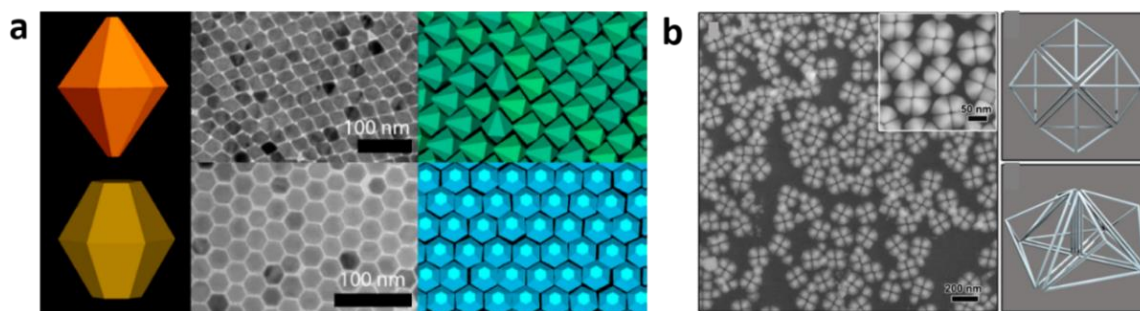


Figure 9. (a) SEM images of self-assembled superlattices of hexagonal bipyramid-shaped and hexagonal bipyramid-shaped ZnS nanoparticles. (b) SEM images and model of self-assembled Au@Ag right bipyramids with a four-leaf-clover-like pattern. Adapted from ref. 144 and 145.

1.5. Self-Assembly of Colloidal Particles into Supraparticles

1.5.1 Supraparticles Made of Spherical Particles

Supraparticles are defined as hierarchical agglomerates assembled from prefabricated building blocks.¹⁴⁶⁻¹⁴⁸ The assembly of colloidal particles into supraparticles usually occurs in confined spaces, such as emulsion droplets, microfluidic capillary or within evaporated droplets.¹⁴⁹⁻¹⁵¹ In a typical process, emulsion droplets (usually made using a surfactant as a stabilizer) are formed by mechanical shearing of water and a colloidal dispersion.¹⁵² Then, removing water or the low-boiling nonpolar phase lead to colloidal assembly. Dijkstra, Blaaderen and colleagues deeply studied the colloidal assembly of spherical particles into droplets. They first prepared a water-in-oil emulsion of spherical particles. After evaporation of the solvents, they obtained crystalline ‘supraparticles’, with three different types of packings depending on their size: a supraparticle with a diameter of 105 nm showing a Mackay icosahedral symmetry; a 216 nm-in-diameter supraparticle with an anti-Mackay rhombicosidodecahedral structure; and finally, a 734 nm-in-diameter supraparticle consisting of a single face-centred cubic (FCC) crystal domain. They concluded that entropy and spherical confinement alone are sufficient for the formation of stable icosahedral clusters (Figure 11a).¹⁵³

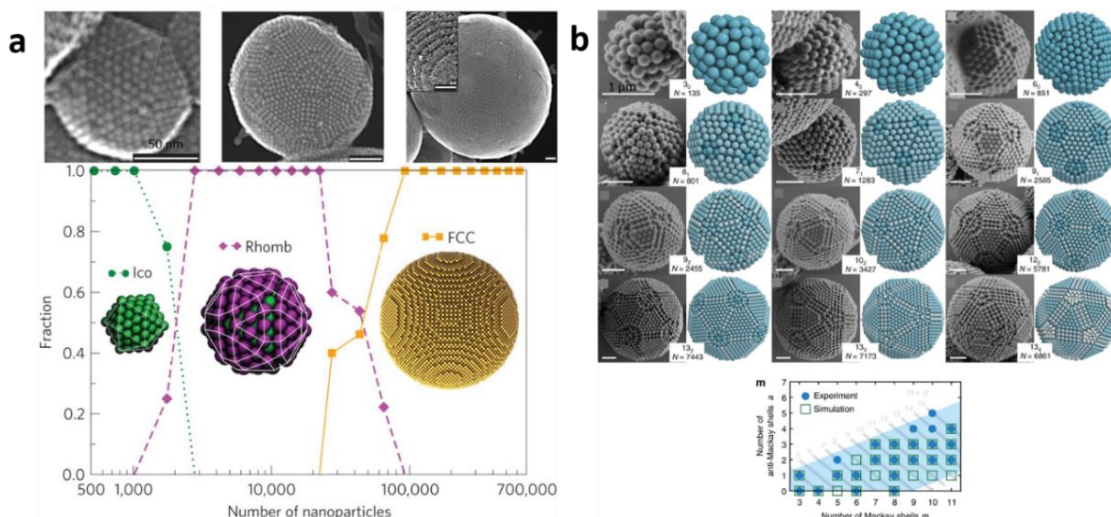


Figure 11. (a) SEM images of supraparticles with Mackay icosahedral symmetry, anti-Mackay rhombicosidodecahedral structure and single face-centered cubic (FCC) structure (top), and simulation results of size dependence of the cluster structure (below). (b) SEM images of various magic number colloidal clusters and comparison to model. Adapted from ref. 153 and 154.

It is worth mentioning the very deep research done by Vogel's and Engel's groups on understanding the formation of colloidal supraparticles.¹⁵⁴⁻¹⁵⁷ For example, they demonstrated that hard sphere-like colloidal particles show a magic number effect when confined in spherical emulsion droplets. In addition, colloidal supraparticles with magic number were shown to be more stable than those without magic number (Figure 11b). The same groups also showed that structural color was a useful tool to investigate the structure and dynamics of colloidal supraparticles. They found that colloidal supraparticles with icosahedral, decahedral and *fcc* structures could be distinguished by characteristic structural color motifs, such as circles, stripes, triangles, or bowties.

Another effective method to confine a colloidal dispersion in small droplets and form supraparticles is spray-drying.¹⁴⁸ Spray drying is a well-known method of particle production which comprises the transformation of a fluid material into dried particles. It consists on pumping a solution or dispersion to an atomizer, breaking up the liquid feed into a spray of fine droplets. Then, the droplets are ejected into a drying gas chamber where the moisture vaporization occurs, resulting in the formation of dry particles. In the case of supraparticles, a particle dispersion is atomized in a hot gas stream into small droplets. When the spray enter in contact with the hot stream, the solvent starts to evaporate from the droplet and the particles are homogeneously distributed. Then, the particles are brought to the meniscus region by the solvent flux and local concentration gradients form at the air/droplet interface. Secondly, the

particles are delivered from the core to the interface by convective flow of the solvent evaporation to lead to the formation of the supraparticle. Many factors (*e.g.* the properties of precursors, liquid flow rate, solvents, temperature, etc.) can affect the morphology of the supraparticles in the spray-drying process.¹⁵⁸⁻¹⁶³ Thus, depending on the fine tuning of these parameters, densely packed supraparticles, mixed component supraparticles, encapsulated supraparticles, and even doughnut-like supraparticles can be obtained. For instance, Mandel and coworkers produced uniformly packed silicon raspberry-like supraparticles using 350–400 nm sized Stöber nanoparticles by carefully tuning the drying temperature.¹⁶⁴ Another example was reported by Okuyama *et al.*, who used an aerosol spray method to produce two types of supraparticles made of small-SiO₂/large-SiO₂ and Al₂O₃/SiO₂ supraparticles.¹⁶⁵

1.5.2 Supraparticles Made of Polyhedral Particles

Compared to spherical particles, there are only limited studies focusing on ordered supraparticles made of polyhedral particles. Some theoretical studies from Prof. Sharon Glotzer and Prof. Marjolein Dijkstra predicted the rich variety of supraparticles assemblies that can be achieved using polyhedral particles. For example, Glotzer *et al.* reported the densest supraparticles expected from five types of Platonic solids in spherical confinement using Monte Carlo simulations, which exhibited a variety of high-symmetry and magic number clusters depending on their different geometry (Figure 12b).¹⁶⁶ However, most of these theoretical, predicted assemblies still demand empirical proofs. To our knowledge, there is only one study reported in 2018 by Blaaderen, Wang and coworkers that demonstrated that the packing of supraparticles was determined by the flat faces of the cubic nanoparticles (Figure 12a).¹⁰⁰ From their study, these authors observed that sharp cubes tended to form simple-cubic superstructures due to their strong orientational correlations, whereas rounded cubes were favorable to assemble into icosahedral supraparticles.

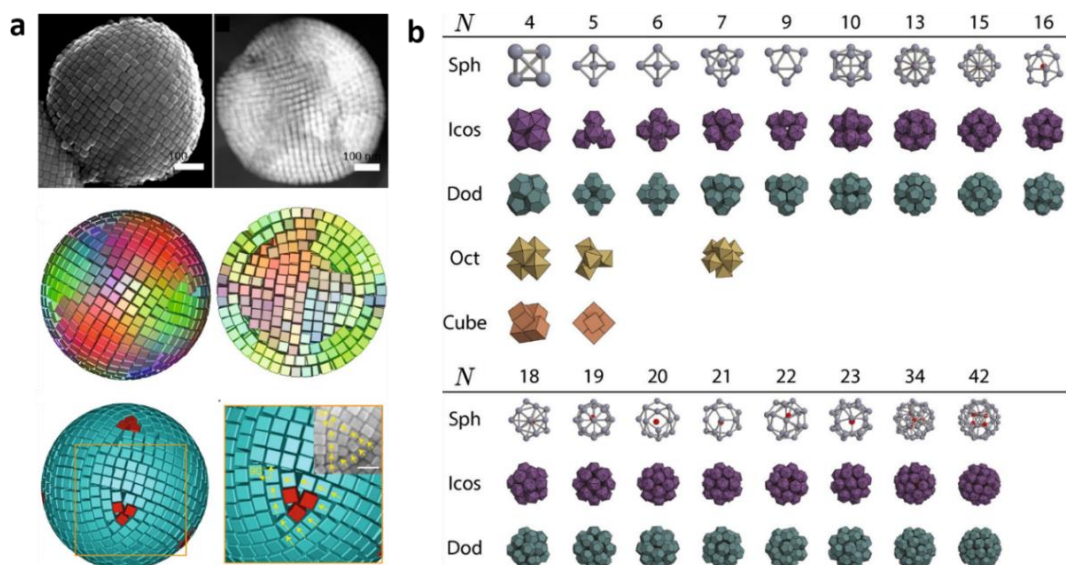


Figure 12. (a) SEM images and simulation results of supraparticles made of sharp nanocubes. (b) Densest clusters structures made of different polyhedra under the spherical confinement using Monte Carlo simulations. Adapted from ref. 100 and 166.

1.6 Self-Assembly of Colloidal Particles into Colloidal Molecules and Patchy Particles

In recent years, much efforts have been focused on the assembly of colloidal clusters or colloidal molecules, in which the components particles are viewed as “big atoms”. The concept of colloidal molecules was firstly introduced by van Blaaderen in 2003 for describing the entities consisting of a small number of spherical particles that mimic the symmetry of molecular structures (Figure 13).^{167,168} From a fundamental point of view, colloidal clusters provide an attractive platform for investigating the structure, thermodynamics, and kinetics of finite-size systems on the mesoscale. The concept of patchy particles is also closely related to colloidal molecules, as they can be described as surface-patterned particles with a limited number of specific interaction areas.¹⁶⁹⁻¹⁷¹ Thus, colloidal molecules can be regarded not only as building particles for assembly, but also as precursors for patchy particles. Hence, it is possible to use both particles for constructing more complex architectures. The latest developments of colloidal molecules and patchy particles have been summarized and presented in several excellent reviews.¹⁷²⁻¹⁷⁷ A brief introduction of their synthesis and self-assembly will be given in this section.

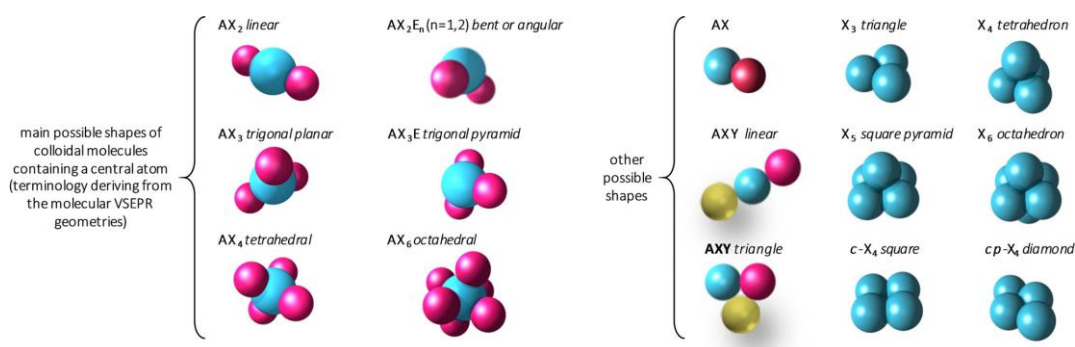


Figure 13. Schematic illustration of the classification of some colloidal molecules. Adapted from ref. 172 and 175.

1.6.1 Synthetic Routes to Form Colloidal Molecules

1. Clustering of isotropic colloidal spheres

These routes consist of generating isotropic colloids and then, clustering them through modulating different forces. In the literature, different examples of clustering of isotropic spheres using van der Waals, electrostatic interaction or covalent bonds can be found. To increase the control on the clustering process, colloids are often contained in confined droplets, such as those of emulsions. Through this approach, Pine, Manoharan and colleagues used this confinement into droplet to synthesize several polymer or silica clusters made of more than two spherical particles (Figure 14a).¹⁷⁸⁻¹⁸⁰ In this process, spherical particles touch each other on the surface of droplets. Then, the evaporation of the liquid caused deformation of the droplet. And finally, clusters generated from the aggregation of the particles due to capillary forces. Kraft and coworkers reported a facile way to synthesize colloidal clusters by delaying the polymerization of the liquid protrusions on polystyrene or poly(methyl methacrylate) spheres (Figure 14b).^{181,182} In this case, the crosslinked spherical particles lead to coalescence of the droplets upon collision, thereby forming colloidal clusters that could be solidified upon polymerization.

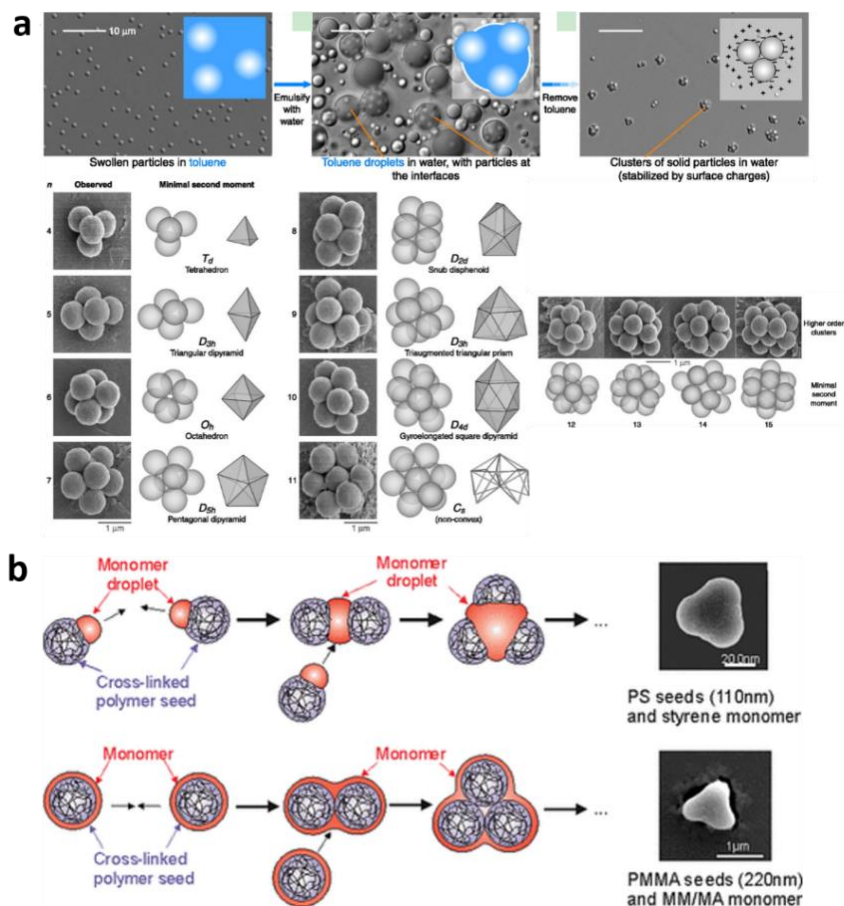


Figure 14. (a) Schematic illustration of the formation of clusters in droplets and corresponding SEM images of several clusters formed using the confinement in emulsion droplets. (b) Schematic illustration and SEM images of the formation of colloidal clusters by coalescence of the liquid protrusions. Adapted from ref. 178 and 182.

2. Controlled phase separation phenomena

The most common approach for synthesizing colloidal molecules is the seeded emulsion polymerization. Controlling the particle morphology, such as the formation of core-shell particles, is one of the advantages of the emulsion polymerization. Moreover, other equilibrium morphologies can be obtained via seeded growth polymerization by successive additions of different monomers. In this process, seed isotropic polymer spherical particles are first swollen with a polymer monomer solution. The polymerization of this monomer induces a phase separation caused by the immiscibility of the second stage polymer in cross-linked polymer networks, which result in a protrusion on one side of the seed particle and results in the formation of anisotropic particles with different geometries. The quality of these clusters can be improved by controlling the directionality of this phase separation by modulating the

crosslinking density gradients of the seed particles, as proposed by Weitz et al.¹⁷² Using controlled phase separation, snowman-like colloids, linear (AX_2) or triangular trimers (X_3) and diamond particles (X_4) and even colloidal molecules with symmetry of water molecule (AX_2E_2) have been synthesized by phase separation in seeded growth emulsion polymerization (Figure 15).^{183,184}

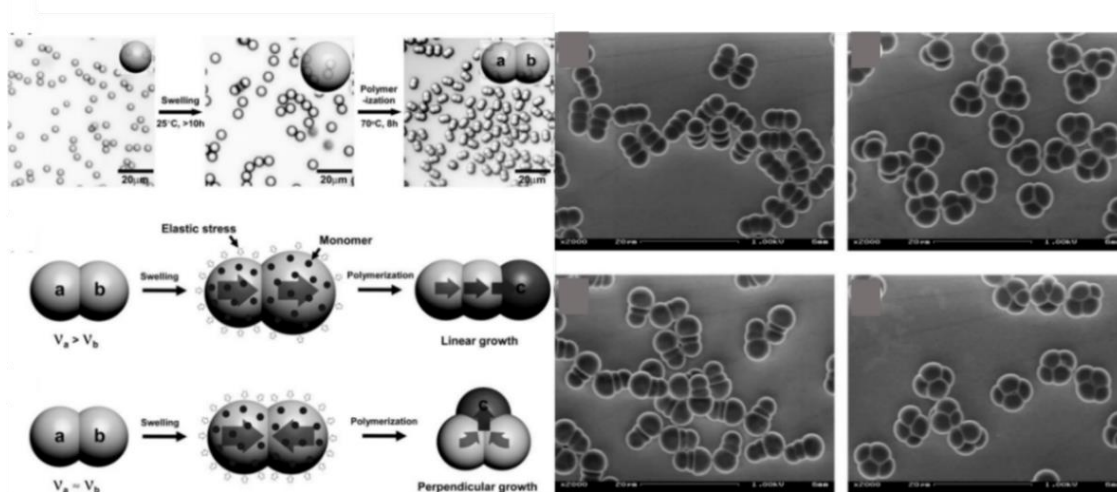


Figure 15. Schematic illustration and SEM images of the formation of nonspherical clusters through controlling phase separations in the seeded-polymerization technique. Adapted from ref. 184.

3. Controlled surface nucleation and growth

If the seed central particle is inorganic, it cannot be swelled. In this case, the nucleation and growth of the satellite colloids occurs on the surface of this central particle. This approach is favorable to synthesize AX_n type colloidal molecules, in which satellite particles nucleate and grow on the surface of the central particles. However, compared to controlled phase phenomena, this method leads to less controlled particles (Figure 16).¹⁸⁵⁻¹⁸⁷ Duguet and colleagues solved this problem treating the seeds with compatibilizers.¹⁸⁸⁻¹⁹⁰ Compatibilizers enhance the blend properties and improve adhesion between the phases, reducing the interfacial tension and stabilizing the final morphology. For example, treating silica particles with methacryloxyalkyltrimethoxysilane as compatibilizer, they created reactive (co)polymerisable sites on the surface of each particle that promote the surface capture of the growing polystyrene macromolecules and therefore, the nucleation of the latex particles. With this method, highly symmetrical colloidal clusters made of polystyrene and silica particles with high homogeneity and yield could be obtained by controlling the surface density of the compatibilizer, the seed concentration and the seed size.¹⁹¹

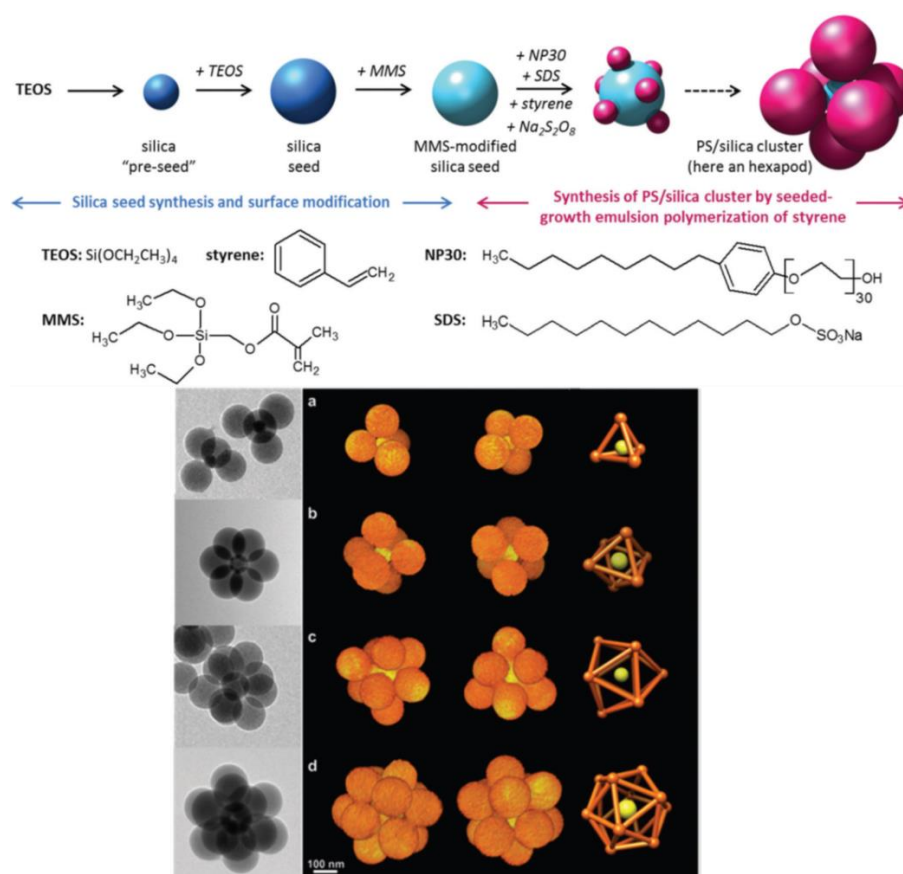


Figure 16. Schematic illustration and SEM images of the formation of polystyrene/silica clusters. Adapted from ref. 186.

1.6.2 Typical Approaches for the Synthesis of Patchy Particles

Several routes have been explored to synthesize spherical patchy particles. The simplest method to create one patch on the surface of one sphere is the vapor deposition onto a close-packed monolayer of spheres. This evaporation can be performed perpendicularly to the monolayer or with an inclination angle. Other methods have also been explored to create particles with more patches. In some of them, pre-clustered colloidal molecules are used as precursors. First, clusters of microspheres are synthesized confining them in emulsion droplets. Then, a particle is swelled from this cluster by polymerization (Figure 14a). For example, Pine, Weck and coworkers obtained colloids with valence and specific directional bonding from amidinated polystyrene spheres containing DNA functionalized patches. They also synthesized colloids with a specific number of cavities starting from silica clusters. These clusters were partially encapsulated with 3-(trimethoxysilyl)propyl methacrylate (TPM) into hybrid patchy particles followed by the selective removal of the silica using hydrofluoric acid (Figure 17a).¹⁹²

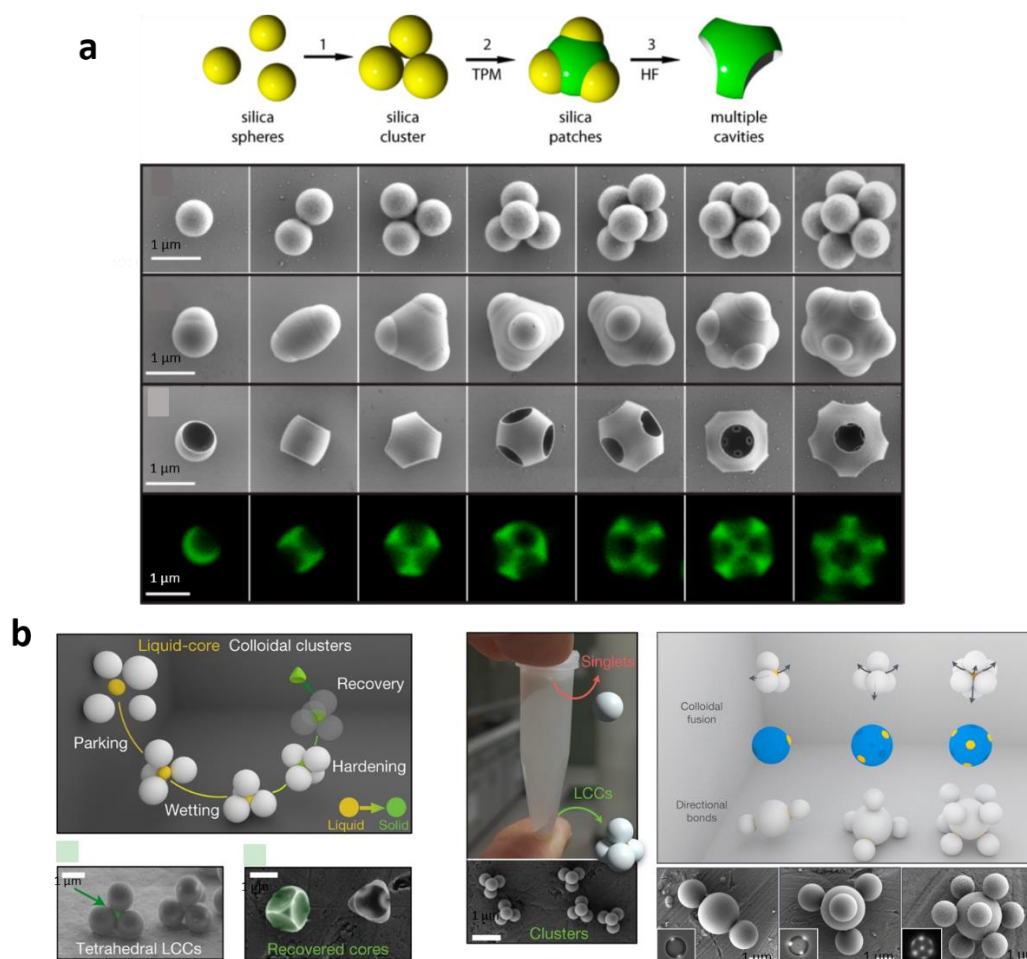


Figure 17. (a) Schematic illustration and SEM images of the synthesis of silica-TPM patchy particles and multicavity particles. (b) Schematic illustration and SEM images of the synthesis of liquid-core colloidal clusters (LCC) and higher-order LCC caused by colloidal fusion. Adapted from ref. 192 and 193.

Recently, a new concept named colloidal fusion for producing patchy particles was presented by Sacanna's group (Figure 17b).¹⁹³ Based on coordination dynamics and wetting forces, uniform patchy particles have been synthesized from hybrid liquid-solid clusters that evolve into particles with a range of patchy surface morphologies via controlling the addition of a plasticizer. Another interesting method is the template free method. Here, Taylor's group reported a simple, one-step and template-free method to fabricate patchy particles that contain silver patches and silica.¹⁹⁴ The formation of these patchy particles was done by heterogeneous nucleation of silver onto the surface of calcined silica and then, by diffused growth on the surface. Moreover, they applied this method to the formation of gold patches onto polystyrene spheres using ascorbic acid.¹⁹⁵ The patchy morphology and number could be tuned by pH and concentration of ascorbic acid.

1.6.3 Self-Assembly of Patchy Particles into Hierarchical Superstructures

Once synthesized, colloidal clusters or patchy particles can be self-assembled into more sophisticated architectures thanks to their diverse geometries and interactions. The aim of this section is to present some latest studies performed in this direction. Granick and coworkers first reported the formation of a 2D kagome structure using triblock Janus patchy particles (microparticles bearing two patches).¹⁹⁶ Such type of structure was also predicted using computational simulation by Sciortino and Romano.^{197,198} They showed that such exciting kagome lattice happened at higher number density when the strength of the interaction between patches is large enough to overcome the random forces arising from the thermal jiggling of the particles. In this experiment, triblock Janus particles consisted of one electrically charged band in the middle made by latex spheres and two patches with hydrophobic caps. Self-assembly occurred slowly in the salt solution in order to avoid repulsion after sedimentation. More recently, Weck's group reported the directional bonding and assembly of non-spherical colloidal hybrid microparticles in 2D superstructures. To this end, they used biphasic triblock polystyrene-3-(trimethoxysilyl)propyl methacrylate-polystyrene (PS-TPM-PS) particles or ellipsoidal di-patch particles with DNA-coated patches.¹⁹⁹ Triblock PS-TPM-PS particles with different aspect ratios were synthesized by polystyrene and polymerized 3-(trimethoxysilyl)propyl methacrylate (TPM) via three steps including the cluster encapsulation method, coalescence TPM in toluene and free radical polymerization. The formation of several types of 1D and 2D superstructures, such as 1D tilted ladder chains and 2D square packing, were induced by the surfactant F127 and driven by pole-to-pole and center-to-center interactions. The same authors also reported the synthesis of colloidal di-patch particles functionalized with DNA on the patches and their assembly into colloidal superstructures via both depletion and DNA-mediated interactions (Figure 18).²⁰⁰ They synthesized di-patch particles with azide-containing polystyrene (PS-N₃) as the patches and 3-(trimethoxysilyl)propyl methacrylate (TPM) as the matrix. By tuning the patch size of the particles and assembly conditions, they formed flower-like Kagome lattice, brick-wall like monolayer, orthogonal packed single or double layers, wrinkled monolayer and colloidal honeycomb superstructures.

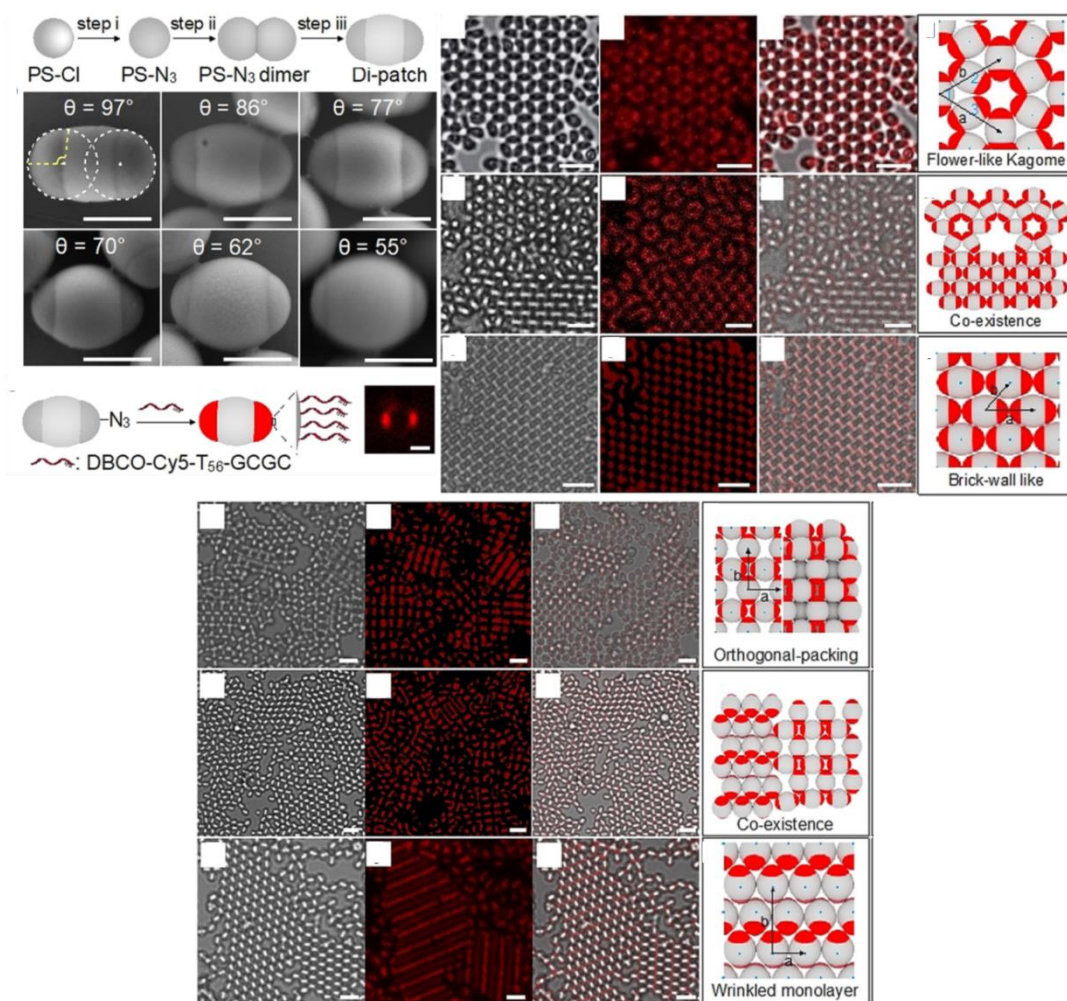


Figure 18. Schematic illustration and SEM images of the synthesis of di-patch particles and their use to assemble open or close-packed 2D or quasi-2D colloidal superstructures. Adapted from ref. 200.

More recently, a very interesting example of 3D self-assembly of patchy particles was reported by Sacanna, Pine *et al.* They showed the self-assembly of tetrahedral patchy particles into a cubic diamond crystal (Figure 19).²⁰¹ To this end, they designed a tetrahedral cluster with retracted sticky patches. In this design, each cluster consisted of one single spherical colloid partially overlapped with four tetrahedral coordinated spherical lobes, and the center of each tetrahedral cluster was a retracted patch modified with DNA. In this model, the DNA modified patches reach each other and bind only when the spherical lobes interlock, which fixes two clusters in the staggered conformation. Tetrahedral clusters were produced firstly by aggregation of non-cross-linked polystyrene spheres and TPM oil droplets through colloidal fusion, and then adding THF to change the compression ratio by deforming the polystyrene lobes. Finally, THF was evaporated and TPM was solidified. TPM can be functionalized by the DNA group through multistep modification. Subsequently, the tetrahedral clusters were

self-assembled into the cubic diamond crystal through steric interlock. The resulting superstructure exhibited a photonic bandgap, which supply the suitable templates for forming photonic materials.

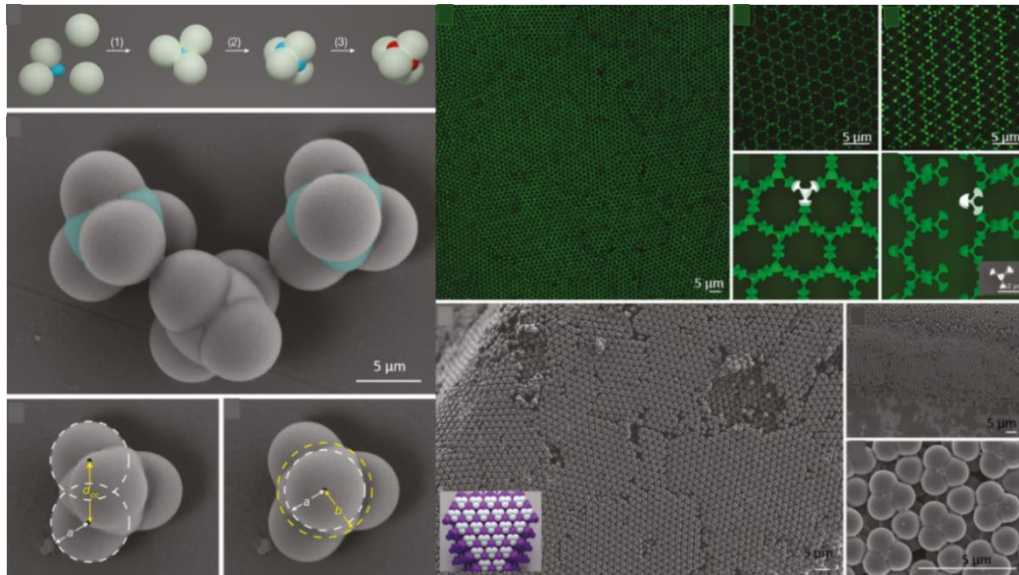


Figure 19. Schematic illustration and SEM images of the synthesis of compressed tetrahedral patchy clusters and their assembly into cubic diamond superstructures. Adapted from ref. 201.

2. Metal-Organic Frameworks (MOFs)

2.1 Introduction to Metal-Organic Frameworks

MOFs are a class of highly porous crystalline materials based on metal fragments connected by organic spacers. The International Union of Pure and Applied Chemistry (IUPAC) defines MOFs as: “A *metal–organic framework, abbreviated to MOF, is a coordination network with organic ligands containing potential voids.*”²⁰² In other words, the coordination bonds act as the connector between the inorganic and organic part, and the word “voids” indicates the porosity of the network (Figure 20). Thus MOFs can be defined as porous crystalline networks assembled by metal ions/clusters and organic ligands through coordination bonds along with one-, two-, or three-dimension. Over the past years, MOFs have been regarded as one of the most attractive porous materials due to their unprecedented porosity, immense surface areas, rich composition, structure variety and myriad properties. To date, over 10,000 structures of MOFs have been collected in the Cambridge Structural Database (CSD) and the number of MOFs reported has been constantly growing in the last 25 years (Figure 21).^{203,204}

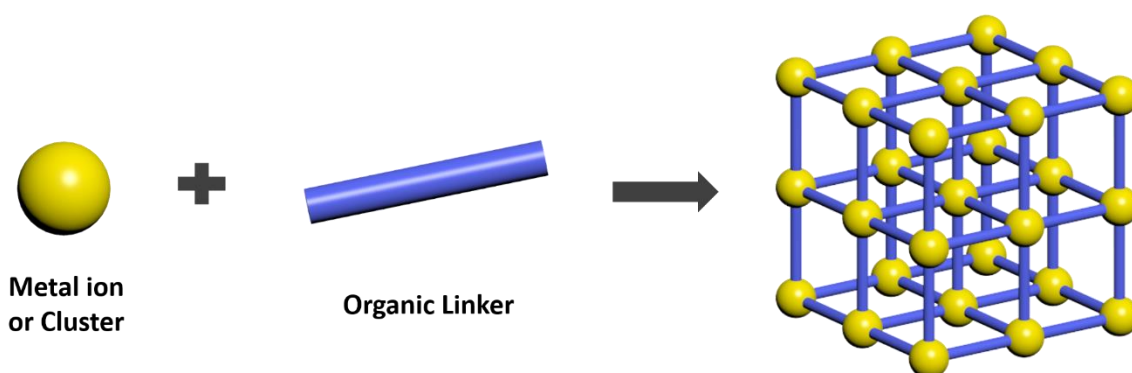


Figure 20. Schematic representation of the formation of MOFs.

When we look back on the development of MOFs, the work of Robson and Hoskins must be highlighted. In 1989, they successfully synthesized the first 3D infinite framework using tetrahedral Cu(I) centers and the tetrahedral ligand 4,4',4'',4'''-tetracyanotetraphenylmethane (TCTPM). The resulting 3D framework exhibited a diamond-like lattice with large tetragonally elongated adamantane-like cavities (Figure 22).²⁰⁵ One year later, they presented the concept of building units for designing and constructing these materials. This concept served for a rational assembly of metal units and organic linkers, such

as periodic diamond-like structures constructed from tetrahedral metal ions and cyano-based ligands.²⁰⁶ Subsequently, this concept was expanded to construct different 3D frameworks by exploring the relevant geometry of the building units. As an example, the tetrahedral PtS building unit was connected through the square-planar porphyrin to form a framework with large channels.²⁰⁷ These pioneering works not only open an avenue in the design and synthesis of coordination polymers but also encourage to start investigating useful properties caused by their special structures. For instance, Fujita *et al.* presented a 2D square network material made by the assembly of Cd ions and 4,4'-bipyridine ligands, which showed heterogeneous catalysis performance.²⁰⁸

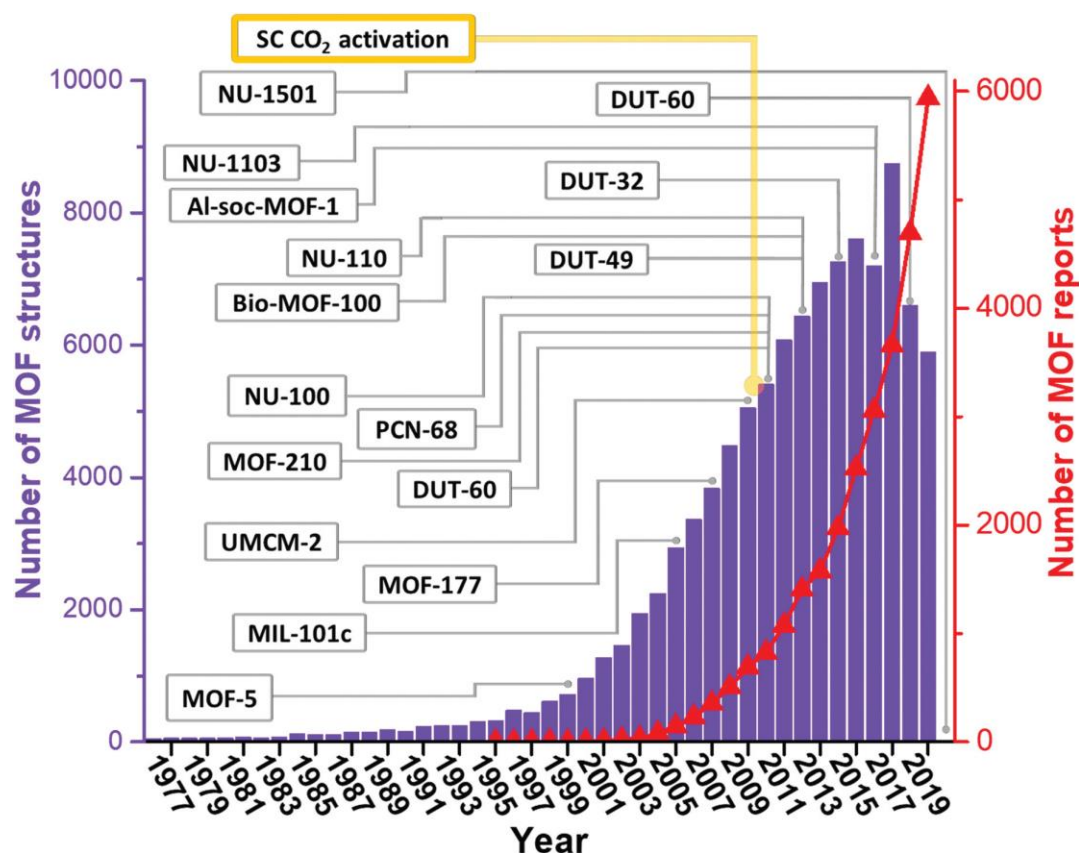


Figure 21. MOF structures reported in the CSD and reported MOFs found in the Web of Science, from 1976 to 2019. Adapted from ref. 203.

The “MOFs” term was first used in 1995 by Prof. Yaghi and coworkers.²⁰⁹ They reported the diamond-like framework $\text{Cu}(\text{4,4'-BPY})_{1.5}\text{NO}_3(\text{H}_2\text{O})_{1.5}$, which was synthesized by connecting trigonal planar copper(I) centers and 4,4'-BPY. This MOF contained two rectangular channels (Figure 23). In this first-generation of MOFs, one of the shortcomings was the lack of permanent porosity because of the poor stability of these MOFs in their evacuated state. It was not until 1997 when Prof. Kitagawa *et al.* measured the gas adsorption

properties under high pressure of a evacuated 3D framework. These measurements were the first evidence that MOFs can store gas molecules inside their channels.²¹⁰

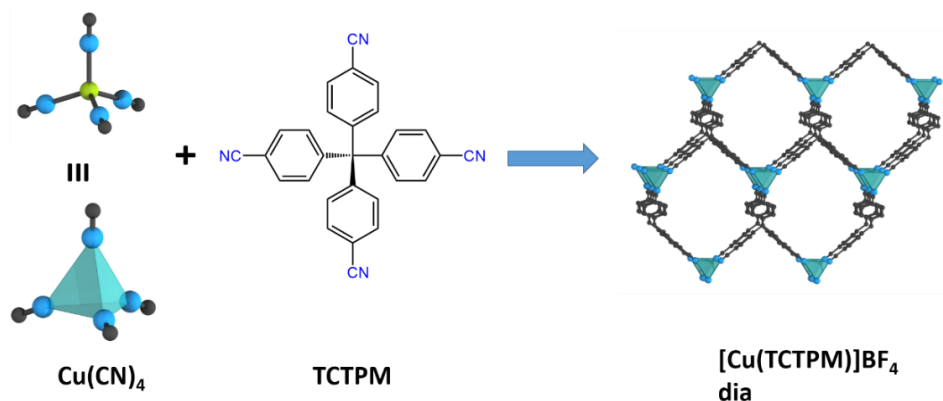


Figure 22. Diamond-like framework consisting of tetrahedral Cu(I) units assembled with tetrahedral organic linkers. Colour scheme: Cu (green), C (grey) and N (blue).

One of the important milestones in the MOF field was the study of MOF-2, reported by Prof. Yaghi and coworkers in 1998. In this publication, the neutral permanent framework $\text{Zn}(\text{BDC})(\text{DMF})(\text{H}_2\text{O})$, named MOF-2, was synthesized using terephthalic acid (BDC) and $\text{Zn}(\text{NO}_3)_2 \cdot 6\text{H}_2\text{O}$. In it, it was observed the formation of rigid metal-carboxyl clusters by bridging or chelating metallic ions with carboxylate ligands. These clusters acted as anionic deprotonated linkers, which lead to the network extension through bimetallic paddlewheel subunits (Figure 24). Also, the adsorption study showed that MOF-2 is microporous with a micropore volume of $0.094 \text{ cm}^3/\text{g}$ and $0.086 \text{ cm}^3/\text{g}$ for N_2 and CO_2 , respectively.²¹¹ This work demonstrated that not only metal ions but also rigid coordination clusters with fixed geometries were ideal building blocks for the formation of porous MOFs. Soon after, two vital porous MOFs were reported following this cluster strategy. The first one was HKUST-1 (HKUST= Hong Kong University of Science and Technology), a 3D framework composed of Cu(II)-paddlewheel clusters and benzene-1,3,5-tricarboxylic acid (BTC), which had a high BET (Brunauer-Emmett-Teller) surface area of $692 \text{ m}^2 \text{ g}^{-1}$ (later reached $1800 \text{ m}^2 \text{ g}^{-1}$) (Figure 24).^{212,213} The second MOF was MOF-5 ($[\text{Zn}_4\text{O}(\text{BDC})_3]$), a 3D framework assembled from octahedral Zn(II) clusters and BDC linkers, that showed a very high surface area of $2900 \text{ m}^2 \text{ g}^{-1}$ (Figure 24).²¹⁴

Soon thereafter, the concept of Secondary Building Units (SBU) was introduced by Prof. Yaghi and colleagues.^{215,216} SBUs are defined as structural and rigid clusters or complexes of metal ions connected with organic ligands that can be used for the rational design of MOFs.

This rational design spawned a new field called Reticular Chemistry, which is defined as “*the linking of well-defined molecular building blocks by strong bonds into crystalline extended frameworks*”.^{217,218} Today, Reticular Chemistry allows, for example, that for a given structure, the distance between SBUs can be increased by modifying the length of linkers. In these isostructural frameworks, the topology is maintained while expanding the volume of their cavities. Based on this possibility, Yaghi *et al.* first presented the reticular expansion of MOFs, in which 16 isorecticular MOFs (IRMOFs) with the same cubic topology were reported (Figure 25). In this family of IRMOFs, the pore size could be extended from 3.8 to 28.8 Å without any change in primitive topology by replacing either the functionalized linkers or the longer aromatic ligands.²¹⁹

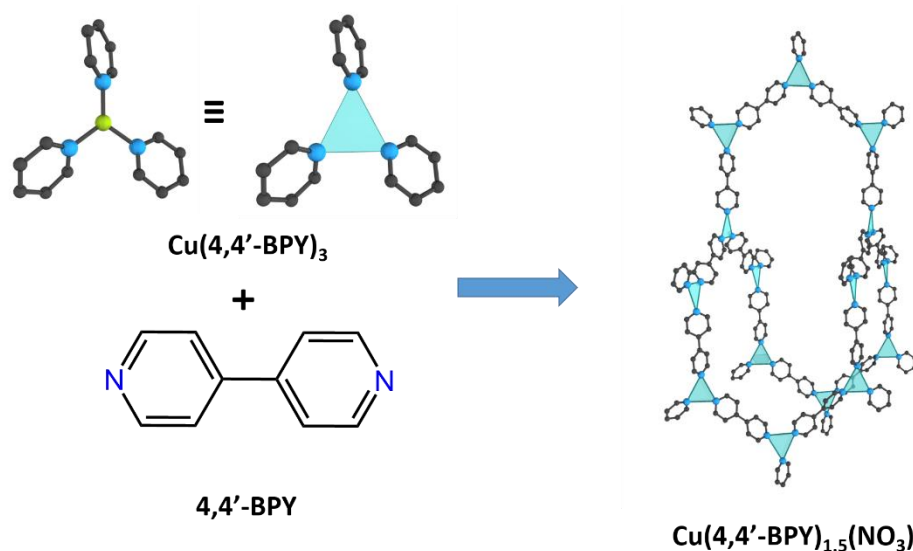


Figure 23. Schematic representation of the MOF $\text{Cu(4,4'-bpy)}_{1.5}\text{NO}_3$. Colour code: Cu (green), C (gray) and N (blue).

Nowadays, reticular chemistry has been proven to be a powerful guidebook in the design, prediction and synthesis of new periodic materials including MOFs and Covalent Organic Frameworks (COFs). Meanwhile, researchers are looking for more extraordinary techniques or applications for broadening and deepening the reticular chemistry in all dimensions.²²⁰

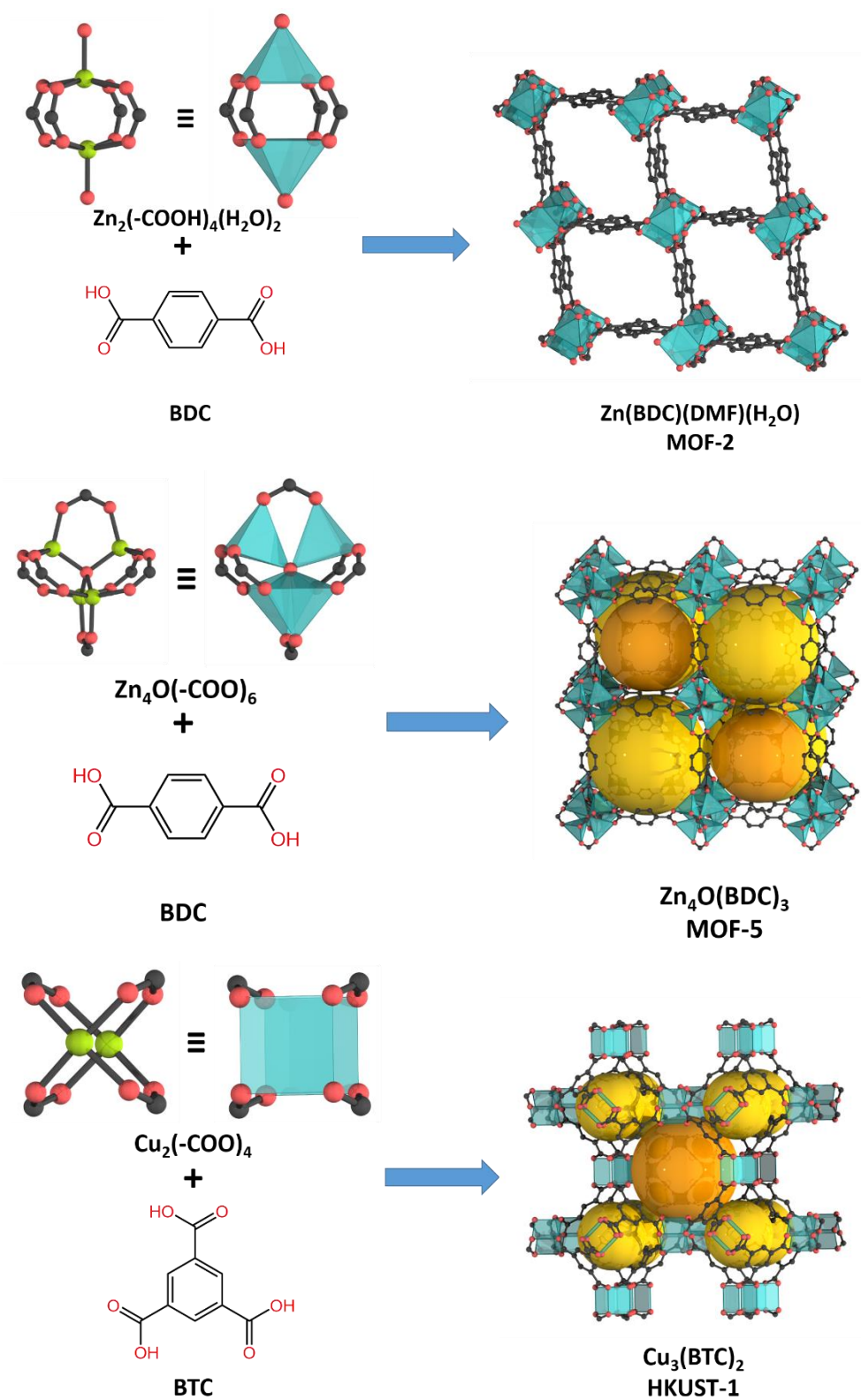


Figure 24. Schematic representation of the structure of MOF-2 (top), MOF-5 (middle) and HKUST-1 (bottom). Colour code: Zn/Cu (green), C (gray), and O (red).

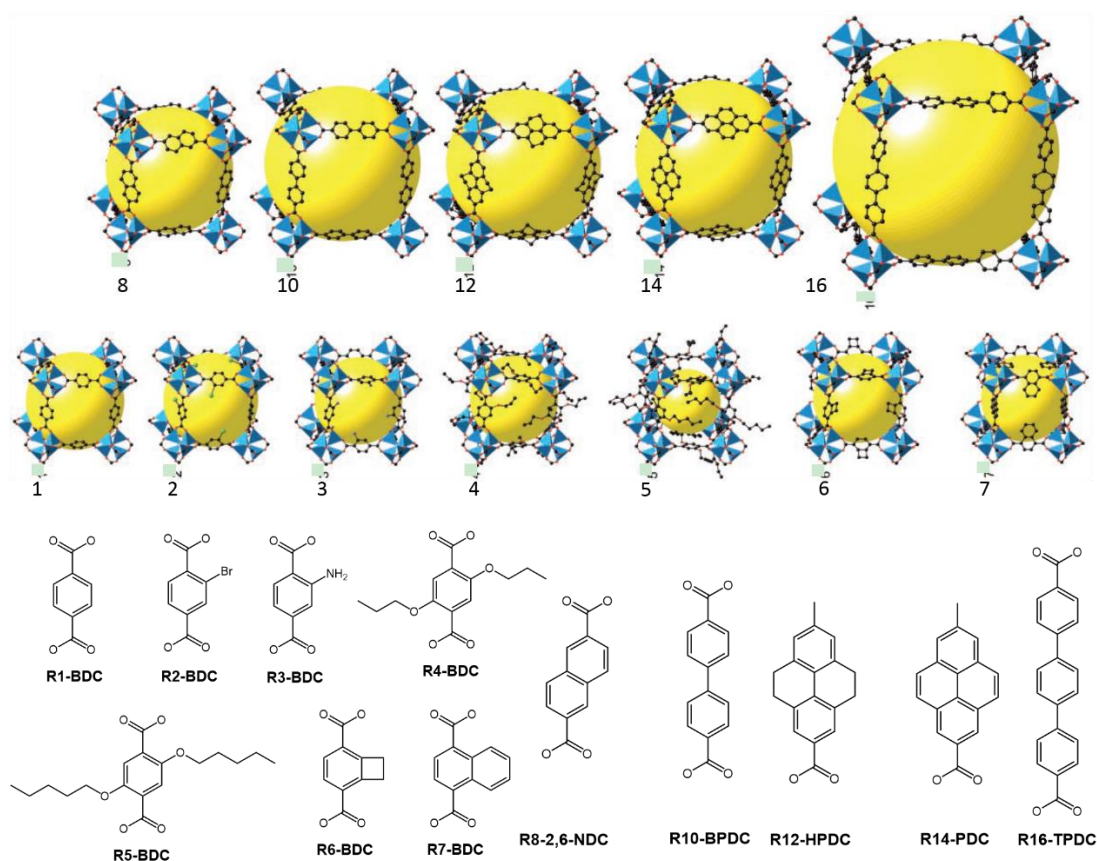


Figure 25. Schematic representation of the IRMOF series synthesized using Reticular Chemistry.

2.2 Applications of MOFs

The ultimate purpose of a material is its application for our daily life. In such a context, MOFs have proven to be outstanding materials for myriad applications due to their extraordinary and intrinsic properties, such as porosity, exposed metal sites and ligands, electronic, magnetic, optical and even hydrophobic properties. To date, multiple applications have been developed and explored around these exceptional properties, including gas storage/separation, vapor sorption, sensor, catalysis and drug delivery, among many others (Figure 26). In this section, a brief overview of some of these applications will be presented.

2.2.1. Gas Storage

Energy shortage and environmental pollution have become an urgent and crucial issue in recent years. In this sense, hydrogen and methane are good energy sources. However, their safe transport and storage is precluding their use in a wide range. Recently, MOFs have been proposed as promising porous materials for the storage of hydrogen and methane due to their

high adsorption and storage capacities and their tunability of the pore dimension. Several studies of these materials for absorbing these two gases are addressed in the next two sections.



Figure 26. Summary of some of the applications of MOFs.

2.2.1.1. Hydrogen storage

Hydrogen is a potentially clean and renewable energy source due to its high energy density and non-pollution byproducts. However, hydrogen has a poor energy density on a volumetric mass compared to fossil fuels, usually in an increased volume to store it at room temperature compared to gasoline (8 MJ L^{-1} vs 32 MJ L^{-1}). Today, hydrogen storage requires extreme conditions such as low temperature or high pressure, making it is neither effective nor safe.²²¹ In this context, MOFs supply a solution to store hydrogen due to their high surface areas and strong physisorption performance. For example, Farha *et al.* recently reported a kind of ultraporous MOFs based on metal trinuclear clusters, namely NU-1501-M ($M = \text{Al}$ or Fe). Among them, NU-1501-Al showed an excellent hydrogen storage capacities of 46.2 g L^{-1} under the combined change of temperature and pressure of $77 \text{ K}/100 \text{ bar}$ to $160 \text{ K}/5 \text{ bar}$ (Figure 27a).²²²

2.2.1.2. Methane storage

Natural gas, mainly composed of methane, is an alternative energy source due to its lower CO₂ emission compared to other fossil fuels. However, similar to H₂, methane has low energy density, also making its transport and storage key parameter to solve for its real application. To date, there are several strategies to overcome these limitations, such as compression or liquidation. However, considering safety and high efficiency, storage of methane in porous materials at room temperature and low pressures can be regarded as one of the most promising strategies.²²³ In this sense, MOFs can be attractive absorbent materials for storing methane under mild conditions. Until now, for example, HKUST-1 has been proved to be the most promising MOF for achieving the target of the U.S Department of Energy (DOE) in methane storage (263 cm³ (STP) cm⁻³).²²⁴ In 2018, Fairen-Jimenez *et al.* reported the fabrication of sol-gel HKUST-1 monoliths that exhibit the record methane work capacity of 259 cm³ (STP) cm⁻³ at 298 K and 65 bar even after shaping and densification; being the first material to achieve the volumetric target of DOE (Figure 27b).²²⁵

2.2.2. CO₂ Sequestration

Carbon neutrality has received more and more attention concern in the recent years. The main target of this concept is to achieve a state of net-zero carbon dioxide emissions by balancing emissions of CO₂ with its removal or by eliminating emissions from society. Therefore, CO₂ capture and sequestration processes play a key role to achieve this target. In these tasks, MOFs can also play a very important role. MOFs can exhibit unsaturated metal sites that can act as Lewis acid centers that coordinate CO₂ molecules, enhancing their CO₂ storage performances. For example, Dietzel and coworkers studied different metal series of M-MOF-74 (including Mg, Mn, Ni, Zn) for CO₂ adsorption.²²⁶ Among them, the microporous Mg-MOF-74 [Mg₂(DHTP)] (where DHTP= 2,5-dihydroxyterephthalic acid) showed an excellent CO₂ uptake capacity of 27.5 wt% thanks to coordination through its unsaturated ions.²²⁷ On the other hand, chemical modification of MOFs with functional Lewis groups such as amines, imines and amides can also improve CO₂ sorption. As an example, Long *et al.* synthesized the alkylamine-functionalized MOF mmen-Mg₂(DOBPDC) (where mmen= *N,N'*-dimethylethylenediamine, and DOBPDC= 4,4'-dioxido-3,3'-biphenyldicarboxylate) via solvothermal and microwave methods. This MOF showed a notable CO₂ capacity of (8.1 wt %) at 0.39 mbar and room temperature (Figure 27c).²²⁸

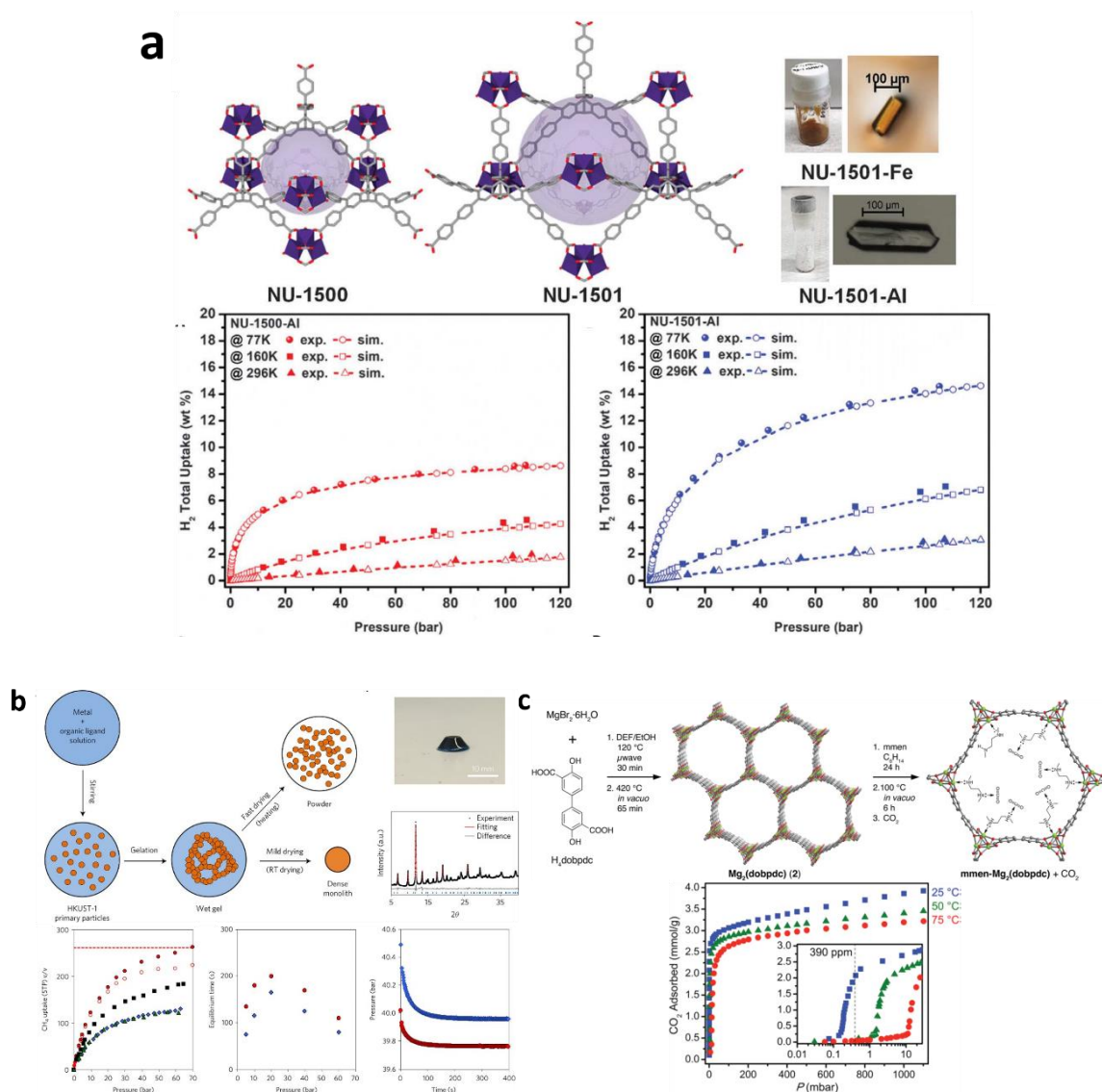


Figure 27. (a) Schematic representation of the crystalline structure of NU-1500 and NU-1501 and the experimental H_2 adsorption isotherms of NU-1500-Al and NU-1501-Al. (b) Schematic representation of the synthesis of monolithic and powder HKUST-1 and its experimental CH_4 adsorption isotherms. (c) Synthesis of mmen- $\text{Mg}_2(\text{DOBPD})$ and its crystalline structure, and its experimental CO_2 adsorption isotherms. Adapted from ref. 222, 225 and 228.

2.2.3. Storage and Separation of Other Gases

Besides the aforementioned gases, other gases such as acetylene, carbon monoxide, or harmful gases such as NO_2 , SO_2 , H_2S and NH_3 also have aroused much interest because they are vital to human health and industrial production. Hence, the diversity of MOFs makes

possible to find good MOF candidates to store and separate most of these gases.²²⁹⁻²³¹ For instance, Long's group studied the selective adsorption of CO in $\text{Fe}_2\text{Cl}_2(\text{BBTA})$ (BBTA=1H,5Hbenzo(1,2-d:4,5-d')bistriazole) where iron(II) sites coordinated with ligands and Cl^- anions forming a special iron(II) centers, enhancing the affinity for CO (Figure 28a).²³² Another important gas for industry is acetylene. One of the defects for acetylene storage is its explosive character under high pressure.²³³ In 2005, $\text{Cu}_2(\text{PZDC})_2(\text{PYZ})$ (PZDC=pyrazine-2,3-dicarboxylate; PYZ= pyrazine) exhibited good storage capability for acetylene. This MOF showed a high sorption ability towards acetylene thanks to the periodic distance caused by hydrogen bonding between two non-coordinated oxygen atoms in the framework and the two hydrogen atoms of the acetylene molecule (Figure 28b).²³⁴

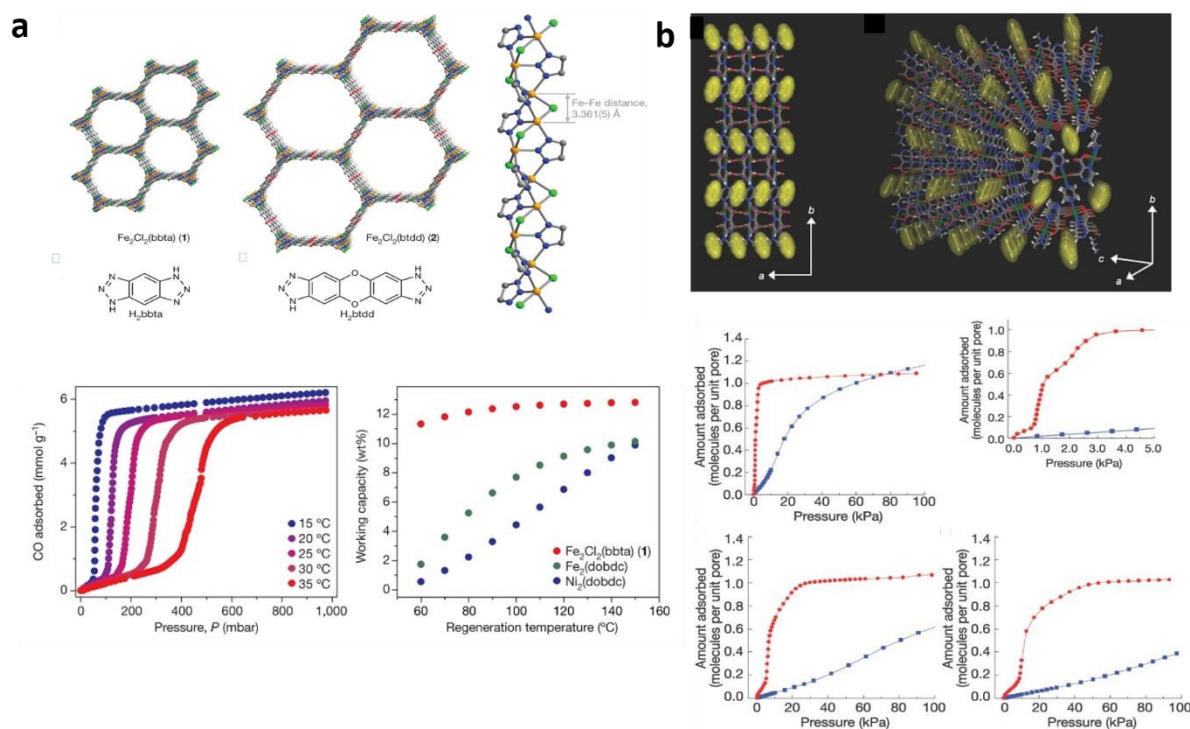


Figure 28. (a) Schematic representation of the crystalline structure of $\text{Fe}_2\text{Cl}_2(\text{BBTA})$ and $\text{Fe}_2\text{Cl}_2(\text{BTDD})$ and their experimental CO adsorption isotherms. (b) Schematic representation of the crystalline structure of $\text{Cu}_2(\text{PZDC})_2(\text{PYZ}) \cdot 2\text{H}_2\text{O}$ and its experimental acetylene adsorption isotherms. Adapted from ref. 232 and 234.

2.2.4. Chemical Sensing

Chemical sensing is a process of converting chemical changes into measurable physical change signals through analytical equipment.²³⁵ MOFs can therefore be used to fabricate sensors as they are porous materials that can be responsive to different chemical and biological

stimuli.²³⁶ For instance, Kitagawa *et al.* reported a novel MOF, $[\text{Zn}_2(\text{BDC})_2(\text{dpNDI})]_n$ (where BDC= 1,4-benzenedicarboxylate; dpNDI= *N,N'*-di(4-pyridyl)-1,4,5,8-naphthalenediimide), to study differentiation caused by host-guest interaction in the framework. They found that the introduction of naphthalenediimine into this entangled porous framework shows structural dynamics caused by the displacement of two chemically non-interlinked frameworks. Then, they observed that the incorporation of different aromatic compounds triggered a turn-on luminescent emission, which color was dependent on the chemical substituent of the aromatics (Figure 29a).²³⁷ Dinca and colleagues produced a conductive 2D MOF chemiresistor using the conductive MOF $\text{Cu}_3(\text{HITP})_2$ (HITP=2,3,6,7,10,11-hexaiminotriphenylene) by drop casting. The resulting device exhibited the capacity for detecting NO , NH_3 , and H_2S under mild conditions.²³⁸ Recently, Zhao, Cai and coworkers fabricated a Mg-MOF-74-based sensor, which was post-modified with ethylenediamine to respond to CO_2 and benzene thanks to the available open metal sites of this MOF (Figure 29b).²³⁹

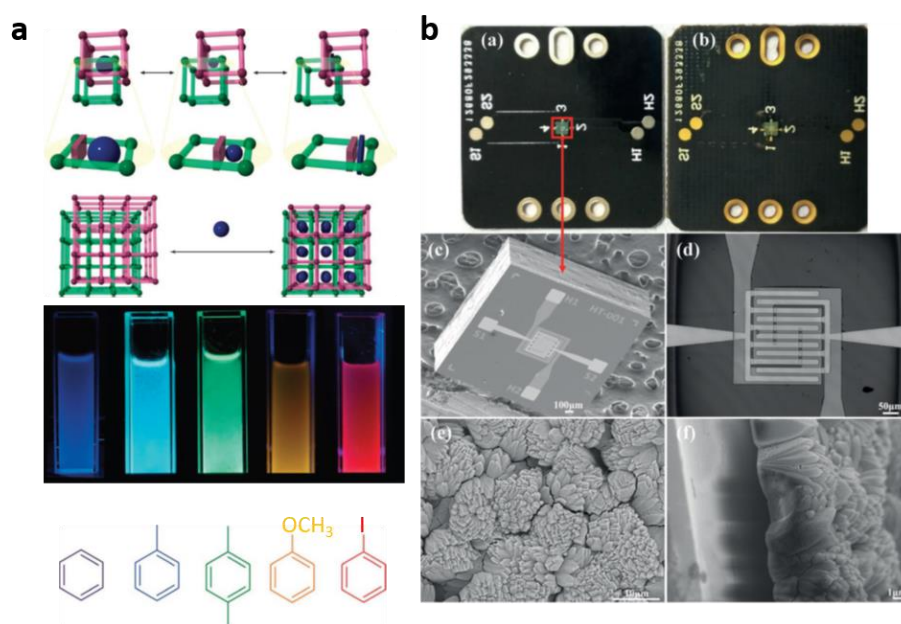


Figure 29. (a) Schematic illustration of the molecular decoding strategy for MOFs and their multicolour luminescence caused by the different substituted aromatics. (b) Photographs of the bare sensor and SEM images of the chip and the as-grown Mg-MOF-74 film on interdigitated electrodes. Adapted from ref. 237 and 239.

2.2.5. Catalysis

Catalysis research is always at the forefront of science and technology because it is an indispensable part of our daily life. Already in the 1990s, the network material $[\text{Cd}(\text{NO}_3)_2(4,4-$

BPY)₂] (4,4-BPY = bipyridine) showed moderate catalytic performance for the cyanosilylation of aldehyde with moderate yield. The special heterogeneous catalytic property was attributed to the cavity size of the framework, opening a new avenue for MOFs to be used as heterogeneous catalysts.²⁴⁰ To date, several structural features of MOFs have been regarded as strategies for designing heterogeneous catalysts, including exposed metal nodes, functionalized ligands, defects of structures, and using MOFs as hosts for additional catalytic sites.²⁴¹ As an example, Lin's group presented a mix-and-match strategy to synthesize UiO-67-like frameworks that contain Ir, Re, and Ru complexes composed of 2-phenylpyridyl or bipyridyl ligands. The resulting MOFs showed good catalysis activity in water oxidation, carbon dioxide reduction, and photocatalysis thanks to the several functional ligands that coexist with metals (Figure 30a).²⁴² On the other hand, highly enantioselective heterogeneous asymmetric catalysis performance of a MOF was reported by Lin's group. They synthesized a porous catalyst composed of 1D [Cd(μ -Cl)₂]_n zigzag chains and chiral bipyridine bridging ligands to be used for the synthesis of a chiral alcohol with high *ee* values (Figure 30b).²⁴³ Nowadays, it has been shown that MOFs can also be used for electrocatalysis and photocatalysis. In this context, Liu and coworkers synthesized the Cu-based MOF [Cu₂(BPDC)₂(DPQ)₂(H₂O)]H₂O (BPDC = biphenyl-4,4'-dicarboxylic acid; DPQ = dipyrido[3,2-d:2',3'-f] quinoxaline) and mixed it with graphite, to prepare carbon paste electrode. This electrode showed good electrocatalytic performance in the reduction of bromate, nitrite and hydrogen peroxide.²⁴⁴

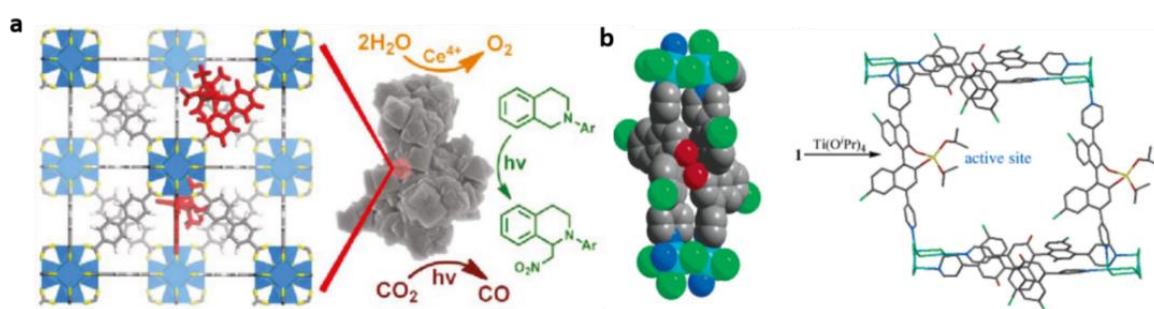


Figure 30. (a) Schematic illustration of the doping UiO-67 frameworks and their catalytic applications. (b) Schematic representation of the homochiral MOF and the active catalytic sites in the open channels. Cyan, green, red, blue, gray, and yellow represent Cd, Cl, O, N, C, and Ti atoms, respectively. Adapted from ref. 242 and 243.

2.3 Colloidal MOFs

As above-mentioned, colloidal particles with uniform size and shape are ideal building blocks for the self-assembly of superstructures. Since their discovery, the majority of studies

of MOFs has focused on bulk powders usually composed of crystal in the microscale range. However, very recently, MOFs have started to be miniaturized at the submicron and nanoscale regime. With this miniaturization, new properties have been discovered for these small MOF particles.²⁴⁵ Some of these new properties are accelerated adsorption/desorption kinetics, suitability for biological applications and their potential use as colloidal particles for subsequent self-assembly of superstructures for optics, photonics or separation –related applications.²⁴⁶ In this part, we will mainly introduce the synthesis of colloidal MOF particles, their surface modification and their assembly.

2.3.1. Synthesis of Colloidal MOF particles

Compared with the random crystal size and shape of MOF bulk powder systems, monodispersity of size and shape is the most significant characteristic of colloidal MOF particles (Figure 32). Although there are today a few methods to synthesize the nanoscale MOF particles, the formation of homogeneous and monodisperse colloidal MOF particles with well-defined sizes and shape is still a challenging task.^{245,247,248} For this, it is important to understand the MOF formation process. In order to synthesize monodispersed colloidal MOF particles with uniform size and shape, we have to consider some factors such as nucleation, crystal growth and agglomeration process. According to the LaMer model,^{250,251} the growth of nanocrystals will follow four steps: 1) the concentration of precursors rapidly increase; 2) the homogeneous nucleation takes place when the concentration of precursors is higher than the critical concentration of nucleation; 3) halting the nucleation process due to the concentration of precursor decreases; and 4) crystals growth begins and continues to reach an equilibrium state. Hence, the pivotal factor to obtaining uniform MOF particles is to shorten the nucleation period and control the growth time of each nucleus. According to this, some of the methods that have been proposed to synthesize colloidal MOF particles are rapid nucleation with microwave-assisted or ultrasound irradiation, nanoreactor confinement and the use of modulators coordination (Figure 31).²⁴⁵

Rapid nucleation is the most directly approach to synthesize colloidal MOFs. Under microwave heating or ultrasound, the precursors are easily dissolved and quickly consumed, rapidly forming small nuclei that evolve into particles with nanoscale and narrow size distributions. The first example was released by Masel and coworkers, who produced 200 nm to 4 μm IRMOF-1 particles with a coefficient of variation (CV) around 30% by using

microwave-assisted solvothermal synthesis.²⁴⁹ Then, in 2010, Feldhoff group synthesized 40 nm to 140 nm ZIF-7 particles with good dispersity (CV=10-20%) using microwave and adding diethylamine to accelerate the nucleation process.²⁵⁰ In the same year, Jung *et al.* investigated the effects of MOF nucleation and growth through comparing three different methods: microwave, ultrasound and conventional heating. They found that microwave and ultrasound radiation were helpful to obtain uniform MOF particles, being ultrasonication much faster than the other two methods.²⁵¹

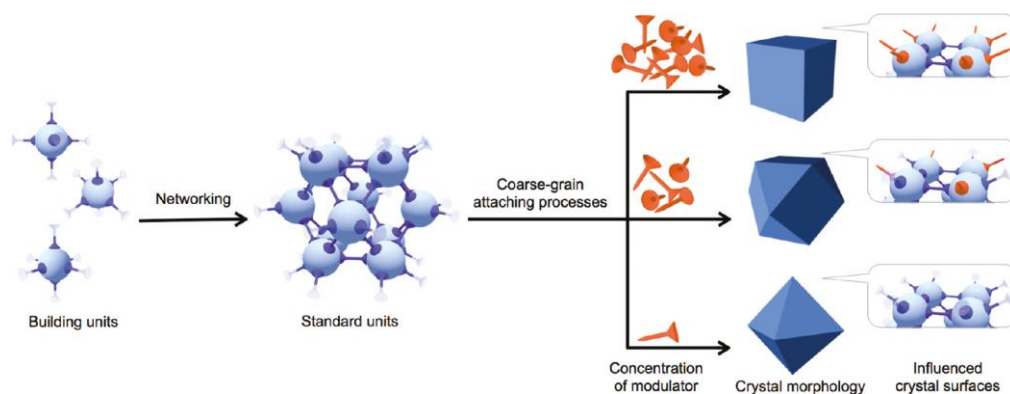


Figure 31. The role of modulators throughout the crystal growth process based on Coarse-Grain Model. Adapted from ref. 245.

Nanoreactor confinement approach is another useful strategy to regulate the MOF particle size. Emulsion droplets can be regarded as a potential reaction container, in which particles size can be tuned by modifying the droplets. For instance, in 2006, Lin and colleagues synthesized crystalline nanorods of $\text{Ln}_2(\text{BDC})_3(\text{H}_2\text{O})_4$ ($\text{Ln} = \text{Eu}^{3+}$, Gd^{3+} or Tb^{3+}) using a micro-emulsion system that contained cetyltrimethylammonium bromide (CTAB)/isooctane/1-hexanol/water.²⁵² The size of the rods could be controlled from $2\ \mu\text{m} \times 100\ \text{nm}$ to $125\ \text{nm} \times 40\ \text{nm}$ through tuning the ratio between water and surfactant. In 2014, a facile and interesting method that uses reverse micelles as nanoreactors was reported by Zheng and colleagues for synthesizing 30 to 300 nm ZIF-8 particles. These homogeneous ZIF-8 particles were synthesized by controlling the reaction temperature, the concentration of the precursors, and even the different types of surfactants.²⁵³

Coordination modulators play an essential role for controlling the size and shape of MOF particles and even their uniformity. They can participate in the reaction and reversibly connect with coordination sites, meaning that the number of nucleation of sites are regulated to achieve a controllable synthesis of MOF particles. Chemical modulators are usually bases, acids, surfactants or cosolvents, which can compete with linkers for metals/ligands reacting

sites. For example, in 2008, Oh *et al.* first reported an efficient method to synthesize $\text{In}_2(\text{BDC})_3$ MOF particles with different shapes by modulating the amount of pyridine. In the presence of the blocking agent (pyridine), the shape of the resulting MOF particles (hexagonal rods, hexagonal lumps, and hexagonal disks) was controlled following the different growth rate of facets of particles.²⁵⁴ Notably, the resulting samples had a good monodispersity ($\text{CV} = \sim 10\text{--}15\%$).

In 2009, Kitagawa and coworkers used acetic acid as a modulator to control the anisotropic growth of $\text{Cu}_2(\text{NDC})_2(\text{DABCO})$ nanocrystals.²⁵⁵ Two years later, the same group successfully controlled the morphology of HKUST-1 through addition of dodecanoic acid and lauric acid as modulators. They found that, due to the modulator intervention in the $\langle 100 \rangle$ direction growth, the morphology of HKUST-1 particles could be changed from octahedron to cuboctahedron to cube by increasing the concentration of the modulator.²⁵⁶ Behrens and colleagues used a similar method to produce homogeneous UiO-66 and UiO-67 particles via addition of a modulator such as benzoic and acetic acid.²⁵⁷ Also, high quality monodispersed ZIF-8 particles were synthesized using sodium formate as modulator by Wiebcke's group.²⁴⁸

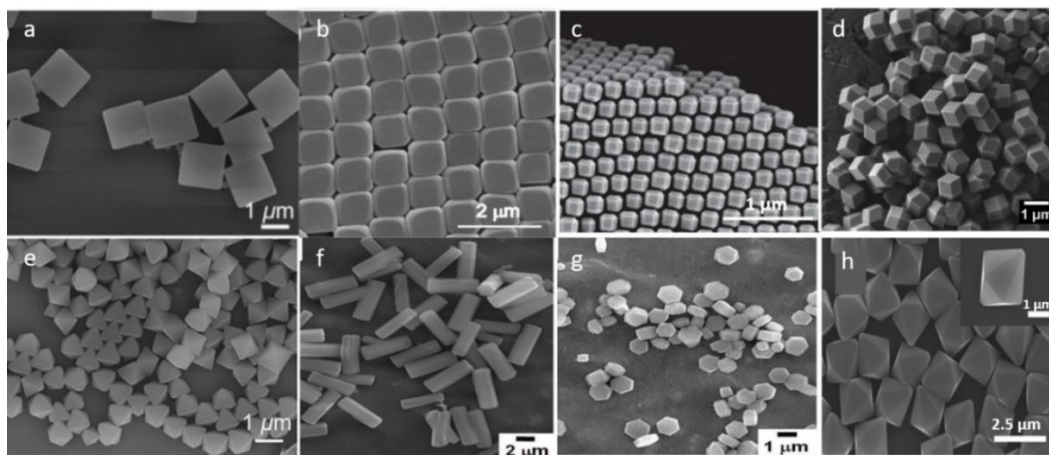


Figure 32. Representative SEM images of monodisperse colloidal MOF particles with different shapes including cubes (a), truncated cube (b), truncated rhombic dodecahedra (c), rhombic dodecahedra (d), octahedra (e), hexagonal rods (f), hexagonal discs (g), and hexagonal bipyramids (h). Adapted from ref. 243, 254, 256, 265, 266, 271, 272.

In 2012, Eddaoudi and coworkers showed the possibility to synthesize monodisperse In- and Ga-soc-MOF particles with cubic and truncated rhombic dodecahedra shape by using different surfactants as modulators.²⁵⁸ Granick's group showed the production of homogenous ZIF-8 particles with a rhombic dodecahedron (RD) shape ($\text{CV} = 4.5\%$) combining PVP and 1-methylimidazole (1-MI) as modulators.²⁵⁹ Later in 2013, the same group synthesized highly

uniform colloidal MIL-96(Al) particles using various aqueous solvent mixtures and acetic acid as the modulator. The morphology of the resulting particles (truncated, rounded and regular hexagonal bipyramid and even spindle shape) could be controlled by using cosolvents, such as THF, DMF and toluene.²⁶⁰ In 2015, Oh *et al.* demonstrated that, controlling the ratio of two organic linkers, homogenous crystalline hexagonal rods could be produced.²⁶¹ One year later, Zhou and coworkers in 2016 reported the size-controlled synthesis of PCN-224 nanoparticles with benzoic acid, ranging from 33 ± 4 nm to 189 ± 11 nm.²⁶² In the same year, Harris and Mirkin presented the efficient synthesis of a series of porphyrinic zirconium MOF nanoparticles (MOF-525, MOF-545 and PCN-223) through a high-throughput screening method.²⁶³ At the same time, highly uniform Fe-MIL-88B particles were synthesized using PVP by Pang *et al.* The shape of these particles evolved from hexagonal bipyramids to bipyramid hexagonal prism by increasing the amount of PVP.²⁶⁴

Since 2017, many other colloidal MOF particles have been synthesized using modulators. For example, Mirkin's group synthesized UiO-66 particles from 20 nm to over 1 μ m with good colloidal stability and polydispersity by adding different carboxylic acid modulators.²⁶⁵ Lu's group also reported the synthesis of monodisperse UiO-66 crystals with tunable sizes ranging from ~ 500 nm to ~ 2 μ m through the use of acetic acid/ triethylamine co-modulation and PVP.^{266,267} Pang *et al.* reported that uniform In-NDC-MOF particles could be prepared via a solvothermal method in the presence of different modulators. By using a base or an acid as modulators, micron-sized ellipsoid and rod-like MOF particles were synthesized, respectively.²⁶⁸ Our group successfully synthesized highly uniform truncated rhombic dodecahedral ZIF-8 particles and octahedral UiO-66 particles (around 200 nm and CV < 5%) using CTAB and acetic acid as modulators.²⁶⁹ And recently, Lu and colleagues prepared uniform MOF-5 particles controlling their size and shape. In this work, concentrations of both TEA and PVP influenced the particle size (ranging from ~ 400 nm to ~ 2500 nm), whereas the shapes of MOF-5 particles could be controlled from a cube to a truncated cube, a truncated octahedron, and an octahedron through tuning the concentration of PVP.²⁷⁰

2.3.2. Surface Modification

Surface modification is an effective tool to endow nanomaterials with unique and practical applications. As we previously introduced, MOFs are porous materials that are composed of metal ions and organic ligands. So, their external surface can be functionalized

using these two sites: through the metal centers using coordination chemistry; and through the organic linkers using covalent chemistry (Figure 33).²⁴⁵

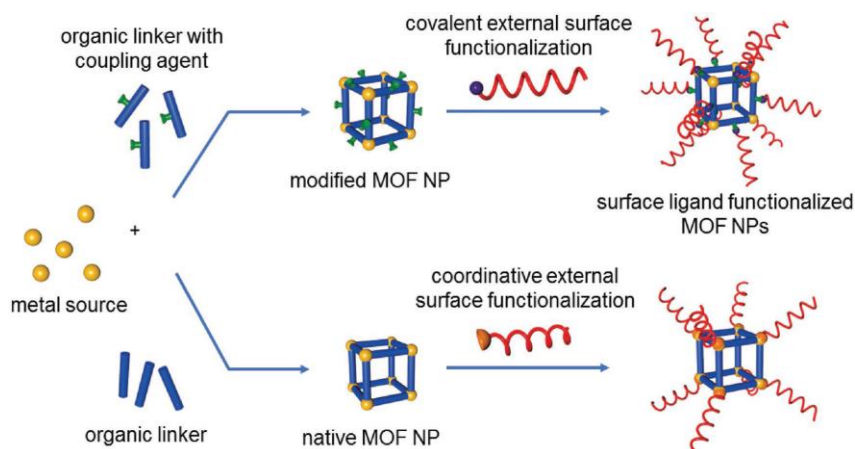


Figure 33. Schematic illustration of the two strategies for the modification of colloidal MOF particles. Adapted from ref. 245.

2.3.2.1. Coordinative Surface Functionalization

Coordinative surface functionalization uses on the exposed metal sites to coordinate targeted molecules. The carboxylate-terminated ligands were first used to coordinate such exposed metal sites. For example, Cha and coworkers reported the synthesis of functionalized PCN-224 particles that contain DNA.²⁷¹ Due to the carboxylic acid groups can coordinate strongly with the exposed surface Zr sites, PCN-224 particles were first reacted with N_{α},N_{α} -bis(carboxymethyl)-l-lysine hydrate containing three carboxylic acid functional groups. Next, the amine-modified MOF particles were produced through surface ligand exchange. And finally, the resulting MOF particles reacted with a NHS–DBCO linker via NHS-amine chemistry, which was followed by DNA conjugation with azido-terminated oligonucleotides. The resulting particles could be further used for photodynamic therapy. Similar approach was achieved using nitrogen-bearing ligands. For example, Granick’s group post-synthetically functionalized ZIF-8 particles using an imidazolate-modified BODIPY dye via surface ligand exchange.²⁵⁹

The phosphate group also can be acted as efficient coordinated units for surface functionalization. For instance, Lin’s group presented the synthesis of bisphosphonate MOF particles using phosphate-terminated lipids through coordinating to the superficial metal ions of MOF particles (Figure 34a and b).^{272,273} The functionalized MOF particles were synthesized in a microemulsion by coordination of the phosphate terminated lipids (1,2-dioleoyl-sn-

glycero-3-phosphate sodium salt (DOPA)) with the superficial exposed calcium ions. The resulting coated-particles could be further used for targeted drug release. Likewise, Mirkin and colleagues reported a facile method to produce surface-specific functionalization of Zr-based MOF particles with phosphate terminated lipids via a one-step phase transfer reaction. Notably, the resulting colloidal particles exhibited good monodispersity and porosity.²⁷⁴ Recently, they also used phosphate modified oligonucleotides instead of phosphate terminated lipids to synthesize several oligonucleotide-functionalized MOFs particles (Figure 34c).²⁷⁵

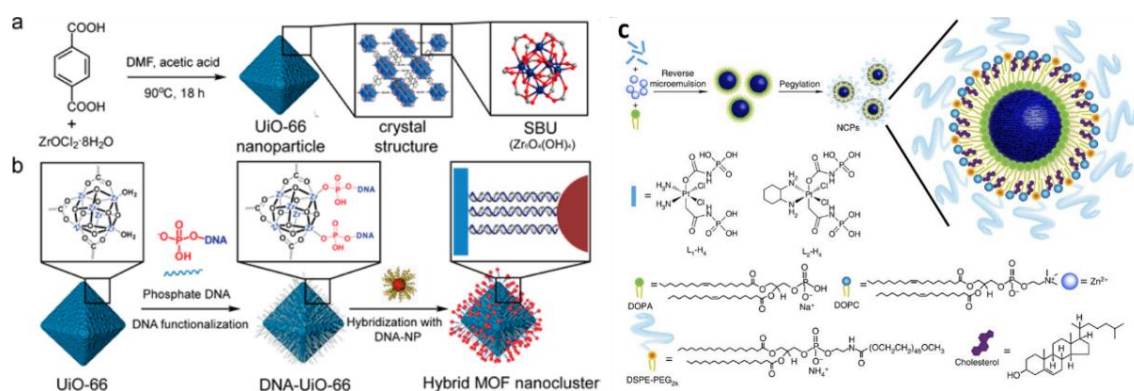


Figure 34. (a and b) Scheme of the synthesis of UiO-66 particles and their DNA modification. (c) General procedure for modification of MOF particles using lipid and PEG. Adapted from ref. 272 and 275.

2.3.2.2. Covalent Surface Functionalization

A second strategy to post-synthetically modify MOF particles is the covalent surface functionalization, which uses the organic linkers. This approach depends on the organic functional groups that are exposed on the surface or that are in the pre-synthesized secondary functional groups on the initial ligands.²⁷⁶ For example, Wuttke and colleagues synthesized surface-functionalized MIL-100(Fe) particles by amidation of carboxylic acid groups on their surface with amino-polyethylene glycol (PEG5000) or Stp10-C (an oligoaminoamide hetero-bifunctional linker). These polymer-functionalized MOF particles exhibited increased colloidal stability in solution and could also be used for biomedical applications.²⁷⁷ In this context, due to abundant reactive sites, linker modification approach provided many possibilities for producing polymer grafted MOF particles. For instance, Webley, Qiao and coworkers reported the synthesis of PEG-grafted UiO-66-NH₂ particles through two functionalization steps. First, Br@MOF particles were synthesized by esterification reaction between bromoisobutyryl bromide (BiBB) and UiO-66-NH₂ particles. And then, the Br@MOF particles were used as an

initiator for the electron transfer-atom transfer radical polymerization (ARGET-ATRP) of a macromonomer poly(ethylene glycol) methyl ether methacrylate (PEGMA) to form PEG grafted UiO-66-NH₂ particles.²⁷⁸ The resulting particles showed good water dispersity and pH sensitivity, and even catalytic effect for the reduction reaction. Similarly, Sada's group produced polymer-grafted MOF particles by modification with a thermoresponsive polymer PNIPAM (Figure 35a).²⁷⁹

Another method to modify the linkers of MOF particles is using click chemistry. For example, Mirkin's group firstly showed the synthesis of nucleic acid-functionalized UiO-66 particles through the strained-alkyne click chemistry between the azido group from UiO-66-N₃ framework and oligonucleotides.²⁸⁰ The resulting colloidal MOF particles show a good colloidal stability and cellular uptake transfection capabilities. Later, Willner's group reported the modification of UiO-68-NH₂ particles with nucleic acid tethers using click chemistry (Figure 35b).²⁸¹ The amine group of MOF particles was firstly converted to azido group. Then, they performed an azide-alkyne cycloaddition to form DNA-grafted MOF particles. Forgan and coworkers also synthesized UiO-66 particles with azido groups via adding acidic modulators containing azido or propargyl groups.²⁸² The azido group was attached to the Zr₆ sites of MOF particles, which were modified with poly(ethylene glycol) (PEG) chains via click chemistry.

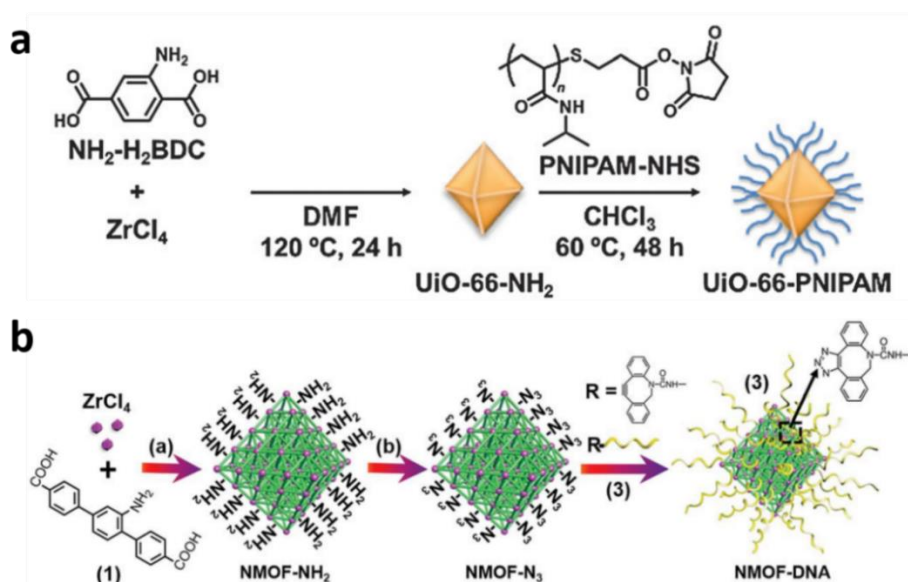


Figure 35. (a) Synthesis of PNIPAM tethered UiO-66-PNIPAM particles. (b) Synthesis of nucleic acid-functionalized UiO-68 particles. Adapted from ref. 279 and 281.

2.3.3. Assembly

As above mentioned, polyhedral particles are excellent building particles for enhancing the variety of packings in self-assembled superstructures. In this sense, the polyhedral nature of MOF particles makes them very attractive building blocks for the discovery and development of new superstructures. MOFs can not only provide a wide range of colloidal polyhedral particles with different shapes and sizes, but also other functionalities such as porosity, magneticity or conductivity, which can also be incorporated into the assembled functional superstructures.

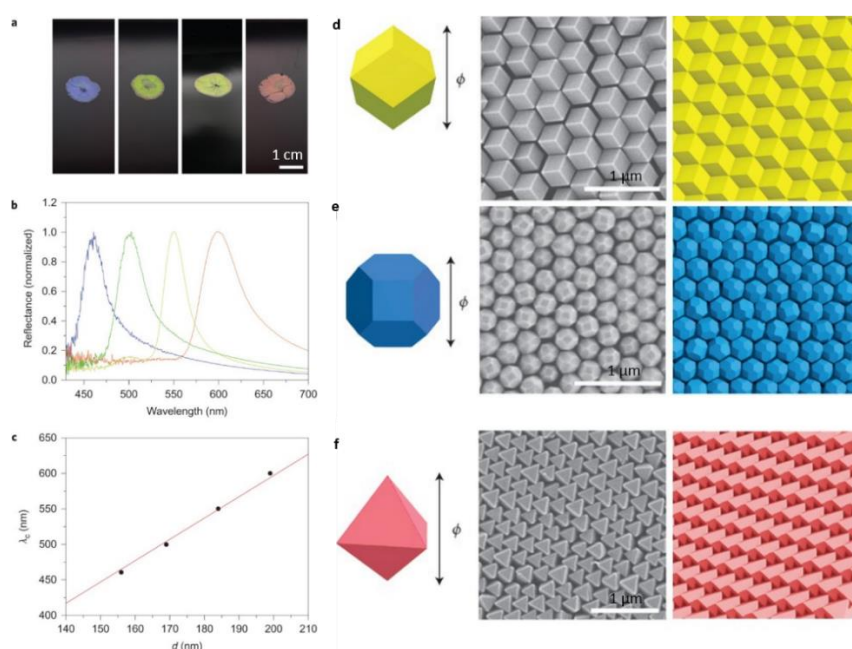


Figure 36. (a-c) Photonic properties of ZIF-8 superstructures and ordered superstructures made of the (d) RD ZIF-8 particles, (e) TRD ZIF-8 particles with $t = 0.57$ and (f) octahedral UiO-66 particles. Adapted from ref. 269.

The first examples of assemblies of colloidal MOFs showing some ordering were reported in 2012. In that year, Kitagawa's group used Langmuir-Blodgett (LB) technique to form 2D monolayers with MOF crystals at the liquid-air interface.²⁸³ In the same year, Granick's group also presented directional self-assembly of rhombic dodecahedral RD ZIF-8 particles.²⁵⁹ Uniform colloidal ZIF-8 particles were self-assembled into ordered monolayers with different facet orientation via the capillary forces. Close-packed hexagonal arrangements with crystal orientation in the $\langle 111 \rangle$ direction were observed after evaporation from a highly concentrated colloidal dispersion, whereas $\langle 110 \rangle$ facets oriented monolayers could be

observed when lower concentration were used. This ordering was however limited to a few microns. One year later, the same authors reported the directional assembly of RD or truncated cubic ZIF-8 particles into 1D chains, which was driven by the external electric field.²⁸⁴ Applying an AC electric field, these particle facets link to form chains with orientational order. The linear chains of RD ZIF-8 particles were preferentially assembled through $\langle 110 \rangle$ facets and resulting in $\langle 110 \rangle$ orientation of crystals along the chain. In contrast, truncated rhombic dodecahedra particles were randomly locked through $\langle 100 \rangle$ and $\langle 110 \rangle$ facets.

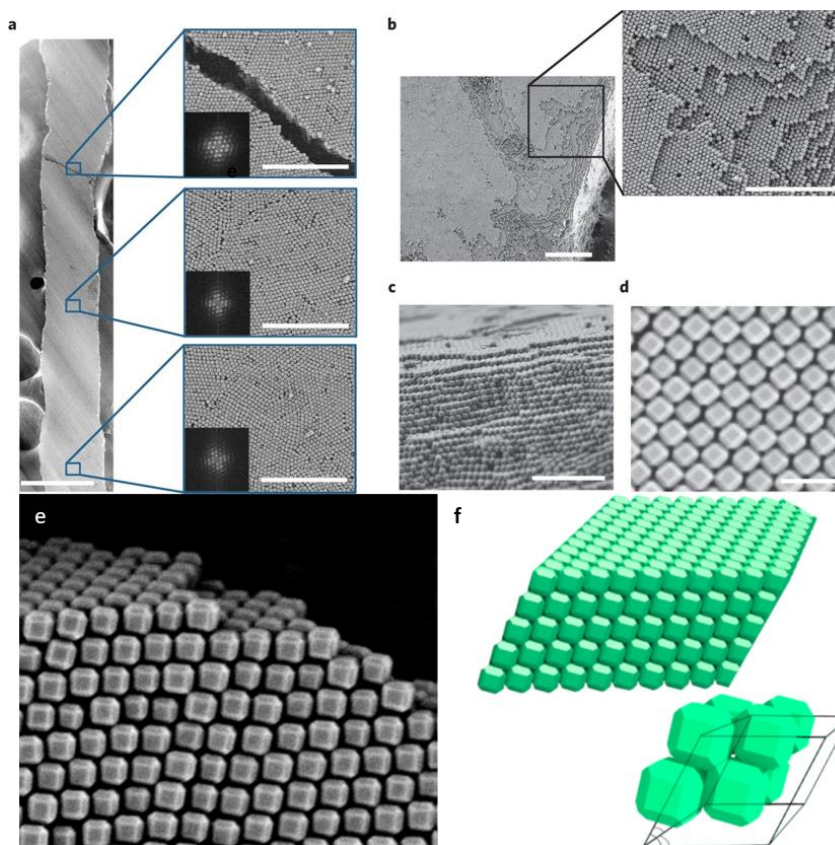


Figure 37. (a-e) SEM images of ordered rhombohedral superstructures made of ZIF-8 particles and (f) computer simulation of the formation of the densest rhombohedral lattice. Adapted from ref. 269.

In the following years, the control on the MOF particles synthesis and self-assembly processes progressed fast, so that the first superstructures showing long-range order and photonic properties started to be developed. Huo *et al.* reported the self-assembly of uniform octahedral UiO-66 particles into 2D monolayers and 3D superlattices using the LB technique and gravity sedimentation method, respectively.^{285,286} These superstructures did not show long extensions of ordering, but they presented photonic properties (attributed to the bandgap between layers). Interestingly, such superstructures were used to create photonic MOF sensors, which exhibited selective absorbance peak shift toward several chemical vapors. Lu and

coworkers reported a very similar work on the self-assembly of UiO-66 particles (1000 nm and 698 nm) into MOF films with preferential orientation and controlled thickness.²⁶⁷ In 2018, our group went one step further and reached the formation of 3D superstructures exhibiting long-range order.²⁶⁹ We demonstrated that highly uniform TRD ZIF-8 particles can self-assemble into millimeter-sized superstructures with an underlying three-dimensional rhombohedral lattice that behave as photonic crystals. We also demonstrated that other superstructures with different packing geometries could be obtained from polyhedral MOF particles, such as RD ZIF-8 and octahedral UiO-66 particles. We also exploited the photonic properties of the resulting superstructure and evaluated their sorption and used them as sensor for alcohols (Figure 36 and 37).

In addition to 1D, 2D and 3D systems, Eddaoudi's group reported the formation of 3D hollow superparticles, also named colloidosomes. These colloidosomes were assembled from monodispersed cubic Fe-soc-MOF particles and Ga-soc-MOF in 2016, through the one-step emulsion-based technique (Figure 36a-d).^{287,288} Khashab *et al.* reported the formation of ZIF-8 colloidosomes *in situ* through the emulsion-free soft template approach. Self-conglobation effect of the hydrated salt in alcohol was the main principle to form the soft template, thus ZIF-8 colloidosomes were not made up of regular shape particles (Figure 36e-h).²⁸⁹

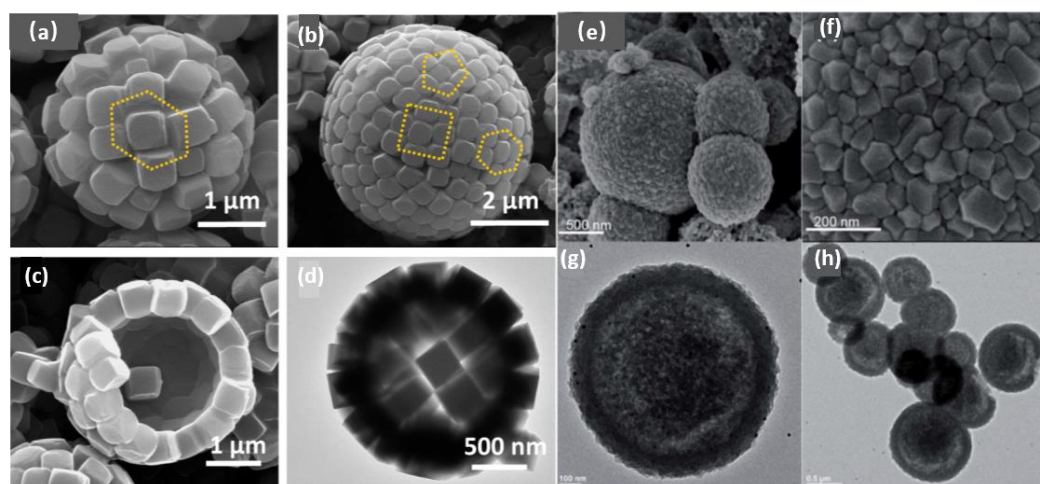


Figure 38. (a-d) small hollow colloidosomes made of Fe-soc-MOF by the emulsion droplet. (e-h) SEM and TEM images of the ZIF-8 colloidosomes via an emulsion-free soft-templating approach. Adapted from ref. 287 and 289.

References

- [1] D. Philp, J. F. Stoddart, *Angew. Chem. Int. Ed. Engl.* **1996**, *35*, 1154-1196.
- [2] G. M. Whitesides, J. P. Mathias, C. T. Seto, *Science* **1991**, *254*, 1312-1319.
- [3] G. R. Desiraju, G. W. Parshall, *Mater. Sci. Monogr.* **1989**, *54*.
- [4] E. L. Thomas, *Science* **1999**, *286*, 1307-1307.
- [5] M. N. Jones, D. Chapman, *Micelles, monolayers, and biomembranes*, Wiley-Liss, **1995**.
- [6] A. Subramanian, *Essays Biochem.* **1985**, *21*, 45-85.
- [7] M. L. Blader, M. F. Dunn, *Trends Biochem. Sci.* **1991**, *16*, 341-345.
- [8] V. Grantcharova, E. J. Alm, D. Baker, A. L. Horwich, *Curr. Opin. Struct. Biol.* **2001**, *11*, 70-82.
- [9] C. R. Cantor, P. R. Schimmel, *Biophysical chemistry: Part III: the behavior of biological macromolecules*, Macmillan, **1980**.
- [10] P. Schimmel, *Annu. Rev. Biochem.* **1987**, *56*, 125-158.
- [11] T. Graham, *Philosophical transactions of the Royal Society of London* **1861**, 183-224.
- [12] R. Brown, *The philosophical magazine* **1828**, *4*, 161-173.
- [13] X. C. Jiang, Q. H. Zeng, C. Y. Chen, A. B. Yu, *J. Mater. Chem.* **2011**, *21*, 16797.
- [14] Q. Li, U. Jonas, X. S. Zhao, M. Kappl, *Asia-Pac. J. Chem. Eng.* **2008**, *3*, 255-268.
- [15] N. Vogel, M. Retsch, C. A. Fustin, A. Del Campo, U. Jonas, *Chem. Rev.* **2015**, *115*, 6265-6311.
- [16] X. Li, X. Liu, X. Liu, *Chem. Soc. Rev.* **2021**, *50*, 2074-2101.
- [17] J. Liu, J. Huang, W. Niu, C. Tan, H. Zhang, *Chem. Rev.* **2021**, *121*, 5830-5888.
- [18] J. N. Israelachvili, *Intermolecular and surface forces*, Academic press, **2015**.
- [19] H. C. Hamaker, *Physica* **1937**, *4*, 1058-1072.
- [20] C. B. Murray, C. R. Kagan, M. G. Bawendi, *Science* **1995**, *270*, 1335-1338.
- [21] D. Langbein, *Physik der kondensierten Materie* **1972**, *15*, 61-86.
- [22] Y. Lalatonne, J. Richardi, M. P. Pileni, *Nat. Mater.* **2004**, *3*, 121-125.
- [23] L. Hong, A. Cacciuto, E. Luijten, S. Granick, *Nano Lett.* **2006**, *6*, 2510-2514.
- [24] A. Ghezelbash, B. Koo, B. A. Korgel, *Nano Lett.* **2006**, *6*, 1832-1836.
- [25] Z. Tang, A. Kotov Nicholas, M. Giersig, *Science* **2002**, *297*, 237-240.
- [26] D. A. Walker, K. P. Browne, B. Kowalczyk, B. A. Grzybowski, *Angew. Chem. Int. Ed. Engl.* **2010**, *49*, 6760-6763.
- [27] B. D. Korth, P. Keng, I. Shim, S. E. Bowles, C. Tang, T. Kowalewski, K. W. Nebesny, J. Pyun, *J. Am. Chem. Soc.* **2006**, *128*, 6562-6563.
- [28] S. Fischer, A. Salcher, A. Kornowski, H. Weller, S. Förster, *Angew. Chem. Int. Ed. Engl.* **2011**, *50*, 7811-7814.
- [29] K. J. Bishop, C. E. Wilmer, S. Soh, B. A. Grzybowski, *Small* **2009**, *5*, 1600-1630.
- [30] Z. Sun, W. Ni, Z. Yang, X. Kou, L. Li, J. Wang, *Small* **2008**, *4*, 1287-1292.
- [31] C. A. Mirkin, R. L. Letsinger, R. C. Mucic, J. J. Storhoff, *Nature* **1996**, *382*, 607-609.
- [32] Z.-G. Wang, B. Ding, *Adv. Mater.* **2013**, *25*, 3905-3914.
- [33] Y. Dong, C. Yao, Y. Zhu, L. Yang, D. Luo, D. Yang, *Chem. Rev.* **2020**, *120*, 9420-9481.
- [34] R. Klajn, K. J. M. Bishop, M. Fialkowski, M. Paszewski, C. J. Campbell, T. P. Gray, B. A. Grzybowski, *Science* **2007**, *316*, 261-264.
- [35] S. Asakura, F. Oosawa, *The Journal of Chemical Physics* **1954**, *22*, 1255-1256.
- [36] D. Baranov, A. Fiore, M. van Huis, C. Giannini, A. Falqui, U. Lafont, H. Zandbergen, M. Zanella, R. Cingolani, L. Manna, *Nano Lett.* **2010**, *10*, 743-749.
- [37] M. Zanella, G. Bertoni, I. R. Franchini, R. Brescia, D. Baranov, L. Manna, *Chem. Commun.* **2011**, *47*, 203-205.
- [38] P. Bolhuis, D. Frenkel, *Phys. Rev. Lett.* **1994**, *72*, 2211-2214.
- [39] G. H. Koenderink, G. A. Vliegenthart, S. G. J. M. Kluijtmans, A. van Blaaderen, A. P. Philipse, H. N. W. Lekkerkerker, *Langmuir* **1999**, *15*, 4693-4696.

- [40] D. Wang, M. J. A. Hore, X. Ye, C. Zheng, C. B. Murray, R. J. Composto, *Soft Matter* **2014**, *10*, 3404-3413.
- [41] D. J. Kraft, R. Ni, F. Smalenburg, M. Hermes, K. Yoon, D. A. Weitz, A. van Blaaderen, J. Groenewold, M. Dijkstra, W. K. Kegel, *Proc. Natl. Acad. Sci. U. S. A.* **2012**, *109*, 10787-10792.
- [42] P. A. Kralchevsky, K. Nagayama, *Langmuir* **1994**, *10*, 23-36.
- [43] K. Zhao, T. G. Mason, *Rep. Prog. Phys.* **2018**, *81*, 126601.
- [44] S. J. Veen, O. Antoniuk, B. Weber, M. A. C. Potenza, S. Mazzoni, P. Schall, G. H. Wegdam, *Phys. Rev. Lett.* **2012**, *109*, 248302.
- [45] J. Zhu, M. Li, R. Rogers, W. Meyer, R. H. Ottewill, W. B. Russel, P. M. Chaikin, S. T. S. S. S. Crew, *Nature* **1997**, *387*, 883-885.
- [46] Z. Xu, L. Wang, F. Fang, Y. Fu, Z. Yin, *Curr. Nanosci.* **2016**, *12*, 725-746.
- [47] N. Denkov, O. Veleev, P. Kralchevski, I. Ivanov, H. Yoshimura, K. Nagayama, *Langmuir* **1992**, *8*, 3183-3190.
- [48] N. D. Denkov, O. D. Veleev, P. A. Kralchevsky, I. B. Ivanov, H. Yoshimura, K. Nagayama, *Nature* **1993**, *361*, 26-26.
- [49] T. Still, P. J. Yunker, A. G. Yodh, *Langmuir* **2012**, *28*, 4984-4988.
- [50] L. Cui, J. Zhang, X. Zhang, L. Huang, Z. Wang, Y. Li, H. Gao, S. Zhu, T. Wang, B. Yang, *ACS Appl. Mater. Interfaces* **2012**, *4*, 2775-2780.
- [51] P. J. Yunker, T. Still, M. A. Lohr, A. G. Yodh, *Nature* **2011**, *476*, 308-311.
- [52] A. S. Dimitrov, K. Nagayama, *Langmuir* **1996**, *12*, 1303-1311.
- [53] L. Malaquin, T. Kraus, H. Schmid, E. Delamarche, H. Wolf, *Langmuir* **2007**, *23*, 11513-11521.
- [54] P. Born, S. Blum, A. Munoz, T. Kraus, *Langmuir* **2011**, *27*, 8621-8633.
- [55] P. Born, A. Munoz, C. Cavelius, T. Kraus, *Langmuir* **2012**, *28*, 8300-8308.
- [56] M. Banik, R. Mukherjee, *ACS Omega* **2018**, *3*, 13422-13432.
- [57] E. Kumacheva, R. K. Golding, M. Allard, E. H. Sargent, *Adv. Mater.* **2002**, *14*, 221-224.
- [58] K. C. Barick, D. Bahadur, *J. Nanosci. Nanotechnol.* **2010**, *10*, 668-689.
- [59] L. He, M. Wang, J. Ge, Y. Yin, *Acc. Chem. Res.* **2012**, *45*, 1431-1440.
- [60] D. Xia, D. Li, Z. Ku, Y. Luo, S. R. J. Brueck, *Langmuir* **2007**, *23*, 5377-5385.
- [61] M. Grzelczak, J. Vermant, E. M. Furst, L. M. Liz-Marzán, *ACS Nano* **2010**, *4*, 3591-3605.
- [62] H. N. Barad, H. Kwon, M. Alarcon-Correa, P. Fischer, *ACS Nano* **2021**, *15*, 5861-5875.
- [63] R. van Dommelen, P. Fanzio, L. Sasso, *Adv. Colloid Interface Sci.* **2018**, *251*, 97-114.
- [64] M. Bardosova, M. E. Pemble, I. M. Povey, R. H. Tredgold, *Adv. Mater.* **2010**, *22*, 3104-3124.
- [65] B. van Duffel, R. H. A. Ras, F. C. De Schryver, R. A. Schoonheydt, *J. Mater. Chem.* **2001**, *11*, 3333-3336.
- [66] N. Vogel, S. Goerres, K. Landfester, C. K. Weiss, *Macromol. Chem. Phys.* **2011**, *212*, 1719-1734.
- [67] L. Cademartiri, K. J. Bishop, P. W. Snyder, G. A. Ozin, *Philos Trans A Math Phys Eng Sci* **2012**, *370*, 2824-2847.
- [68] K. Deng, Z. Luo, L. Tan, Z. Quan, *Chem. Soc. Rev.* **2020**.
- [69] H. Cong, B. Yu, J. Tang, Z. Li, X. Liu, *Chem. Soc. Rev.* **2013**, *42*, 7774-7800.
- [70] Y. Xia, B. Gates, Y. Yin, Y. Lu, *Adv. Mater.* **2000**, *12*, 693-713.
- [71] X. Bouju, E. Duguet, F. Gauffre, C. R. Henry, M. L. Kahn, P. Melinon, S. Ravaine, *Adv. Mater.* **2018**, *30*, e1706558.
- [72] F. Li, D. P. Josephson, A. Stein, *Angew. Chem. Int. Ed. Engl.* **2011**, *50*, 360-388.
- [73] W. Xu, Z. Li, Y. Yin, *Small* **2018**, *14*, e1801083.
- [74] X. Liang, R. Dong, J. C. Ho, *Adv. Mater. Technol.* **2019**, *4*, 1800541.
- [75] K. E. Davis, W. B. Russel, W. J. Glantschnig, *Science* **1989**, *245*, 507-510.
- [76] S. Takeda, P. Wiltzius, *Chem. Mater.* **2006**, *18*, 5643-5645.
- [77] Y. Xia, B. Gates, Z.-Y. Li, *Adv. Mater.* **2001**, *13*, 409-413.
- [78] J. Zhang, Z. Sun, B. Yang, *Curr. Opin. Colloid Interface Sci.* **2009**, *14*, 103-114.
- [79] Y. Huang, J. Zhou, B. Su, L. Shi, J. Wang, S. Chen, L. Wang, J. Zi, Y. Song, L. Jiang, *J. Am. Chem. Soc.* **2012**, *134*, 17053-17058.

- [80] M. R. Kim, S. H. Im, Y.-S. Kim, K. Y. Cho, *Adv. Funct. Mater.* **2013**, *23*, 5700-5705.
- [81] S. Wong, V. Kitaev, G. A. Ozin, *J. Am. Chem. Soc.* **2003**, *125*, 15589-15598.
- [82] J. Wang, Q. Li, W. Knoll, U. Jonas, *J. Am. Chem. Soc.* **2006**, *128*, 15606-15607.
- [83] J. Wang, S. Ahl, Q. Li, M. Kreiter, T. Neumann, K. Burkert, W. Knoll, U. Jonas, *J. Mater. Chem.* **2008**, *18*, 981.
- [84] T. Hueckel, G. M. Hocky, J. Palacci, S. Sacanna, *Nature* **2020**, *580*, 487-490.
- [85] P. F. Damasceno, M. Engel, S. C. Glotzer, *Science* **2012**, *337*, 453-457.
- [86] S. Yamamuro, K. Sumiyama, *Chem. Phys. Lett.* **2006**, *418*, 166-169.
- [87] M. N. O'Brien, H.-X. Lin, M. Girard, M. Olvera de la Cruz, C. A. Mirkin, *J. Am. Chem. Soc.* **2016**, *138*, 14562-14565.
- [88] T. Wang, X. Wang, D. LaMontagne, Z. Wang, Z. Wang, Y. C. Cao, *J. Am. Chem. Soc.* **2012**, *134*, 18225-18228.
- [89] Y. H. Lee, C. L. Lay, W. Shi, H. K. Lee, Y. Yang, S. Li, X. Y. Ling, *Nat. Commun.* **2018**, *9*, 2769.
- [90] L. X. Dai, X. Y. Wang, X. Y. Zheng, Y. W. Zhang, *Chem. Commun. (Camb.)* **2016**, *52*, 5023-5026.
- [91] D. Zang, H. Huang, R. Qin, X. Wang, X. Fang, N. Zheng, *Sci. China Chem.* **2016**, *59*, 452-458.
- [92] D. Caruntu, T. Rostamzadeh, T. Costanzo, S. S. Parizi, G. Caruntu, *Nanoscale* **2015**, *7*, 12955-12969.
- [93] C. W. Liao, Y. S. Lin, K. Chanda, Y. F. Song, M. H. Huang, *J. Am. Chem. Soc.* **2013**, *135*, 2684-2693.
- [94] C. Y. Chiu, C. K. Chen, C. W. Chang, U. S. Jeng, C. S. Tan, C. W. Yang, L. J. Chen, T. J. Yen, M. H. Huang, *J. Am. Chem. Soc.* **2015**, *137*, 2265-2275.
- [95] Y.-S. Cho, S.-H. Lee, M.-J. Kim, Y.-D. Huh, *Bull. Korean Chem. Soc.* **2014**, *35*, 1837-1840.
- [96] L. Hu, C. Wang, R. M. Kennedy, L. D. Marks, K. R. Poeppelmeier, *Inorg. Chem.* **2015**, *54*, 740-745.
- [97] K. Tsukiyama, M. Takasaki, Y. Oaki, H. Imai, *Langmuir* **2019**, *35*, 8025-8030.
- [98] J. S. van der Burgt, J. J. Geuchies, B. van der Meer, H. Vanrompay, D. Zanaga, Y. Zhang, W. Albrecht, A. V. Petukhov, L. Filion, S. Bals, I. Swart, D. Vanmaekelbergh, *J Phys Chem C Nanomater Interfaces* **2018**, *122*, 15706-15712.
- [99] J. Gong, R. S. Newman, M. Engel, M. Zhao, F. Bian, S. C. Glotzer, Z. Tang, *Nat. Commun.* **2017**, *8*, 14038.
- [100] D. Wang, M. Hermes, R. Kotni, Y. Wu, N. Tasios, Y. Liu, B. de Nijs, E. B. van der Wee, C. B. Murray, M. Dijkstra, A. van Blaaderen, *Nat. Commun.* **2018**, *9*, 2228.
- [101] X. S. Shen, G. Z. Wang, X. Hong, W. Zhu, *CrystEngComm* **2009**, *11*, 753.
- [102] J. Henzie, M. Grunwald, A. Widmer-Cooper, P. L. Geissler, P. Yang, *Nat. Mater.* **2011**, *11*, 131-137.
- [103] K. Bian, R. Li, H. Fan, *Chem. Mater.* **2018**, *30*, 6788-6793.
- [104] J. Brunner, I. A. Baburin, S. Sturm, K. Kvashnina, A. Rossberg, T. Pietsch, S. Andreev, E. Sturm née Rosseeva, H. Cölfen, *Adv. Mater. Interfaces* **2017**, *4*, 1600431.
- [105] S. Disch, E. Wetterskog, R. P. Hermann, G. Salazar-Alvarez, P. Busch, T. Bruckel, L. Bergstrom, S. Kamali, *Nano Lett.* **2011**, *11*, 1651-1656.
- [106] Y. Zhang, F. Lu, D. van der Lelie, O. Gang, *Phys. Rev. Lett.* **2011**, *107*, 135701.
- [107] M. Xu, G. Tu, M. Ji, X. Wan, J. Liu, J. Liu, H. Rong, Y. Yang, C. Wang, J. Zhang, *Nano Res.* **2019**, *12*, 1375-1379.
- [108] F. Lu, T. Vo, Y. Zhang, A. Frenkel, K. G. Yager, S. Kumar, O. Gang, *Sci. Adv.* **2019**, *5*, eaaw2399.
- [109] Z. Quan, H. Xu, C. Wang, X. Wen, Y. Wang, J. Zhu, R. Li, C. J. Sheehan, Z. Wang, D. M. Smilgies, Z. Luo, J. Fang, *J. Am. Chem. Soc.* **2014**, *136*, 1352-1359.
- [110] S. Torquato, Y. Jiao, *Nature* **2009**, *460*, 876-879.
- [111] A. P. Gantapara, J. de Graaf, R. van Roij, M. Dijkstra, *Phys. Rev. Lett.* **2013**, *111*, 015501.
- [112] J. Zhang, Z. Luo, B. Martens, Z. Quan, A. Kumbhar, N. Porter, Y. Wang, D. M. Smilgies, J. Fang, *J. Am. Chem. Soc.* **2012**, *134*, 14043-14049.

- [113] R. Li, J. Zhang, R. Tan, F. Gerdes, Z. Luo, H. Xu, J. A. Hollingsworth, C. Klinke, O. Chen, Z. Wang, *Nano Lett.* **2016**, *16*, 2792-2799.
- [114] J. Zhang, Z. Luo, Z. Quan, Y. Wang, A. Kumbhar, D. M. Smilgies, J. Fang, *Nano Lett.* **2011**, *11*, 2912-2918.
- [115] T. R. Gordon, T. Paik, D. R. Klein, G. V. Naik, H. Caglayan, A. Boltasseva, C. B. Murray, *Nano Lett.* **2013**, *13*, 2857-2863.
- [116] Z. Zhao, J. Zhang, F. Dong, B. Yang, *J. Colloid Interface Sci.* **2011**, *359*, 351-358.
- [117] S.-C. Lu, M.-C. Hsiao, M. Yorulmaz, L.-Y. Wang, P.-Y. Yang, S. Link, W.-S. Chang, H.-Y. Tuan, *Chem. Mater.* **2015**, *27*, 8185-8188.
- [118] Y. Liu, J. Zhou, L. Zhou, E. Yue-Bun Pun, T. Jiang, L. Petti, P. Mormile, *RSC Adv.* **2016**, *6*, 57320-57326.
- [119] L. Qiao, Z. Fu, J. Li, J. Ghosen, M. Zeng, J. Stebbins, P. N. Prasad, M. T. Swihart, *ACS Nano* **2017**, *11*, 6370-6381.
- [120] D. C. Reifsnnyder, X. Ye, T. R. Gordon, C. Song, C. B. Murray, *ACS Nano* **2013**, *7*, 4307-4315.
- [121] W. Lu, Q. Liu, Z. Sun, J. He, C. Ezeolu, J. Fang, *J. Am. Chem. Soc.* **2008**, *130*, 6983-6991.
- [122] X. Huang, J. Zhu, B. Ge, F. Gerdes, C. Klinke, Z. Wang, *J. Am. Chem. Soc.* **2021**, *143*, 4234-4243.
- [123] Y. H. Lee, W. Shi, H. K. Lee, R. Jiang, I. Y. Phang, Y. Cui, L. Isa, Y. Yang, J. Wang, S. Li, X. Y. Ling, *Nat. Commun.* **2015**, *6*.
- [124] A. Haji-Akbari, M. Engel, S. C. Glotzer, *J. Chem. Phys.* **2011**, *135*, 194101.
- [125] S. Torquato, Y. Jiao, *Phys. Rev. E Stat. Nonlin. Soft Matter Phys.* **2009**, *80*, 041104.
- [126] A. Haji-Akbari, M. Engel, A. S. Keys, X. Zheng, R. G. Petschek, P. Palfy-Muhoray, S. C. Glotzer, *Nature* **2009**, *462*, 773-777.
- [127] P. F. Damasceno, M. Engel, S. C. Glotzer, *ACS Nano* **2012**, *6*, 609-614.
- [128] M. A. Boles, D. V. Talapin, *J. Am. Chem. Soc.* **2014**, *136*, 5868-5871.
- [129] Y. Nagaoka, R. Tan, R. Li, H. Zhu, D. Eggert, Y. A. Wu, Y. Liu, Z. Wang, O. Chen, *Nature* **2018**, *561*, 378-382.
- [130] Y. Nagaoka, H. Zhu, D. Eggert, O. Chen, *Science* **2018**, *362*, 1396-1400.
- [131] Z. Zhu, H. Meng, W. Liu, X. Liu, J. Gong, X. Qiu, L. Jiang, D. Wang, Z. Tang, *Angew. Chem. Int. Ed. Engl.* **2011**, *50*, 1593-1596.
- [132] D. Dong, L. W. Yap, D. M. Smilgies, K. J. Si, Q. Shi, W. Cheng, *Nanoscale* **2018**, *10*, 5065-5071.
- [133] H. Zhang, C. Guan, N. Song, Y. Zhang, H. Liu, J. Fang, *Phys. Chem. Chem. Phys.* **2018**, *20*, 3571-3580.
- [134] J. Nai, B. Y. Guan, L. Yu, X. W. Lou, *Sci. Adv.* **2017**, *3*, e1700732.
- [135] Y. Nakagawa, H. Kageyama, Y. Oaki, H. Imai, *J. Am. Chem. Soc.* **2014**, *136*, 3716-3719.
- [136] Y. Nakagawa, H. Kageyama, Y. Oaki, H. Imai, *Chem. Commun. (Camb.)* **2016**, *52*, 5597-5600.
- [137] R. Matsumoto, Y. Nakagawa, H. Kageyama, Y. Oaki, H. Imai, *CrystEngComm* **2016**, *18*, 6138-6142.
- [138] R. Matsumoto, M. Takasaki, K. Tsukiyama, Y. Oaki, H. Imai, *Inorg. Chem.* **2018**, *57*, 11655-11661.
- [139] R. Matsumoto, Y. Nakagawa, K. Kato, Y. Oaki, H. Imai, *Langmuir* **2017**, *33*, 13805-13810.
- [140] Y. Nakagawa, H. Kageyama, Y. Oaki, H. Imai, *Langmuir* **2015**, *31*, 6197-6201.
- [141] Y. Nakagawa, H. Kageyama, R. Matsumoto, Y. Oaki, H. Imai, *Nanoscale* **2015**, *7*, 18471-18476.
- [142] Y. Yang, G. Chen, S. Thanneeru, J. He, K. Liu, Z. Nie, *Nat. Commun.* **2018**, *9*, 4513.
- [143] Q. Shi, K. J. Si, D. Sikdar, L. W. Yap, M. Premaratne, W. Cheng, *ACS Nano* **2016**, *10*, 967-976.
- [144] W. van der Stam, A. P. Gantapara, Q. A. Akkerman, G. Soligno, J. D. Meeldijk, R. van Roij, M. Dijkstra, C. de Mello Donega, *Nano Lett.* **2014**, *14*, 1032-1037.
- [145] F. Ji, Q. Zhong, J. Chen, L. Chen, H. Hu, Q. Liu, P. Yang, J. Yu, L. Jiang, Y. Xu, E. Gross, Q. Zhang, *Part Part Syst Charact* **2018**, *35*, 1700114.
- [146] Z. Lu, Y. Yin, *Chem. Soc. Rev.* **2012**, *41*, 6874-6887.
- [147] T. Wang, D. LaMontagne, J. Lynch, J. Zhuang, Y. C. Cao, *Chem. Soc. Rev.* **2013**, *42*, 2804-2823.

- [148] S. Wintzheimer, T. Granath, M. Oppmann, T. Kister, T. Thai, T. Kraus, N. Vogel, K. Mandel, *ACS Nano* **2018**, *12*, 5093-5120.
- [149] F. Bai, D. Wang, Z. Huo, W. Chen, L. Liu, X. Liang, C. Chen, X. Wang, Q. Peng, Y. Li, *Angew. Chem. Int. Ed. Engl.* **2007**, *46*, 6650-6653.
- [150] M. I. Bodnarchuk, L. Li, A. Fok, S. Nachtergaele, R. F. Ismagilov, D. V. Talapin, *J. Am. Chem. Soc.* **2011**, *133*, 8956-8960.
- [151] S. Park, H. Hwang, M. Kim, J. H. Moon, S. H. Kim, *Nanoscale* **2020**, *12*, 18576-18594.
- [152] J. Lacava, P. Born, T. Kraus, *Nano Lett.* **2012**, *12*, 3279-3282.
- [153] B. de Nijs, S. Dussi, F. Smalenburg, J. D. Meeldijk, D. J. Groenendijk, L. Fillion, A. Imhof, A. van Blaaderen, M. Dijkstra, *Nat. Mater.* **2015**, *14*, 56-60.
- [154] J. Wang, C. F. Mbah, T. Przybilla, B. Apeleo Zubiri, E. Spiecker, M. Engel, N. Vogel, *Nat. Commun.* **2018**, *9*, 5259.
- [155] J. Wang, C. F. Mbah, T. Przybilla, S. Englisch, E. Spiecker, M. Engel, N. Vogel, *ACS Nano* **2019**, *13*, 9005-9015.
- [156] J. Wang, U. Sultan, E. S. A. Goerlitzer, C. F. Mbah, M. Engel, N. Vogel, *Adv. Funct. Mater.* **2019**, *30*, 1907730.
- [157] N. Vogel, S. Utech, G. T. England, T. Shirman, K. R. Phillips, N. Koay, I. B. Burgess, M. Kolle, D. A. Weitz, J. Aizenberg, *Proc. Natl. Acad. Sci. U. S. A.* **2015**, *112*, 10845-10850.
- [158] K. Okuyama, M. Abdullah, I. Wuled Lenggoro, F. Iskandar, *Adv Powder Technol* **2006**, *17*, 587-611.
- [159] A. B. D. Nandiyanto, K. Okuyama, *Advanced Powder Technology* **2011**, *22*, 1-19.
- [160] D. E. Walton, *Drying Technol.* **2000**, *18*, 1943-1986.
- [161] C. Stauch, T. Ballweg, W. Stracke, R. Luxenhofer, K. Mandel, *J. Colloid Interface Sci.* **2017**, *490*, 401-409.
- [162] S. Zellmer, M. Lindenau, S. Michel, G. Garnweitner, C. Schilde, *J. Colloid Interface Sci.* **2016**, *464*, 183-190.
- [163] R. Vehring, W. R. Foss, D. Lechuga-Ballesteros, *J. Aerosol Sci.* **2007**, *38*, 728-746.
- [164] T. Ballweg, C. Gellermann, K. Mandel, *ACS Appl. Mater. Interfaces* **2015**, *7*, 24909-24914.
- [165] F. Iskandar, H. Chang, K. Okuyama, *Adv Powder Technol* **2003**, *14*, 349-367.
- [166] E. G. Teich, G. van Anders, D. Klotz, J. Dshemuchadse, S. C. Glotzer, *Proc. Natl. Acad. Sci. U. S. A.* **2016**, *113*, E669-678.
- [167] A. v. Blaaderen, *Science* **2003**, *301*, 470-471.
- [168] S. Radcliffe, *Nature* **2006**, *439*, 2.
- [169] A. B. Pawar, I. Kretschmar, *Macromol. Rapid Commun.* **2010**, *31*, 150-168.
- [170] H. Rezvantlab, S. Shojaei-Zadeh, *Phys. Chem. Chem. Phys.* **2014**, *16*, 8283-8293.
- [171] S. Ravaine, E. Duguet, *Curr. Opin. Colloid Interface Sci.* **2017**, *30*, 45-53.
- [172] E. Duguet, A. Desert, A. Perro, S. Ravaine, *Chem. Soc. Rev.* **2011**, *40*, 941-960.
- [173] D. Morphew, D. Chakrabarti, *Curr. Opin. Colloid Interface Sci.* **2017**, *30*, 70-80.
- [174] W. Li, H. Palis, R. Merindol, J. Majimel, S. Ravaine, E. Duguet, *Chem. Soc. Rev.* **2020**, *49*, 1955-1976.
- [175] R. Merindol, E. Duguet, S. Ravaine, *Chem. Asian J.* **2019**, *14*, 3232-3239.
- [176] E. Elacqua, X. Zheng, C. Shillingford, M. Liu, M. Weck, *Acc. Chem. Res.* **2017**, *50*, 2756-2766.
- [177] B. Yu, H. Cong, Q. Peng, C. Gu, Q. Tang, X. Xu, C. Tian, F. Zhai, *Adv. Colloid Interface Sci.* **2018**, *256*, 126-151.
- [178] V. N. Manoharan, M. T. Elsesser, D. J. Pine, *Science* **2003**, *301*, 483-487.
- [179] V. N. Manoharan, *Solid State Commun.* **2006**, *139*, 557-561.
- [180] Y.-S. Cho, G.-R. Yi, S.-H. Kim, D. J. Pine, S.-M. Yang, *Chem. Mater.* **2005**, *17*, 5006-5013.
- [181] V. Meester, R. W. Verweij, C. van der Wel, D. J. Kraft, *ACS Nano* **2016**, *10*, 4322-4329.
- [182] D. J. Kraft, W. S. Vlug, C. M. van Kats, A. van Blaaderen, A. Imhof, W. K. Kegel, *J. Am. Chem. Soc.* **2009**, *131*, 1182-1186.
- [183] J. G. Park, J. D. Forster, E. R. Dufresne, *Langmuir* **2009**, *25*, 8903-8906.

- [184] J. W. Kim, R. J. Larsen, D. A. Weitz, *Adv. Mater.* **2007**, *19*, 2005-2009.
- [185] A. Thill, A. Desert, S. Fouilloux, J. C. Taveau, O. Lambert, M. Lansalot, E. Bourgeat-Lami, O. Spalla, L. Belloni, S. Ravaine, E. Duguet, *Langmuir* **2012**, *28*, 11575-11583.
- [186] A. Desert, J. Morele, J. C. Taveau, O. Lambert, M. Lansalot, E. Bourgeat-Lami, A. Thill, O. Spalla, L. Belloni, S. Ravaine, E. Duguet, *Nanoscale* **2016**, *8*, 5454-5469.
- [187] C. Hubert, C. Chomette, A. Desert, M. Sun, M. Treguer-Delapierre, S. Mornet, A. Perro, E. Duguet, S. Ravaine, *Faraday Discuss.* **2015**, *181*, 139-146.
- [188] A. Désert, I. Chaduc, S. Fouilloux, J.-C. Taveau, O. Lambert, M. Lansalot, E. Bourgeat-Lami, A. Thill, O. Spalla, S. Ravaine, E. Duguet, *Polym. Chem.* **2012**, *3*, 1130.
- [189] A. Perro, S. Reculosa, F. Pereira, M. H. Delville, C. Mingotaud, E. Duguet, E. Bourgeat-Lami, S. Ravaine, *Chem. Commun. (Camb.)* **2005**, 5542-5543.
- [190] A. Perro, E. Duguet, O. Lambert, J. C. Taveau, E. Bourgeat-Lami, S. Ravaine, *Angew. Chem. Int. Ed. Engl.* **2009**, *48*, 361-365.
- [191] J. C. Taveau, D. Nguyen, A. Perro, S. Ravaine, E. Duguet, O. Lambert, *Soft Matter* **2008**, *4*, 311-315.
- [192] Y. Wang, Y. Wang, X. Zheng, G. R. Yi, S. Sacanna, D. J. Pine, M. Weck, *J. Am. Chem. Soc.* **2014**, *136*, 6866-6869.
- [193] Z. Gong, T. Hueckel, G. R. Yi, S. Sacanna, *Nature* **2017**, *550*, 234-238.
- [194] H. Bao, W. Peukert, R. Klupp Taylor, *Adv. Mater.* **2011**, *23*, 2644-2649.
- [195] H. Bao, T. Bihl, A. S. Smith, R. N. Klupp Taylor, *Nanoscale* **2014**, *6*, 3954-3966.
- [196] Q. Chen, S. C. Bae, S. Granick, *Nature* **2011**, *469*, 381-384.
- [197] F. Romano, F. Sciortino, *Soft Matter* **2011**, *7*, 5799.
- [198] F. Romano, F. Sciortino, *Nat. Mater.* **2011**, *10*, 171-173.
- [199] M. Liu, X. Zheng, V. Grebe, D. J. Pine, M. Weck, *Nat. Mater.* **2020**, *19*, 1354-1361.
- [200] M. Liu, X. Zheng, V. Grebe, M. He, D. J. Pine, M. Weck, *Angew. Chem. Int. Ed. Engl.* **2021**, *60*, 5744-5748.
- [201] M. He, J. P. Gales, E. Ducrot, Z. Gong, G. R. Yi, S. Sacanna, D. J. Pine, *Nature* **2020**, *585*, 524-529.
- [202] S. R. Batten, N. R. Champness, X.-M. Chen, J. Garcia-Martinez, S. Kitagawa, L. Öhrström, M. O'Keeffe, M. Paik Suh, J. Reedijk, *Pure Appl. Chem.* **2013**, *85*, 1715-1724.
- [203] A. Li, R. Bueno-Perez, S. Wiggins, D. Fairen-Jimenez, *CrystEngComm* **2020**, *22*, 7152-7161.
- [204] X. Zhang, Z. Chen, X. Liu, S. L. Hanna, X. Wang, R. Taheri-Ledari, A. Maleki, P. Li, O. K. Farha, *Chem. Soc. Rev.* **2020**, *49*, 7406-7427.
- [205] B. F. Hoskins, R. Robson, *J. Am. Chem. Soc.* **1989**, *111*, 5962-5964.
- [206] B. F. Hoskins, R. Robson, *J. Am. Chem. Soc.* **1990**, *112*, 1546-1554.
- [207] B. F. Abrahams, B. F. Hoskins, D. M. Michail, R. Robson, *Nature* **1994**, *369*, 727-729.
- [208] M. Fujita, Y. J. Kwon, S. Washizu, K. Ogura, *J. Am. Chem. Soc.* **1994**, *116*, 1151-1152.
- [209] O. M. Yaghi, H. Li, *J. Am. Chem. Soc.* **1995**, *117*, 10401-10402.
- [210] M. Kondo, T. Yoshitomi, H. Matsuzaka, S. Kitagawa, K. Seki, *Angew. Chem. Int. Ed. Engl.* **1997**, *36*, 1725-1727.
- [211] H. Li, M. Eddaoudi, T. L. Groy, O. M. Yaghi, *J. Am. Chem. Soc.* **1998**, *120*, 8571-8572.
- [212] S. S.-Y. Chui, S. M.-F. Lo, J. P. H. Charmant, A. G. Orpen, I. D. Williams, *Science* **1999**, *283*, 1148-1150.
- [213] H. K. Kim, W. S. Yun, M. B. Kim, J. Y. Kim, Y. S. Bae, J. Lee, N. C. Jeong, *J. Am. Chem. Soc.* **2015**, *137*, 10009-10015.
- [214] H. Li, M. Eddaoudi, M. O'Keeffe, O. M. Yaghi, *Nature* **1999**, *402*, 276-279.
- [215] M. Eddaoudi, D. B. Moler, H. Li, B. Chen, T. M. Reineke, M. O'Keeffe, O. M. Yaghi, *Acc. Chem. Res.* **2001**, *34*, 319-330.
- [216] D. J. Tranchemontagne, J. L. Mendoza-Cortes, M. O'Keeffe, O. M. Yaghi, *Chem. Soc. Rev.* **2009**, *38*, 1257-1283.
- [217] H. Jiang, D. Alezi, M. Eddaoudi, *Nat. Rev. Mater.* **2021**, *6*, 466-487.

- [218] O. M. Yaghi, *J. Am. Chem. Soc.* **2016**, *138*, 15507-15509.
- [219] M. Eddaoudi, J. Kim, N. Rosi, D. Vodak, J. Wachter, M. O'Keeffe, O. M. Yaghi, *Science* **2002**, *295*, 469-472.
- [220] O. M. Yaghi, *ACS Cent Sci* **2019**, *5*, 1295-1300.
- [221] M. P. Suh, H. J. Park, T. K. Prasad, D. W. Lim, *Chem. Rev.* **2012**, *112*, 782-835.
- [222] Z. Chen, P. Li, R. Anderson, X. Wang, X. Zhang, L. Robison, L. R. Redfern, S. Moribe, T. Islamoglu, D. A. Gómez-Gualdrón, T. Yildirim, J. F. Stoddart, O. K. Farha, *Science* **2020**, *368*, 297-303.
- [223] Y. He, W. Zhou, G. Qian, B. Chen, *Chem. Soc. Rev.* **2014**, *43*, 5657-5678.
- [224] J. Gallagher, *Nat. Energy* **2018**, *3*, 86-86.
- [225] T. Tian, Z. Zeng, D. Vulpe, M. E. Casco, G. Divitini, P. A. Midgley, J. Silvestre-Albero, J. C. Tan, P. Z. Moghadam, D. Fairen-Jimenez, *Nat. Mater.* **2018**, *17*, 174-179.
- [226] C. A. Trickett, A. Helal, B. A. Al-Maythaly, Z. H. Yamani, K. E. Cordova, O. M. Yaghi, *Nature Reviews Materials* **2017**, *2*.
- [227] P. D. C. Dietzel, V. Besikiotis, R. Blom, *J. Mater. Chem.* **2009**, *19*, 7362.
- [228] T. M. McDonald, W. R. Lee, J. A. Mason, B. M. Wiers, C. S. Hong, J. R. Long, *J. Am. Chem. Soc.* **2012**, *134*, 7056-7065.
- [229] N. A. Khan, Z. Hasan, S. H. Jhung, *J. Hazard. Mater.* **2013**, *244-245*, 444-456.
- [230] E. Barea, C. Montoro, J. A. Navarro, *Chem. Soc. Rev.* **2014**, *43*, 5419-5430.
- [231] T. Islamoglu, Z. Chen, M. C. Wasson, C. T. Buru, K. O. Kirlikovali, U. Afrin, M. R. Mian, O. K. Farha, *Chem. Rev.* **2020**, *120*, 8130-8160.
- [232] D. A. Reed, B. K. Keitz, J. Oktawiec, J. A. Mason, T. Runcevski, D. J. Xiao, L. E. Darago, V. Crocella, S. Bordiga, J. R. Long, *Nature* **2017**, *550*, 96-100.
- [233] Y. Li, G. Wen, *Eur. J. Inorg. Chem.* **2020**, *2020*, 2303-2311.
- [234] R. Matsuda, R. Kitaura, S. Kitagawa, Y. Kubota, R. V. Belosludov, T. C. Kobayashi, H. Sakamoto, T. Chiba, M. Takata, Y. Kawazoe, Y. Mita, *Nature* **2005**, *436*, 238-241.
- [235] J. F. Olorunyomi, S. T. Geh, R. A. Caruso, C. M. Doherty, *Mater. Horizons* **2021**, *8*, 2387-2419.
- [236] L. E. Kreno, K. Leong, O. K. Farha, M. Allendorf, R. P. Van Duyne, J. T. Hupp, *Chem. Rev.* **2012**, *112*, 1105-1125.
- [237] Y. Takashima, V. M. Martinez, S. Furukawa, M. Kondo, S. Shimomura, H. Uehara, M. Nakahama, K. Sugimoto, S. Kitagawa, *Nat. Commun.* **2011**, *2*, 168.
- [238] M. G. Campbell, D. Sheberla, S. F. Liu, T. M. Swager, M. Dinca, *Angew. Chem. Int. Ed. Engl.* **2015**, *54*, 4349-4352.
- [239] H. Yuan, J. Tao, N. Li, A. Karmakar, C. Tang, H. Cai, S. J. Pennycook, N. Singh, D. Zhao, *Angew. Chem. Int. Ed. Engl.* **2019**, *58*, 14089-14094.
- [240] D. Yang, B. C. Gates, *ACS Catalysis* **2019**, *9*, 1779-1798.
- [241] A. Dhakshinamoorthy, Z. Li, H. Garcia, *Chem. Soc. Rev.* **2018**, *47*, 8134-8172.
- [242] C. Wang, Z. Xie, K. E. deKrafft, W. Lin, *J. Am. Chem. Soc.* **2011**, *133*, 13445-13454.
- [243] C.-D. Wu, A. Hu, L. Zhang, W. Lin, *J. Am. Chem. Soc.* **2005**, *127*, 8940-8941.
- [244] H. Lin, X. Wang, H. Hu, B. Chen, G. Liu, *Solid State Sci.* **2009**, *11*, 643-650.
- [245] S. Wang, C. M. McGuirk, A. d'Aquino, J. A. Mason, C. A. Mirkin, *Adv. Mater.* **2018**, *30*, e1800202.
- [246] M. Sindoro, N. Yanai, A.-Y. Jee, S. Granick, *Acc. Chem. Res.* **2014**, *47*, 459-469.
- [247] N. Stock, S. Biswas, *Chem. Rev.* **2012**, *112*, 933-969.
- [248] J. Cravillon, R. Nayuk, S. Springer, A. Feldhoff, K. Huber, M. Wiebcke, *Chem. Mater.* **2011**, *23*, 2130-2141.
- [249] Z. Ni, R. I. Masel, *J. Am. Chem. Soc.* **2006**, *128*, 12394-12395.
- [250] Y. S. Li, H. Bux, A. Feldhoff, G. L. Li, W. S. Yang, J. Caro, *Adv. Mater.* **2010**, *22*, 3322-3326.
- [251] E. Haque, N. A. Khan, J. H. Park, S. H. Jhung, *Chem. Eur. J.* **2010**, *16*, 1046-1052.
- [252] W. J. Rieter, K. M. L. Taylor, H. An, W. Lin, W. Lin, *J. Am. Chem. Soc.* **2006**, *128*, 9024-9025.
- [253] X. Zhao, X. Fang, B. Wu, L. Zheng, N. Zheng, *Sci. China Chem.* **2013**, *57*, 141-146.
- [254] W. Cho, H. J. Lee, M. Oh, *J. Am. Chem. Soc.* **2008**, *130*, 16943-16946.

- [255] T. Tsuruoka, S. Furukawa, Y. Takashima, K. Yoshida, S. Isoda, S. Kitagawa, *Angew. Chem. Int. Ed. Engl.* **2009**, *48*, 4739-4743.
- [256] A. Umemura, S. Diring, S. Furukawa, H. Uehara, T. Tsuruoka, S. Kitagawa, *J. Am. Chem. Soc.* **2011**, *133*, 15506-15513.
- [257] A. Schaate, P. Roy, A. Godt, J. Lippke, F. Waltz, M. Wiebcke, P. Behrens, *Chem. Eur. J.* **2011**, *17*, 6643-6651.
- [258] M. Pang, A. J. Cairns, Y. Liu, Y. Belmabkhout, H. C. Zeng, M. Eddaoudi, *J. Am. Chem. Soc.* **2012**, *134*, 13176-13179.
- [259] N. Yanai, S. Granick, *Angew. Chem. Int. Ed. Engl.* **2012**, *51*, 5638-5641.
- [260] M. Sindoro, A. Y. Jee, S. Granick, *Chem. Commun. (Camb.)* **2013**, *49*, 9576-9578.
- [261] H. J. Lee, J. We, J. O. Kim, D. Kim, W. Cha, E. Lee, J. Sohn, M. Oh, *Angew. Chem. Int. Ed. Engl.* **2015**, *54*, 10564-10568.
- [262] J. Park, Q. Jiang, D. Feng, L. Mao, H. C. Zhou, *J. Am. Chem. Soc.* **2016**, *138*, 3518-3525.
- [263] M. L. Kelty, W. Morris, A. T. Gallagher, J. S. Anderson, K. A. Brown, C. A. Mirkin, T. D. Harris, *Chem. Commun. (Camb.)* **2016**, *52*, 7854-7857.
- [264] X. Cai, J. Lin, M. Pang, *Cryst. Growth Des.* **2016**, *16*, 3565-3568.
- [265] W. Morris, S. Wang, D. Cho, E. Auyeung, P. Li, O. K. Farha, C. A. Mirkin, *ACS Appl. Mater. Interfaces* **2017**, *9*, 33413-33418.
- [266] Y. Zhao, Q. Zhang, Y. Li, R. Zhang, G. Lu, *ACS Appl. Mater. Interfaces* **2017**, *9*, 15079-15085.
- [267] Y. Li, Y. Zhao, R. Zhang, G. Lu, *Inorg. Chem. Commun.* **2017**, *82*, 68-71.
- [268] S. Bao, X. Cai, Y. Shi, M. Pang, *CrystEngComm* **2017**, *19*, 1875-1878.
- [269] C. Avci, I. Imaz, A. Carne-Sanchez, J. A. Pariente, N. Tasios, J. Perez-Carvajal, M. I. Alonso, A. Blanco, M. Dijkstra, C. Lopez, D. Maspoch, *Nat. Chem.* **2017**, *10*, 78-84.
- [270] S. Wang, Y. Lv, Y. Yao, H. Yu, G. Lu, *Inorg. Chem. Commun.* **2018**, *93*, 56-60.
- [271] L. He, M. Brasino, C. Mao, S. Cho, W. Park, A. P. Goodwin, J. N. Cha, *Small* **2017**, *13*.
- [272] D. Liu, S. A. Kramer, R. C. Huxford-Phillips, S. Wang, J. Della Rocca, W. Lin, *Chem. Commun. (Camb.)* **2012**, *48*, 2668-2670.
- [273] D. Liu, C. Poon, K. Lu, C. He, W. Lin, *Nat. Commun.* **2014**, *5*, 4182.
- [274] S. Wang, W. Morris, Y. Liu, C. M. McGuirk, Y. Zhou, J. T. Hupp, O. K. Farha, C. A. Mirkin, *Angew. Chem. Int. Ed. Engl.* **2015**, *54*, 14738-14742.
- [275] S. Wang, C. M. McGuirk, M. B. Ross, S. Wang, P. Chen, H. Xing, Y. Liu, C. A. Mirkin, *J. Am. Chem. Soc.* **2017**, *139*, 9827-9830.
- [276] N. Nakajima, Y. Ikada, *Bioconj. Chem.* **1995**, *6*, 123-130.
- [277] A. Zimpel, T. Preiß, R. Röder, H. Engelke, M. Ingrisch, M. Peller, J. O. Rädler, E. Wagner, T. Bein, U. Lächelt, S. Wuttke, *Chem. Mater.* **2016**, *28*, 3318-3326.
- [278] K. Xie, Q. Fu, Y. He, J. Kim, S. J. Goh, E. Nam, G. G. Qiao, P. A. Webley, *Chem. Commun. (Camb.)* **2015**, *51*, 15566-15569.
- [279] S. Nagata, K. Kokado, K. Sada, *Chem. Commun. (Camb.)* **2015**, *51*, 8614-8617.
- [280] W. Morris, W. E. Briley, E. Auyeung, M. D. Cabezas, C. A. Mirkin, *J. Am. Chem. Soc.* **2014**, *136*, 7261-7264.
- [281] W. H. Chen, X. Yu, A. Cecconello, Y. S. Sohn, R. Nechushtai, I. Willner, *Chem Sci* **2017**, *8*, 5769-5780.
- [282] I. Abanades Lazaro, S. Haddad, S. Sacca, C. Orellana-Tavra, D. Fairen-Jimenez, R. S. Forgan, *Chem* **2017**, *2*, 561-578.
- [283] M. Tsotsalas, A. Umemura, F. Kim, Y. Sakata, J. Reboul, S. Kitagawa, S. Furukawa, *J. Mater. Chem.* **2012**, *22*, 10159.
- [284] N. Yanai, M. Sindoro, J. Yan, S. Granick, *J. Am. Chem. Soc.* **2013**, *135*, 34-37.
- [285] G. Lu, C. Cui, W. Zhang, Y. Liu, F. Huo, *Chem. Asian J.* **2013**, *8*, 69-72.
- [286] C. Cui, Y. Liu, H. Xu, S. Li, W. Zhang, P. Cui, F. Huo, *Small* **2014**, *10*, 3672-3676.
- [287] M. Pang, A. J. Cairns, Y. Liu, Y. Belmabkhout, H. C. Zeng, M. Eddaoudi, *J. Am. Chem. Soc.* **2013**, *135*, 10234-10237.

- [288] X. Cai, X. Deng, Z. Xie, S. Bao, Y. Shi, J. Lin, M. Pang, M. Eddaoudi, *Chem. Commun. (Camb.)* **2016**, 52, 9901-9904.
- [289] N. Singh, S. Ahmed, A. Fakim, S. Qutub, O. Alahmed, O. El Tall, O. Shekhah, M. Eddaoudi, N. M. Khashab, *Chem Sci* **2020**, 11, 11280-11284.

Chapter 2

Objectives

Objectives

As presented in the first Chapter, MOFs as an emerging class of porous materials with a high impact in several fields thanks to their high porosity, structural diversity and high chemical tenability. Beyond their “classical ” properties related to their internal structures, the production of MOFs in the form of colloids has brought a paradigm shift in the design of new functional porous materials. Along with their intrinsic interest as porous solids, colloidal MOF particles can additionally be dispersed, shaped and functionalized, and show different polyhedral shapes. Thanks to these properties, colloidal polyhedral MOFs could become a new family of functional building particles that can be used to create novel self-assembled functional materials.

Self-assembly of colloidal particles into multidimensional superstructures is a promising and effective approach to explore and achieve some interesting and unexpected applications. Traditionally, spherical colloidal particles (mainly silica, or polymers such as polystyrene and acrylates) have been used to develop such artificial self-assembled colloidal materials. However, recently, the use of non-spherical polyhedral particles has begun to be considered as a viable approach to diversify possible self-assembled materials, including the formation of crystals, liquid crystals, plastic crystals and quasicrystals. To date, only a few studies have illustrated the use of polyhedral particles to generate long-range ordered arrangements that pack into different lattices; none of which exhibited photonic properties. In this context, the use and self-assembly of colloidal polyhedral MOFs can represent a paradigm shift in the field of self-assembly. However, the use of colloidal polyhedral MOFs to create such functional superstructures is still in the embryonic stage.

In this context, this Thesis aimed to approach the use of MOFs in the self-assembly field and explore MOFs as a rich source of polyhedral particles that can be assembled like “atoms” and “molecules” to provide access to a new generation of self-assembled materials. To achieve these targets, three specific objectives have been proposed:

- Demonstrate that polyhedral MOF particles can be used to direct the assembly of colloidal clusters. This strategy will focus on the use of polyhedral MOF particles as core particles to control the coordination number and geometry of colloidal clusters, by attaching single spherical polystyrene particles on each facet of the MOF particles. This objective is addressed in the first publication in Chapter 5.

- Demonstrate that the orientation of self-assembled MOF supercrystals can be modulated without templates, using surfactants. We aim to synthesize supercrystals of ZIF-8 particles with well-defined truncation. Then, we will study how the presence of surfactants can affect the orientation growth of these supercrystals, and how these different orientations show different photonic properties. This objective is presented in the second publication in Chapter 6.
- Finally, we aim to explore polyhedral MOF particles as building blocks to synthesize supraparticles with ordered structure and study their structural color. We will study how various polyhedral MOF particles can self-assemble within the confinement of an emulsion droplet and form spherical, consolidated and ordered photonic supraparticles. We will analyze the structural coloration as a function of the size of these anisotropic building blocks and their internal structure. This objective is addressed in the third study in the Appendix.

Chapter 3

Summary of the Results and Discussion

Objective 1. Assembly of Colloidal Clusters Driven by the Polyhedral Shape of Metal-Organic Framework Particles

In the first publication, we have studied on the use of polyhedral-shaped MOFs crystals to direct the assembly of colloidal clusters. Colloidal molecules or clusters are an essential component for assembling and designing more complex architectures, such as patchy particles and self-assembled colloidal crystals (*e.g.*, with diamond or pyrochlore structures), and provides unique routes for the formation of new photonic crystals, micromotors and drug delivery systems.¹⁻⁹ To date, there are several synthetic approaches to form such clusters, including phase separation, heterogeneous nucleation or growth and DNA hybrids bridging.^{10,11} However, the vast majority of reported examples are made of spherical particles like silica, polymers and inorganic particles. In the case of spherical particles, the coordination number and geometry of the colloidal clusters can be modulated by adjusting particle size ratios or phase separation phenomena.

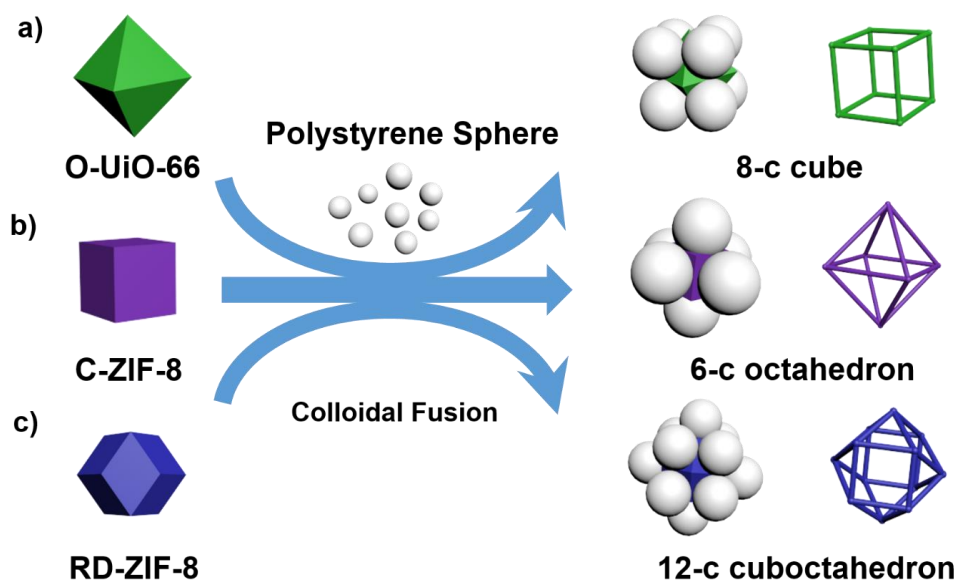


Figure 39. Schematic illustration of the formation of colloidal 8-c cubic, 6-c octahedral, and 12-c cuboctahedral clusters. Polyhedral MOF crystals are used as core particles to assemble these coordination clusters. The polyhedral shape of MOF particles dictates the coordination number and geometry of the resulting clusters.

In the first study of this Thesis, we proposed a new strategy that uses the polyhedral shape of MOF particles to direct the assembly of colloidal clusters. The MOF crystal faces directed

both the position and number of assembled satellite polystyrene particles determining the final coordination number of the colloidal cluster. The colloidal clusters were assembled by controlling the attachment of single spherical polystyrene particles on each face of MOF polyhedral particle via colloidal fusion synthesis (Figure 39).^{5,12,13}

Firstly, we synthesized homogeneous octahedral UiO-66 particles (O-UiO-66), cubic and rhombic dodecahedral ZIF-8 particles (C-ZIF-8 and RD-ZIF-8), respectively. The O-UiO-66 particles were synthesized by heating a mixture solution of ZrCl_4 , terephthalic acid, and acetic acid in DMF at 120 °C for 12 hours. Afterwards, the synthesized particles were washed with DMF and methanol upon centrifugation, and finally dispersed in water containing polyvinylpyrrolidone (PVP). C-ZIF-8 particles were formed by mixing an aqueous solution of $\text{Zn}(\text{NO}_3)_2 \cdot 6\text{H}_2\text{O}$, 2-methylimidazole (2-MiM) and hexadecyltrimethylammonium bromide (CTAB) at room temperature for 5 hours. Finally, RD-ZIF-8 particles were synthesized by combining an aqueous solution of zinc acetate with 2-methylimidazole for 24 hours. The resulting particles were collected by centrifugation, washed with water, and finally redispersed in an aqueous solution of tetrabutylammonium bromide (TBAB). All above particles were characterized by field-emission scanning electron microscopy (FESEM), powder X-ray diffraction (PXRD), and zeta-potential, which revealed the formation of uniform polyhedral MOF particles. The edge size of octahedral UiO-66 particles was 735 ± 21 nm (diameter: 1039 ± 30 nm) and the surface charge of particles was approximately + 45 mV. The size of cubic and rhombic dodecahedral ZIF-8 particles were 205 ± 10 nm and 526 ± 27 nm, both with zeta potential of approximately + 40 mV (Figure 40).

We initially targeted the synthesis of eight-coordinated (8-c) cubic colloidal clusters using O-UiO-66 core particles. In a typical experiment, colloidal clusters were assembled by adding 100 μL of the negatively charged PS colloid into 100 μL of the O-UiO-66 suspension. Then, the water-soluble plasticizer tetrahydrofuran (THF) was rapidly added to the mixture to give a final THF concentration of 18% (v/v), followed by handshaking for 10 seconds. This process can be explained by the change of the surface tension of PS spheres due to the presence of plasticizers, leading to melting and deformation, and promoting better adhesion to the MOF core particles. After that, the as-obtained sediments of the mixture suspensions were purified via density gradient centrifugation and washed with deionized water several times. Following this method, the assembly of spherical polystyrene particles with different diameters (400 nm, 700 nm, and 1 μm) was first systematically investigated to determine the optimal particle size of a single polystyrene particle attached to each triangle facet of the O-UiO-66 octahedron. The

concentration of polystyrene and O-UiO-66 colloidal particles were kept at 160 and 2 mg/mL, respectively. In the case of polystyrene spheres with a diameter of 400 nm, SEM images showed that two or more particles were attached to each facet of octahedron, preventing the formation of the desired cubic colloidal clusters. Conversely, the 700 nm diameter of polystyrene spheres was the ideal object for the individual assembly of clusters, only one polystyrene sphere was attached one polyhedral facet of O-UiO-66 colloidal particle. Due to the steric hindrance between the particles, we only observed very low connection between O-UiO-66 colloidal particle and the polystyrene sphere with 1 μm diameter (Figure 41).

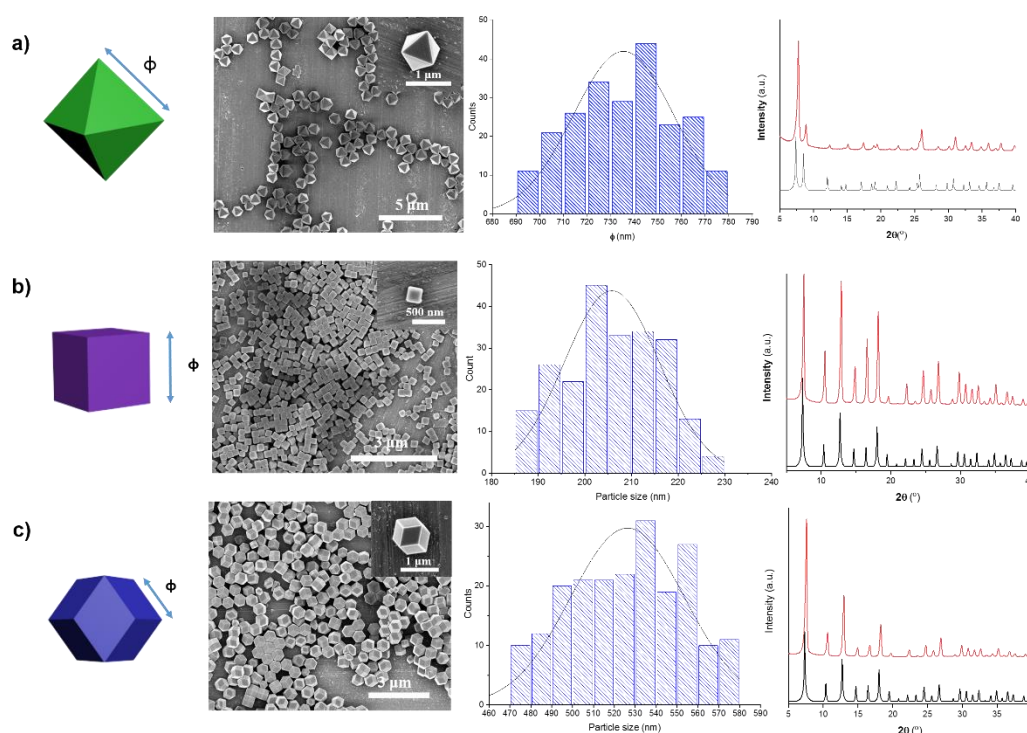


Figure 40. Scheme and FESEM image of an as-synthesized MOF particles. (a-c) O-UiO-66 particles with a mean ϕ of 735 ± 21 nm (a), C-ZIF-8 particles with a mean ϕ of 205 ± 10 nm (b), and RD-ZIF-8 particles with a mean ϕ of 526 ± 27 nm (b). From Left to right are: Scheme of an as-synthesized MOF particles highlighting the particle size (ϕ); Representative FESEM images; Size-distribution histograms; and PXRD patterns of simulated (black) and as-synthesized MOF particles (red).

The ideal cubic colloidal clusters are composed of eight polystyrene spheres and a single polyhedral O-UiO-66 particle: each facet of the octahedron is occupied by a single polystyrene sphere. Noted that we consider defective clusters those clusters in which one or more of the eight polystyrene particles are missing. To maximize the assembly of cubic cluster, we

modified the $w_{\text{PS}}:w_{\text{UiO-66}}$ ratio between two colloids from 40:1 to 300:1. Figure 42 shows the statistical distribution of the coordination number of clusters synthesized using $w_{\text{PS}}:w_{\text{UiO-66}}$ ratios of 40:1, 80:1, 150:1, and 300:1. At a ratio of 40:1, the number of cubic colloidal clusters was only 35%. The majority of clusters were defective with coordinative numbers 5, 6 and 7, whereby the latter accounting for up to 44%. As the ratio rose to 80:1, cubic clusters began to predominate. At this ratio, defective clusters with coordination numbers of five and six gradually disappeared, leaving those with 7-coordinated number exhibited 38% of the total population. When the ratio rose to 150:1, the cubic colloidal clusters still kept the highest proportion, which presented the optimum condition for the assembly cubic cluster. More precisely, the majority of cases were perfect cubic clusters (61%) and defective colloidal clusters (32%) lacking only one polystyrene sphere, respectively. At the higher ratio, we still achieved a similar distribution in the total population of the formation of cubic colloidal clusters (Figure 42).

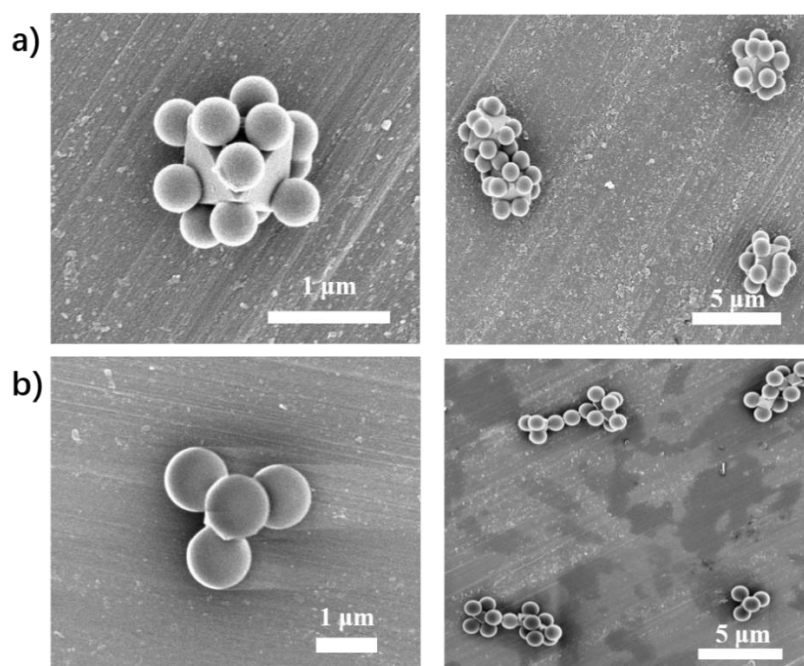


Figure 41. (a) Representative FESEM images corresponding to the experiment in which 8-c cubic clusters were assembled by combining O-UiO-66 particles with 400 nm-in-diameter of polystyrene spheres, and (b) with 1 μm -in-diameter of polystyrene spheres.

To validate that polyhedral shapes can be used as templates and guide the formation of other colloidal clusters, we also extended it to ZIF-8 particles with different shapes, namely cube and rhombic dodecahedron. According to our strategy, the attachment of a single PS

sphere to the six facets of C-ZIF-8 particles and the twelve facets of RD-ZIF-8 particles should lead to the formation of colloidal octahedral (coordination number 6) and cuboctahedra (coordination number 12), respectively. In Figure 43, it can be observed that 6 coordinated polystyrene spheres were perfectly attached on each surface of the C-ZIF-8 nanoparticle, forming the 6-c octahedral colloidal clusters. Also, the RD-ZIF-8 particle with different crystal facets allowed 12 polystyrene spheres attachment, hence constructing 12-c cuboctahedral clusters.

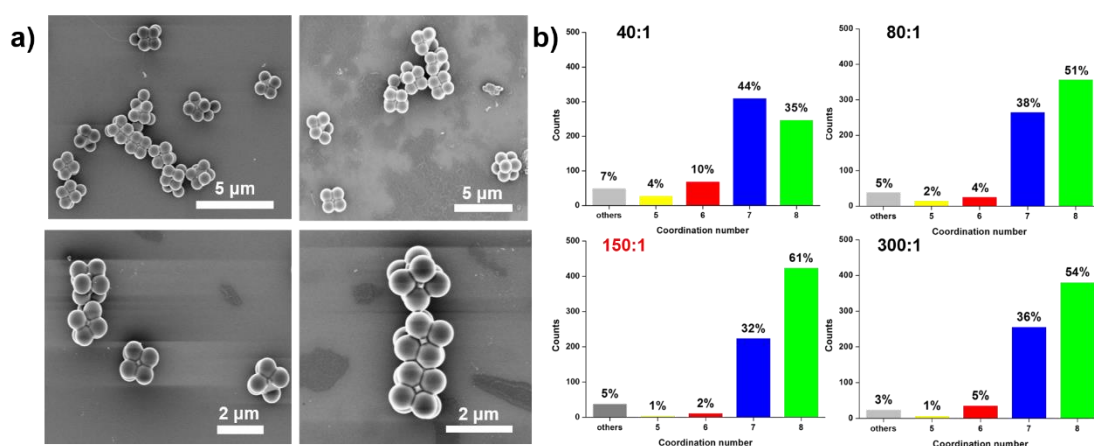


Figure 42. (a) FESEM images of the colloidal cubic clusters synthesized at $w_{PS}:w_{UiO-66} = 150:1$; (b) Statistical distributions of the coordination number for clusters with different $w_{PS}:w_{UiO-66}$ ratios.

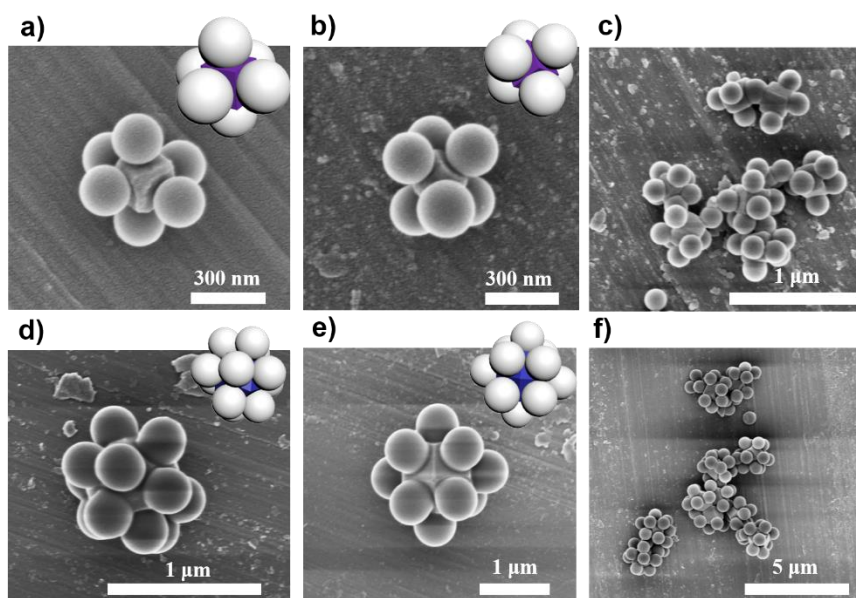


Figure 43. (a–c) Schematic illustrations and corresponding FESEM images of 6-c octahedral and (d–f) 12-c cuboctahedral clusters.

The synthesis of colloidal clusters was based on the mix and melt process described by Sacanna by using a plasticizer.¹³ The melting process depended on the concentration of plasticizer used during the assembly. At low concentration of plasticizer, we could assemble colloidal clusters, whereas high plasticizer concentration lead to the formation of core-shell particles. In the second part of study, we decided to increase the concentration of the plasticizer (THF solution). The synthesis of 8-c cubic clusters was repeated increasing the amount of THF to 26% or 30% (v/v). When the THF concentration was increased to 26% v/v, the eight polystyrene spheres merged with each other and engulfed the core O-UiO-66 particle, thus the resulting cubic clusters evolved into cellular-type particles. Increment of THF contents to 30% v/v directly led to the full melting of all the coordinated polystyrene spheres, forming spherical core-shell particles in which individual O-UiO-66 particles were encapsulated inside a polystyrene sphere (Figure 44).

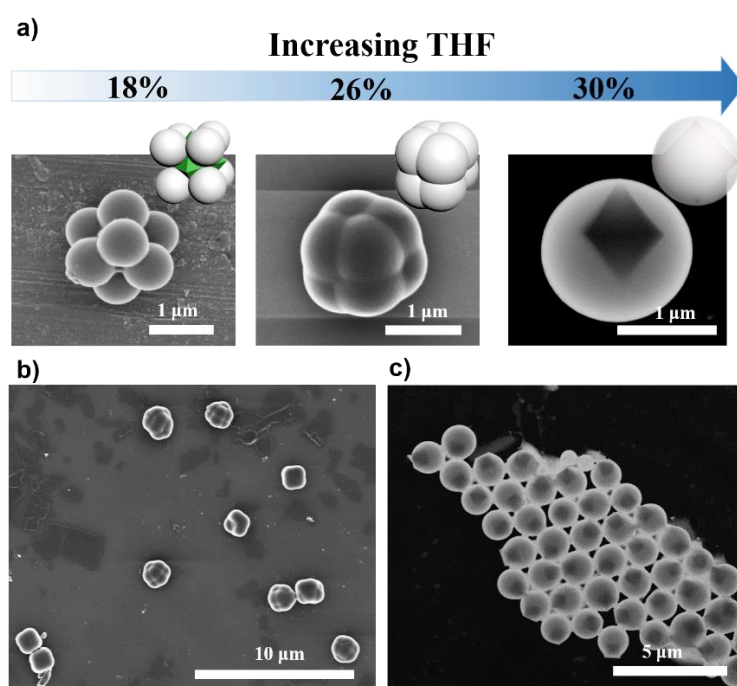


Figure 44. (a) Schematic illustration and corresponding FESEM and dark-field STEM images of the evolution from 8-c cubic colloidal clusters to core-shell particles upon increasing the concentration of THF. (b) FESEM image of the cellular-type particles synthesized at 26% v/v THF. (c) Dark-field STEM image of spherical core-shell O-UiO-66@polystyrene particles synthesized at 30% v/v THF.

In conclusion, we demonstrated the successful synthesis of a series of MOF based colloidal clusters, which were composed of a polyhedral MOF core particle and coordinated

spherical PS surroundings. We confirmed that MOF polyhedral shape define the coordinated number of the synthesized colloidal clusters. We synthesized six-coordinated (6-c) octahedral, 8-c cubic and 12-c cuboctahedral clusters using C-ZIF-8, O-UiO-66, and RD-ZIF-8 core particles, respectively. Moreover, we extended the use of this approach creating core-shell MOF@polymer particles through deep fusion.

Objective 2. Template-Free, Surfactant-Mediated Orientation of Self-Assembled Supercrystals of Metal-Organic Framework Particles

In the second study, we investigated the control of the orientation of three-dimensional supercrystals made of colloidal polyhedral ZIF-8 particles. Based on the investigation, we developed a facile template-free method to self-assemble (111)-, (100)- and (110)-oriented 3-D supercrystals of ZIF-8 particles by adjusting the amount of surfactant (CTAB) used. In a single crystal, the physical and mechanical properties often differ with orientation, due to different atomic interactions and bond distances along with the crystal orientation.¹⁴ For this reason, there has been an increasing interest in controlling the oriented growth of crystals on surfaces to maximize their performance and discover unusual phenomena. Various methods, including the vapor/liquid/solid (VLS) growth mechanism, oxide-assisted growth and template-based growth, have been developed to control the oriented growth of crystals on different surfaces.¹⁵⁻¹⁹ Controlled orientation of crystals on surfaces is also critical for improving gas separation performance and mass transfer, especially for porous materials integrated into devices or membranes.²⁰⁻²⁴ Similar trends are also expected from MOFs, this study starts from previous results reported from our group in 2018.²⁵ In these previous results, we first demonstrated the synthesis of highly monodisperse MOF particles and their self-assembly into densest packings to form ordered 3-D supercrystals. Such supercrystals were 3-D well-ordered assemblies formed by truncated rhombic dodecahedral (TRD) shapes with distinct truncations. We showed that in these supercrystals, the densest packings are the *fcc* or the rhombohedral lattices, and that every constituent ZIF-8 crystal exhibits the same orientation of crystal plane.

Starting from these results, here we developed a template-free, controllable method to self-assemble different oriented *fcc* supercrystals of TRD-ZIF-8 crystals using surfactants. To

this end, we initially synthesized highly monodispersed TRD-ZIF-8 particles with a truncation value (t) $= 2x/(\phi + x) = 0.63$ (where ϕ is the distance between opposing square facets, and x is the side of the square facets) using CTAB as surfactant. This synthesis was done by adding a water solution containing 0.3 g of $\text{Zn}(\text{OAc})_2 \cdot 2\text{H}_2\text{O}$ into a solution of 1.56 g of 2-MiM and 0.40 mg CTAB in 5 mL of water with gentle stirring for a few seconds. The resulting transparent mixture turned first turbid and then white after 15 seconds. The mixture was left undisturbed at room temperature for 2 hours. The resulting ZIF-8 particles were washed with water, and characterized by FESEM, PXRD, and Brunauer–Emmett–Teller (BET) measurements, resulting revealed the formation of highly monodispersed TRD-ZIF-8 particles showing the following dimensions: $t = 0.63$; size (ϕ) $= 233 \pm 14$ nm; and edge-length of square facets (x) $= 106 \pm 8$ nm (Figure 45).

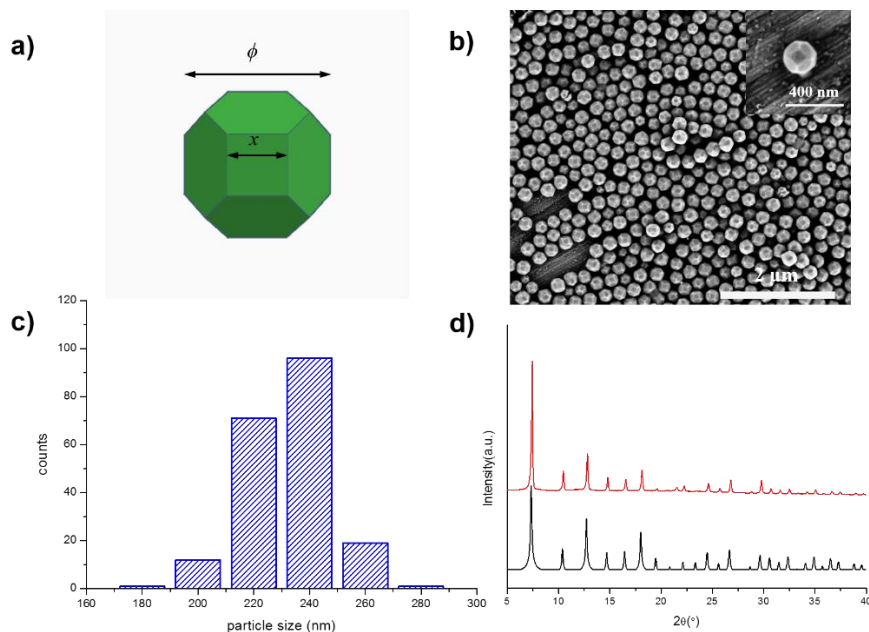


Figure 45. (a) Schematic illustrations of the TRD-ZIF-8 particles, highlighting: particle size ϕ and edge length x ; (b) Representative FESEM images of as-synthesized ZIF-8 particles with $t = 0.63$; (c) Size-distribution histograms of as-synthesized ZIF-8 particles with $t = 0.63$; and (d) PXRD patterns of simulated (black) and as-synthesized particles (red).

Next, we studied the self-assembly process to form ZIF-8 supercrystals. The above-synthesized particles were redispersed in water with a concentration of 50 mg/mL, and then a droplet of 40 μL of the dispersion was placed on a polydimethylsiloxane (PDMS) coated SEM pin at 120 $^{\circ}\text{C}$ for 3 minutes until total evaporation. After evaporation, we achieved a round-

shaped, colorful monolith, which showed structural color that can be observed by naked eye. This result indicated the formation of an ordered supercrystalline phase. Further study revealed the formation of an ordered supercrystal that adopts an *fcc* lattice, oriented in the entropically favored $\langle 111 \rangle$ direction. The $\langle 111 \rangle$ orientation of all TRD-ZIF-8 particles is perpendicular to the monolith surface and therefore, parallel to its (111) orientation. To obtain other orientation supercrystals, we prepared colloidal solutions of ZIF-8 particles using various concentrations of CTAB. Using a CTAB concentration of 3.00 mg/mL, a homogeneous (100)-oriented *fcc* supercrystal was assembled. Interestingly, by further increasing the CTAB concentration, we started to observe $\langle 110 \rangle$ oriented domains as well. Although a purely $\langle 110 \rangle$ oriented supercrystal could not be obtained even at a CTAB concentration of 4.00 mg/ml, we still found a large, homogeneous, (110)-oriented area, together with some (100)-oriented domains near the center of the monolith (Figure 46).

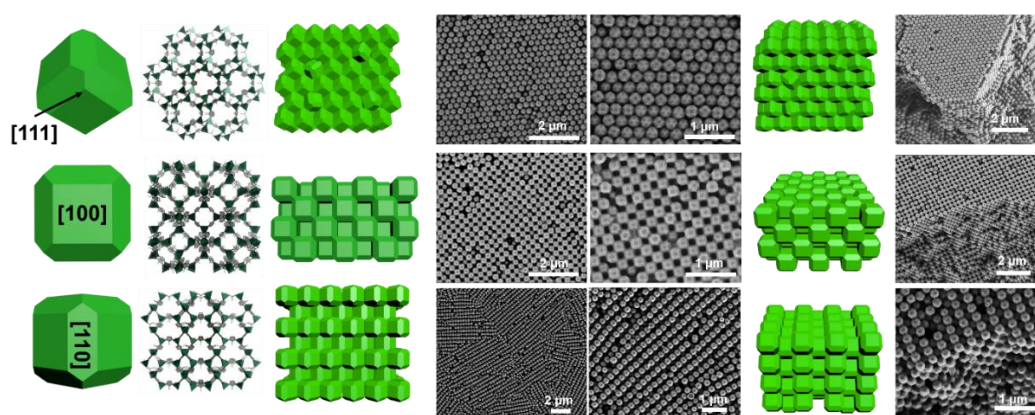


Figure 46. Formation of a) (111)-, b) (100)-, and c) (110)-oriented *fcc* supercrystals of TRD-ZIF-8 particles. Each section contains (from left to right) a schematic view of a single TRD-ZIF-8 particle oriented along the corresponding plane; a view of the oriented crystal structure of ZIF-8; a schematic view of the packing of the supercrystals, and corresponding FESEM images; and a schematic view of the 3D packing of the supercrystals, and corresponding FESEM image.

To further study the possible influence of other surfactant on the self-assembly of TRD-ZIF-8 particles, we investigated different surfactants including cationic surfactant CTAB and the anionic surfactant sodium dodecyl sulfate (SDS). We stepwise increased the concentration of both surfactants from 1 to 6 mg/mL, and then analyzed the resulting supercrystals growth. As we discussed before, at 1 mg/mL and 3 mg/mL of CTAB solution, the whole monoliths were (111)-oriented and (100)-oriented supercrystals, respectively. For other concentrations of

CTAB, the monolith showed domains with different orientations. On the other hand, at a concentration of SDS lower than 2 mg/mL, disordered TRD-ZIF-8 particle assemblies were obtained. For SDS concentrations between 2 to 5 mg/mL, only (111)-oriented supercrystals were observed. When increasing the SDS concentration up to 6 mg/mL, we began to detect the formation of (100)-oriented domains. All these results further convinced of the importance of the surfactant concentration to control the growth orientation of supercrystal (Figure 47).

We speculated that the possible effects of surfactant on the self-assembly process are: firstly, the repulsive interaction can increase during the assembly of TRD-ZIF-8 particles due to the addition of more positive charges from the surfactant; secondly, the reduction of droplet surface tension and/or the formation of CTAB micelles can adjust the particle assembly.

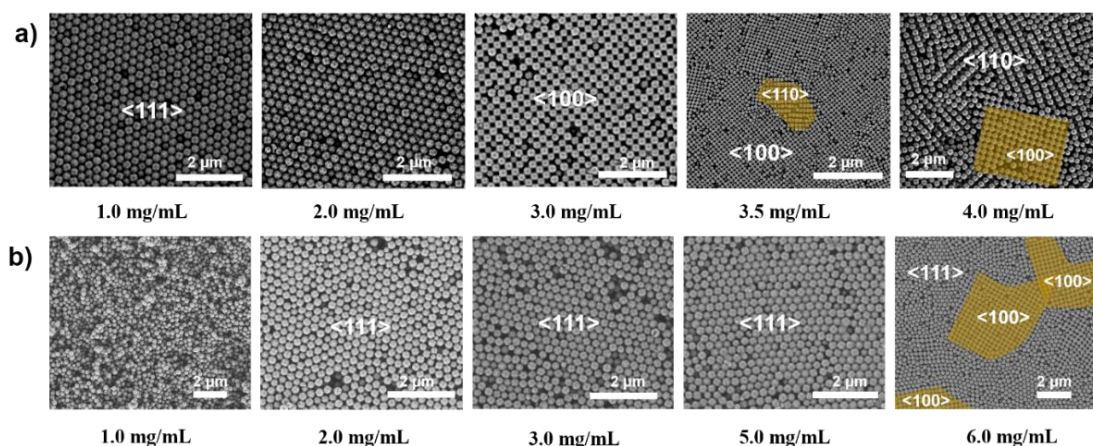


Figure 47. (a) Representative FESEM images of TRD-ZIF-8 supercrystals self-assembled using CTAB. (b) Representative FESEM images of TRD-ZIF-8 supercrystals self-assembled using SDS.

As these materials are periodic dielectric structures made of TRD-ZIF-8 particles (size: ≈ 230 nm), they also showed angle-dependent opalescence visible to the naked eye that originates from a photonic bandgap. For this reason, we studied the photonic properties of these supercrystals. We observed that the monolith was accompanied by a color change from green to blue when the CTAB concentration was increased from 1 mg/mL to 3 mg/mL. Further characterization using UV-Visible reflectance spectrometry confirmed that a shift of photonic bandgap in supercrystals orientation, exhibiting the reflectance peak at $\lambda_{111} = 578$ nm and $\lambda_{100} = 505$ nm, corresponding to (111)-oriented and (100)-oriented supercrystals, respectively. The theoretical analysis of the photonic properties of ZIF-8 supercrystals showed that the (100)-oriented supercrystals presented a *fcc* symmetry, which was confirmed by calculating the

refractive index and defining the geometry. In this case, the $\langle 100 \rangle$ axes of the ZIF-8 supercrystals were oriented parallel to the axis in an fcc crystal of an air cube. The reflectance peak in the (001) orientation exhibited the first gap in the X point of the Brillouin zone. We calculated the refractive index that was suitable to the X-gap frequency ($\lambda_{100} = 505$ nm), and the results corresponded to previously reported values (1.535).²⁵ However, due to the facet that $\langle 111 \rangle$ crystallites axes of ZIF-8 supercrystals were preferentially oriented along the (111) supercrystal axis, the (111)-oriented supercrystals exhibited plastic *fcc* configuration, in which the particles are placed in lattice positions of an *fcc* but in random orientation (Figure 48).

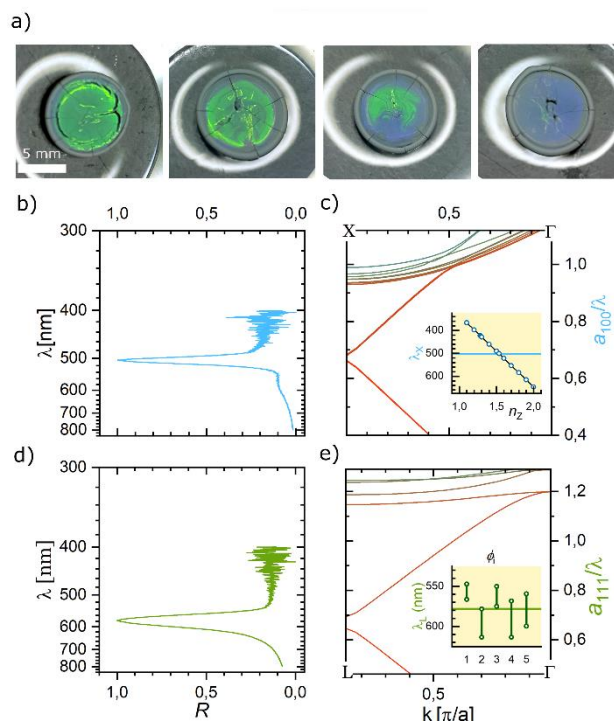


Figure 48. (a) Change in color of the supercrystals obtained upon increasing the CTAB concentration (left to right: 1, 2, 2.5, and 3 mg/mL). Normalized specular optical reflectance plots from b) (100) and d) (111) arrangements, and the corresponding photonic band structures in the c) ΓX and e) ΓL directions. The insets in panels (c) and (e) show the photonic gap positions λ_X and λ_L as functions of refractive index and mean particle size ϕ_i , respectively.

In conclusion, we have demonstrated the self-assembly of TRD-ZIF-8 particles into differently oriented *fcc* supercrystals. These monolithic structures are composed of monodisperse crystalline particles, in which the $\langle 111 \rangle$ ZIF-8 particle direction normally orients as the (111) supercrystal direction. However, when increasing the amount of CTAB,

this entropically favored $\langle 111 \rangle$ orientation of these ZIF-8 supercrystals can be tuned to the $\langle 100 \rangle$ and even $\langle 110 \rangle$ orientation.

Objective 3. Coloration in Supraparticles Assembled from Polyhedral Metal-Organic Framework Particles

In the first study, we presented the polyhedral MOF particles as core particles to assemble the colloidal clusters directly. In the second study, we developed the self-assembly of TRD-ZIF-8 crystals into (111)-, (100)-, and (110)-oriented *fcc* supercrystals via tuning the amount of surfactant without template-assisted. These two studies demonstrated the advantages and prospects of colloidal polyhedral MOF particles in the self-assembly field. In the last study of this Thesis, we continued expanding the use of MOF particles in self-assembly. In particular, we studied the self-assembly of colloidal polyhedral MOF in confined spaces (in this case, using emulsions) to create MOF-based supraparticles.

This study was done using four different polyhedral MOF particles to systematically study the relationship between these MOF particles and their resultant self-assembled supraparticles and their photonic properties. We began this study with the synthesis of the different polyhedral MOF particles. We chose four different polyhedral shapes from two MOF families: the rhombic dodecahedron (RD-ZIF-8), truncated rhombic dodecahedron (TRD-ZIF-8) and cube (C-ZIF-8) from the ZIF-8 family, and the octahedron (O-UiO-66) from the UiO-66 family. C-ZIF-8 particles were synthesized by adding $\text{Zn}(\text{NO}_3)_2 \cdot 6\text{H}_2\text{O}$, 2-MiM and CTAB in water for 5 hours at room temperature. Both RD-ZIF-8 and TRD-ZIF-8 particles were synthesized by mixing an aqueous solution of $\text{ZnAc}_2 \cdot 2\text{H}_2\text{O}$, 2-Mim and CTAB (only in the case of TRD-ZIF-8) at room temperature for 2 hours. As for O-UiO-66 particles, a DMF solution of ZrCl_4 , terephthalic acid and acetic acid was heated for 12 hours at 120 °C. All these colloids were washed with water or DMF and then redispersed in water at a certain concentration. The resulting colloids were characterized by FESEM, PXRD and zeta-potential measurements, revealing the formation of the following colloidal MOF particles: C-ZIF-8 (191 ± 9 nm), TRD-ZIF-8 (181 ± 9 nm; 198 ± 10 nm; 229 ± 9 nm; and 247 ± 10 nm), RD-ZIF-8 (246 ± 12 nm; 267 ± 12 nm; and 293 ± 13 nm) and O-UiO-66 (edge size: 194 ± 12 nm; 238 ± 13 nm; and 247 ± 13 nm).

We next performed to self-assembly experiments using emulsions. For this, 0.5 wt% non-ionic alcohol ethoxylate surfactant (Lutensol TO-8, BASF) was added to the ZIF-8 particles

dispersion, or 0.1 wt% PVP was added into a dispersion of the UiO-66 particles to improve colloidal stability. The dispersion is centrifuged three times to remove residue reactants and excess of surfactants. The aqueous particle dispersion was emulsified in perfluorinated oil (HFE 7500) either by vigorous shaking or droplet-based microfluidics. The droplets were stabilized using a perfluorsurfactant, and MOF supraparticles were formed by drying the droplets overnight in an open glass vial.

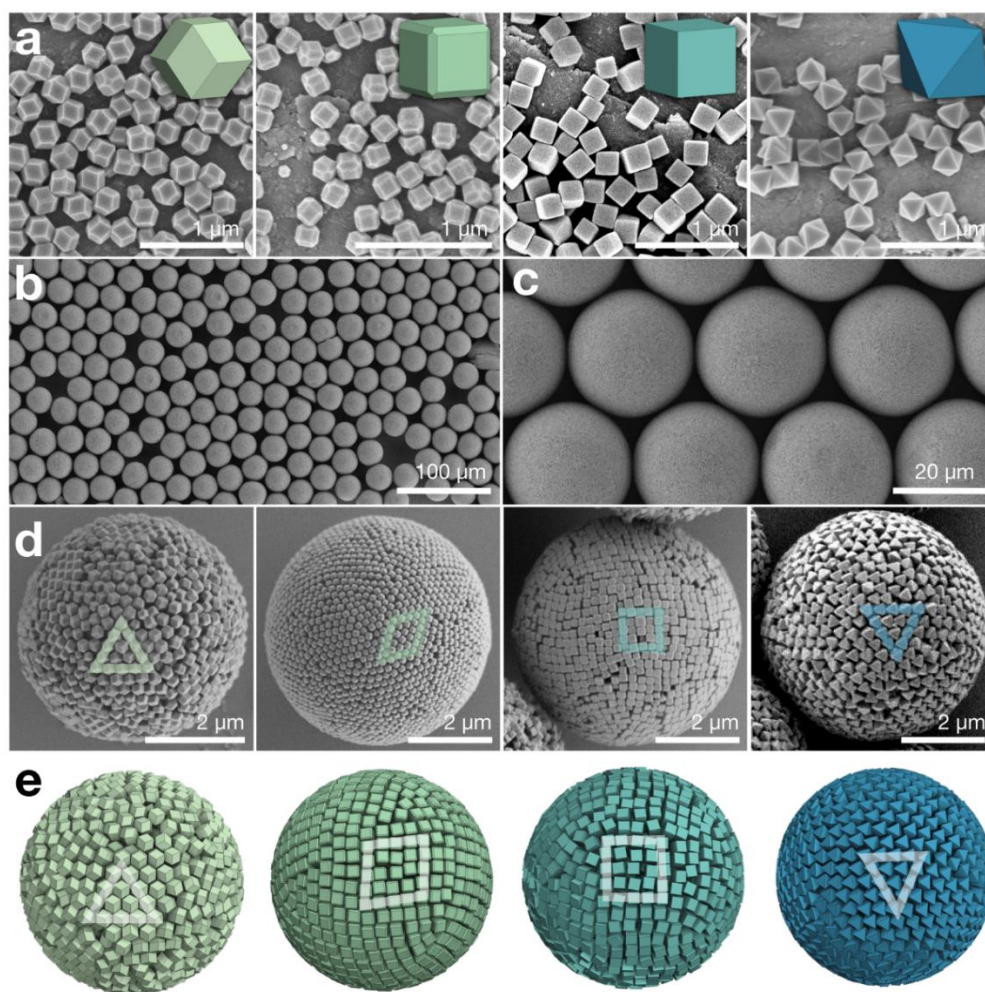


Figure 49. (a) FESEM of monodisperse RD-ZIF-8, TRD-ZIF-8, C-ZIF-8, and O-UiO-66 particles (left to right). (b, c) Monodisperse TRD-ZIF-8 supraparticles prepared by emulsifying the MOF particle dispersion using droplet-based microfluidics. (d) FESEM (from left to right) of RD-ZIF-8, TRD-ZIF-8, C-ZIF-8 and O-UiO-66 supraparticles, exhibiting ordered surfaces and characteristic packings. (e) Snapshots of Monte Carlo simulations with polyhedra in spherical confinement.

We characterized all these supraparticles by FESEM. All four types of supraparticles exhibited spherical morphology and ordered surface with a characteristic packing from the polyhedral shape of primary MOF particles. A triangular unit cell and a rhombic unit cell were observed on the RD- and TRD-ZIF-8 supraparticles surface, respectively, agreeing with their bulk *fcc* packing and rhombohedral packings. The C-ZIF-8 particles formed a square unit cell at the spherical supraparticle surface, and the O-UiO-66 particles formed a triangular cell. Except for the RD particles, particles of all other shapes exposed their flat faces to form a smooth supraparticle surface, both in experiment and simulation. This is caused by entropic force that favors face to face contact, instead of the vertex to face configuration in polyhedral packing, which tends to align flat faces of particles to the droplet interface. All these supraparticles were confirmed by Monte Carlo simulation of hard polyhedra with excluded volume interaction in spherical confinement (Figure 49).

Then, we applied two direct imaging techniques, namely X-ray tomography (XRM) and focused ion and beam (FIB)-assisted cross-sectioning, to investigate the inner structure of the different supraparticles. X-ray transmission image (Figure 50) of C-ZIF-8 supraparticle with cube particles showed that up to ten concentric layers are evident near the surface, which meant formed an ordered, onion-like structure. Similarly, other types of supraparticles also exhibited onion-like layers structure. Thick onion-like layers were observed in TRD-ZIF-8 supraparticles, whereas the RD-ZIF-8 and the O-UiO-66 supraparticles showed only little onion-like layers. To visualize the onion-like structure in a supraparticle, we used focused-ion beam to reveal the cross-section of the supraparticles. Concentric layers were observed for all four particle shapes near the supraparticle surface, conforming to the spherical curvature. The RD-ZIF-8 supraparticles had the thinnest onion-like layers, with most of their interior being amorphous or short-range ordered. In comparison, the TRD-ZIF-8 and C-ZIF-8 supraparticles consisted of thick onion-like layers near the surface and small disordered interior. Noteworthily, the TRD-ZIF-8 supraparticles exhibited very high crystallinity throughout the interior, although in multiple crystalline domains. We believed that sufficient equilibration may allow TRD-ZIF-8 supraparticle to evolve towards complete crystallization with global symmetry, similar to those observed for spherical particles or small nanocrystals.

Our discovery of the internal order of the MOF supraparticles prompted us to study their photonic properties. To this end, four types of MOF supraparticles were illuminated with a white light under a reflective optical microscope, from which a colored circle appeared at the center of the TRD-ZIF-8 and C-ZIF-8 supraparticles. This unique color motif agrees with

constructive interference of light reflected at the spherical-symmetric ordered onion layers. In contrast, a less pronounced reflection color was observed in the RD-ZIF-8 and the O-UiO-66 supraparticles, which indicated a low degree of internal ordering. Microscopic reflection spectra recorded a narrow and defined peak for the TRD- and C-ZIF-8 supraparticles; the RD-ZIF-8 and O-UiO-66 supraparticles exhibited a broader peak, which confirmed these observations. Note that the large, ordered domains throughout the all supraparticle surfaces, indicating that polydispersity is not the origin of the reduced order of some shapes (Figure 51).

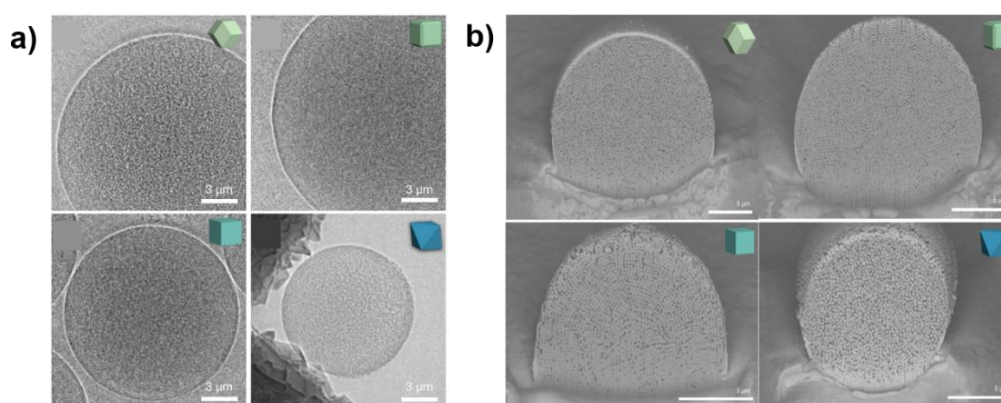


Figure 50. (a) Transmissive X-ray images of each MOF supraparticle; (b) Cross-section images of each supraparticle revealed by focused-ion beam milling.

We then systematically studied the relationship between initial particle dimensions and the structural color of the supraparticles using reflection spectra measurements. To this end, we varied the sizes of the differently-shaped MOF particles from the formed MOF supraparticles. The reflection peaks for all samples shifted linearly with increasing initial particle size. Compared to other shapes, larger RD-ZIF-8 particles were required to generate the same reflection peaks. As shown in Figure 52, all types of supraparticles exhibited a green reflection color with similar particles size (197 nm, 191 nm and 194 nm, corresponding to the TRD-ZIF-8, C-ZIF-8 and O-UiO-66 particles, respectively) except the RD-ZIF-8 particle with larger size (246 nm). These differences are caused by the packing of the differently-shaped particles. Entropy favors the particles to align their faces within each layer and between layers. According to the close-packed model, for the TRD-ZIF-8 and C-ZIF-8 particles, the surface of packing layer is close to “flat”, thus the layer distance is the same as the distance between the two opposite faces of the TRD-ZIF-8 and C-ZIF-8 particles. However, as for RD-ZIF-8

particles, there are jagged protrusions and indentations on the surface of packing layer, resulting the distance between layers smaller than the size of the RD-shaped particles.

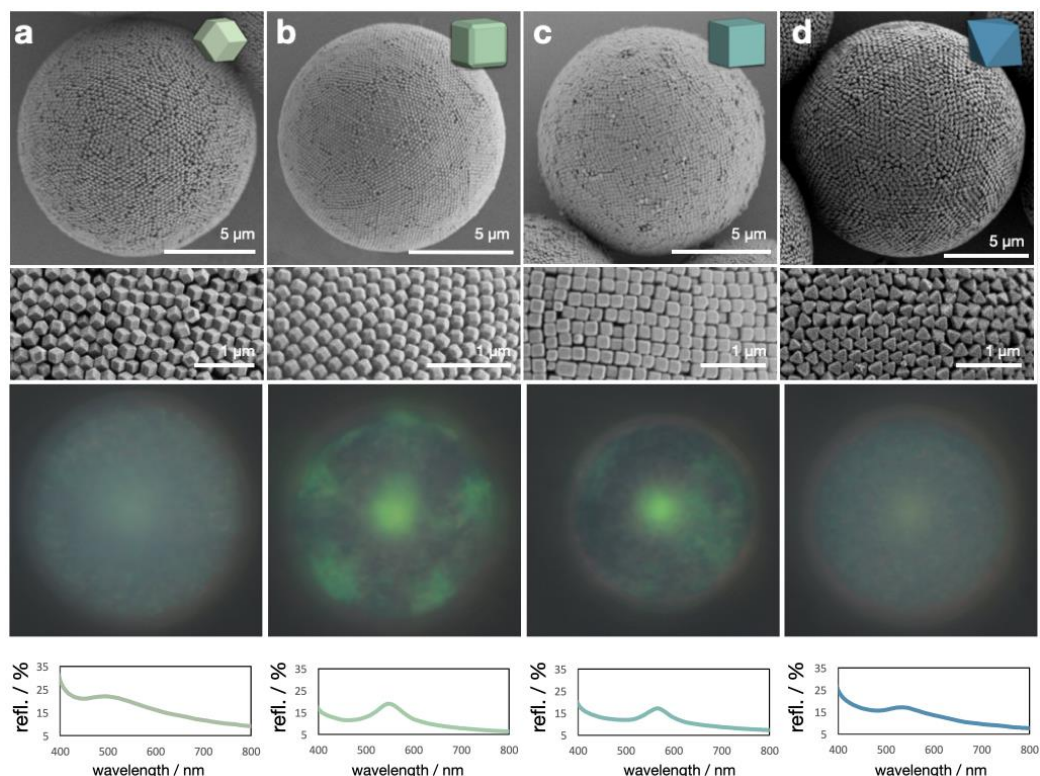


Figure 51. Top row: FESEM of RD-ZIF-8 (a), TRD-ZIF-8 (b), C-ZIF-8 (c) and O-UiO-66 (d) supraparticles, exhibiting structural coloration from the interaction of the incident light and the supraparticle structure (optical microscopy images in inset). Middle row: magnification of the particle surfaces, showing well-ordered arrangements of the primary particles; bottom row: reflection spectra measured for individual supraparticles.

Finally, we investigated the macroscopic, angle-dependent coloration of the different MOF supraparticles, measured directly in suspension with different angles. To compare intuitively, we measured the reflectance spectra of different supraparticles suspensions that were assembled from similar-sized initial particles of different shapes. The reflection peak shifted to lower wavelengths with increasing angles from 30° to 90° between incident light and observation. A quantitative comparison between all samples revealed that the particle size, shape and material type do not show a discernable influence on the peak shift, which indicates that the leading color mechanism originates from the interference of light reflected at the onion-like layers. In addition, we observed that the buckled RD-ZIF-8 supraparticles also showed the evident reflection peak and even maintain the angle-dependent coloration. It is possible that the RD-ZIF-8 particles also form stacked, nonconcentric layers near the supraparticles surface,

but only a few layers can be expected under the heavily buckled surface. We speculated that other mechanisms may conduce to this phenomenon. One possibility is additional surface grating effects. Some ordered arrangements with close-packed made by RD-ZIF-8 were observed on the surface of buckled RD-ZIF-8 supraparticles, similar to the surface of spherical supraparticles. We observed faint and localized patches of color in the light microscope images, so another possible source of color is the presence of large numbers of tiny crystallites consisting of dozens of particles randomly distributed in the supraparticles (Figure 52).

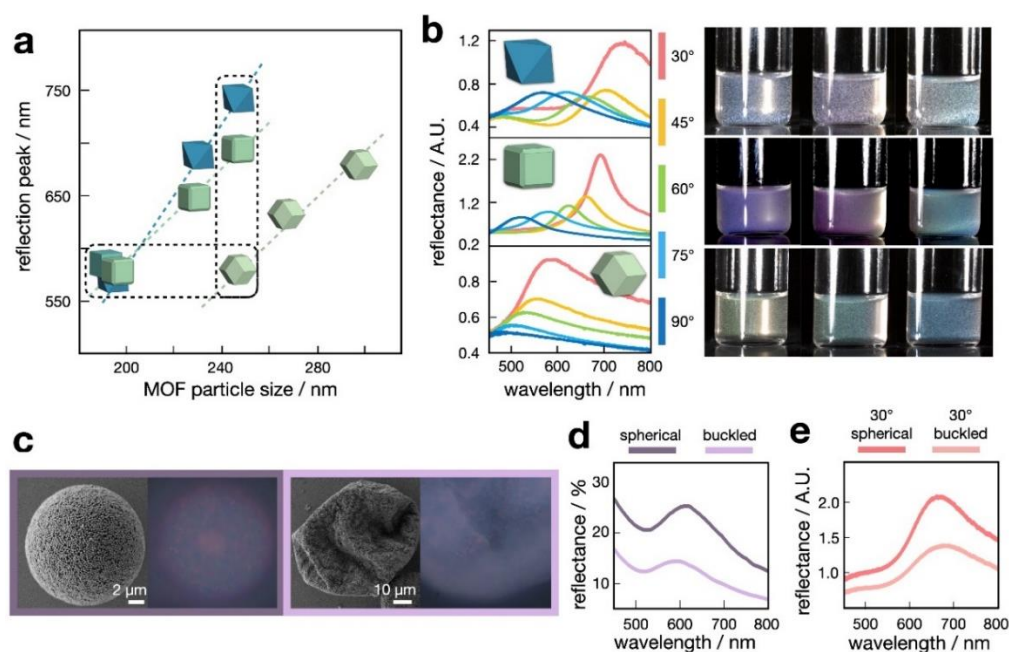


Figure 52. (a) Relationship between size and shape of the primary particles on the wavelength of the reflection peak, measured in suspension; (b) Angle-dependent reflectance spectra of MOF supraparticles consisting of the same colloidal particle size but different shapes, along with corresponding photographs showing the observable coloration; (c) FESEM of spherical and buckled MOF supraparticles, with optical microscopy images showing differences in structural color; (d) Reflectance spectra of individual spherical and buckled MOF supraparticles; (e) Reflectance spectra of spherical and buckled supraparticles measured in suspension.

In conclusion, we have demonstrated the generality of assembling polyhedral MOF particles into highly-ordered supraparticles using four different shapes. We showed the effect of the spherical geometry on the particle arrangement inside the supraparticle. Detailed shape-size-optical property relations connecting the properties of the individual particles with their propensity to assembly in the spherical confinement and the resultant coloration have been established.

References

- [1] A. v. Blaaderen, *Science* **2003**, *301*, 470-471.
- [2] V. N. Manoharan, M. T. Elsesser, D. J. Pine, *Science* **2003**, *301*, 483-487.
- [3] S. Radcliffe, *Nature* **2006**, *439*, 2.
- [4] Q. Liu, Z. Sun, Y. Dou, J. H. Kim, S. X. Dou, *J. Mater. Chem. A* **2015**, *3*, 11688-11699.
- [5] M. He, J. P. Gales, E. Ducrot, Z. Gong, G. R. Yi, S. Sacanna, D. J. Pine, *Nature* **2020**, *585*, 524-529.
- [6] E. Ducrot, M. He, G. R. Yi, D. J. Pine, *Nat. Mater.* **2017**, *16*, 652-657.
- [7] S. Ravaine, E. Duguet, *Curr. Opin. Colloid Interface Sci.* **2017**, *30*, 45-53.
- [8] B. W. Longbottom, S. A. F. Bon, *Scientific Reports* **2018**, *8*, 4622.
- [9] M. Yoshida, J. Lahann, *ACS Nano* **2008**, *2*, 1101-1107.
- [10] R. Merindol, E. Duguet, S. Ravaine, *Chem. Asian J.* **2019**, *14*, 3232-3239.
- [11] W. Li, H. Palis, R. Merindol, J. Majimel, S. Ravaine, E. Duguet, *Chem. Soc. Rev.* **2020**, *49*, 1955-1976.
- [12] Z. Gong, T. Hueckel, G. R. Yi, S. Sacanna, *Nature* **2017**, *550*, 234-238.
- [13] T. Hueckel, S. Sacanna, *ACS Nano* **2018**, *12*, 3533-3540.
- [14] S. Haussühl, *Physical properties of crystals: an introduction*, John Wiley & Sons, **2008**.
- [15] D. P. Norton, A. Goyal, J. D. Budai, D. K. Christen, D. M. Kroeger, E. D. Specht, Q. He, B. Saffian, M. Paranthaman, C. E. Klabunde, D. F. Lee, B. C. Sales, F. A. List, *Science* **1996**, *274*, 755-757.
- [16] K. Nomura, H. Ohta, K. Ueda, T. Kamiya, M. Hirano, H. Hosono, *Science* **2003**, *300*, 1269-1272.
- [17] R.-Q. Zhang, Y. Lifshitz, S.-T. Lee, *Adv. Mater.* **2003**, *15*, 635-640.
- [18] Z. Pan, H.-L. Lai, F. C. K. Au, X. Duan, W. Zhou, W. Shi, N. Wang, C.-S. Lee, N.-B. Wong, S.-T. Lee, S. Xie, *Adv. Mater.* **2000**, *12*, 1186-1190.
- [19] G. Cao, D. Liu, *Adv. Colloid Interface Sci.* **2008**, *136*, 45-64.
- [20] Z. Lai, G. Bonilla, I. Diaz, J. G. Nery, K. Sujaoti, M. A. Amat, E. Kokkoli, O. Terasaki, R. W. Thompson, M. Tsapatsis, D. G. Vlachos, *Science* **2003**, *300*, 456-460.
- [21] E. Biemmi, C. Scherb, T. Bein, *J. Am. Chem. Soc.* **2007**, *129*, 8054-8055.
- [22] D. Zacher, A. Baunemann, S. Hermes, R. A. Fischer, *J. Mater. Chem.* **2007**, *17*, 2785-2792.
- [23] O. Shekhah, M. Eddaoudi, *Chem. Commun.* **2013**, *49*, 10079-10081.
- [24] P. Falcaro, K. Okada, T. Hara, K. Ikigaki, Y. Tokudome, Aaron W. Thornton, Anita J. Hill, T. Williams, C. Doonan, M. Takahashi, *Nat. Mater.* **2017**, *16*, 342-348.
- [25] C. Avci, I. Imaz, A. Carne-Sanchez, J. A. Pariente, N. Tasios, J. Perez-Carvajal, M. I. Alonso, A. Blanco, M. Dijkstra, C. Lopez, D. Maspoch, *Nat. Chem.* **2017**, *10*, 78-84.

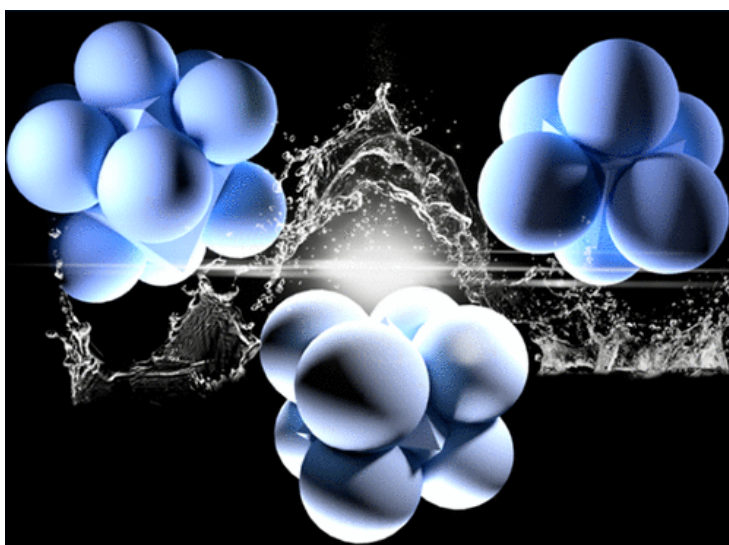
Chapter 4

General Conclusion

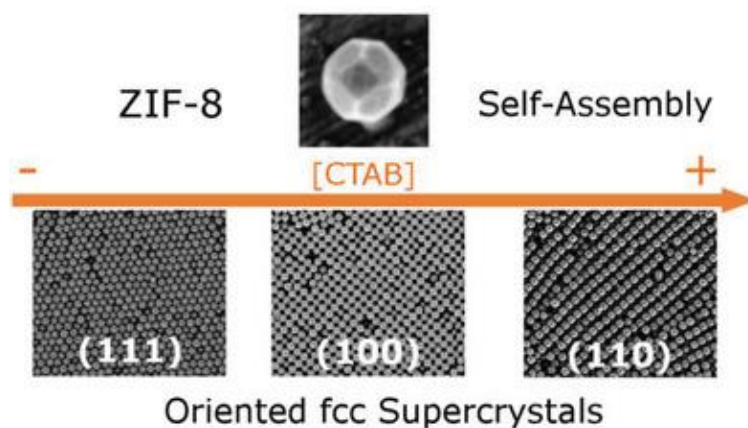
General Conclusion

The efforts of this Thesis orbited around evaluating the potential of MOF polyhedral particles (instead of traditional spherical particles) as a new type building blocks for the self-assembly of functional superstructures; and the related photonic properties of these new superstructures. Our work showed that, targeting different types of self-assemblies, polyhedral MOF particles can indeed constitute a new family of building particles to create new self-assembled porous architectures and explore new photonic properties.

First, we developed a new way to synthesize colloidal clusters using the polyhedral shape of MOF particles. This approach basically focused on the polyhedral shape of MOF particles, which served as core particles to control the final coordination number and geometry of the assembled colloidal clusters. In this approach, colloidal clusters with well-defined coordination numbers can be assembled by controlling the attachment of a single polystyrene particle on each facet of the polyhedral MOF particle via colloidal fusion method. As a proof of concept, we first assembled eight-coordinated (8-c) cubic colloidal clusters using octahedral UiO-66 core particles. Notably, we optimized two key parameters: the suitable size and the ratio between polyhedral UiO-66 particles and spherical polystyrene particles. We successfully extended the use of cubic and rhombic dodecahedral ZIF-8 particles to form colloidal clusters with an octahedral geometry (6-c) and with a much higher coordinated cuboctahedral geometry (12-c), respectively. Moreover, further study revealed that the resulting colloidal clusters could evolve into spherical core-shell MOF@polystyrene particles by tuning the concentration of the plasticizer. In these core-shell particles, the single MOF crystal that was initially used as the core particle is encapsulated into a polystyrene sphere.

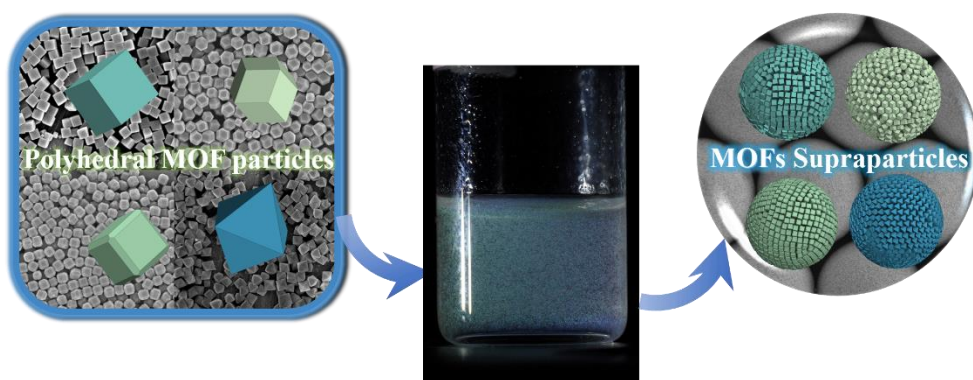


Then, we studied a template-free method to control the self-assembly of MOF particles into oriented superstructures. Instead of using a patterned surface that acts as a template for the self-assembly of superstructures, our approach emphasized on controlling the growth orientation of the face-centered cubic (*fcc*) superstructures using surfactants. To this end, we selected truncated rhombic dodecahedral (TRD) ZIF-8 particles (truncation $t = 0.63$), as they present all $\langle 111 \rangle$, $\langle 100 \rangle$, and $\langle 110 \rangle$ crystalline facets. In an initial self-assembly experiment, a colorful entropically favored (111)-oriented ZIF-8 superstructure was obtained using low CTAB concentration. Here, all TRD ZIF-8 particles were oriented along the $\langle 111 \rangle$ direction vertical to the surface of the monolith and parallel to the (111) direction of the superstructure. We then formed self-assembled (100)- and (110)-oriented superstructures by increasing the concentration of CTAB. With the generation of these latter structures, we demonstrated that CTAB plays a key role in the self-assembly process of these superstructures due: (i) to the positive charges that can induce an increase of the number of repulsive interactions; and (ii) to the formation of micelles or modification of the surface tensions of the droplet. In addition, we also observed that the different growth orientations induced by the surfactant concentration also originate a shift in the photonic properties.



Finally, we demonstrated the self-assembly of polyhedral MOF particles into uniform supraparticles with ordered structures and structural coloration. In this study, four types of colloidal polyhedral MOF particles, including cubic, truncated rhombic dodecahedral and rhombic dodecahedral ZIF-8 particles and octahedral O-UiO-66 particles, were first synthesized. We then confined the self-assembly of these colloidal particles into emulsion droplets, resulting in the formation of spherical ordered photonic supraparticles upon

evaporation of these droplets. These supraparticles showed an ordered surface, in which each type of polyhedral MOF particles adopts the entropic-favored packing arrangement. The study of the internal structure revealed that such MOF supraparticles exhibit ordered onion-like layer structures. The detailed study on the coloration of these supraparticles confirmed that it is due to the ordered internal structure, which act as Bragg reflectors and generate an interference effect. Indeed, supraparticles assembled from different sizes of MOF particles showed the periodicity of the Bragg diffraction in the reflection spectra. Meanwhile, the macroscopic, angle-dependent coloration of MOF supraparticles was attributed to the interference of light caused by the different shapes of the primary MOF particles. We also established the shape-size-coloration relationship between the individual MOF particles with their different assembly propensity and resultant coloration.



Overall, the three self-assembly processes developed in this Thesis illustrate the potential of using colloidal polyhedral MOF particles to access to new multidimensional functional assemblies that can incorporate porosity and photonic properties.

Chapter 5

Assembly of Colloidal Clusters Driven by the Polyhedral Shape of Metal- Organic Framework Particles

Assembly of Colloidal Clusters Driven by the Polyhedral Shape of Metal–Organic Framework Particles

Yang Liu, Jiemin Wang, Inhar Imaz,* and Daniel Maspoch*

Cite This: *J. Am. Chem. Soc.* 2021, 143, 12943–12947

Read Online

ACCESS |



Metrics & More



Article Recommendations



Supporting Information

ABSTRACT: Control of the assembly of colloidal particles into discrete or higher-dimensional architectures is important for the design of myriad materials, including plasmonic sensing systems and photonic crystals. Here, we report a new approach that uses the polyhedral shape of metal–organic-framework (MOF) particles to direct the assembly of colloidal clusters. This approach is based on controlling the attachment of a single spherical polystyrene particle on each face of a polyhedral particle via colloidal fusion synthesis, so that the polyhedral shape defines the final coordination number, which is equal to the number of faces, and geometry of the assembled colloidal cluster. As a proof of concept, we assembled six-coordinated (6-c) octahedral and 8-c cubic clusters using cubic ZIF-8 and octahedral UiO-66 core particles. Moreover, we extended this approach to synthesize a highly coordinated 12-c cuboctahedral cluster from a rhombic dodecahedral ZIF-8 particle. We anticipate that the synthesized colloidal clusters could be further evolved into spherical core–shell MOF@polystyrene particles under conditions that promote a higher fusion degree, thus expanding the methods available for the synthesis of MOF–polymer composites.

The assembly of colloidal molecules or clusters^{1–5} is a crucially important step in the design of more sophisticated architectures such as patchy particles^{6–8} and self-assembled colloidal crystals⁹ (e.g., with diamond or pyrochlore structures) and opens novel avenues for the formation of new photonic crystals,¹⁰ micromotors,¹¹ and drug-delivery systems.¹² Recently, great progress has been made in the development of synthetic strategies to form such particle clusters.¹³ These strategies are mainly based on either the growth of particles on the surface of a preformed particle, via phase-separation phenomena or surface nucleation and growth, or the controlled assembly of presynthesized particles via attractive interactions such as DNA hybridization, electrostatic interactions, and/or van der Waals forces.¹⁴ These synthetic methods typically use spherical particles, such as silica, polymers, and inorganic particles. Consequently, they all must accomplish the difficult task of directing the assembly and/or growth of particles on the surface of isotropic spherical particles via methods such as tuning the size ratio between the particles or phase-separation phenomena to control the coordination number and geometry of the synthesized colloidal cluster. Building this type of clusters is therefore not an easy task, especially for those involving geometries with high coordination numbers, in which the assembly or growth of many particles must be controlled.

Herein, we propose a new strategy for controlling colloidal assembly, based on replacing the spherical particles with polyhedral ones, whose faces are used to direct both the position and number of assembled satellite polystyrene (PS) particles (Figure 1). The polyhedral particles thus act as core particles with predetermined “instructions” that direct the coordination number and geometry of the synthesized colloidal clusters. For example, an octahedral core particle would direct the formation of an eight-coordinated (8-c) cubic

colloidal cluster, or a cubic core particle would template the synthesis of a 6-c octahedral colloidal cluster. In this way, polyhedral particles with a high number of faces could ideally be used to form clusters exhibiting geometries with high coordination numbers.

To implement our colloidal strategy, we selected metal–organic framework (MOF) particles as the core polyhedral particles. MOFs are a widely known class of porous crystalline materials that exhibit very high surface areas and have found a broad variety of applications, including gas storage and separation as well as catalysis and contaminant removal.^{15,16} However, in the present work, we targeted MOFs mainly because they are an excellent source of crystalline particles (Figure 1a–c) covering most known polyhedral shapes, thanks to the discovery of thousands of MOFs during the last 25 years.^{17–19} Moreover, recent advances in MOF synthesis allow them to be obtained as colloidal particles with highly homogeneous size and shape.^{20–23} Furthermore, their particle size can easily be tuned from ~50 nm to ~1 μm.^{24–27}

Taking advantage of these properties, we report herein the use of polyhedral MOF particles to direct the assembly of spherical polystyrene particles in terms of both number and position, allowing the synthesis of colloidal clusters through mix-and-melt or colloidal fusion synthesis (Figure 1). This synthesis has previously been reported by Sacanna et al.^{10,28,29} and is based on the use of liquid oil droplets or inorganic

Received: May 25, 2021

Published: August 12, 2021



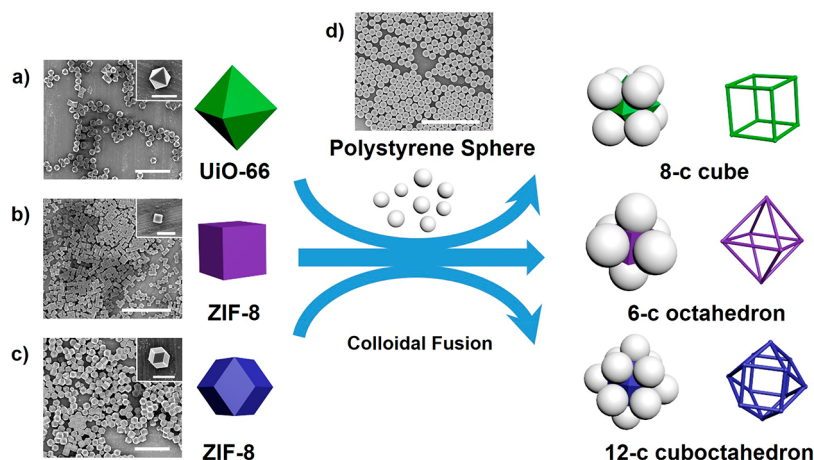


Figure 1. Schematic illustration of the use of polyhedral MOF crystals as core particles to assemble coordination clusters and the way in which their polyhedral shape dictates their coordination number and geometry. Using this strategy, colloidal 8-c cubic, 6-c octahedral, and 12-c cuboctahedral clusters were synthesized using octahedral UiO-66 particles, cubic ZIF-8 particles and rhombic dodecahedral ZIF-8 particles, respectively. Scale bars: 5 μm (parts a, b, c, d), 1 μm (insets in parts a, c), and 500 nm (inset in part b).

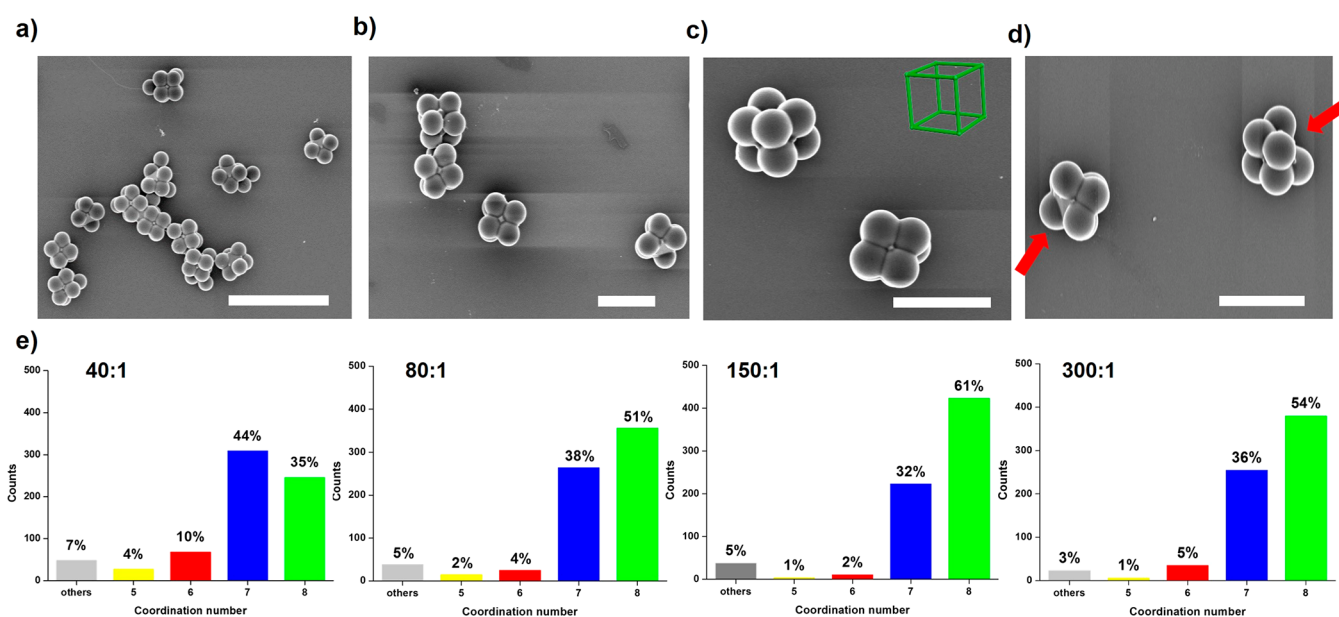


Figure 2. (a,b) FESEM images of the colloidal cubic clusters synthesized at $w_{\text{PS}}:w_{\text{UiO-66}} = 150:1$. (c) FESEM image of two cubic clusters positioned in different orientations. (d) FESEM image of two defective colloidal clusters with a coordination number of 7; arrows highlight the missing polystyrene sphere. (e) Statistical distributions of the coordination number for clusters with different $w_{\text{PS}}:w_{\text{UiO-66}}$ ratios. Scale bars: 5 μm (part a) and 2 μm (parts b–d).

nanoparticles as core particles onto which oppositely charged colloidal particles are stochastically aggregated. A plasticizer is then added to fuse the particles to form stable colloidal clusters, patchy particles, or core–shell particles.

To demonstrate the feasibility of our proposed strategy, we initially targeted the synthesis of 8-c cubic colloidal clusters using octahedral UiO-66 core particles (Figure 1a). The octahedral UiO-66 particles were first synthesized by heating a solution of ZrCl_4 , terephthalic acid, and acetic acid in DMF at 120 $^{\circ}\text{C}$ for 12 h. The synthesized particles were then collected by centrifugation, cleaned with DMF and methanol, and finally dispersed in water containing polyvinylpyrrolidone. Field-emission scanning electron microscopy (FESEM), X-ray powder diffraction (XRPD), and zeta-potential measurements of the resulting colloid revealed the formation of homogeneous octahedral UiO-66 particles with an edge size of 735 ± 21 nm

(diameter: 1039 ± 30 nm) and a surface charge of approximately +45 mV (Figures S1,S2). Commercial aqueous colloids of spherical sulfonated polystyrene particles with diameters of 400 nm, 700 nm, and 1 μm as well as a surface charge of approximately –30 mV were used as satellite particles (Figure 1d).

In a typical experiment, colloidal clusters were assembled by adding 100 μL of the polystyrene colloid on top of 100 μL of the dispersion of UiO-66 particles. Then, tetrahydrofuran (THF), which acts as the plasticizer, was added to the mixture to give a final THF concentration of 18% (v/v), and the mixture was mixed by hand for 10 s. After this short period, the assembled colloidal clusters were isolated using density gradient centrifugation (10–30 wt % sucrose in water), washed with water, and finally dispersed in water.

Following this protocol, the assembly of spherical polystyrene particles with various diameters (400 nm, 700 nm, and 1 μm) was first systematically studied to determine the optimum particle size for the attachment of a single polystyrene particle on each triangular facet of the UiO-66 octahedron. For this set of experiments, the concentrations of polystyrene and the UiO-66 colloid were kept constant at 160 and 2 mg/mL, respectively (i.e., $w_{\text{PS}}:w_{\text{UiO-66}} = 80:1$). Under these conditions, the 700 nm diameter polystyrene spheres proved to be ideal for individual particle assembly. The use of spherical polystyrene particles with a diameter of 400 nm resulted in the attachment of two or more particles on some facets of the octahedra, thus preventing the templating of cubic colloidal clusters by the polyhedral shape of the MOF particle (Figure S3). The 1 μm diameter polystyrene particles did not result in high occupancies of the eight facets of the octahedra, which was attributed to steric hindrance among themselves (Figure S4).

The synthesis of cubic colloidal clusters requires the attachment of a single polystyrene particle on each of the eight facets of the UiO-66 octahedra, i.e., achieving a coordination number of eight. Clusters missing one or more of the eight polystyrene particles can thus be considered defective. To maximize the formation of assemblies with eight polystyrene spheres on each UiO-66 particle, we performed a series of syntheses in which the $w_{\text{PS}}:w_{\text{UiO-66}}$ ratio was systematically varied (Figure 2, S5–S8). Figure 2e shows the statistical distribution of the coordination number of clusters synthesized using $w_{\text{PS}}:w_{\text{UiO-66}}$ ratios of 40:1, 80:1, 150:1, and 300:1. At a ratio of 40:1, the population of cubic colloidal clusters was 35%. However, in this case, most of the clusters were defective with coordination numbers of five, six, and seven, whereby the latter exhibited the highest population (44%). When the ratio was increased to 80:1, cubic clusters began to predominate (51%). At this ratio, the formation of defective clusters with coordination numbers of five and six was low, whereas those with a coordination number of seven represented 38% of the total population. This tendency continued at a ratio of 150:1, which provided the optimum conditions for the synthesis of cubic clusters. Under these conditions, 93% of the population consisted of perfect cubic colloidal clusters (61%; Figure 2a–c) or defective cubic clusters missing only one polystyrene sphere (32%; Figure 2d). Here, dynamic light scattering measurements further confirmed the formation of the clusters having a mean diameter of approximately 1.5 μm (Figure S9), which match those measured by FESEM (edge size: $1.34 \pm 0.06 \mu\text{m}$; diagonal size: $1.62 \pm 0.08 \mu\text{m}$). The use of higher ratios did not improve the formation of cubic colloidal clusters, but resulted in similar population percentages.

Having demonstrated the utility of the polyhedral shape of the core particles to serve as templates and guide the formation of cubic colloidal clusters, we extended the use of polyhedral MOF particles to form colloidal clusters with an octahedral geometry (coordination number: six) and with a much higher coordinated cuboctahedral geometry (coordination number: 12). To this end, we selected ZIF-8 particles due to their ability to be isolated as both cubic and rhombic dodecahedral colloidal particles (Figure 1b,c). According to our strategy, the attachment of a single polystyrene sphere to the six facets of ZIF-8 cubes and the 12 facets of rhombic dodecahedral ZIF-8 particles should lead to the formation of colloidal octahedra and cuboctahedra, respectively. Initially, ZIF-8 cubes were

formed by incubating an aqueous solution of $\text{Zn}(\text{NO}_3)_2 \cdot 6\text{H}_2\text{O}$, 2-methylimidazole, and hexadecyltrimethylammonium bromide (CTAB) at room temperature for 5 h. Rhombic dodecahedral ZIF-8 particles were synthesized by incubating an aqueous solution of zinc acetate and 2-methylimidazole for 24 h. In both reactions, the particles were collected by centrifugation, washed with water, and redispersed in the presence of CTAB. FESEM and XRPD measurements confirmed the formation of cubic and rhombic dodecahedral ZIF-8 particles with edge dimensions of $205 \pm 10 \text{ nm}$ and $526 \pm 27 \text{ nm}$, respectively (Figures S10–S13). Zeta-potential measurements of either particles showed a surface charge of approximately +40 mV. For the assemblies, we used negatively charged polystyrene particles with diameters of 200 and 600 nm in combination with the cubic and rhombic dodecahedral ZIF-8 particles, respectively, to optimize the attachment of a single polystyrene particle on each face of the ZIF-8 particles. Both 6-c octahedral (Figure 3a–c) and 12-c cuboctahedral

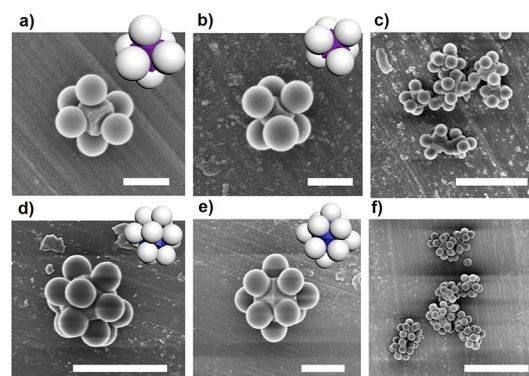


Figure 3. Schematic illustrations and corresponding FESEM images of 6-c octahedral (a–c) and 12-c cuboctahedral (d–f) clusters. Scale bars: 5 μm (part f), 1 μm (parts c–e), and 300 nm (parts a,b).

(Figure 3d–f) colloidal clusters were then assembled following a similar process to that used for the assembly of the 8-c cubic clusters. It should be noted here that the purification step in these assemblies involved multiple sedimentation–redispersion processes, as density gradient centrifugation (10–30 wt % sucrose in water) caused etching of the ZIF-8 particles (Figure S14).

Synthesis by colloidal fusion is a method that provides access not only to colloidal clusters but also to patchy and core–shell particles. The latter type of particles can be synthesized by controlling the amount of plasticizer (in this case: THF) added to the reaction. Indeed, the melting process in these reactions is usually controlled by tuning the concentration of the plasticizer. As described above, stable colloidal molecules can be formed when low concentrations of the plasticizer are used. However, the addition of higher concentrations of plasticizer allows further melting of the particles to form core–shell or patchy particles.²⁹ In conjunction with the use of MOFs as core particles, this possibility opens the door for the creation of MOF@polymer composites in which one MOF particle is encapsulated in a polymer shell (Figure 4). Accordingly, the above-described synthesis of 8-c cubic clusters was repeated with the amount of THF increased to 26% or 30% (v/v). FESEM images of the resulting assemblies showed that the cubic clusters evolved into cellular-type particles when the THF concentration was

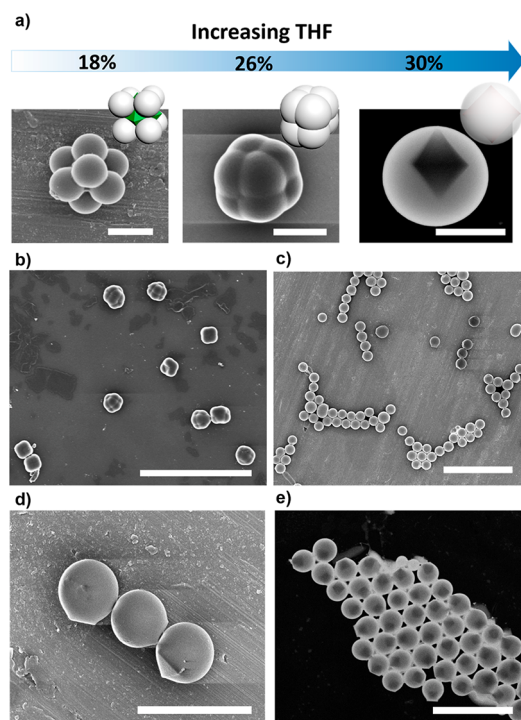


Figure 4. (a) Schematic illustration and corresponding FESEM and dark-field STEM images of the evolution from 8-c cubic colloidal clusters to core-shell particles upon increasing the concentration of THF. (b) FESEM image of the cellular-type particles synthesized at 26% v/v THF. (c–e) FESEM (parts c,d) and dark-field STEM (part e) images of spherical core-shell UiO-66@polystyrene particles synthesized at 30% v/v THF. Scale bars: 10 μm (parts b,c), 5 μm (part e), 3 μm (part d), and 1 μm (part a).

increased to 26% v/v (Figure 4a,b). In these particles, the eight polystyrene spheres merged with one another and engulfed the core UiO-66 particle. This melting process was completed at 30% v/v THF, where spherical core-shell particles consisting of a single UiO-66 particle encapsulated in a polystyrene shell were formed (Figure 4a,c–e).

In conclusion, we have demonstrated that the attachment of polystyrene particles on each face of a polyhedral metal-organic framework (MOF) particle can be controlled at the single-particle level. This control opens the door to using the polyhedral shape of MOF particles to drive the formation of colloidal clusters. Within this strategy, both the coordination number and geometry of the colloidal cluster are defined by the type of polyhedron used as the core particle. As a proof of concept, we synthesized six-coordinated (6-c) octahedral, 8-c cubic, and 12-c cuboctahedral clusters using cubic ZIF-8, octahedral UiO-66, and rhombic dodecahedral ZIF-8 core particles, respectively. Moreover, we extended the use of this approach to create core-shell MOF@polymer particles in which a single MOF crystal that is used as the core particle is encapsulated in a polystyrene sphere. We believe that this assembly approach will open new avenues for the synthesis of novel colloidal clusters with unprecedented geometries, including those with high connectivity, as well as for increasing the repertoire of colloidal clusters to assemble new three-dimensional superlattices.

■ ASSOCIATED CONTENT

Supporting Information

The Supporting Information is available free of charge at <https://pubs.acs.org/doi/10.1021/jacs.1c05363>.

Detailed syntheses, FESEM data and images, as well as PXRD diagrams (PDF)

■ AUTHOR INFORMATION

Corresponding Authors

Inhar Imaz – Catalan Institute of Nanoscience and Nanotechnology (ICN2), CSIC, and Barcelona Institute of Science and Technology, 08193 Barcelona, Spain; orcid.org/0000-0002-0278-1141; Email: inhar.imaz@icn2.cat

Daniel MasPOCH – Catalan Institute of Nanoscience and Nanotechnology (ICN2), CSIC, and Barcelona Institute of Science and Technology, 08193 Barcelona, Spain; ICREA, Barcelona 08010, Spain; orcid.org/0000-0003-1325-9161; Email: daniel.masPOCH@icn2.cat

Authors

Yang Liu – Catalan Institute of Nanoscience and Nanotechnology (ICN2), CSIC, and Barcelona Institute of Science and Technology, 08193 Barcelona, Spain

Jiemin Wang – Catalan Institute of Nanoscience and Nanotechnology (ICN2), CSIC, and Barcelona Institute of Science and Technology, 08193 Barcelona, Spain

Complete contact information is available at:

<https://pubs.acs.org/doi/10.1021/jacs.1c05363>

Notes

The authors declare no competing financial interest.

■ ACKNOWLEDGMENTS

This work was supported by the Spanish MINECO (project RTI2018-095622–B-I00), the Catalan AGAUR (project 2017 SGR 238), and by the CERCA Program/Generalitat de Catalunya. ICN2 is supported by the Severo Ochoa program from the Spanish MINECO (grant SEV-2017-0706). Y.L. acknowledges the China Scholarship Council for scholarship support.

■ REFERENCES

- (1) van Blaaderen, A. Chemistry: Colloidal molecules and beyond. *Science* **2003**, 301 (5632), 470–471.
- (2) Manoharan, V. N.; Elsesser, M. T.; Pine, D. J. Dense packing and symmetry in small clusters of microspheres. *Science* **2003**, 301 (5632), 483–487.
- (3) van Blaaderen, A. Colloids get complex. *Nature* **2006**, 439 (7076), 545–546.
- (4) Liu, Q.; Sun, Z.; Dou, Y.; Kim, J. H.; Dou, S. X. 2015. Two-step self-assembly of hierarchically-ordered nanostructures. *J. Mater. Chem. A* **2015**, 3, 11688–11699.
- (5) Nai, J.; Wang, S.; Lou, X. W. Ordered Colloidal Clusters Constructed by Nanocrystals with Valence for Efficient CO₂ Photoreduction. *Sci. Adv.* **2019**, 5, eaax095.
- (6) Pawar, A. B.; Kretzschmar, I. Fabrication, assembly, and application of patchy particles. *Macromol. Rapid Commun.* **2010**, 31 (2), 150–168.
- (7) Rezvantalab, H.; Shojaei-Zadeh, S. Designing patchy particles for optimum interfacial activity. *Phys. Chem. Chem. Phys.* **2014**, 16 (18), 8283–8293.

- (8) Ravaine, S.; Duguet, E. Synthesis and assembly of patchy particles: Recent progress and future prospects. *Curr. Opin. Colloid Interface Sci.* **2017**, *30*, 45–53.
- (9) Ducrot, É.; He, M.; Yi, G.-R.; Pine, D. J. Colloidal alloys with preassembled clusters and spheres. *Nat. Mater.* **2017**, *16* (6), 652–657.
- (10) He, M.; Gales, J. P.; Ducrot, É.; Gong, Z.; Yi, G.-R.; Sacanna, S.; Pine, D. J. Colloidal diamond. *Nature* **2020**, *585* (7826), 524–529.
- (11) Longbottom, B. W.; Bon, S. A. F. Improving the engine power of a catalytic Janus-sphere micromotor by roughening its surface. *Sci. Rep.* **2018**, *8* (1), 4622.
- (12) Yoshida, M.; Lahann, J. Smart nanomaterials. *ACS Nano* **2008**, *2* (6), 1101–1107.
- (13) Méridol, R.; Duguet, E.; Ravaine, S. Synthesis of colloidal molecules: Recent advances and perspectives. *Chem. - Asian J.* **2019**, *14* (19), 3232–3239.
- (14) Li, W.; Palis, H.; Méridol, R.; Majimel, J.; Ravaine, S.; Duguet, E. Colloidal molecules and patchy particles: Complementary concepts, synthesis and self-assembly. *Chem. Soc. Rev.* **2020**, *49* (6), 1955–1976.
- (15) Themed Issue Metal-Organic Frameworks: *Chem. Soc. Rev.* Zhou, H. C., Kitagawa, S., Eds.; **2014**, *43*(5), 5415–6172.
- (16) Themed Issue Porous Framework Chemistry: *Chem. Rev. Long*, J.; Dinca, M., Eds; **2020**, *120*(16), 8037–9014.
- (17) Stock, N.; Biswas, S. Synthesis of metal-organic frameworks (MOFs): Routes to various MOF topologies, morphologies, and composites. *Chem. Rev.* **2012**, *112* (2), 933–969.
- (18) Seoane, B.; Castellanos, S.; Dikhtiarenko, A.; Kapteijn, F.; Gascon, J. Multi-scale crystal engineering of metal organic frameworks. *Coord. Chem. Rev.* **2016**, *307*, 147–187.
- (19) Liu, B.; Vellingiri, K.; Jo, S.-H.; Kumar, P.; Ok, Y. S.; Kim, K.-H. Recent advances in controlled modification of the size and morphology of metal-organic frameworks. *Nano Res.* **2018**, *11* (9), 4441–4467.
- (20) Sindoro, M.; Yanai, N.; Jee, A.-Y.; Granick, S. Colloidal-sized metal–organic frameworks: Synthesis and applications. *Acc. Chem. Res.* **2014**, *47* (2), 459–469.
- (21) Troyano, J.; Carné-Sánchez, A.; Avci, C.; Imaz, I.; Maspoch, D. Colloidal metal–organic framework particles: The pioneering case of ZIF-8. *Chem. Soc. Rev.* **2019**, *48* (23), 5534–5546.
- (22) Usman, K. A. S.; Maina, J. W.; Seyedin, S.; Conato, M. T.; Payawan, L. M., Jr.; Dumée, L. F.; Razal, J. M. Downsizing metal–organic frameworks by bottom-up and top-down methods. *NPG Asia Mater.* **2020**, *12* (1), 58.
- (23) Nai, J.; Guan, B. Y.; Yu, L.; Lou, X. W. Oriented assembly of anisotropic nanoparticles into frame-like superstructures. *Sci. Adv.* **2017**, *3*, e1700732.
- (24) Wang, S.; McGuirk, C. M.; d’Aquino, A.; Mason, J. A.; Mirkin, C. A. Metal–organic framework nanoparticles. *Adv. Mater.* **2018**, *30* (37), 1800202.
- (25) Cai, X.; Xie, Z.; Li, D.; Kassymova, M.; Zang, S.-Q.; Jiang, H.-L. Nano-sized metal-organic frameworks: Synthesis and applications. *Coord. Chem. Rev.* **2020**, *417*, 213366.
- (26) Katayama, Y.; Kalaj, M.; Barcus, K. S.; Cohen, S. M. Self-Assembly of Metal–Organic Framework (MOF) Nanoparticle Monolayers and Free-Standing Multilayers. *J. Am. Chem. Soc.* **2019**, *141*, 20000–20003.
- (27) Avci, C.; Imaz, I.; Carné-Sánchez, A.; Pariente, J. A.; Tasios, N.; Pérez-Carvajal, J.; Alonso, M. I.; Blanco, A.; Dijkstra, M.; López, C.; Maspoch, D. Self-assembly of polyhedral metal–organic framework particles into three-dimensional ordered superstructures. *Nat. Chem.* **2018**, *10*, 78.
- (28) Gong, Z.; Hueckel, T.; Yi, G.-R.; Sacanna, S. Patchy particles made by colloidal fusion. *Nature* **2017**, *550* (7675), 234–238.
- (29) Hueckel, T.; Sacanna, S. Mix-and-melt colloidal engineering. *ACS Nano* **2018**, *12* (4), 3533–3540.

Supporting Information

Assembly of Colloidal Clusters Driven by the Polyhedral Shape of Metal-Organic Framework Particles

Yang Liu,[†] Jiemin Wang,[†] Inhar Imaz,^{*†} and Daniel Maspoch^{*†,‡}

[†]Catalan Institute of Nanoscience and Nanotechnology (ICN2), CSIC, and Barcelona Institute of Science and Technology, Campus UAB, Bellaterra, 08193 Barcelona, Spain

[‡]ICREA, Pg. Lluís Companys 23, Barcelona, 08010, Spain

Table of Contents

Materials	S3
Synthesis of octahedral UiO-66 particles	S3
Synthesis of cubic ZIF-8 particles	S3
Synthesis of rhombic dodecahedral (RD) ZIF-8 particles	S3
Synthesis of 8-coordinated cubic clusters	S4
Synthesis of cellular-type particles and core-shell UiO-66@polystyrene particles	S4
Synthesis of 6-coordinated octahedral clusters	S4
Synthesis of 12-coordinated cuboctahedral clusters	S5
Characterization	S5
Figure S1 FESEM images and size-distribution histograms of octahedral UiO-66 particles	S6
Figure S2 PXRD pattern of as-synthesized octahedral UiO-66 particles	S7
Figure S3 FESEM images of 400 nm diameter of PS assembly with UiO-66 particles	S8
Figure S4 FESEM images of 1 μm diameter of PS assembly with UiO-66 particles	S9
Figure S5 FESEM images of the colloidal cubic clusters synthesized at the ratio of 40:1	S10
Figure S6 FESEM images of the colloidal cubic clusters synthesized at the ratio of 80:1	S11
Figure S7 FESEM images of the colloidal cubic clusters synthesized at the ratio of 150:1	S12
Figure S8 FESEM images of the colloidal cubic clusters synthesized at the ratio of 300:1	S13
Figure S9 DLS histogram of the size distribution	S14
Figure S10 FESEM images and size-distribution histograms of cubic ZIF-8 particles	S15
Figure S11 PXRD pattern of as-synthesized cubic ZIF-8 particles	S16
Figure S12 FESEM images and size-distribution histograms of RD ZIF-8 particles	S17
Figure S13 PXRD pattern of as-synthesized RD ZIF-8 particles	S18
Figure S14 FESEM images of the 12-c cuboctahedral clusters etched by gradient solution	S19
References	S20

Experimental Section

Materials. Zirconium (IV) chloride (ZrCl_4), hexadecyltrimethylammonium bromide (CTAB), terephthalic acid (1,4-BDC) and polyvinylpyrrolidone (PVP, $M_n=10,000$) were purchased from Sigma Aldrich. Glacial acetic acid, tetrahydrofuran (THF) and *N,N*-dimethylformamide (DMF) were purchased from Fisher Chemical. 2-methylimidazole (2-MiM), zinc acetate dihydrate ($\text{Zn}(\text{CH}_3\text{COO})_2 \cdot 2\text{H}_2\text{O}$), zinc nitrate hexahydrate ($\text{Zn}(\text{NO}_3)_2 \cdot 6\text{H}_2\text{O}$), sucrose and tetra-*n*-butylammonium bromide (TBAB) were purchased from TCI Chemical. Amino and sulfonated polystyrene (PS) particles were purchased from Thermo Fisher and Polysciences Europe. All chemical reagents and solvents were used as received without further purification. De-ionized (DI) water was obtained from a Milli-Q water purification system.

Synthesis of octahedral UiO-66 particles. ZrCl_4 (56 mg) and 1,4-BDC (40 mg) were dissolved in 20 mL of DMF containing 4 mL acetic acid and transferred to a scintillation vial. This mixture was heated at 120 °C for 12 h. Afterwards, the synthesized particles were washed twice with DMF (10 mL) and twice with methanol (10 mL) upon centrifugation at 9000 rpm in 50-mL Falcon tubes. Once washed, the collected particles were redispersed in 10 mL of an aqueous solution of PVP (2 mg mL^{-1}), stirred for 30 min, and washed once with 10 mL of DI water upon centrifugation at 9000 rpm in 50-mL Falcon tubes. The collected particles were finally redispersed in 5 mL of an aqueous solution of PVP (2 mg mL^{-1}) at a final concentration of UiO-66 particles of 10 mg mL^{-1} . The zeta potential of the resulting octahedral UiO-66 particles was approximately +45 mV. Note here that PVP was added to improve the colloidal stability of UiO-66 particles in water.

Synthesis of cubic ZIF-8 particles. In a typical synthesis, $\text{Zn}(\text{NO}_3)_2 \cdot 6\text{H}_2\text{O}$ (140 mg) dissolved in 8 mL of water was added to 24 mL of an aqueous solution containing 2-MiM (1920 mg) and 4 mL of 0.85 mg mL^{-1} CTAB solution. After standing for 5 hours, the resulting ZIF-8 particles were washed with deionized water (10 mL) upon centrifugation at 9000 rpm in 50-mL Falcon tubes, and finally dispersed in 10 mL of an aqueous solution of TBAB (1 mg/mL) at a final concentration of ZIF-8 particles of 10 mg mL^{-1} . The zeta potential of the resulting cubic ZIF-8 particles was approximately +40 mV. Note here that TBAB was added to improve the colloidal stability of ZIF-8 particles in water.

Synthesis of rhombic dodecahedral (RD) ZIF-8 particles. RD ZIF-8 particles were produced by following the protocol reported in a previous work.¹ An aqueous solution (5 mL) of $\text{Zn}(\text{CH}_3\text{COO})_2 \cdot 2\text{H}_2\text{O}$ (300 mg) was added to 5 mL of an aqueous solution of 2-MiM (1.12 g) with gentle stirring. Then, the mixture was left at room temperature for 24 h. The resulting ZIF-8 particles were washed with deionized water (10 mL) upon centrifugation at 9000 rpm in 50-mL Falcon tubes, and finally dispersed in 10 mL of an aqueous solution of TBAB (1 mg/mL) at a final concentration of ZIF-8 particles of 20 mg mL^{-1} . The zeta potential of the resulting RD ZIF-8 particles was approximately + 40 mV. Note here that TBAB was added to improve the colloidal stability of ZIF-8 particles in water.

Synthesis of 8-coordinated cubic clusters using octahedral UiO-66 particles. In general, colloidal clusters were assembled by i) rapid addition of negatively charged polystyrene spheres suspension to an equal volume of suspension with monodispersed positively charged MOF particles; immediately addition of a water-soluble plasticizer (THF) to the resulting suspension; and iii) mixing and shaking the suspension by hand within 10 seconds. Specifically, for the 8-coordinated cubic clusters, they were assembled by adding 100 μL of the PS colloid (700 nm, 150 mg mL^{-1}) into 100 μL of the octahedral UiO-66 suspension (1 mg mL^{-1}). Then, 400 μL of THF/ H_2O (18 % v/v) were rapidly added to the mixture, followed by hand shaking for 10 seconds. After that, the as-obtained sediments of the mixture suspensions were collected by further purification via density gradient centrifugation (10-30 wt% sucrose in water) and washed with deionized water for several times. The resulting colloidal clusters were finally re-dispersed in DI water.

Note here that the density gradient centrifugation is a common technique used to separate particles that have different density or size of components. In it, the mixture is placed into a centrifuge, in which the spinning from the centrifuge causes more dense particles to move to the outside edge, creating a sorted solution that is layered by particle density from least to most. In this technique, density gradient reagents (usually glycerol, sucrose and caesium chloride) are used to speed up the process and increase the purity and throughput. In our experiments, we found that a density gradient of 10-40 wt% sucrose in water was optimum to purify the mixture.

Synthesis of cellular-type particles and core-shell UiO-66@polystyrene particles using octahedral UiO-66 particles. The syntheses were identical to the formation of the above-mentioned 8-coordinated cubic clusters, except that these two types of particles were obtained by adding higher concentration of THF plasticizer: 400 μL of THF/ H_2O (26% v/v)

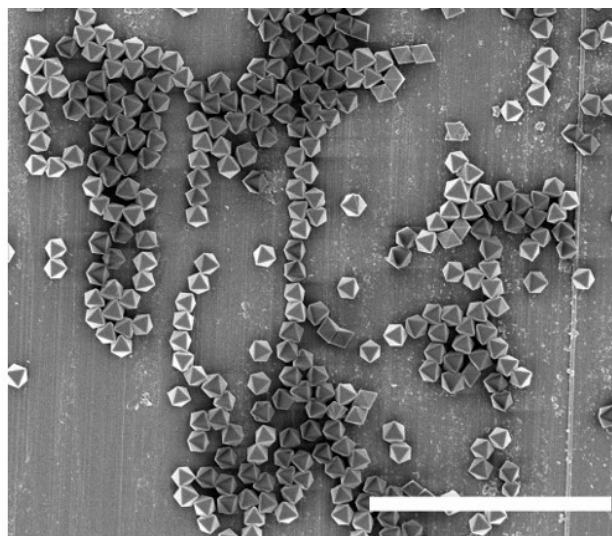
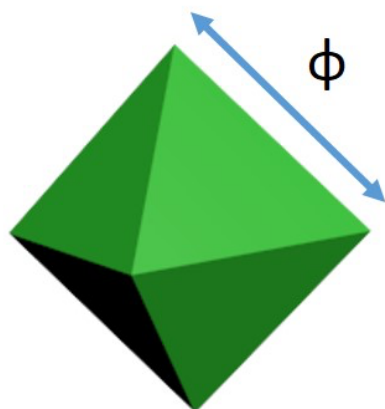
for the synthesis of the cellular-type particles; and 400 μL of THF/ H_2O solution (30% v/v) for the core-shell UiO-66@polystyrene particles.

Synthesis of 6-coordinated octahedral clusters using cubic ZIF-8. These colloidal clusters were assembled by adding 100 μL of the PS spheres colloid (200 nm, 10 mg mL^{-1}) into 100 μL of the cubic ZIF-8 particles colloid (3 mg mL^{-1}). Then, 350 μL of THF/ H_2O (14 % v/v) were rapidly added to the mixture, followed by hand shaking for 10 seconds. After standing for 10 minutes without disturbing, the upper supernatant of the mixture suspension was removed carefully while the sediments were collected. The collected solid was redispersed in DI water (2 mL) and this sedimentation-redispersion process was repeated three more times. Finally, the collected colloidal clusters were redispersed in DI water.

Synthesis of 12-coordinated cuboctahedral clusters using RD ZIF-8 particles. These colloidal clusters were assembled by adding 100 μL of the PS colloid (600 nm, 20 mg mL^{-1}) in 100 μL of the RD ZIF-8 particles colloid (3 mg mL^{-1}). Then, 400 μL of THF/ H_2O (17 % v/v) were rapidly added to the mixture, followed by hand shaking for 10 seconds. After standing for 10 minutes without disturbing, the upper supernatant of the mixture suspension was removed carefully while the sediments were collected. The collected solid was redispersed in DI water (2 mL) and this sedimentation-redispersion process was repeated three more times. Finally, the collected colloidal clusters were redispersed in DI water.

Characterization. Field-emission scanning electron microscopy (FE-SEM) images were collected on a scanning electron microscope (FEI Magellan 400L XHR) at acceleration voltage of 2.0 kV, using aluminum-tape or silicon wafer as support. Bright or dark field scanning transmission electron microscopy (STEM) images were obtained with scanning electron microscope (FEI Magellan 400L XHR) at acceleration voltage of 20.0 kV. The average size distributions of synthesized particles/clusters were statistically estimated from FE-SEM images by counting the edge/diagonal of 200 particles/clusters at different areas from one sample. The diameter of UiO-66 particles was calculated from the previously measured edge size. PXRD measurements were carried out on an X'Pert PRO MPDP analytical diffractometer, $\lambda_{\text{Cu}} = 1.5406 \text{ \AA}$ (PANalytical). The surface charge of MOF particles (expressed as zeta potential (ζ)) was measured by using a Malvern Zetasizer, (Malvern Instruments, UK).

a)



b)

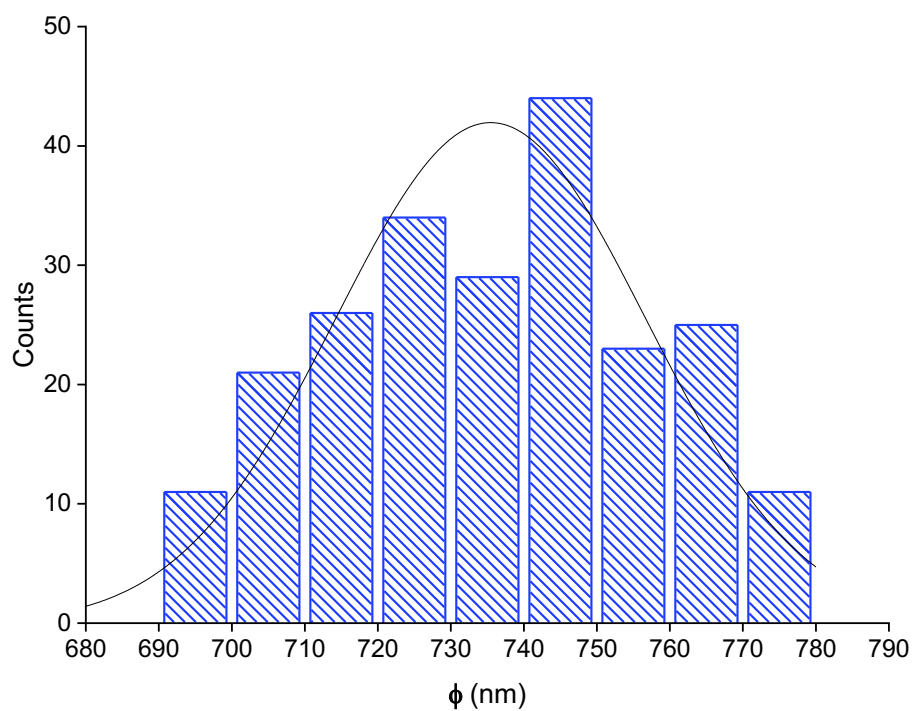


Figure S1. (a) Scheme and FESEM image of as-synthesized octahedron UiO-66 particles, highlighting the edge length of particles (ϕ). Scale bar: 10 μm . (b) Size-distribution histogram of as-synthesized UiO-66 particles with a mean ϕ of 735 ± 21 nm.

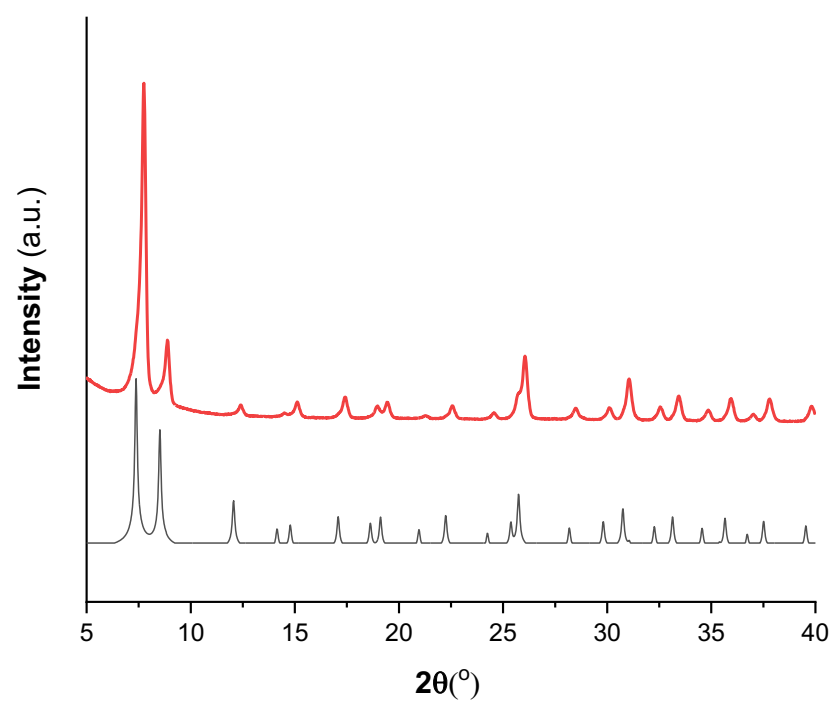
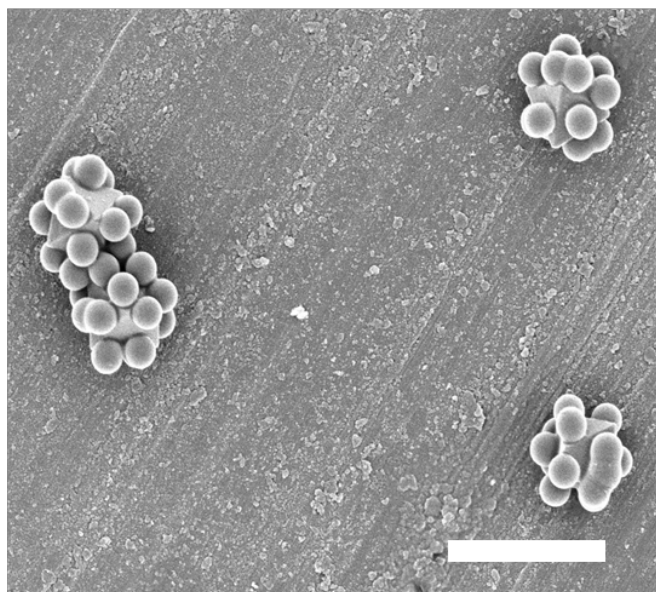


Figure S2. XRPD pattern of simulated (black) and as-synthesized UiO-66 particles (red).

a)



b)

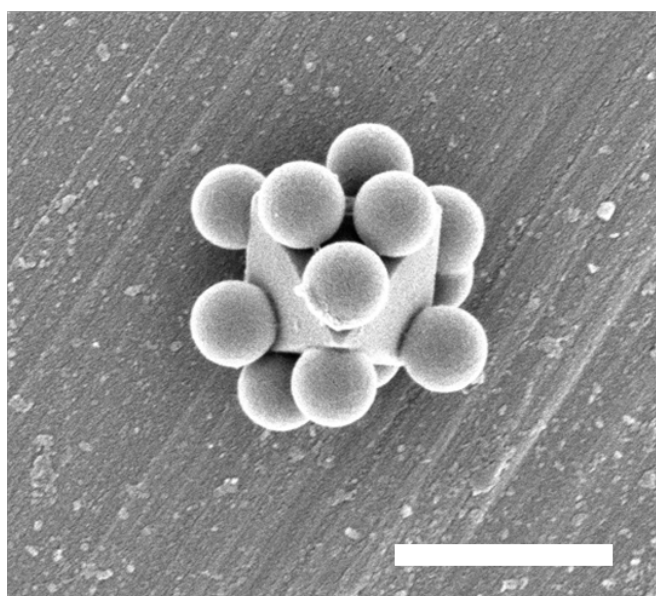
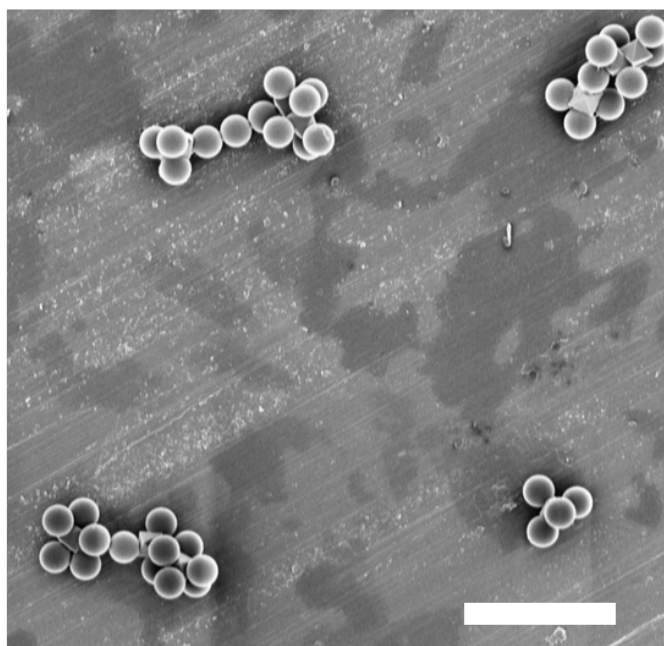


Figure S3. Representative FESEM images corresponding to the experiment in which 8-c cubic clusters were assembled by combining octahedron UiO-66 particles with 400 nm-in-diameter of polystyrene spheres. Scale bars: (a) 5 μm and (b) 1 μm .

a)



b)

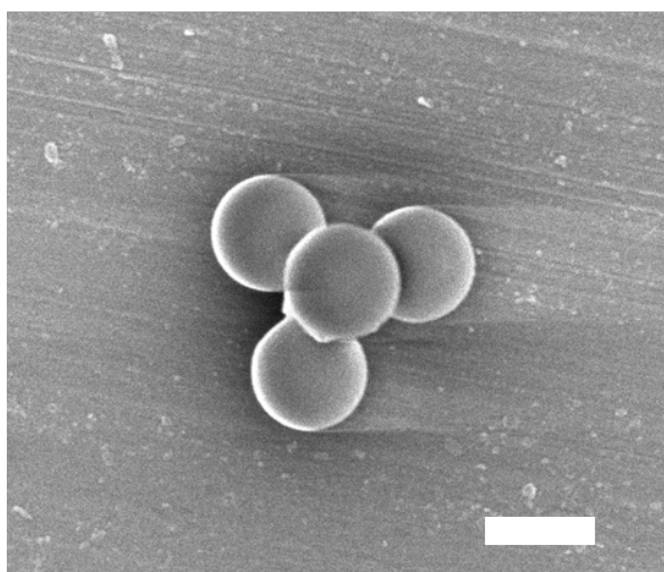


Figure S4. Representative FESEM images corresponding to the experiment in which 8-cubic clusters were assembled by combining octahedron UiO-66 particles with 1 μm -in-diameter of polystyrene spheres. Scale bars: (a) 5 μm and (b) 1 μm .

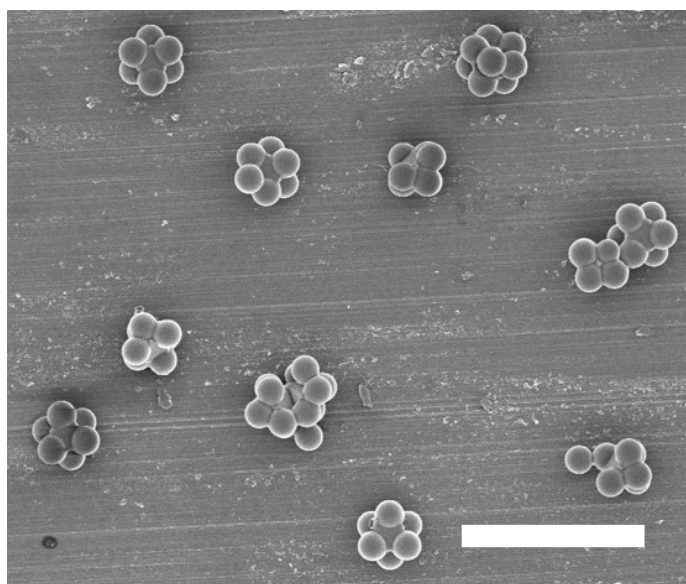


Figure S5. Representative FESEM image of the colloidal cubic clusters synthesized at the ratio of 40:1. Scale bar: 10 μm .

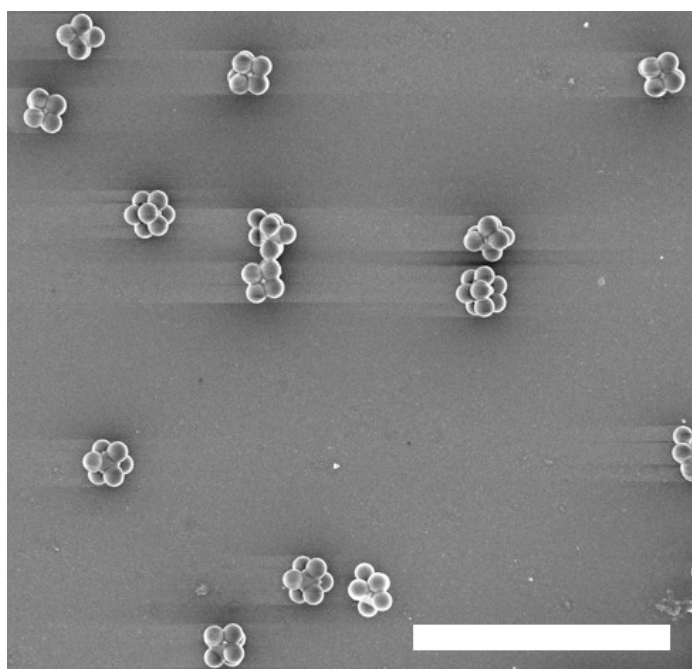


Figure S6. Representative FESEM image of the colloidal cubic clusters synthesized at the ratio of 80:1. Scale bar: 10 μm .

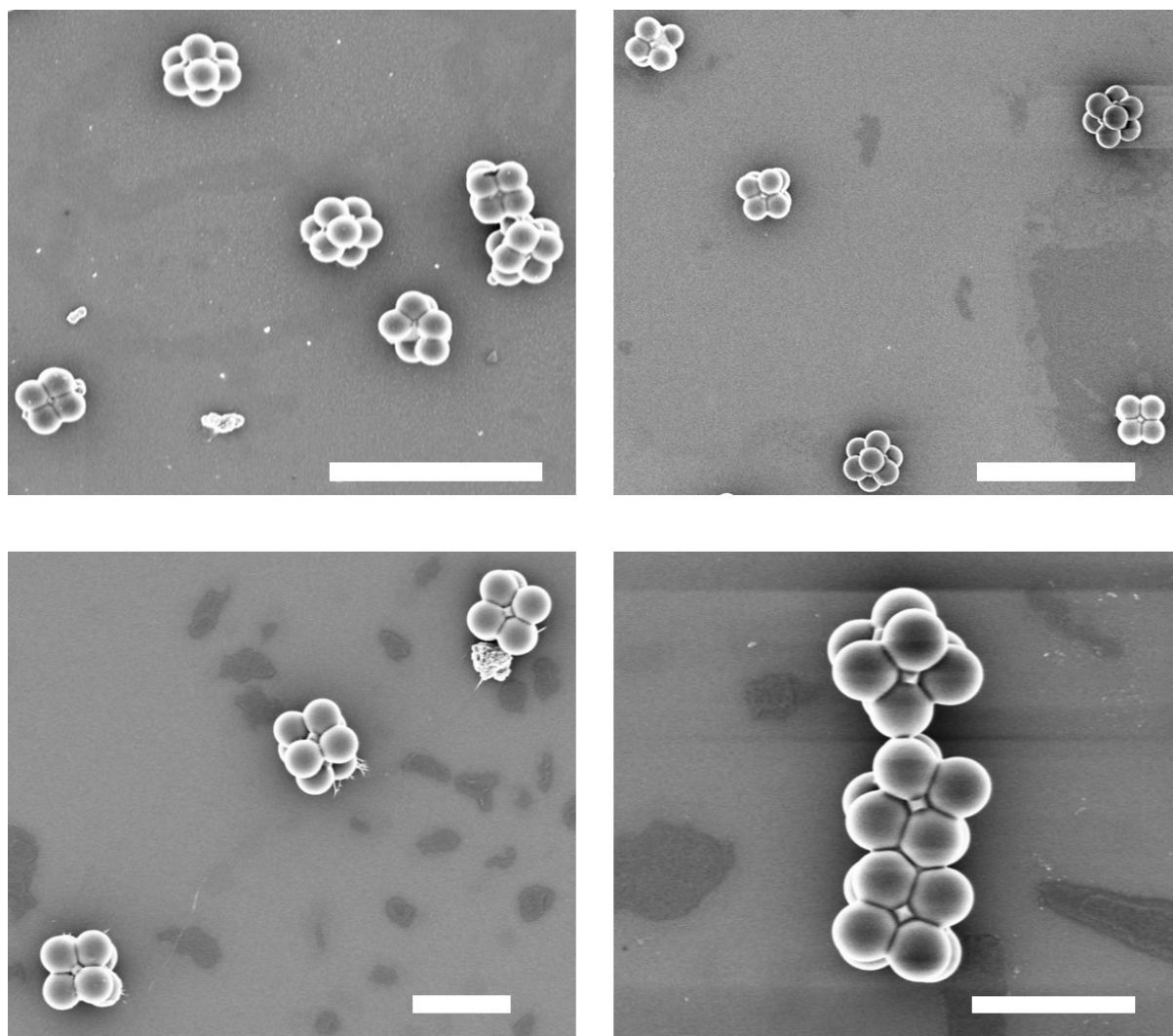


Figure S7. Representative FESEM images of the colloidal cubic clusters synthesized at the ratio of 150:1. Scale bars: (top row) 5 μm and (bottom row) 2 μm .

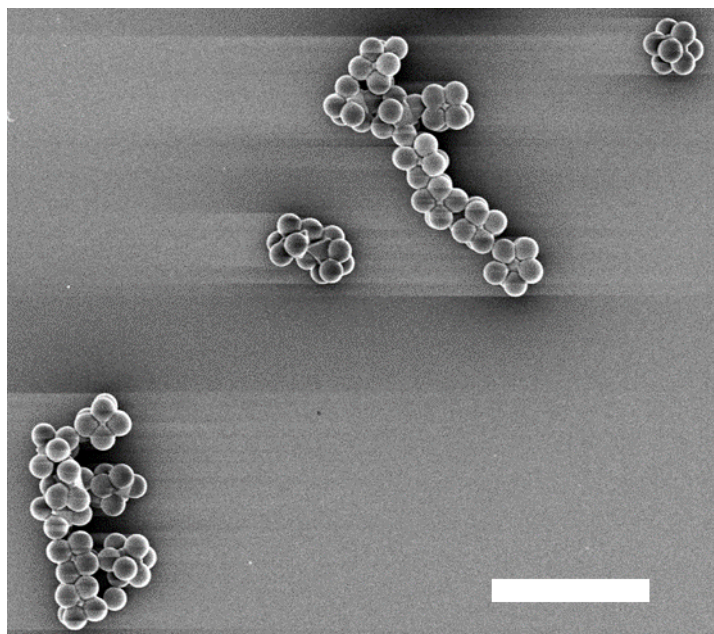


Figure S8. Representative FESEM image of the colloidal cubic clusters synthesized at the ratio of 300:1. Scale bar: 5 μm .

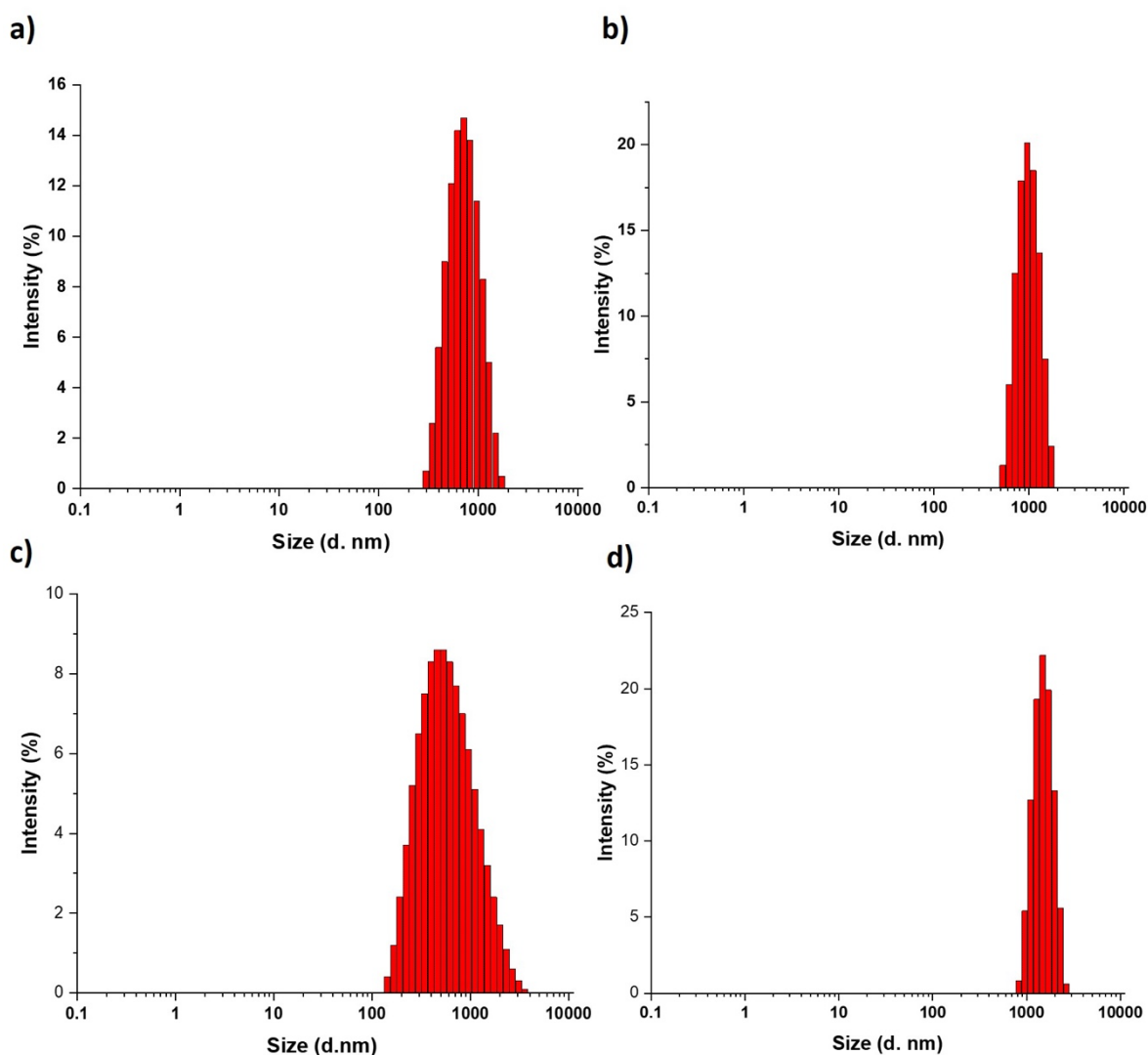
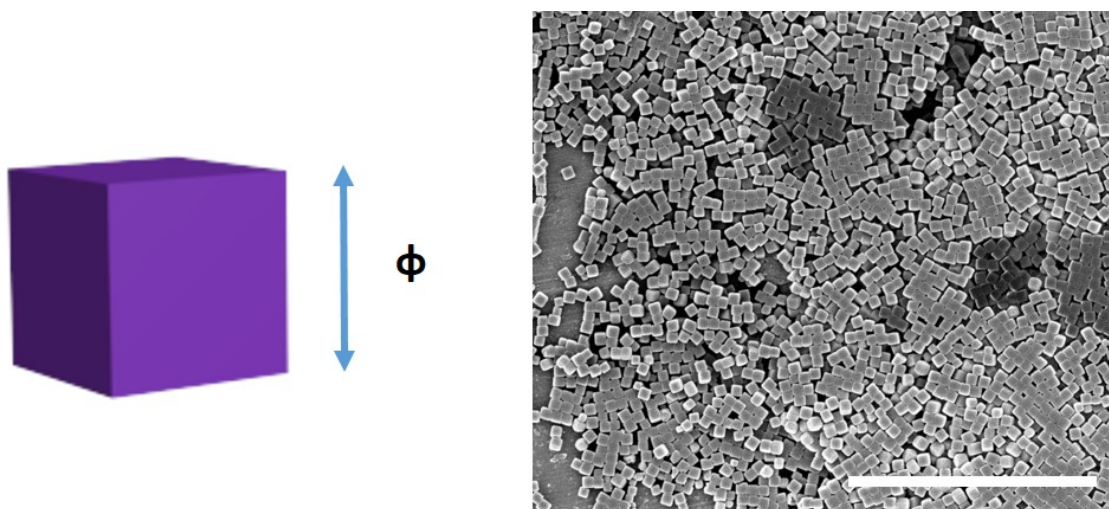


Figure S9. DLS histogram of the size distribution of a) polystyrene spheres (mean average size: 782 ± 31 (PDI: 0.163); b) UiO-66 particles (mean average size: 1022 ± 20 (PDI: 0.098); c) the mixture of polystyrene spheres and UiO-66 particles (mean average size: 717 ± 30 (PDI: 0.328); and d) purified colloidal cubic clusters (mean average size: 1453 ± 73 nm (PDI: 0.385). Note that the later mean size measured by DLS matches with the size of the cubic clusters measured by FESEM.

a)



b)

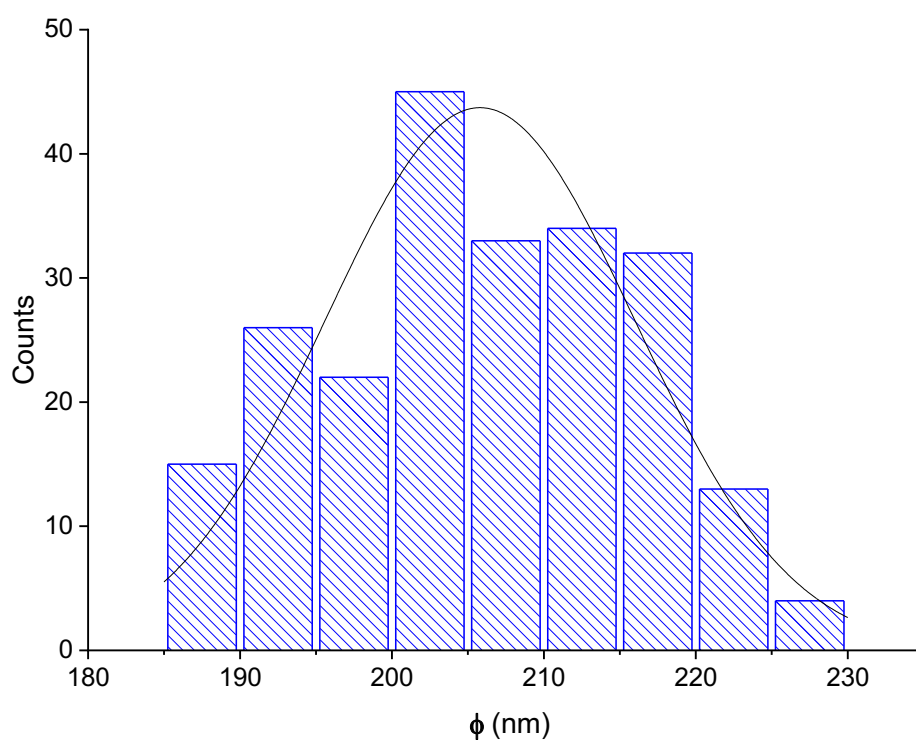


Figure S10. (a) Scheme and FESEM image of as-synthesized cubic ZIF-8 particles, highlighting the edge length of particles (ϕ). Scale bar: 5 μm . (b) Size-distribution histogram of as-synthesized cubic ZIF-8 particles with a mean ϕ of 205 ± 10 nm.

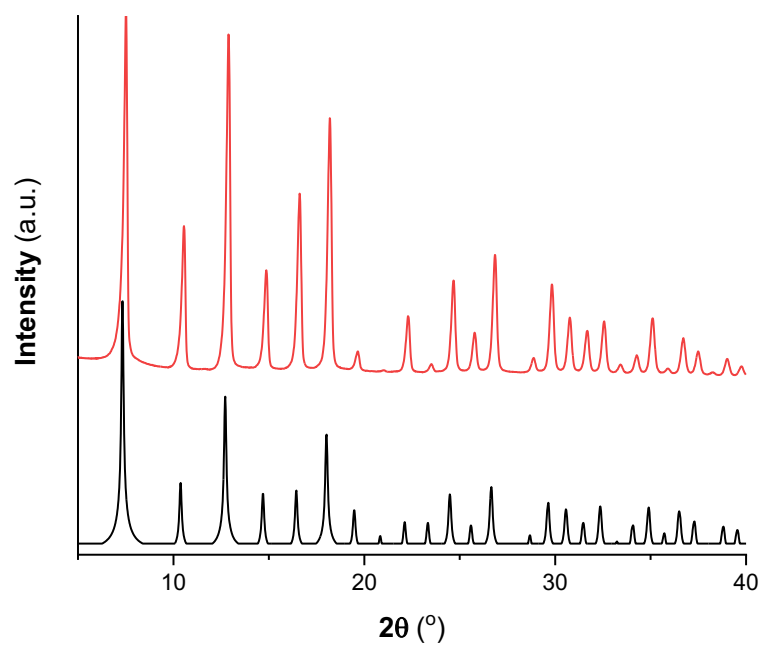
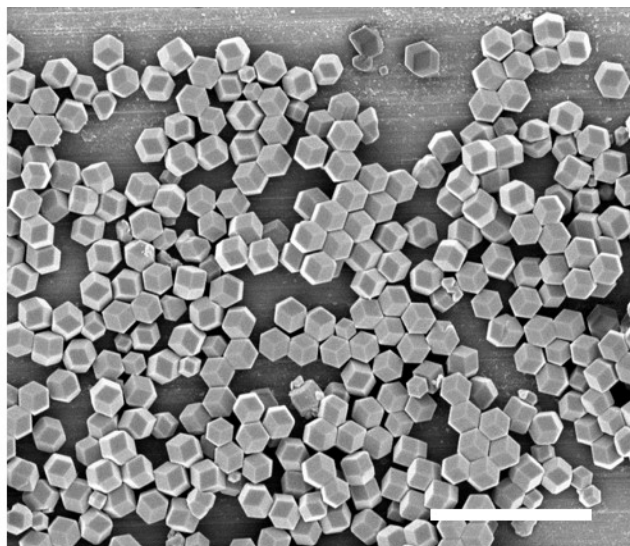
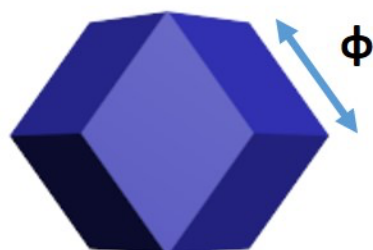


Figure S11. XRPD pattern of simulated (black) and as-synthesized cubic ZIF-8 particles (red).

a)



b)

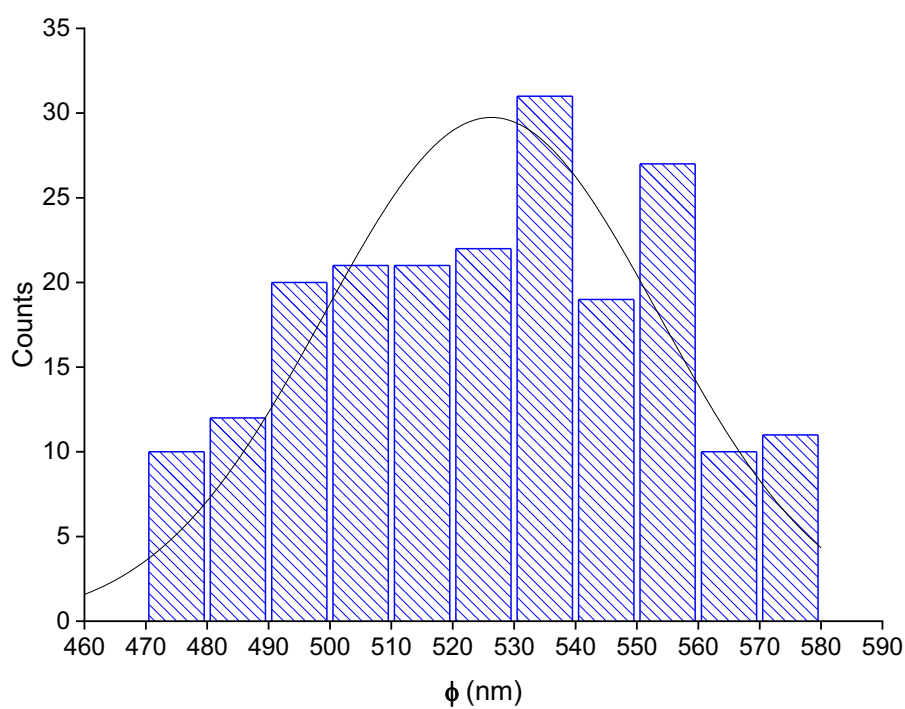


Figure S12. (a) Scheme and FESEM image of as-synthesized RD ZIF-8 particles, highlighting the edge length of particles (ϕ). Scale bar: 5 μm . (b) Size-distribution histogram of as-synthesized RD ZIF-8 particles with a mean ϕ of 526 ± 27 nm.

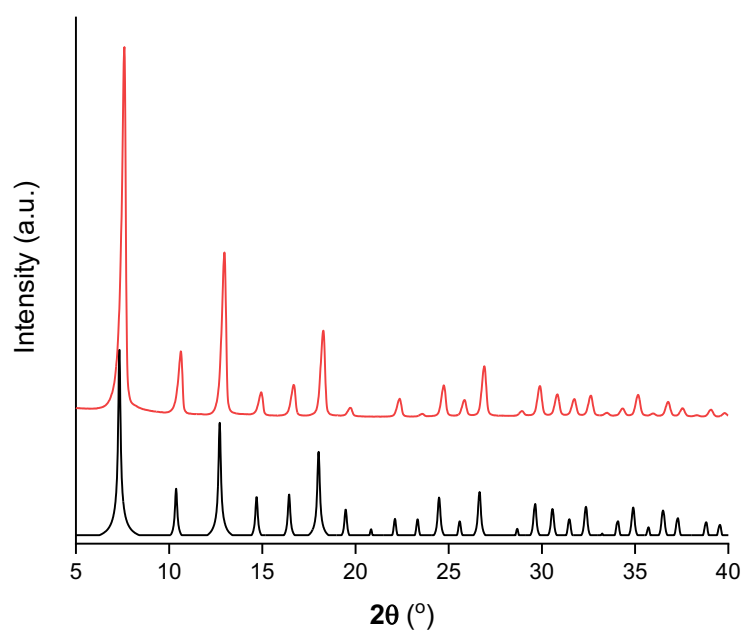
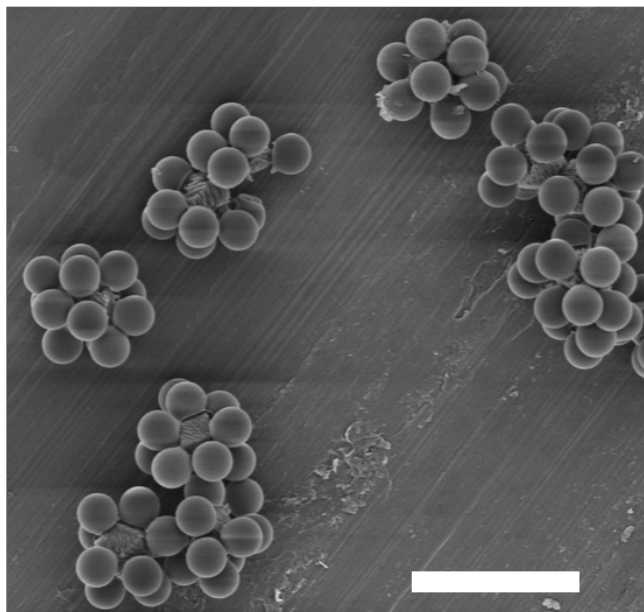


Figure S13. XRPD pattern of simulated (black) and as-synthesized RD ZIF-8 particles (red).

a)



b)

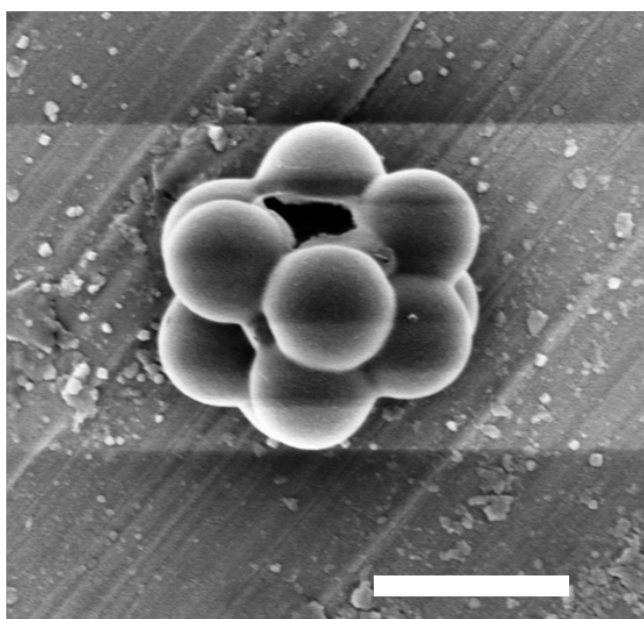


Figure S14. Representative FESEM images of 12-c cuboctahedron clusters, in which the central ZIF-8 particles have been etched by the gradient solution. Scale bars: (a) 5 μm and (b) 1 μm .

References

1. Avci, C.; Ariñez-Soriano, J.; Carné-Sánchez, A.; Guillerm, V.; Carbonell, C.; Imaz, I.; MasPOCH, D. Post-Synthetic Anisotropic Wet-Chemical Etching of Colloidal Sodalite ZIF Crystals. *Angew. Chem., Int. Ed.* **2015**, 54(48), 14417-14421.

Chapter 6

Template-Free, Surfactant-Mediated Orientation of Self-Assembled Supercrystals of Metal-Organic Framework Particles

Template-Free, Surfactant-Mediated Orientation of Self-Assembled Supercrystals of Metal–Organic Framework Particles

Civan Avci, Yang Liu, Jose Angel Pariente, Alvaro Blanco, Cefe Lopez,* Inhar Imaz,* and Daniel Maspoch*

Mesoscale self-assembly of particles into supercrystals is important for the design of functional materials such as photonic and plasmonic crystals. However, while much progress has been made in self-assembling supercrystals adopting diverse lattices and using different types of particles, controlling their growth orientation on surfaces has received limited success. Most of the latter orientation control has been achieved via templating methods in which lithographic processes are used to form a patterned surface that acts as a template for particle assembly. Herein, a template-free method to self-assemble (111)-, (100)-, and (110)-oriented face-centered cubic supercrystals of the metal–organic framework ZIF-8 particles by adjusting the amount of surfactant (cetyltrimethylammonium bromide) used is described. It is shown that these supercrystals behave as photonic crystals whose properties depend on their growth orientation. This control on the orientation of the supercrystals dictates the orientation of the composing porous particles that might ultimately facilitate pore orientation on surfaces for designing membranes and sensors.

The physical and even chemical properties of crystals often differ with crystal orientation,^[1] due to the distinct atomic interactions and bond distances along the crystal directions, which can strongly affect the electronic, mechanical, and/or magnetic characteristics. Accordingly, the integration of crystals into devices requires control of their surface orientation.^[2]

Dr. C. Avci, Y. Liu, Dr. I. Imaz, Prof. D. Maspoch
Catalan Institute of Nanoscience and Nanotechnology (ICN2)
Consejo Superior de Investigaciones Científicas (CSIC)
and the Barcelona Institute of Science and Technology
Campus UAB, Bellaterra, 08193 Barcelona, Spain
E-mail: inhar.imaz@icn2.cat; daniel.maspoch@icn.cat

J. A. Pariente, Dr. A. Blanco, Prof. C. Lopez
Materials Science Factory
Instituto de Ciencia de Materiales de Madrid (ICMM)
Consejo Superior de Investigaciones Científicas (CSIC)
Calle Sor Juana Inés de la Cruz, 3, 28049 Madrid, Spain
E-mail: c.lopez@csic.es

Prof. D. Maspoch
ICREA

Pg. Lluís Companys 23, 08010 Barcelona, Spain

The ORCID identification number(s) for the author(s) of this article can be found under <https://doi.org/10.1002/smll.201902520>.

DOI: 10.1002/smll.201902520

For instance, the importance of controlled growth of oriented crystalline (111)-silicon and (0001)-ZnO nanowires,^[3,6] (001)-YBCO superconductors,^[4] and phosphorene semiconductors^[5] on surfaces in electronic, photovoltaic, and photonic devices has been described. To date, crystal orientation is controlled chiefly via direct growth methods, including vapor/liquid/solid,^[7] oxide-assisted,^[8] and template-based growth methods.^[9]

Controlled orientation of crystals on surfaces can also improve the performance of porous materials integrated into devices or membranes. For example, Tsapatsis and coworkers demonstrated that zeolite ZSM-5 membranes in the (010) orientation perform better at separation of xylene isomers than those in other orientations do. They attributed this advantage to the larger, straighter pores accessible along the *b*-axis throughout the membrane thickness, compared to the narrower, sinusoidal pores along the *a*-axis.^[10] Likewise, MFI-type zeolite membranes in the (010) orientation showed better separation performance and mass transfer than those in other orientations did.^[11] Similar trends are expected for metal–organic frameworks (MOFs), an emerging class of porous materials that can be synthesized in various shapes and pore sizes and that show extremely large surface areas and tailored internal surfaces.^[12,13] Preliminary advances in controlling the orientation of MOF crystal growth on surfaces have been reported by Biemmi et al.,^[14] for HKUST-1, and by Zacher et al.,^[15] for MOF-5, using in situ growth crystallization methods on substrates functionalized with self-assembled monolayers, and by Shekhah and Eddaoudi,^[16] for ZIF-8, using layer-by-layer liquid-phase epitaxy growth on substrates functionalized with self-assembled monolayers. Moreover, Falcaro et al. recently demonstrated the heteroepitaxial growth of centimeter-scale-oriented MOF films using crystalline copper hydroxide-covered silicon as a template substrate.^[17] Remarkably, when a fluorescent dye was adsorbed in the MOF crystals, these pore-oriented MOF films exhibited optical response as “ON/OFF” switching upon film rotation.

The earliest methods to control the orientation of MOF crystals rely on their coherent growth to form a continuous film of a given orientation.^[14–17] We recently reported that

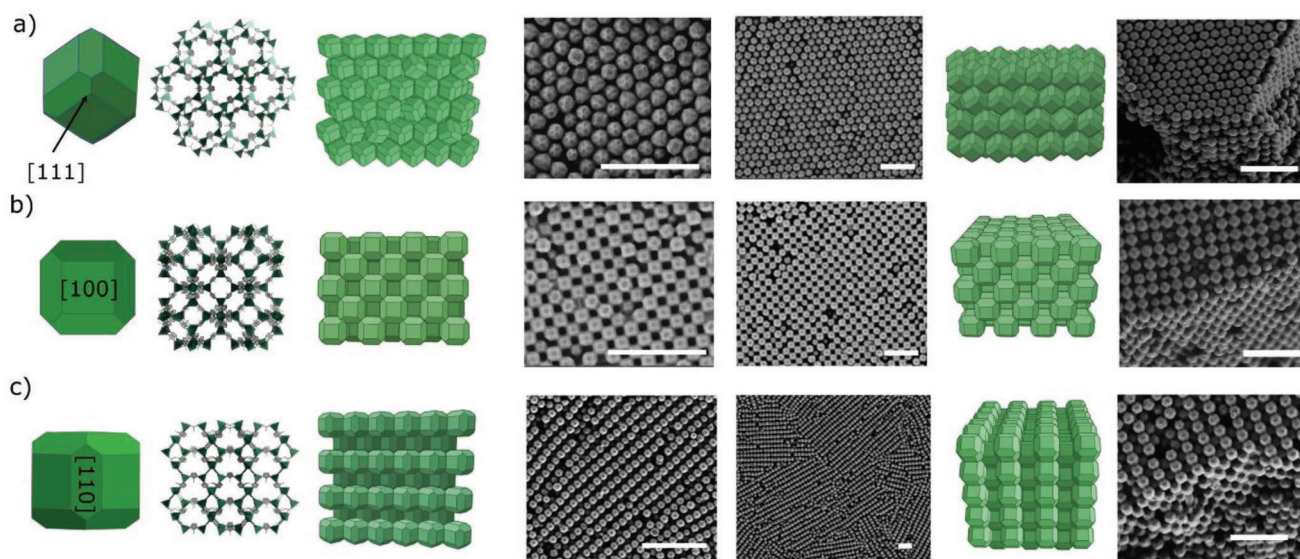


Figure 1. Formation of a) (111)-, b) (100)-, and c) (110)-oriented fcc supercrystals of TRD ZIF-8 particles. Each section contains (from left to right) a schematic view of a single TRD ZIF-8 particle oriented along the corresponding plane; a view of the oriented crystal structure of ZIF-8; a schematic view of the packing of the supercrystals, and corresponding FESEM images; and a schematic view of the 3D packing of the supercrystals, and corresponding FESEM image. Scale bars are 2 μm (fourth column) and 1 μm (fifth and seventh columns).

colloidal crystals of ZIF-8 can self-assemble into centimeter-scale supercrystals on surfaces to create a structured film of singular building blocks with internal and interparticle available porosity.^[18] The term supercrystal is often used to refer to 3D well-ordered assemblies formed by colloidal crystalline particles^[19,20] that, in the case of ZIF-8, are truncated rhombic dodecahedral (TRD) crystals of controllable truncation. In these supercrystals, whose particles are single-crystalline and faceted, every constituent ZIF-8 crystal has the same orientation. This observation prompted us to hypothesize that supercrystal formation could serve as an alternative to the aforementioned direct growth methods for controlling the orientation of porous crystals on surfaces.

Herein, we develop this approach by controlling the growth orientation of a face-centered cubic (fcc) supercrystal assembled from TRD ZIF-8 crystals (truncation $t = 0.63$). Previous studies on the formation of fcc supercrystals with an orientation different from the most common one ((111)-oriented) are limited. In these few studies, fcc supercrystals (typically, (100)-oriented) were assembled via templating methods in which lithographic processes are exploited to form a patterned substrate that acts as a template for particle assembly.^[21–23] In our new method described here, we report that orientation of fcc supercrystals can be controlled with the surfactant cetyltrimethylammonium bromide (CTAB); same used for the synthesis of TRD ZIF-8 crystals. This template-free approach enabled us to generate (111)-, (100)-, and (110)-oriented ZIF-8 supercrystals (**Figure 1**), in which all the constituent ZIF-8 crystals are oriented along the $\langle 111 \rangle$, $\langle 100 \rangle$, and $\langle 110 \rangle$ crystallite directions, respectively. This property implies that in the (111)-oriented supercrystals, the ZIF-8 particles with the largest pore apertures are aligned perfectly perpendicular to the surface.

We first chose to study TRD ZIF-8 particles in which the truncation value (t) = $2x/(\phi + x)$ = 0.63 (where ϕ is the distance between opposing square facets, and x is the side of the

square facets), as these particles self-assemble into fcc supercrystals.^[18] The particles were synthesized by adding a solution of $\text{ZnAc}_2 \cdot 2\text{H}_2\text{O}$ (300 mg) in 5 mL of water to a solution of 1.56 g of 2-methylimidazole (2-MiM) and 0.40 mg of CTAB in 5 mL of water. The resulting transparent mixture was gently stirred for 15 s, causing it to evolve into a white colloidal suspension, which was left undisturbed at room temperature for 2 h. The resulting ZIF-8 particles were washed three times with deionized (DI) water upon centrifugation at 9000 rpm in 50 mL Falcon tubes. Field-emission scanning electron microscopy (FESEM) images revealed the formation of TRD particles of the following dimensions for $t = 0.63$: size (ϕ) = 233 ± 14 nm and edge length of square facets (x) = 106 ± 8 nm (Figure S1, Supporting Information). The size polydispersity of ZIF-8 particles was $\approx 6\%$ (Figure S1, Supporting Information). A powder X-ray diffraction (PXRD) pattern of the as-synthesized particles confirmed the formation of pure ZIF-8 (Figure S2, Supporting Information). A N_2 sorption isotherm taken at 77 K confirmed the porosity and indicated a Brunauer–Emmett–Teller surface area of $1215 \text{ m}^2 \text{ g}^{-1}$ (Figure S3, Supporting Information).

We next performed an initial self-assembly experiment, in which we redispersed the synthesized particles in water (50 mg mL^{-1}). A droplet of $40 \mu\text{L}$ of this dispersion was placed on a polydimethylsiloxane (PDMS)-coated SEM pin, which was then heated in an oven at 120°C for 3 min until the droplet fully evaporated. Note here that the substrate was covered with PDMS to provide better homogeneity and robustness to the supercrystals, facilitating their handling, as they become slightly attached to the PDMS surface. Upon evaporation, a round-shaped, colorful ZIF-8 monolith was obtained with a diameter of ≈ 6 mm. The monoliths obtained this way exhibited structural green color visible to the naked eye, signaling the formation of an ordered assembly. FESEM images revealed the formation of the (entropically favored) (111)-oriented fcc plastic supercrystal, in which all TRD ZIF-8 particles are oriented

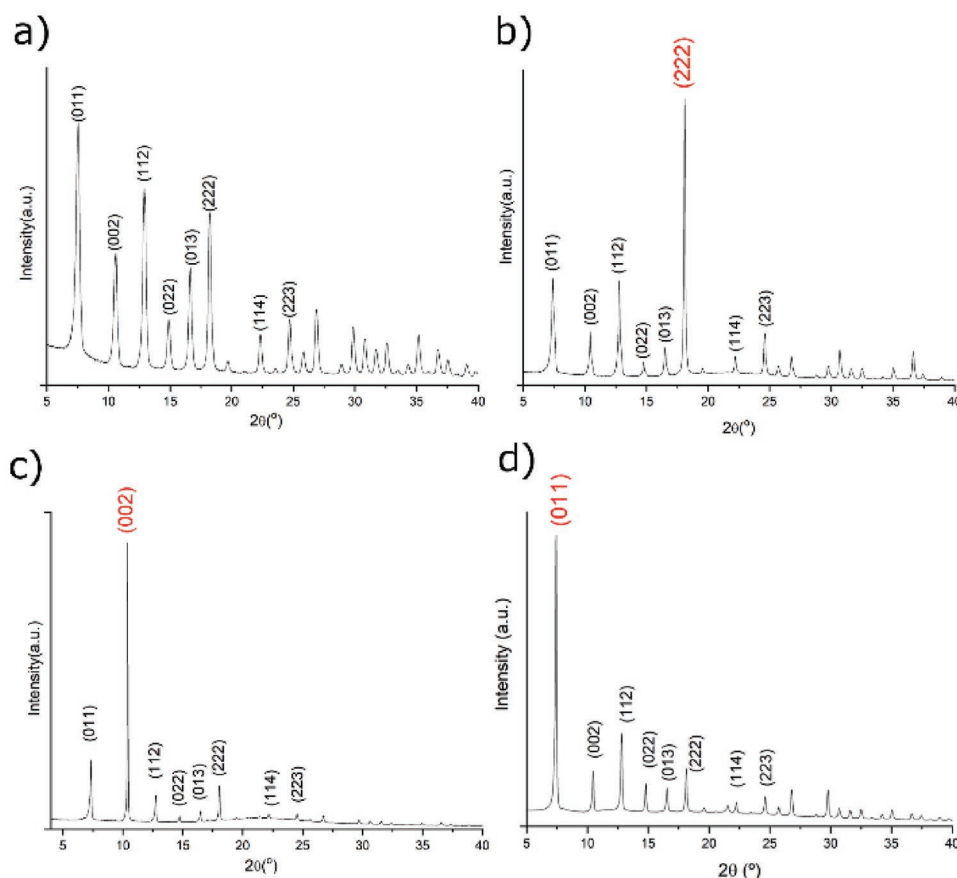


Figure 2. PXRD for a) the disordered ZIF-8 monolith and b) the (111)-, c) (100)-, and d) (110)-oriented supercrystals.

with their $\langle 111 \rangle$ direction perpendicular to the surface of the monolith and thus parallel to its $\langle 111 \rangle$ direction (Figure 1a). PXRD analysis of a (111)-oriented fcc supercrystal assembled on a silicon sample holder of the PXRD instrument showed the typical ZIF-8 pattern, with its highest intensity peak at $2\theta = 16^\circ$ (Figure 2). This peak corresponds to diffraction from the (222) plane of ZIF-8 (i.e., parallel to the $\langle 111 \rangle$ planes of the supercrystal), and thus confirmed the orientation of the ZIF-8 particles along the $\langle 111 \rangle$ direction. Hence, in this (111)-oriented supercrystal, the larger pore apertures (3.4 \AA) connecting the 11.6 \AA in. diameter cavities of ZIF-8 running along the $\langle 111 \rangle$ direction are vertically aligned.

We next studied the possible influence of the surfactant CTAB on the self-assembly of TRD ZIF-8 particles. Specifically, we sought conditions that would provide alternate growth directions. Thus, we systematically prepared a series of dispersions of ZIF-8 particles at a concentration of 50 mg mL^{-1} , in which we stepwise increased the concentration of CTAB from 1.00 to 4.00 mg mL^{-1} , and then studied the resulting supercrystal growth. At 1.00 mg mL^{-1} , results similar to those of the supercrystals self-assembled without addition of CTAB were obtained: the entire sample was (111)-oriented (Figure S4, Supporting Information). When the CTAB concentration was increased to 2.00 mg mL^{-1} , the formation of (100)-oriented domains on the perimeter of the monolith, and (111)-oriented domains in the center, was observed

(Figure S5, Supporting Information). Upon increasing the CTAB concentration further, these (100)-oriented domains grew and became more abundant, gradually propagating toward the center. By a CTAB concentration of 3.00 mg mL^{-1} , a homogeneous (100)-oriented fcc supercrystal had been assembled (Figure 1b). Remarkably, the PXRD pattern of the (100)-oriented supercrystals showed its highest intensity peak at $2\theta = 11^\circ$, corresponding to the diffraction from (002) planes of ZIF-8 (Figure 2c). This observation confirmed that the ZIF-8 particles forming this supercrystal were oriented along the $\langle 100 \rangle$ direction. Again, the crystallite orientation was parallel to that of the supercrystal.

When increasing the CTAB concentration up to 3.25 mg mL^{-1} , we began observing the formation of (110)-oriented domains. As previously, these new (110)-oriented domains started occurring on the perimeter of the monolith (Figure S7, Supporting Information) and propagated toward the center for increasing CTAB concentration. Although a purely (110)-oriented supercrystal could not be obtained filling the entirety of the monolith, even at a CTAB concentration of 4.00 mg mL^{-1} , the FESEM images of supercrystals obtained at this CTAB concentration revealed formation of a large, homogeneous, (110)-oriented area (Figure 1c), together with some (100)-oriented domains near the center of the monolith (Figure S8, Supporting Information). For the (110)-oriented crystals, PXRD showed a strong (twofold) reinforcement of the

preferential Bragg diffraction (Figure 2d), as in the (111) and (100) orientations.

Snapshots of the self-assembly process of ZIF-8 supercrystals revealed that the droplet surface had become opalescent after only 20 s of incubation (Figure S9, Supporting Information). This opalescence in turn suggested that the supercrystal formation begins at the droplet interface, meaning that the self-assembly of ZIF-8 particles evolves from the droplet surface through the inside of the droplet.^[24] It also suggested that the first layer of ZIF-8 particles that assembles at this interface governs further 3D self-assembly. In fact, this assisted colloidal self-assembly resembles the colloidal epitaxy method, in which patterned substrates usually act as templates to direct the 3D colloidal crystallization.^[25] One intriguing question that remains is how CTAB directs the formation of the first (111), (100), or (110) layer. Considering a spherical particle, the planar packing fraction of the hexagonal (111) plane is 0.907, whereas the packing fractions of the (100) and (110) planes are 0.785 and 0.555, respectively. Thus, an increase in CTAB favors formation of less dense layers. Certain factors must be considered in this CTAB dependence. First, introduction of more positive charges in the dispersion can cause an increase in the number of repulsive interactions during ZIF-8 particle assembly. Second, formation of CTAB micelles and/or a decrease in the droplet surface tension can each alter particle assembly.

To validate the role of the surfactant (i.e., charge in the dispersion, micelles, and the droplet surface tension), we investigated the use of another surfactant such as the anionic sodium dodecyl sulfate (SDS) to control the self-assembly of ZIF-8 particles (Figure S10, Supporting Information). We observed completely disordered assemblies at SDS concentrations lower than 2 mg mL⁻¹, whereas ordered (111)-oriented supercrystals were obtained upon increasing the SDS concentration from 2 to 5 mg mL⁻¹. When increasing the SDS concentration up to 6 mg mL⁻¹, we started detecting the formation of (110)-oriented domains. These results further evidenced the importance of the surfactant concentration to change the growth orientation of these fcc ZIF-8 supercrystals.

In addition to enabling control over pore-channel direction, the orientation of fcc supercrystals also determines the photonic properties.^[26] Accordingly, we next sought to study how changes in CTAB concentration might influence the photonic behavior of our MOF supercrystals. These supercrystals are periodic dielectric structures comprising ZIF-8 particles (size: ≈ 230 nm); thus, they exhibit angle-dependent iridescence that is visible to the naked eye and that originates from a photonic band structure. We observed that increasing

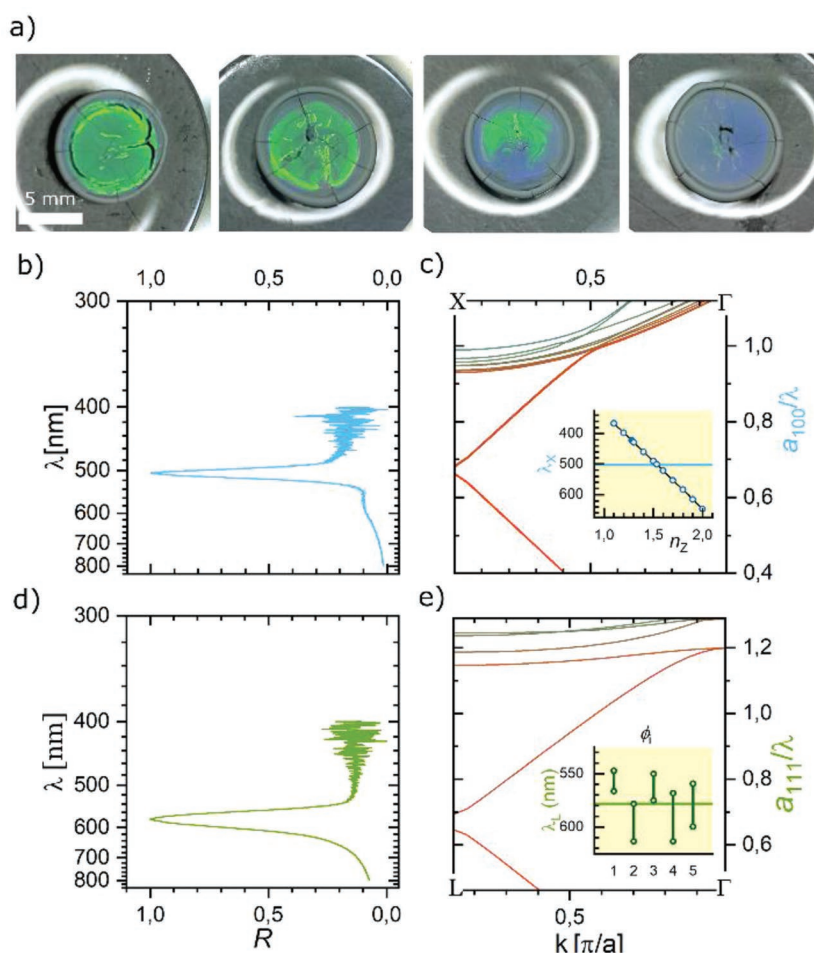


Figure 3. a) Change in color of the supercrystals obtained upon increasing the CTAB concentration (left to right: 1, 2, 2.5, and 3 mg mL⁻¹). Note that the photo on the far left corresponds to a (111)-oriented supercrystal, whereas the one on the right corresponds to a (100)-oriented supercrystal. The two intermediate photos correspond to mixtures of the two orientations, showing that the (100) domains start at the perimeter, and then propagate to the center of the monolith, with increasing CTAB concentration. Normalized specular optical reflectance plots from b) (100) and d) (111) arrangements, and the corresponding photonic band structures in the c) ΓX and e) ΓL directions. The insets in panels (c) and (e) show the photonic gap positions λ_X and λ_L as functions of refractive index and mean particle size ϕ_i , respectively.

the CTAB concentration from 1 to 3 mg mL⁻¹ led not only to a shift in supercrystal orientation, from (111)-oriented to (100)-oriented, but also to a concomitant change in color from green to blue (Figure 3a), thus providing preliminary evidence of a shift in photonic properties. To further corroborate that the photonic behavior was orientation-dependent, we characterized both pure (111)- and (100)-oriented supercrystals with UV-vis reflectance spectrometry to determine their respective photonic bandgaps. Interestingly, unlike the other orientations, the (110)-oriented supercrystal did not show any similar iridescence. This was probably due to poor crystal quality and/or the heterogeneity of the entire monolith in terms of orientation. Indeed, the (100)-oriented supercrystal had a $\lambda_{100} = 505$ nm (Figure 3b), whereas the (111)-oriented supercrystal exhibited a reflectance peak at $\lambda_{111} = 578$ nm (Figure 3d).

The theoretical analysis of the photonic properties of ZIF-8 supercrystals was carried out by calculating the photonic

band structure with the MIT Photonic Bands free package.^[27] This calculation begins by defining the geometry and setting the refractive index of the material to be analyzed. The structure formed by TRD particles joined by the hexagonal facets is exactly an fcc crystal of air cubes of side x oriented parallel to the axes in a ZIF-8 background and with a lattice parameter $a = 2x/t$, where t is the truncation. The band structure provides the first gap in the X point of the Brillouin zone, which corresponds to the reflectance peak in the (001) orientation directly comparable with experimental results. In this calculation, we varied the refractive index to match the X-gap frequency ($\lambda_{100} = 505$ nm; Figure 3c), since the former is the only unknown parameter, because it depends on the amount of water absorbed during synthesis. For the ZIF-8, this calculation yielded a refractive index value of 1.535, which is consistent with previously reported values (inset in Figure 3c).^[18]

As we mentioned earlier, the (111)-oriented supercrystal is singular, in that it is plastic and the orientation of its polyhedra is less regular than in the other two cases (i.e., only the $\langle 111 \rangle$ crystallites axes are preferentially oriented along the (111) supercrystal axis; Figure 1a). Consequently, such a structure presents photonic properties that do not respond to the photonic bands calculated for the aforementioned, perfect, close-packed fcc supercrystal. Thus, for the plastic fcc supercrystal, we had to model the TRDs as effective spheres with a diameter to be determined and a refractive index known from (001) reflection. We analyzed candidate sizes (ϕ_i) in the TRD that could be defined by joining diametrically opposing singular points on the surface (e.g., facet centers and corners) and that depend on the truncation of the particle (Figures S12 and S13, Supporting Information). Spheres of these diameters arranged in a close-packed fcc define lattice parameters $a_i = \phi_i \sqrt{2}$ and corresponding filling fractions. We examined the photonic bands of such lattices to determine the effective diameter at which the photonic gap at the L-point in reciprocal space would match the experimentally measured value ($\lambda_{111} = 578$ nm). We concluded that the best fit is ϕ_5 , which is the distance between the corner of opposing square facets (inset in Figure 3e). The corresponding photonic band structure is shown in Figure 3e, and the spectrum of reflectance in Figure 3d, where the accordance can be observed.

In conclusion, we have reported the self-assembly of TRD ZIF-8 crystals into well-ordered fcc supercrystals. These monolithic structures comprise monodisperse crystalline particles and, when no additional CTAB is added to the colloidal solution, the $\langle 111 \rangle$ ZIF-8 particle direction orients as the (111) supercrystal direction. We demonstrated that the entropically favored (111) orientation of these ZIF-8 supercrystals can be forced through the (100) orientation—and even the (110) orientation—by increasing the concentration of CTAB in the colloidal solution. To the best of our knowledge, this is the first reported example of orientation control in self-assembled polyhedral particles. Moreover, it is one of only a few examples demonstrating orientation control in colloidal crystals. Given that the ability to manipulate supercrystal orientation is important not only for MOFs, but also for all colloidal crystals, our method should provide a powerful tool for pore alignment, property tuning, and/or crystal orientation engineering.

Experimental Section

Materials and Characterization: All chemical reagents and solvents were purchased from Sigma-Aldrich and used as received without further purification. DI water was obtained from a Milli-Q water purification system. FESEM images were collected on a scanning electron microscope (FEI Magellan 400L XHR) at acceleration voltage of 1.0 kV, using PDMS-coated aluminum tape as support. The size of crystals was calculated from FESEM images by averaging the diameter of 200 particles from images of different areas of the same samples. PXRD measurements were done on an X'Pert PRO MPDP analytical diffractometer, $\lambda_{Cu} = 1.5406$ Å (PANalytical). Volumetric N_2 sorption isotherms were collected at 77 K using an ASAP 2020 HD (Micromeritics). The reflectance spectra were taken with a Hyperion 2000 FT-IR microscope coupled to a Vertex 80 spectrometer (both from Bruker) with a 15× Schwarzschild standard objective, tungsten lamp (in the Vertex 80), and a Si diode detector.

Synthesis of TRD ZIF-8 Crystals with $t = 0.63$: A solution of 0.3 g of $Zn(OAc)_2 \cdot 2H_2O$ in 5 mL of DI water was added into a solution of 1.56 g of 2-MiM and 0.40 mg CTAB in 5 mL of DI water, and the resulting mixture was homogenized by stirring it for 15 s. Then, the mixture was left at room temperature for 2 h to form TRD ZIF-8 crystals with $t = 0.63$. The resulting ZIF-8 particles were washed three times with DI water upon centrifugation at 9000 rpm in 50 mL Falcon tubes. The collected wet pellets were finally redispersed at a concentration of 50 mg mL⁻¹ in DI water or in aqueous CTAB solution with varying concentrations from 1 to 4 mg mL⁻¹. Note that to prevent aggregation, the particles were dispersed while they were still wet.

Formation of the ZIF-8 Supercrystals: The desired substrates (glass microscope slides, SEM pins, and PXRD substrate) were initially washed with water and ethanol, and dried with a pressurized N_2 gun. Then, PDMS was mixed with the curing agent with a mass ratio of 10:1, and the resulting mixture was applied to the corresponding substrate and cured for 15 min at 120 °C. Then, 40 μ L of the ZIF-8 colloidal solution was dropped on the PDMS-coated surface and left in the oven to dry at 120 °C.

Supporting Information

Supporting Information is available from the Wiley Online Library or from the author.

Acknowledgements

C.A. and Y.L. contributed equally to this work. This work was supported by the Spanish MINECO (project RTI2018-095622-B-I00); the Catalan AGAUR (project 2014 SGR 80); the ERC, under the EU-FP7 (ERC-Co 615954); and the CERCA Program/Generalitat de Catalunya. ICN2 is supported by the Severo Ochoa program from Spanish MINECO (grant no. SEV-2017-0706). J.A.P. acknowledges an FPI grant. Y.L. acknowledges the China Scholarship Council for scholarship support.

Conflict of Interest

The authors declare no conflict of interest.

Keywords

crystal orientation, mesoscale assembly, metal–organic frameworks, photonic crystals, supercrystals

Received: May 16, 2019
Published online: June 18, 2019

- [1] S. Haussühl, *Physical Properties of Crystals: An Introduction*, Wiley-VCH, Weinheim **2007**.
- [2] N. T. Nesbitt, M. J. Naughton, *Ind. Eng. Chem. Res.* **2017**, *56*, 10949.
- [3] M. H. Huang, S. Mao, H. Feick, H. Yan, Y. Wu, H. Kind, E. Weber, R. Russo, P. Yang, *Science* **2001**, *292*, 1897.
- [4] D. P. Norton, A. Goyal, J. D. Budai, D. K. Christen, D. M. Kroeger, E. D. Specht, Q. He, B. Saffian, M. Paranthaman, C. E. Klabunde, D. F. Lee, *Science* **1996**, *274*, 755.
- [5] K. Nomura, H. Ohta, K. Ueda, T. Kamiya, M. Hirano, H. Hosono, *Science* **2003**, *300*, 1269.
- [6] Z. Pan, H. L. Lai, F. C. Au, X. Duan, W. Zhou, W. Shi, N. Wang, C. S. Lee, N. B. Wong, S. T. Lee, S. Xie, *Adv. Mater.* **2000**, *12*, 1186.
- [7] a) R. S. Wagner, W. C. Ellis, *Appl. Phys. Lett.* **1964**, *4*, 89;
b) E. I. Givargizov, *J. Cryst. Growth* **1975**, *31*, 20.
- [8] R. Q. Zhang, Y. Lifshitz, S. T. Lee, *Adv. Mater.* **2003**, *15*, 635.
- [9] G. Cao, D. Liu, *Adv. Colloid Interface Sci.* **2008**, *136*, 45.
- [10] Z. Lai, G. Bonilla, I. Diaz, J. G. Nery, K. Sujaoti, M. A. Amat, E. Kokkoli, O. Terasaki, R. W. Thompson, M. Tsapatsis, D. G. Vlachos, *Science* **2003**, *300*, 456.
- [11] M. Y. Jeon, D. Kim, P. Kumar, P. S. Lee, N. Rangnekar, P. Bai, M. Shete, B. Elyassi, H. S. Lee, K. Narasimharao, S. N. Basahel, *Nature* **2017**, *543*, 690.
- [12] Special issue on metal–organic framework materials: H. C. Zhou, S. Kitagawa, *Chem. Soc. Rev.* **2014**, *43*, 5415.
- [13] Special issue on metal–organic frameworks and porous polymers—current and future challenges: G. Maurin, C. Serre, A. Cooper, G. Férey, *Chem. Soc. Rev.* **2017**, *46*, 3104.
- [14] E. Biemmi, C. Scherb, T. Bein, *J. Am. Chem. Soc.* **2007**, *129*, 8054.
- [15] D. Zacher, A. Baunemann, S. Hermes, R. A. Fischer, *J. Mater. Chem.* **2007**, *17*, 2785.
- [16] O. Shekhah, M. Eddaoudi, *Chem. Commun.* **2013**, *49*, 10079.
- [17] P. Falcaro, K. Okada, T. Hara, K. Ikigaki, Y. Tokudome, A. W. Thornton, A. J. Hill, T. Williams, C. Doonan, M. Takahashi, *Nat. Mater.* **2017**, *16*, 342.
- [18] C. Avci, I. Imaz, A. Carné-Sánchez, J. A. Pariente, N. Tasios, J. Pérez-Carvajal, M. I. Alonso, A. Blanco, M. Dijkstra, C. López, D. Maspoch, *Nat. Chem.* **2018**, *10*, 78.
- [19] J. Henzie, M. Grünwald, A. Widmer-Cooper, P. L. Geissler, P. Yang, *Nat. Mater.* **2012**, *11*, 131.
- [20] P. F. Damasceno, M. Engel, S. C. Glotzer, *Science* **2012**, *337*, 453.
- [21] C. Jin, M. A. McLachlan, D. W. McComb, R. M. De la Rue, N. P. Johnson, *Nano Lett.* **2005**, *5*, 2646.
- [22] Y. Zhong, L. Wu, H. Su, K. S. Wong, H. Wang, *Opt. Express* **2006**, *14*, 6837.
- [23] Y. Yin, Z. Y. Li, Y. Xia, *Langmuir* **2003**, *19*, 622.
- [24] S. H. Im, Y. T. Lim, D. J. Suh, O. O. Park, *Adv. Mater.* **2002**, *14*, 1367.
- [25] N. V. Dziomkina, G. J. Vancso, *Soft Matter* **2005**, *1*, 265.
- [26] P. D. García, J. F. Galisteo-López, C. López, *Appl. Phys. Lett.* **2005**, *87*, 201109.
- [27] S. G. Johnson, J. D. Joannopoulos, *Opt. Express* **2001**, *8*, 173.



Supporting Information

for *Small*, DOI: 10.1002/smll.201902520

Template-Free, Surfactant-Mediated Orientation of
Self-Assembled Supercrystals of Metal–Organic Framework
Particles

*Civan Avci, Yang Liu, Jose Angel Pariente, Alvaro Blanco,
Cefe Lopez,* Inhar Imaz,* and Daniel Maspoch**

Copyright WILEY-VCH Verlag GmbH & Co. KGaA, 69469 Weinheim, Germany, 2019.

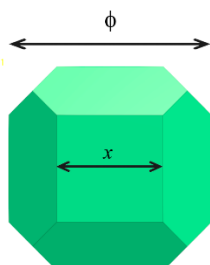
Supporting Information

Template-free, Surfactant-Mediated Orientation of Self-Assembled Supercrystals of Metal-Organic Frameworks Particles

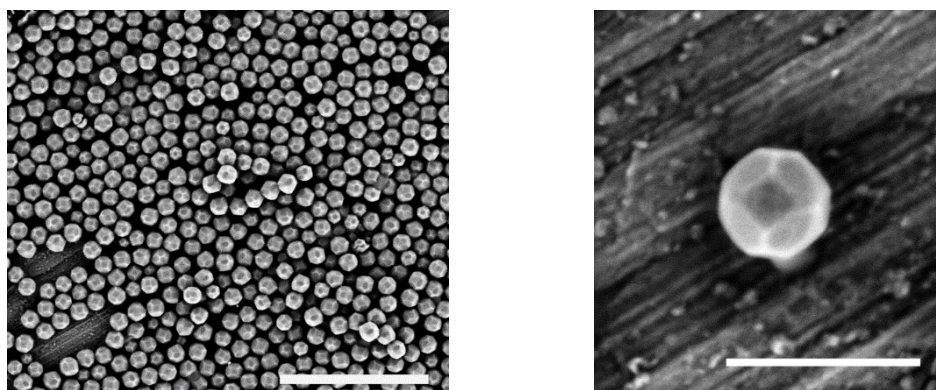
Civan Avci, Yang Liu, Jose Angel Pariente, Alvaro Blanco, Cefe Lopez, Inhar Imaz,* Daniel Maspoch**

Figure S1. (a) Schematic illustrations of the ZIF-8 TRD particles, highlighting: particle size ϕ and edge length x (b) Representative FE-SEM images of as-synthesized ZIF-8 particles with $t = 0.63$. Scale bars: 2 μm (left) and 400 nm (right); (c) Size-distribution histograms of as-synthesized ZIF-8 particles with $t = 0.63$.

a)



b)



c)

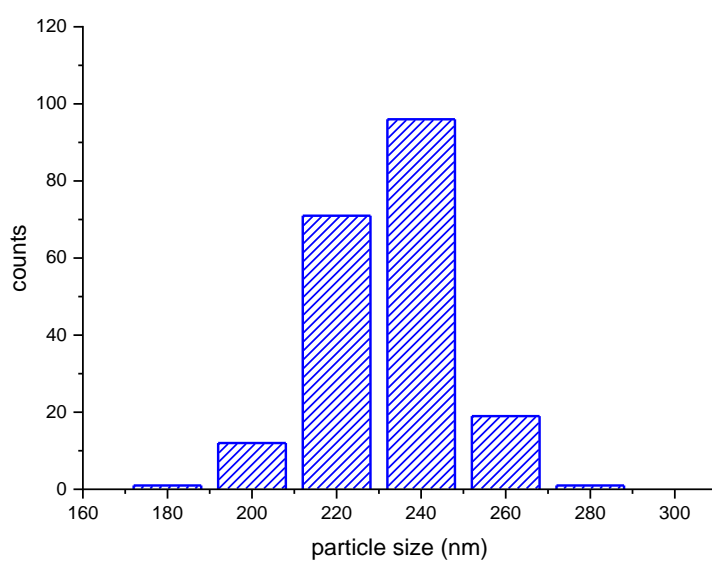


Figure S2. PXRD pattern of simulated (black) and as-synthesized ZIF-8 particles with $t = 0.63$ (red).

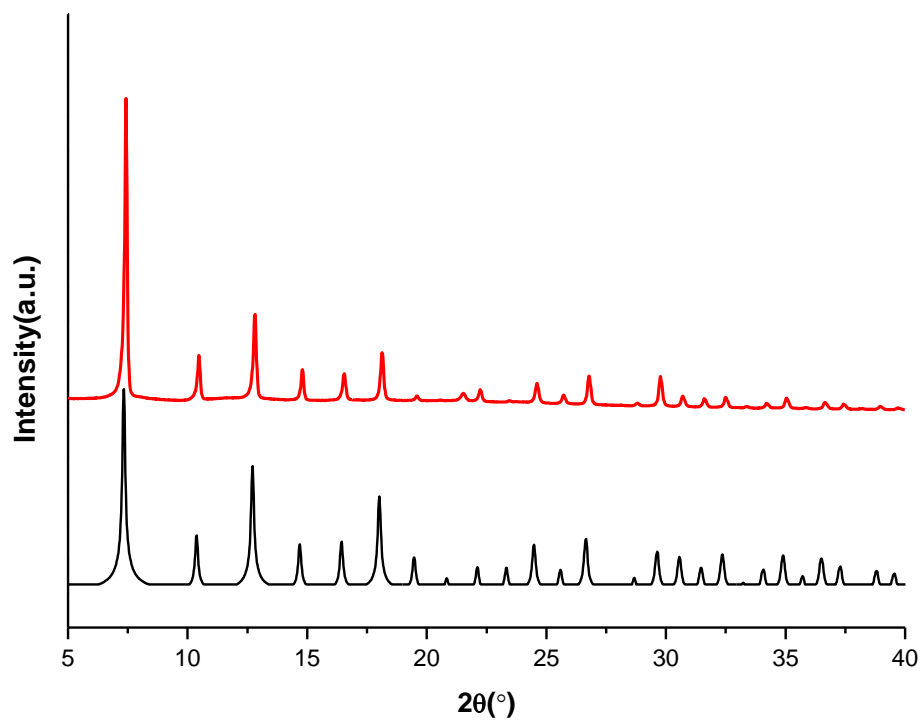
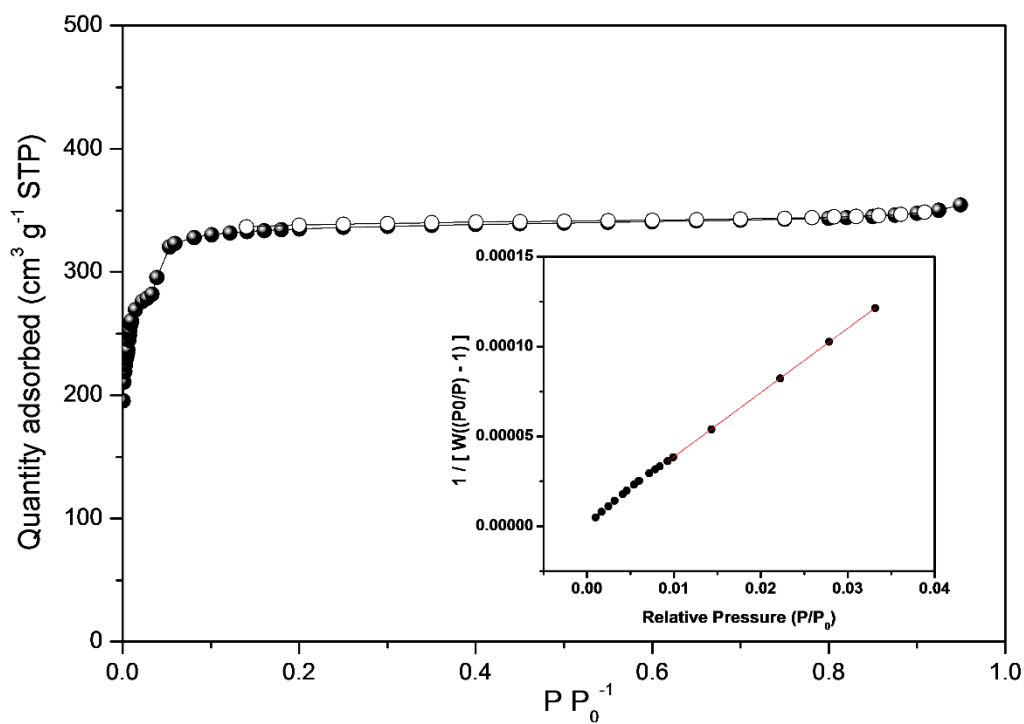


Figure S3. N₂ isotherm and BET linear fit of as-synthesized ZIF-8 particles with t = 0.63.

Surface area = 1215 m²/g

Slope = 3.58

Intercept = 3.00e-03

Correlation coefficient, r = 0.9999

C constant = 1237

Pore volume = 0.52 cm³/g

Figure S4. Representative FE-SEM images of ZIF-8 supercrystals self-assembled using CTAB concentration of 1.00 mg/mL. Images correspond to the perimeter (a) and to the center (b). Scale bars are 2 μm .

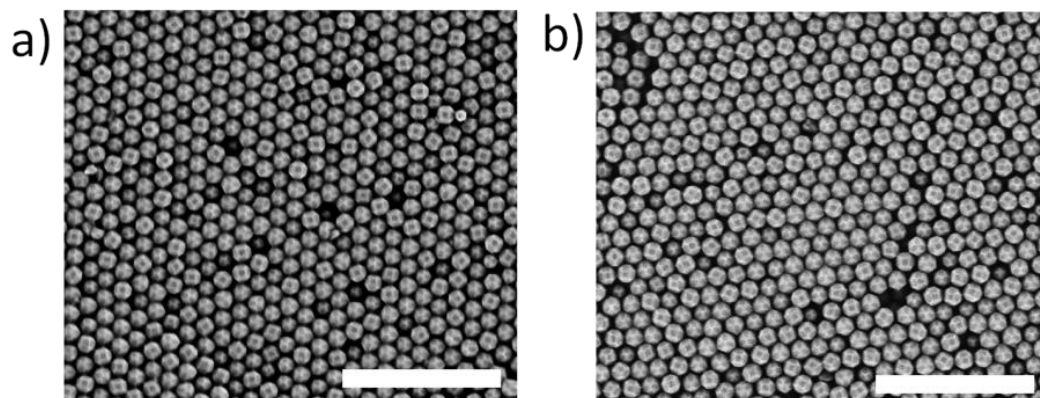


Figure S5. Representative FE-SEM images of ZIF-8 supercrystals self-assembled using CTAB concentration of 2.00 mg/mL. Images correspond to the perimeter (a) and to the center (b). Scale bars are 2 μm .

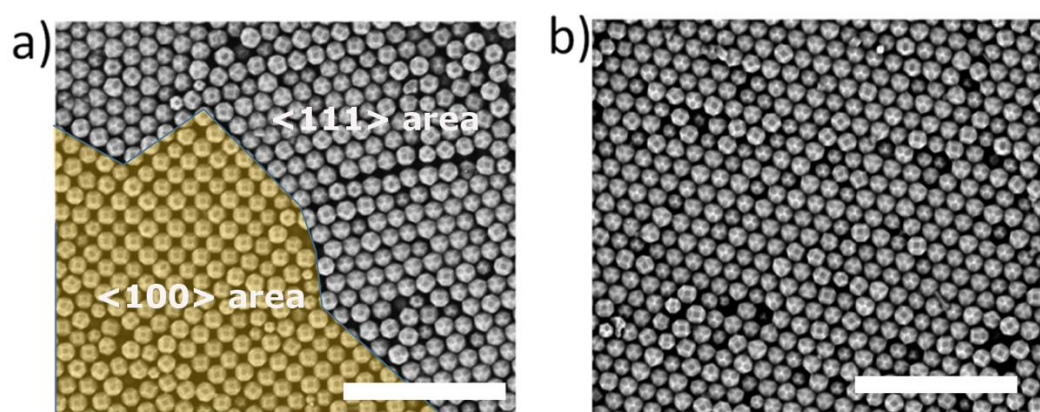


Figure S6. Representative FE-SEM images ZIF-8 supercrystals self-assembled using CTAB concentration of 3.00 mg/mL. Images correspond to the perimeter (a) and to the center (b). Scale bars are 2 μm .

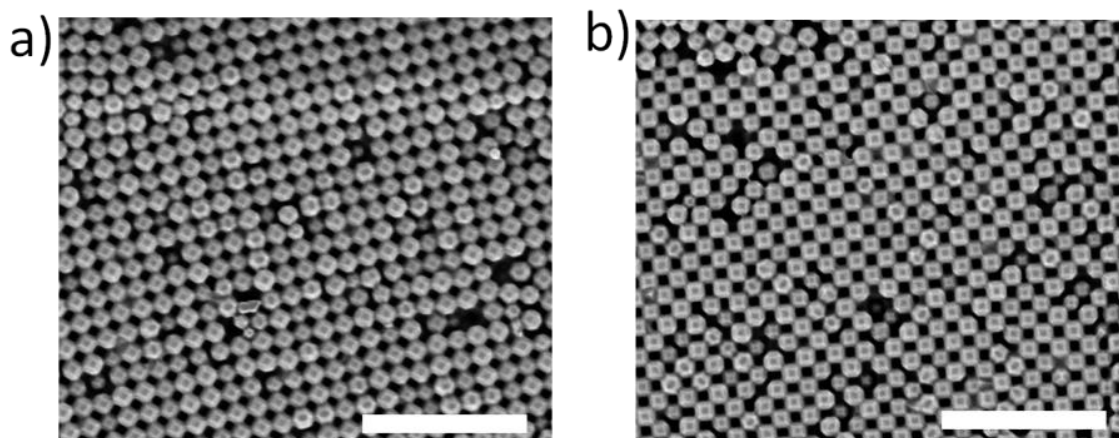


Figure S7. Representative FE-SEM images of ZIF-8 supercrystals self-assembled using CTAB concentration of 3.25 mg/mL. Images correspond to the perimeter (a) and to the center (b). Scale bars are 2 μm .

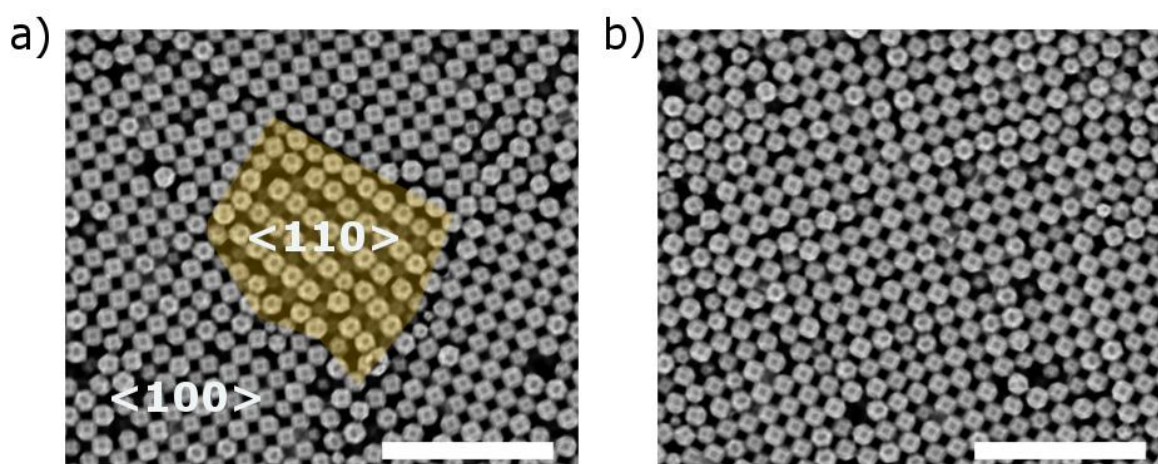


Figure S8. Representative FE-SEM images of ZIF-8 supercrystals self-assembled using CTAB concentration of 4.00 mg/mL. Images correspond to the perimeter (a) and to the center (b). Scale bars: (a) 3 μm and (b) 2 μm .

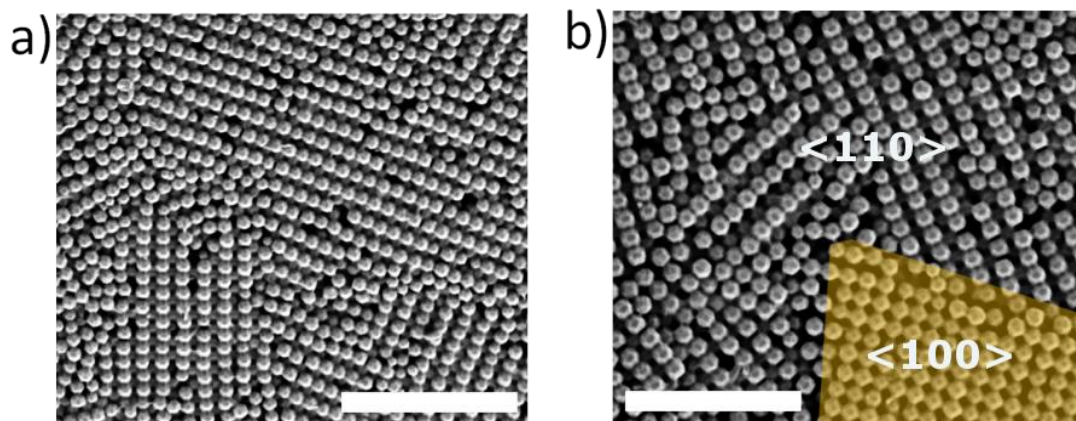


Figure S9. Representative photograph of the droplet after only 20 seconds of incubation, showing that the surface droplet has become opalescent.

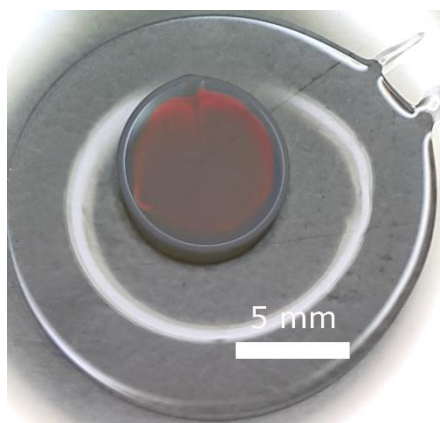
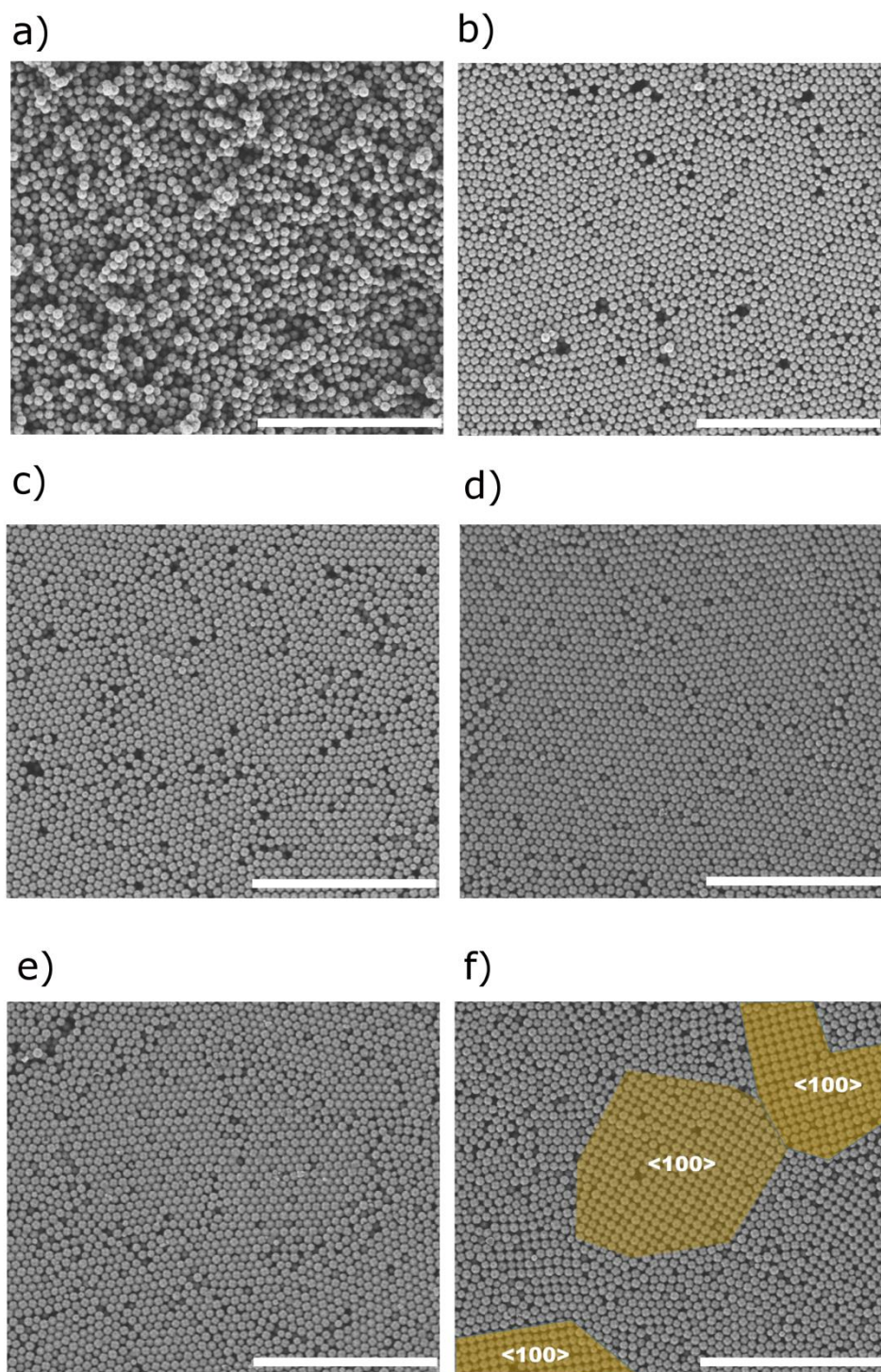


Figure S10. a) Representative FE-SEM images of disordered ZIF-8 assembly obtained using SDS concentration of 1.00 mg/mL. b-f) Representative FE-SEM images of ZIF-8 supercrystals self-assembled using SDS concentration of 2.00 mg/mL (b), 3.00 mg/mL (c), 4.00 mg/mL (d), 5.00 mg/mL (e) and 6.00 mg/mL (f). Scale bars are 5 μm .



Analysis of the Photonic Properties

The theoretical analysis of the photonic properties of ZIF-8 supercrystals was carried out by calculating the photonic band structure with the MIT Photonic Bands (MPB) free package. Figure S11 shows the photonic bands for several high-symmetry directions for a photonic crystal for a given refractive index. The variation of the photonic X-gap as a function of n_z is plotted in Figure 3 of main text and fit the experimental λ_{001} for $n_z = 1.535$.

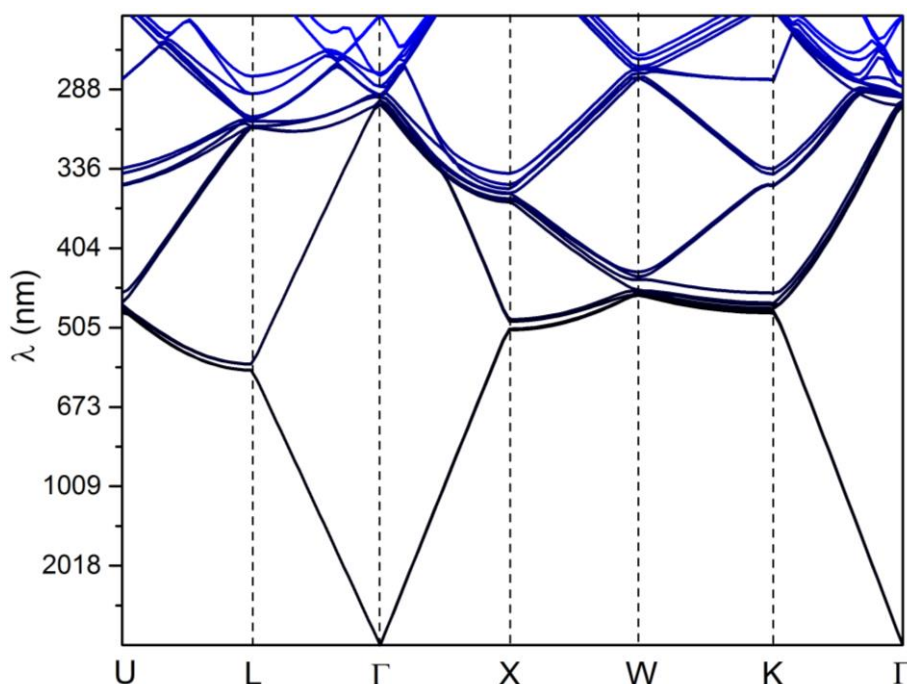


Figure S11. Full photonic band calculation for $n_z=1.535$.

"Plastic" oriented *fcc*

Once the refractive index of our ZIF-8 particles was settled, a simulation of the "plastic" *fcc* structure can be done. In this configuration, no preferred orientation of the TRD particles is achieved so they can only be modelled as close packed effective spheres. Different diameters, and their respective filling fractions that depend on the truncation of the TRD particles were tested (Figure S12). In Table S1, filling fractions are calculated for $t = 0.63$ which have an impact on the photonic bands as they determine the effective refractive index.

For this configuration, the band gap at the L point of the Brillouin zone (that gives rise to the reflectance peak in the (111) orientation) is calculated as a function of the refractive index

(that depends on the filling fraction and the ZIF-8 particles –already determined in the previous section). These gaps for different effective diameters are plotted as a function of n_Z in Figure S13.

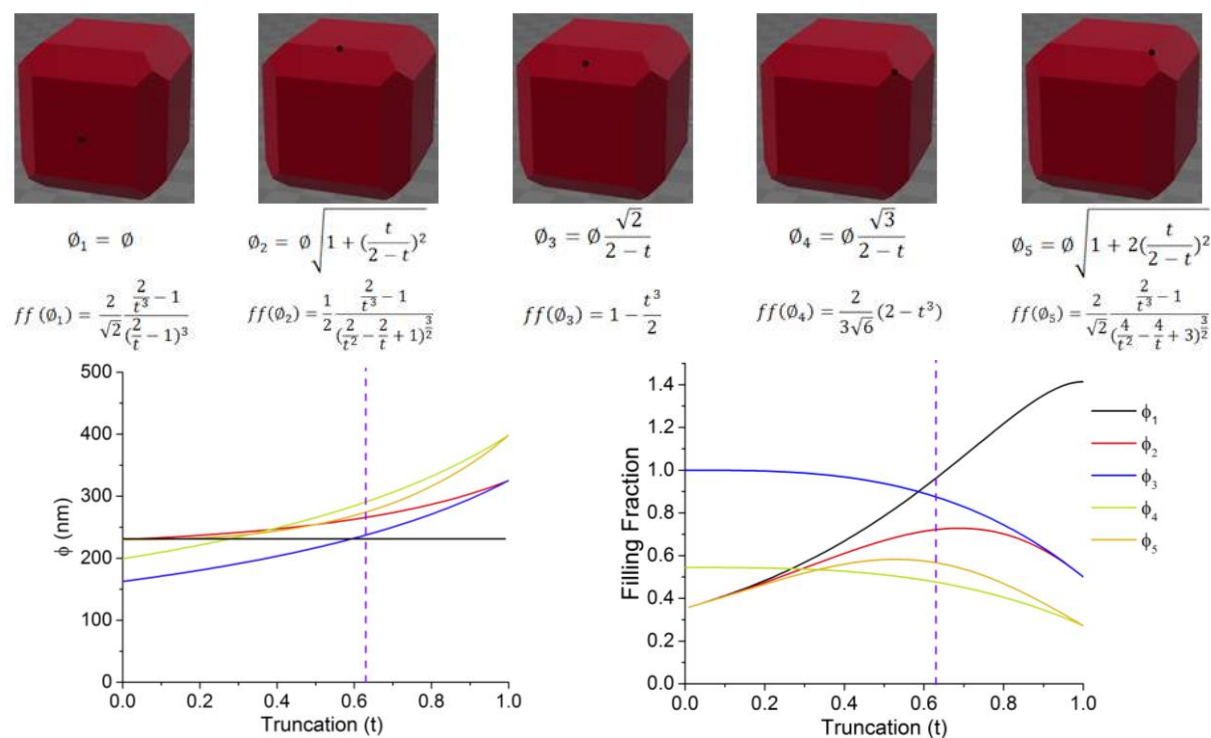


Figure S12. Possible diameters as a function of the truncation and their corresponding filling fractions.

ϕ	$ff(t = 0.63)$
1	0.96245
2	0.72179
3	0.87498
4	0.47628
5	0.56703

Table S1. Calculated filling fraction for $t = 0.63$ for the different diameters.

he last panel in Figure S13 summarizes the edges of the L gap for $n_Z=1.535$ for the various effective diameters. The gap for the effective diameter ϕ_5 is the only reasonable candidate as it predicts to be precisely centred around the experimentally measured value for $n_Z = 1.535$. This diameter, ϕ_5 , corresponds to the second largest for the current truncation (See Figure S12). This is in a good agreement with the "plastic" configuration in which the particles are placed in lattice positions of a *fcc* but in a random orientation. As a preferred orientation does not exist, a lessening in the packing will be expected and thus, a decrease in the filling fraction of the structure.

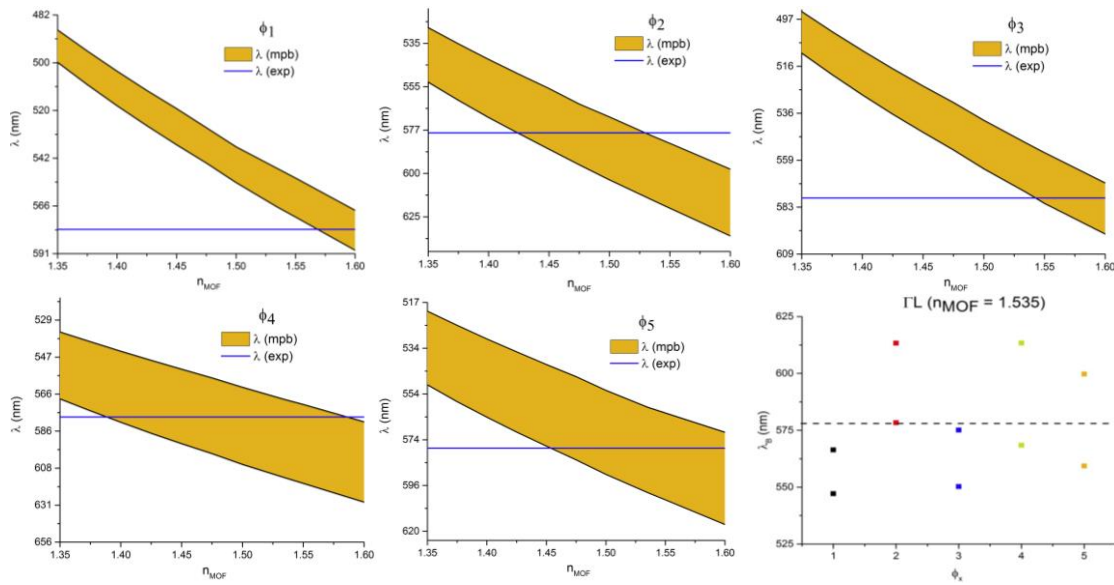


Figure S13. Evolution of the L band gap for different test diameters as a function of the refractive index of the ZIF-8. For $n_Z = 1.535$, the value obtained in the previous analysis, the best fit diameter is ϕ_5 .

In the light of the above, a comparison between theory and experiment can now be done. Figure 3 in the main text shows the spectra and the bands for the principal symmetries obtained as the concentration of CTAB increases. A Bragg peak in $\langle 111 \rangle$ direction corresponds to a gap in the L point of a plastic *fcc* photonic crystal when the amount of CTAB is around 1 mg/ml. A similar result can be seen for the $\langle 100 \rangle$ direction, which corresponds to a 3 mg/ml concentration of CTAB; in this case, accounted for by a gap at the X point for a compact fcc lattice. Moreover, no peak has been measured in the $\langle 110 \rangle$ direction in good agreement with the configuration of bands at the K point where no gap opens.

Appendix

Coloration in Supraparticles Assembled from Polyhedral Metal-Organic Framework Particles

Metal–Organic Frameworks

How to cite: *Angew. Chem. Int. Ed.* **2022**, *61*, e202117455

International Edition: doi.org/10.1002/anie.202117455

German Edition: doi.org/10.1002/ange.202117455

Coloration in Supraparticles Assembled from Polyhedral Metal–Organic Framework Particles

Junwei Wang[†], Yang Liu[†], Gudrun Bleyer, Eric S. A. Goerlitzer, Silvan Englisch, Thomas Przybilla, Chrameh Fru Mbah, Michael Engel, Erdmann Spiecker, Inhar Imaz,^{*} Daniel Maspoch,^{*} and Nicolas Vogel^{*}

Abstract: Supraparticles are spherical colloidal crystals prepared by confined self-assembly processes. A particularly appealing property of these microscale structures is the structural color arising from interference of light with their building blocks. Here, we assemble supraparticles with high structural order that exhibit coloration from uniform, polyhedral metal–organic framework (MOF) particles. We analyse the structural coloration as a function of the size of these anisotropic building blocks and their internal structure. We attribute the angle-dependent coloration of the MOF supraparticles to the presence of ordered, onion-like layers at the outermost regions. Surprisingly, even though different shapes of the MOF particles have different propensities to form these onion layers, all supraparticle dispersions show well-visible macroscopic coloration, indicating that local ordering is sufficient to generate interference effects.

Introduction

Emerging functional materials for applications in photonics, plasmonics, and mechanics are created by assembling smaller particles into defined structures.^[1] Among various assembly strategies, using spherical confinements (e.g. in drying emulsion droplets) to guide the self-assembly process is garnering increasing interest.^[2] This hierarchical approach entails assembly of a finite number of particles into a larger supraparticle. The finite number can provide additional effects, such as fluctuations of the thermodynamic stability of defined clusters.^[2a] More generally, ordered supraparticles exhibit the collective properties present in their corresponding bulk assemblies, while remaining dispersible, discrete objects that are easy to handle and post-process. For supraparticles whose constituent particles are of a size in the range of visible light wavelengths, the regular internal structure causes light diffraction, with constructive and destructive interference occurring for specific ranges of wavelengths that depend on the particle size, lattice spacing, degree of order, and materials composition (namely the variations in the refractive index), all of which affect the resulting structural color and its angle dependence, thus generating structural color. The hue, intensity and saturation of this color depends on the refractive index, degree of crystallinity and crystal-type of the supraparticle.^[3,4a]

To date, most supraparticles exhibiting structural color are assembled from spherical primary particles. Significant efforts have been focused on varying the type of the primary spherical particles, including polystyrene, silica and melanin and other biopolymers.^[1c,4] The extensive use of spherical primary particles in supraparticles stems from their availability and strong tendency to form close-packed, ordered structures. At the same time, the type of resulting crystal lattices is often limited to close-packings of equal spheres. In contrast, the variety of ordered structures that can be formed by polyhedral particles with potential distinct optical functionalities is massive.^[5] Although researchers can now exercise precise control over the size and shape of diverse polyhedral particles (mainly metallic ones), they continue to face the challenge of assembling these particles within droplets to generate supraparticles with structural color. This is because the particles are either too small to produce Bragg diffraction color or too heavy to remain dispersed within the droplets, so that sedimenta-

[*] Dr. J. Wang,[†] G. Bleyer, Dr. E. S. A. Goerlitzer, Prof. Dr. N. Vogel
Institute of Particle Technology, Friedrich-Alexander Universität
Erlangen-Nürnberg, 91058 Erlangen (Germany)
E-mail: nicolas.vogel@fau.de

Y. Liu,[†] Dr. I. Imaz, Prof. Dr. D. Maspoch
Catalan Institute of Nanoscience and Nanotechnology (ICN2),
CSIC & The Barcelona Institute of Science and Technology,
Bellaterra, 08193 Barcelona (Spain)
E-mail: inhar.imaz@icn2.cat
daniel.maspoch@icn2.cat

S. Englisch, Dr. T. Przybilla, Prof. Dr. E. Spiecker
Institute of Micro- and Nanostructure Research (IMN),
Center for Nanoanalysis and Electron Microscopy (CENEM),
IZNF, Friedrich-Alexander Universität Erlangen-Nürnberg,
91058 Erlangen (Germany)

Dr. C. F. Mbah, Prof. Dr. M. Engel
Institute for Multiscale Simulation,
IZNF, Friedrich-Alexander Universität Erlangen-Nürnberg,
91058 Erlangen (Germany)

Prof. Dr. D. Maspoch
ICREA, Pg. Lluís Companys 23, 08010 Barcelona (Spain)

[†] These authors contributed equally to this work.

© 2022 The Authors. Angewandte Chemie International Edition published by Wiley-VCH GmbH. This is an open access article under the terms of the Creative Commons Attribution Non-Commercial NoDerivs License, which permits use and distribution in any medium, provided the original work is properly cited, the use is non-commercial and no modifications or adaptations are made.

tion impedes efficient equilibration.^[6] This, in turn, precludes the use of many functional materials that are intrinsically polyhedral in the assembly of new multifunctional supraparticles.

To face this challenge, we envisaged using polyhedral metal–organic frameworks (MOFs) as primary particles for the formation of supraparticles. MOFs are functional porous materials with large surface areas and potential for myriad applications such as gas storage, catalysis and separation.^[7] MOFs also exist in the form of crystalline particles that encompass most known polyhedral shapes. Moreover, they have been recently synthesized with highly homogeneous, tunable size and shape.^[8] Together with their low density and their amenability to surface functionalization, MOFs can also be obtained as stable colloids, with particle sizes in the range of ≈ 200 nm to 400 nm, which is in the ideal range to interact with visible light and thus, produce structural color. Indeed, we have recently demonstrated the use of such polyhedral MOF particles for three-dimensional photonic MOF superstructures.^[9,10] Here, we demonstrate that similar complex-shaped MOF particles can self-assemble within the confinement of an emulsion droplet and form spherical, consolidated and ordered photonic supraparticles. In the following, we examine in detail how the spherical confinement affects the resultant self-assembled structure and how this internal structure translates into macroscopically observable structural color.

The polyhedral MOF particles used in this study are cubic zeolitic imidazolate framework-8 (C-ZIF-8), truncated rhombic dodecahedral TRD-ZIF-8, perfect rhombic dodecahedral RD-ZIF-8 and octahedral Universitetet i Oslo-66 (O-UiO-66) particles. ZIF-8 is a porous MOF made of Zn^{II} ions and 2-methylimidazolate (2-Mim) linkers that exhibits a sodalite-type structure and a large surface area (≈ 1200 – $1500 \text{ m}^2 \text{ g}^{-1}$).^[11] UiO-66 is a MOF built up from bridging $[\text{Zr}_6\text{O}_4(\text{OH})_4]$ clusters by terephthalic acid linkers, also showing a large surface area ($\approx 1200 \text{ m}^2 \text{ g}^{-1}$).^[12] We found that the spherical geometry of each supraparticle enforces ordered, onion-like layered structures of polyhedral MOF particles, which, in turn, act as Bragg reflectors and cause interference effects leading to structural coloration. Based on our results, we discuss the angle-dependent coloration as a function of the size and shape of the building blocks and the internal order of the resultant supraparticles.

Results and Discussion

We began with the synthesis of different colloidal polyhedral MOF particles (Figure 1a; Figure S1–S4). C-ZIF-8 particles were synthesized by reacting an aqueous mixture of $\text{Zn}(\text{NO}_3)_2 \cdot 6\text{H}_2\text{O}$, 2-Mim and cetyltrimethylammonium bromide (CTAB) at room temperature for 5 h. Similarly, both TRD- and RD-ZIF-8 particles were prepared by reacting an aqueous solution of $\text{ZnAc}_2 \cdot 2\text{H}_2\text{O}$, 2-Mim and CTAB (only in the case of TRD-ZIF-8) at room temperature for 2 h. In the case of O-UiO-66, a dimethylformamide (DMF) solution of ZrCl_4 , terephthalic acid and acetic acid was heated at 120°C for 12 h. Afterwards, the three types of ZIF-8

particles were washed with deionized water and O-UiO-66 with DMF by centrifugation at 9000 rpm in 50 mL Falcon tubes. Colloids were finally prepared at concentrations of 40 mg mL^{-1} (C-ZIF-8), 40 mg mL^{-1} (TRD-ZIF-8), 20 mg mL^{-1} (RD-ZIF-8) and 6 mg mL^{-1} (O-UiO-66). Field-emission scanning electron microscopy (FESEM), powder X-ray diffraction (PXRD), and zeta-potential measurements of the resulting colloids revealed the formation of the following homogeneous particles, listed here with their respective particle sizes: C-ZIF-8 (191 ± 9 nm; Figure S1), TRD-ZIF-8 (181 ± 9 nm; 198 ± 10 nm; 229 ± 9 nm; and 247 ± 10 nm; Figure S2), RD-ZIF-8 (246 ± 12 nm; 267 ± 12 nm; and 293 ± 13 nm; Figure S3) and O-UiO-66 (edge size: 194 ± 12 nm; 238 ± 13 nm; and 247 ± 13 nm; Figure S4). The truncation in TRD-ZIF-8 particles was 0.68. The surface charge of all the ZIF-8 particles was approximately +30 mV, for the O-UiO-66 particles, ca. +45 mV.

Having prepared the four types of MOF particles, we then synthesized the corresponding supraparticles. This began with addition of 0.5 wt% non-ionic alcohol ethoxylate surfactant (Lutensol TO-8, BASF) into separate 1.0 mL dispersions of the ZIF-8 particles, and of polyvinylpyrrolidone into a dispersion of the UiO-66 particles to improve colloidal stability. Three centrifugation cycles removed residual reagents, including excess surfactant. Next, the aqueous MOF particle dispersions were emulsified in perfluorinated oil (HFE 7500), either by vigorous shaking (Figure S5) or by droplet-based microfluidics (Figure 1b,c, Figure S6). The droplets were stabilized by a perfluorosurfactant and left in an open glass vial overnight to allow evaporation and self-organization of the building blocks inside the droplets.

Next, we characterized the supraparticles assembled from each of the four polyhedral MOF particles by FESEM (Figures 1d). Each supraparticle was spherical and had an ordered surface, in which each class of polyhedral MOF particle was packed in agreement with the corresponding Monte Carlo simulations of hard polyhedra in spherical confinement (Figures 1e). The RD- and TRD-ZIF-8 particles formed a triangular unit cell and a rhombic unit cell at the supraparticle surface, respectively, agreeing with their bulk face-centered cubic packing and rhombohedral packing.^[9] The C-ZIF-8 particles formed the expected square unit cell on the spherical supraparticle surface, whereas the O-UiO-66 particles formed a triangular cell. Careful analysis of FESEM images also showed that the flat faces of the TRD-ZIF-8, C-ZIF-8 and O-UiO-66 particles were exposed to form a smooth, ordered, supraparticle surface. This was observed both experimentally and in the simulations. We reason that this packing is caused by entropic force that favors face-to-face configurations and disfavors vertex-to-face configurations in polyhedral packing, which tends to align the flat faces of particles to the droplet interface.^[13]

Spherical confinement distorts crystalline lattices; consequently, it distorts the arrangement of MOF particles inside the supraparticles.^[2f,g,14,15] The spherical curvature forces the primary particle to form a spherical particle monolayer at the supraparticle surface, which can in turn

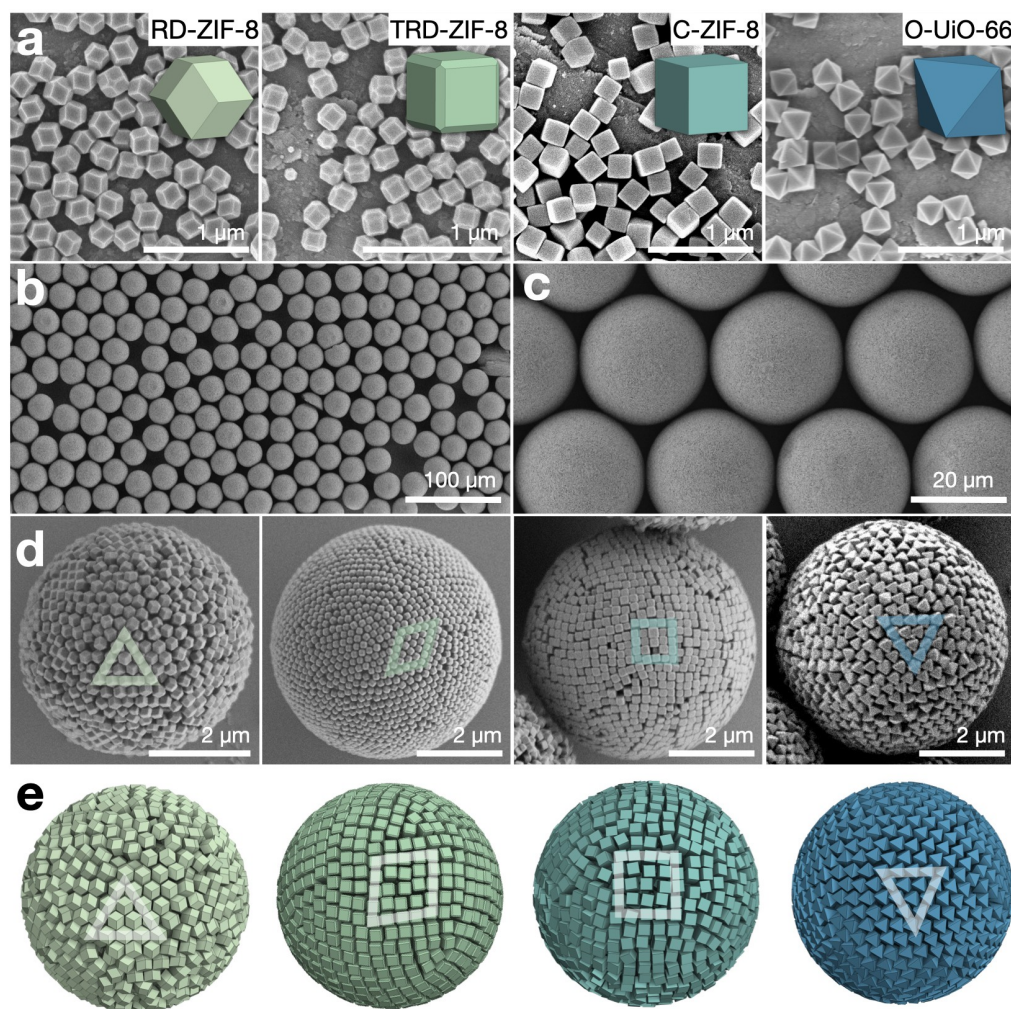


Figure 1. Supraparticles from uniform, polyhedral MOF building blocks. a) FESEM of monodisperse rhombic dodecahedron (RD-ZIF-8), truncated rhombic dodecahedron (TRD-ZIF-8), cube (C-ZIF-8) and octahedron (O-UiO-66) particles (left to right). b, c) Monodisperse TRD-ZIF-8 supraparticles prepared by emulsifying the MOF particle dispersion using droplet-based microfluidics. d) FESEM (from left to right) of RD-ZIF-8, TRD-ZIF-8, C-ZIF-8 and O-UiO-66 supraparticles, exhibiting ordered surfaces and characteristic packings. e) Snapshots of Monte Carlo simulations with polyhedra in spherical confinement.

cause the particles underneath to form another ordered layer. This curvature effect propagates from the surface of the supraparticle towards the interior and attenuates as the curvature increases up to infinity at the core. This suggests that the supraparticle might exhibit onion-like concentric layer structures under the surface,^[2c] and that the thickness of these onion layers may differ depending on the propensity of the differently-shaped particles to assemble in the spherical confinement.

We confirmed this hypothesis by two independent imaging techniques, namely X-ray tomography and focused ion beam (FIB)-assisted cross-sectioning, providing direct insight into the inner structure of the different supraparticles (Figure 2). Figure 2a shows an X-ray transmission image of a supraparticle assembled from C-ZIF-8 particles, where up to ten concentric layers, forming an ordered, onion-like structure, are evident near the surface. Towards the center,

the image appears homogeneous, indicating the particles are less ordered at the core of the supraparticle. Similarly, pronounced onion-like layer structures were observed in TRD-ZIF-8 supraparticles, while RD-ZIF-8 and O-UiO-66 supraparticles showed only little onion layers (Figure S7). The impression of the X-ray tomography was corroborated by SEM-FIB cross sectioning (Figure 2b–e). Onion-like layers were observed for all ZIF-8 polyhedral MOF particles near the supraparticle surface, conforming to the spherical curvature. Corroborating the X-ray images, the RD-ZIF-8 and the O-UiO-66 supraparticles only showed lower propensities to form onion-like layers and mostly regions with short-range order (Figure 2b,e; Figure S8,S11), whereas TRD- and C-ZIF-8 supraparticles exhibited pronounced onion-like layers penetrating far towards the interior (Figure 2c,d; Figure S9,S10). Intriguingly, the TRD-ZIF-8 supraparticles exhibited very high crystallinity throughout

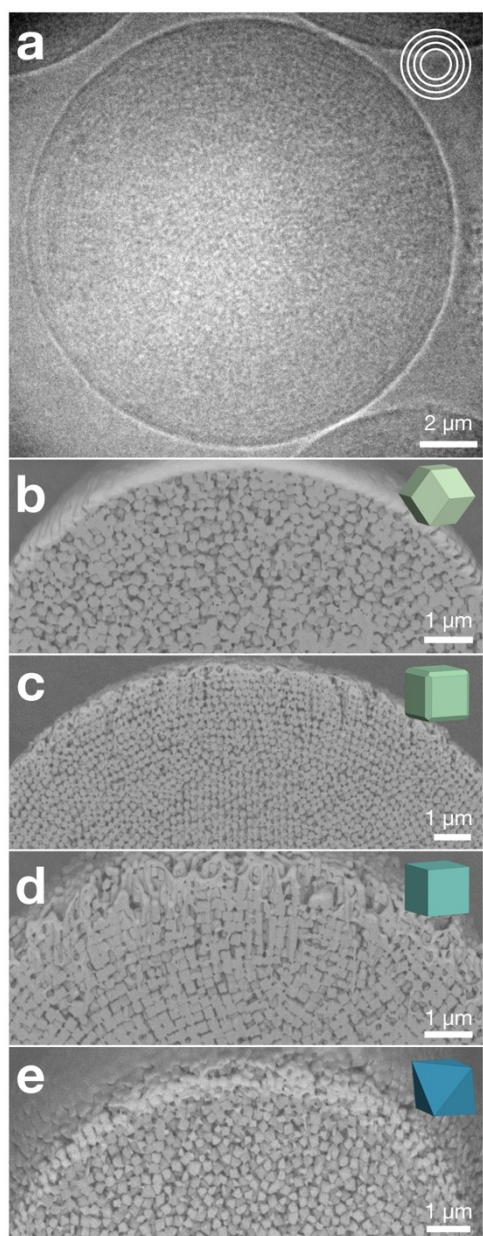


Figure 2. Internal structure of the supraparticles assembled from polyhedral MOFs. a) X-ray transmission image of a C-ZIF-8 supraparticle, showing its onion-like structure near the outer surface. b)–e) Focused ion beam cross-sections of a RD-ZIF-8 (b), TRD-ZIF-8 (c), C-ZIF-8 (d) and O-UiO-66 (e) supraparticles, showing their corresponding thicknesses of the onion-like layers.

the interior, albeit in multiple crystalline domains. We reason that sufficient equilibration may enable them to evolve towards complete crystallization with global symmetry, similar to what has been observed in spherical particles or ultra-small nanocrystals in spherical confinement.^[2f,g,6a] Indeed, we occasionally found local five-fold patterns in small supraparticles of TRD-ZIF-8 particles, indicative of an emerging icosahedral symmetry, corroborating results on the equilibrium structure of cubic nanoparticles with truncated edges (Figure S12).^[6a] Interestingly, in the Monte-

Carlo simulations, all four hard polyhedral particles form onion-like layers of similar thickness, indicating that shape itself does not cause the different propensity to form onion-like layers in differently-shaped MOF particles (Figure 1e, Figure S13). However, in a simple bulk crystallization induced by centrifugation, we observed coloration for the TRD- and C-ZIF-8 particles, but not for the RD-ZIF-8 and O-UiO-66 particles (Figure S14), agreeing with the observed trend in the supraparticles. We therefore hypothesize that the effect may be caused by the anisotropic electrostatic repulsions of polyhedral particles. It is likely that there is more screening of charges at sharp edges, i.e. the RD-ZIF-8 particles, making them more prone to aggregate at close distance, compared to C-ZIF-8 with less edges. TRD-ZIF-8 particles on the other hand have rounded and smoothened edges, making such particles even more stable.^[16]

The ability to form well-ordered MOF supraparticles with defined internal structure enabled us to study their photonic properties as a function of primary particle shape and degree of internal order (Figure 3). To this end, we combined micro-spectroscopy at the individual supraparticle level on a substrate in air with macroscopic angle-dependent spectroscopy of the supraparticle dispersions. First, we assembled four types of supraparticles and chose the primary particle sizes that produce a green reflection color under the microscope (Figure 3, top). As expected from the investigation of internal order (Figure 2), C-ZIF-8 and TRD-ZIF-8 supraparticles showed a pronounced green coloration with a well-resolved central colored dot, which results from constructive interference of light reflected at the spherical-symmetric ordered onion layers (Figure 3b,c). In contrast, RD-ZIF-8 and O-UiO-66 supraparticles showed a less pronounced reflection color (Figure 3a,d), indicative of the lower degree of internal ordering. Noteworthy, the surfaces of all supraparticles exhibited well-ordered arrangements of particles (Figure 3a–d, middle), indicating that polydispersity is not the origin of the reduced order of some shapes. Microscopic reflection spectra (Figure 3a–d, bottom) corroborated these observations. TRD- and C-ZIF-8 supraparticles showed narrower and more defined photonic stop bands (full width at half maximum (FWHM)=66 nm and 56 nm, respectively), while RD-ZIF-8 and O-UiO-66 supraparticles exhibited broader peaks (FWHM=84 nm and 83 nm, respectively).

Next, we used the TRD-ZIF-8 (229 nm) sample to exemplarily establish the relationship between supraparticle size and the reflection color intensity, measured at the peak of the photonic stop band (Figure 3e), using a polydisperse supraparticle sample prepared by simple shaking emulsification. A clear increase in color intensity was observed with increasing supraparticle size, which can be rationalized from the diminishing effect of frustrated crystallization caused by the curvature of the spherical confinement.

We then established the relationship between primary particle dimensions and the structural color of the supraparticles. We systematically varied the sizes of the differently-shaped MOF particles and measured reflection spectra from the formed MOF supraparticles suspended in the oil phase in a glass vial (Figure 3f). The reflection peaks of all

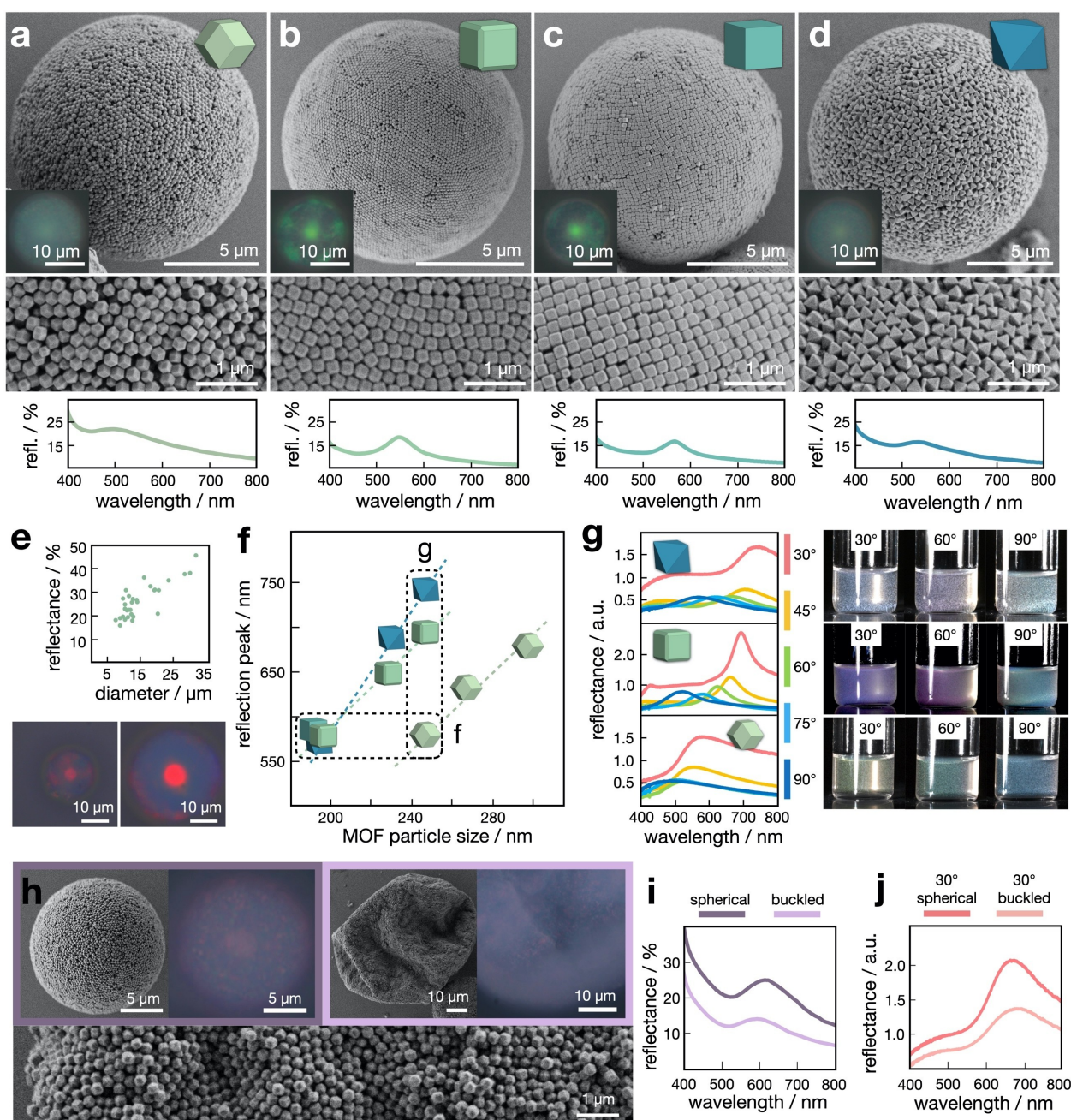


Figure 3. Optical properties of MOF supraparticles. a)–d) Top row: FESEM of RD-ZIF-8 (a), TRD-ZIF-8 (b), C-ZIF-8 (c) and O-Uio-66 (d) supraparticles, exhibiting structural coloration from the interaction of the incident light and the supraparticle structure (optical microscopy images in inset). Middle row: magnification of the particle surfaces, showing well-ordered arrangements of the primary particles; bottom row: reflection spectra measured for individual supraparticles. e) Effect of supraparticle size on the intensity of the photonic stop band, exemplarily shown for TRD-ZIF-8 supraparticles. f) Relationship between size and shape of the primary particles on the wavelength of the reflection peak, measured in suspension. g) Angle-dependent reflectance spectra of MOF supraparticles consisting of the same colloidal particle size but different shapes, along with corresponding photographs showing the observable coloration. h) FESEM of spherical and buckled MOF supraparticles, with optical microscopy images showing differences in structural color. The surface of the buckled supraparticle shows the hexagonally-packed particle layer. i) Reflectance spectra of individual spherical and buckled MOF supraparticles. j) Reflectance spectra of spherical and buckled supraparticles measured in suspension.

samples shifted linearly with increasing primary particle size, as the periodicity in the Bragg diffractor scales linearly with the particle size. Noteworthy, larger RD-ZIF-8 particles are required to produce the same reflection peak compared to other shapes (horizontal box in Figure 3f). As shown in

Figure 3a–d, a green reflection color was produced for TRD-ZIF-8 (197 nm), C-ZIF-8 (191 nm) and O-Uio-66 (194 nm) of similar sizes, while RD-ZIF-8 had significantly larger dimensions (246 nm). These differences are caused by the packing of the differently-shaped particles. Entropy

favors the particles to align their faces within each layer and between layers (Figure S15).^[17] For TRD- (and similar for C-shaped) particles, the surface of a close-packed layer is “flat”, leaving only small grooves from the truncation at particle edges. As a result, the distance between two stacked layers is the same as the distance between the two opposite faces of the TRD, which is the particle size by definition (note that this does not equal the edge length, Figure S2). However, for RD-ZIF-8 particles, the surface of a close-packed layer has jagged protrusions and indentations (Figure S15). When two such layers stack, protrusions and indentations can register, bringing the two layers closer. As a result, the distance between layers is smaller than the size of RD-shaped particles. From Figure 3f, we estimate that RD-shaped particles need to be 1.25 larger in size (than TRD-shaped particles) to produce a similar Bragg reflection peak.

We then focused on the macroscopic, angle-dependent coloration of the different MOF supraparticles, which was measured directly in suspension using a collimated white light source at different angles for illumination (Figure S16). Figure 3g shows the spectra of supraparticle suspension prepared by shaking using similar-sized primary particles of different shapes (≈ 247 nm; vertical box in Figure 3f). As established above, the different packings of the individual shapes lead to different layer spacing and therefore a different photonic stop band at the same illumination angle (Figure 3f). Note that the reduced refractive index contrast in suspension efficiently suppress incoherent scattering, manifested by reduced reflection at lower wavelengths around 400 nm compared to samples measured in air (Figure 3a–d). As the angle between incident light and detector increases from 30° to 90° , all supraparticle suspensions showed a blue shift of the photonic stop band (Figure 3g, Figure S17). A quantitative comparison between all samples revealed nearly identical angle-dependent blue shifts of the stop band, regardless of the primary particle shape (Figure S18), suggesting that interference of light reflected at the onion-like layers is the dominating color mechanism. However, it is noteworthy that the RD-ZIF-8 and O-Uio-66 supraparticles with low propensity to form onion layers and thus low reflected color intensity under the microscope (Figure 3a, d), also showed evident macroscopic coloration. We note that the spectral intensities of the different samples cannot be directly compared, as the mobile supraparticles rapidly accumulate on the top of the suspension due to the density difference, causing a non-uniform concentration during measurements. Nevertheless, the macroscopic photographs (Figure 3g) of the different dispersions document the visible, angle-dependent coloration of the RD-ZIF-8 and O-Uio-66 supraparticle dispersions with comparably low order.

Interestingly, even buckled MOF supraparticles with supposedly compromised internal order exhibited observable structural color (Figure 3h). We fabricated spherical and buckled RD-ZIF-8 supraparticles by systematically removing surfactant via additional centrifugation steps (Figure S19). The buckled supraparticles did not show the typical central dot attributed to the onion-like layers in the

optical microscopy images (Figure 3h).^[3a] Their spectral properties, however, showed the presence of a reflection peak (Figure 3i,j). A similar phenomenon was recently reported for nanocellulose crystals in droplets, where multi-layer structures persist through a buckled morphology.^[18] It is possible that the MOF particles also form stacked, non-concentric layers near the supraparticles surface. However, due to the larger and more rigid particle nature, only a few layers can be reasonably expected under the heavily buckled surface. Additionally, the reported buckled nanocellulose structures exhibit angle-independent color, while the buckled MOF supraparticles maintain the same angle-dependency observed in spherical supraparticles (Figure S20). We hypothesize that other mechanisms may contribute to this coloration. One possibility is an additional surface grating effect (Figure S21).^[19–21] We noticed that even for buckled supraparticles, the surface consists of hexagonally close-packed particles with sufficient structural order (Figure 3h, inset, Figure S22), similar to the surface of spherical supraparticles (Figure S23). The inclined angle enabled by the polyhedral particles may efficiently diffract part of the incident light, which adds to the weaker Bragg reflection color for the buckled supraparticles. Another possible source for the color is the existence of numerous tiny crystallites consisting of a few dozen particles randomly distributed in the supraparticles, which can be seen in the weak and localized color patches in the optical microscopic image (Figure 3h). While the exact mechanism and the individual contributions to the observed structural color of MOF supraparticles requires more detailed studies supported by numerical simulations, the existence of macroscopic coloration in less ordered structure with non-spherical, buckled morphology is promising for the design of structurally colored materials and pigments.

Conclusion

In conclusion, we assembled various type of polyhedral MOF particles into well-defined MOF supraparticles and investigated the shape-dependent internal structure. We then correlated this internal order with microscopic and macroscopic structural coloration and established shape-size-coloration relationships. With the growing library of MOF particle materials and shapes, our study opens a new avenue to fabricate discrete hierarchical ordered structures that combine intrinsic MOF functionality with additional emerging collective properties.

Acknowledgements

We thank C.X. Du and E.G. Teich for discussion of polyhedra packing in confinement. This work was supported by the Spanish MINECO (project RTI2018-095622-B-I00) and the Catalan AGAUR (project 2017 SGR 238). It was also funded by the CERCA Pro-gram/Generalitat de Catalunya. ICN2 is supported by the Severo Ochoa program from the Spanish MINECO (Grant No. SEV-2017-0706).

Y.L. acknowledges the China Scholarship Council for scholarship support. T.P. and S.E. acknowledges support by DFG within the framework of the research training group GRK 1896. This research was supported by the Deutsche Forschungsgemeinschaft (DFG, German Research Foundation)—Project-ID 416229255—SFB 1411. N.V. and M.E. also acknowledge funding by the DFG under projects VO 1824/7-1 and EN 905/2-1, respectively. Open Access funding enabled and organized by Projekt DEAL.

Conflict of Interest

The authors declare no conflict of interest.

Data Availability Statement

The data that support the findings of this study are available from the corresponding author upon reasonable request.

Keywords: Emulsion • Metal–Organic Frameworks • Self-Assembly • Structural Color • Supraparticles

- [1] a) J. F. Galisteo-López, M. Ibisate, R. Sapienza, L. S. Froufe-Pérez, Á. Blanco, C. López, *Adv. Mater.* **2011**, *23*, 30; b) M. He, J. P. Gales, É. Ducrot, Z. Gong, G.-R. Yi, S. Sacanna, D. J. Pine, *Nature* **2020**, *585*, 524–529; c) A. Dreyer, A. Feld, A. Kornowski, E. D. Yilmaz, H. Noei, A. Meyer, T. Krekeler, C. Jiao, A. Stierle, V. Abetz, H. Weller, G. A. Schneider, *Nat. Mater.* **2016**, *15*, 522; d) N. S. Mueller, Y. Okamura, B. G. M. Vieira, S. Juergensen, H. Lange, E. B. Barros, F. Schulz, S. Reich, *Nature* **2020**, *583*, 780.
- [2] a) M. A. Boles, M. Engel, D. V. Talapin, *Chem. Rev.* **2016**, *116*, 11220; b) N. Vogel, M. Retsch, C. A. Fustin, A. Del Campo, U. Jonas, *Chem. Rev.* **2015**, *115*, 6265; c) R. M. Parker, B. Frka-Petescic, G. Guidetti, G. Kamita, G. Consani, C. Abell, S. Vignolini, *ACS Nano* **2016**, *10*, 8443; d) T. Wang, D. LaMontagne, J. Lynch, J. Q. Zhuang, Y. C. Cao, *Chem. Soc. Rev.* **2013**, *42*, 2804; e) S. Wintzheimer, T. Granath, M. Oppmann, T. Kister, T. Thai, T. Kraus, N. Vogel, K. Mandel, *ACS Nano* **2018**, *12*, 5093; f) B. de Nijs, S. Dussi, F. Smalenburg, J. D. Meeldijk, D. J. Groenendijk, L. Filion, A. Imhof, A. van Blaaderen, M. Dijkstra, *Nat. Mater.* **2015**, *14*, 56; g) J. W. Wang, C. F. Mbah, T. Przybilla, B. A. Zubiri, E. Spiecker, M. Engel, N. Vogel, *Nat. Commun.* **2018**, *9*, 5259; h) J. Wang, C. F. Mbah, T. Przybilla, S. Englisch, E. Spiecker, M. Engel, N. Vogel, *ACS Nano* **2019**, *13*, 9005; i) S. Park, H. Hwang, M. Kim, J. H. Moon, S. H. Kim, *Nanoscale* **2020**, *12*, 18576–18594; j) J. Lacava, P. Born, T. Kraus, *Nano Lett.* **2012**, *12*, 3279; k) V. N. Manoharan, M. T. Elseser, D. J. Pine, *Science* **2003**, *301*, 483.
- [3] a) N. Vogel, S. Utech, G. T. England, T. Shirman, K. R. Phillips, N. Koay, I. B. Burgess, M. Kolle, D. A. Weitz, J. Aizenberg, *Proc. Natl. Acad. Sci. USA* **2015**, *112*, 10845; b) E. S. A. Goerlitzer, R. N. K. Taylor, N. Vogel, *Adv. Mater.* **2018**, *30*, 1706654; c) Y. J. Zhao, L. Shang, Y. Cheng, Z. Z. Gu, *Acc. Chem. Res.* **2014**, *47*, 3632; d) P. M. Parker, G. Guidetti, C. A. Williams, T. Zhao, A. Narkevicius, S. Vignolini, B. Frka-Petescic, *Adv. Mater.* **2018**, *30*, 1704477; e) Y. Takeoka, S. Yoshioka, A. Takano, S. Arai, K. Nueangnoraj, H. Nishihara, M. Teshima, Y. Ohtsuka, T. Seki, *Angew. Chem. Int. Ed.* **2013**, *52*, 7261; *Angew. Chem.* **2013**, *125*, 7402.
- [4] a) J. Wang, U. Sultan, E. S. A. Goerlitzer, C. F. Mbah, M. Engel, N. Vogel, *Adv. Funct. Mater.* **2020**, *30*, 1907730; b) M. Xiao, Z. Y. Hu, Z. Wang, Y. W. Li, A. D. z Tormo, N. L. Thomas, B. X. Wang, N. C. Gianneschi, M. D. Shawkey, A. Dhinojwala, *Sci. Adv.* **2017**, *3*, 170115; c) T. H. Zhao, G. Jacucci, X. Chen, D.-P. Song, S. Vignolini, R. M. Parker, *Adv. Mater.* **2020**, *32*, 2002681; d) T. Iwasaki, Y. Tamai, M. Yamamoto, T. Taniguchi, K. Kishikawa, M. Kohri, *Langmuir* **2018**, *34*, 11814; e) S. M. Klein, V. N. Manoharan, D. J. Pine, F. F. Lange, *Langmuir* **2005**, *21*, 6669; f) S. H. Kim, S. Y. Lee, G. R. Yi, D. J. Pine, S. M. Yang, *J. Am. Chem. Soc.* **2006**, *128*, 10897.
- [5] a) P. F. Damasceno, M. Engel, S. C. Glotzer, *Science* **2012**, *337*, 453; b) E. G. Teich, G. van Anders, D. Klotsa, J. Dshemuchadse, S. C. Glotzer, *Proc. Natl. Acad. Sci. USA* **2016**, *113*, E669; c) C. X. Du, G. van Anders, R. S. Newman, S. C. Glotzer, *Proc. Natl. Acad. Sci. USA* **2017**, *114*, E3892–E3899; d) C. X. Du, G. van Anders, J. Dshemuchadse, P. M. Dodd, S. C. Glotzer, *Mol. Simul.* **2020**, *46*, 1037; e) R. K. Cersonsky, J. Dshemuchadse, J. Antonaglia, G. van Anders, S. C. Glotzer, *Phys. Rev. Mater.* **2018**, *2*, 125201; f) Y. Lu, Y. Yin, Y. Xia, *Adv. Mater.* **2001**, *13*, 415; g) R. K. Cersonsky, J. Antonaglia, B. D. Dice, S. C. Glotzer, *Nat. Commun.* **2021**, *12*, 2543.
- [6] a) D. Wang, M. Hermes, R. Kotni, Y. T. Wu, N. Tasios, Y. Liu, B. de Nijs, E. B. vander Wee, C. B. Murray, M. Dijkstra, A. van Blaaderen, *Nat. Commun.* **2018**, *9*, 2228; b) J. Henzie, M. Gruenwald, A. Widmer-Cooper, P. L. Geissler, P. Yang, *Nat. Mater.* **2012**, *11*, 131–137; c) T. Wang, J. Zhuang, J. Lynch, O. Chen, Z. Wang, X. Wang, D. LaMontagne, H. Wu, Z. Wang, Y. C. Cao, *Science* **2012**, *338*, 358; d) J. M. Meijer, L. Rossi, *Soft Matter* **2021**, *17*, 2354.
- [7] a) O. Yaghi, H. Li, *J. Am. Chem. Soc.* **1995**, *117*, 10401; b) H.-C. Zhou, S. Kitagawa, *Chem. Soc. Rev.* **2014**, *43*, 5415; c) H.-C. Zhou, J. R. Long, O. M. Yaghi, *Chem. Rev.* **2012**, *112*, 673; d) J. R. Long, O. M. Yaghi, *Chem. Soc. Rev.* **2009**, *38*, 1213.
- [8] a) J. Cravillon, C. A. Schröder, R. Nayuk, J. Gummel, K. Huber, M. Wiebcke, *Angew. Chem. Int. Ed.* **2011**, *50*, 8067; *Angew. Chem.* **2011**, *123*, 8217; b) S. Wang, S. S. Park, C. T. Buru, H. Lin, P.-C. Chen, E. W. Roth, O. K. Farha, C. A. Mirkin, *Nat. Commun.* **2020**, *11*, 2495; c) J. Troyano, A. Carné-Sánchez, C. Avci, I. Imaz, D. Maspoch, *Chem. Soc. Rev.* **2019**, *48*, 5534; d) M. Pang, A. J. Cairns, Y. Liu, Y. Belmabkhout, H. C. Zeng, M. Eddaoudi, *J. Am. Chem. Soc.* **2013**, *135*, 10234.
- [9] C. Avci, I. Imaz, A. Carné-Sánchez, J. A. Pariente, N. Tasios, J. Pérez-Carvajal, M. I. Alonso, A. Blanco, M. Dijkstra, C. López, D. Maspoch, *Nat. Chem.* **2018**, *10*, 78.
- [10] C. Avci, Y. Liu, J. A. Pariente, A. Blanco, C. Lopez, I. Imaz, D. Maspoch, *Small* **2019**, *15*, 1902520.
- [11] a) K. S. Park, Z. Ni, A. P. Côté, J. Y. Choi, R. Huang, F. J. Uribe-Romo, H. K. Chae, M. O’Keeffe, O. M. Yaghi, *Proc. Natl. Acad. Sci. USA* **2006**, *103*, 10186; b) X.-C. Huang, Y.-Y. Lin, J.-P. Zhang, X.-M. Chen, *Angew. Chem. Int. Ed.* **2006**, *45*, 1557; *Angew. Chem.* **2006**, *118*, 1587.
- [12] J. Hafizovic Cavka, S. Jakobsen, U. Olsbye, N. Guillou, C. Lamberti, S. Bordiga, K. P. Lillerud, *J. Am. Chem. Soc.* **2008**, *130*, 13850.
- [13] G. van Anders, D. Klotsa, N. K. Ahmed, M. Engel, S. C. Glotzer, *Proc. Natl. Acad. Sci. USA* **2014**, *111*, E4812.
- [14] R. E. Guerra, C. P. Kelleher, A. D. Hollingsworth, P. M. Chaikin, *Nature* **2018**, *554*, 346.
- [15] G. Meng, J. Paulose, D. R. Nelson, V. N. Manoharan, *Science* **2014**, *343*, 634.
- [16] M. Rosenberg, F. Dekker, J. G. Donaldson, A. P. Philipse, S. S. Kantorovich, *Soft Matter* **2020**, *16*, 4451.
- [17] a) G. van Anders, N. K. Ahmed, R. Smith, M. Engel, S. C. Glotzer, *ACS Nano* **2014**, *8*, 931–940; b) P. F. Damasceno, M. Engel, S. Glotzer, *ACS Nano* **2012**, *6*, 609–614.

- [18] R. M. Parker, T. H. Zhao, B. Frka-Petesic, S. Vignolini, *arXiv preprint* arXiv:2110.00410, **2021**.
- [19] R. Ohnuki, S. Isoda, M. Sakai, Y. Takeoka, S. Yoshioka, *Adv. Opt. Mater.* **2019**, 7, 1900227.
- [20] R. Ohnuki, M. Sakai, Y. Takeoka, S. Yoshioka, *Langmuir* **2020**, 36, 5579.
- [21] a) T. Aoyagi, Y. Aoyagi, S. Namba, *Appl. Phys. Lett.* **1976**, 29, 303; b) E. G. Loewen, M. Nevière, D. Maystre, *Appl. Opt.* **1977**, 16, 2711; c) A. Wirgin, R. Deleuil, *J. Opt. Soc. Am.* **1969**, 59, 1348; d) J. E. Harvey, R. N. Pfisterer, *Opt. Eng.* **2019**, 58, 87105.
- Manuscript received: December 22, 2021
Accepted manuscript online: February 7, 2022
Version of record online: February 23, 2022
-

Supporting Information

Coloration in Supraparticles Assembled from Polyhedral Metal-Organic Framework Particles

J. Wang, Y. Liu, G. Bleyer, E. S. A. Goerlitzer, S. Englisch, T. Przybilla, C. F. Mbah, M. Engel, E. Spiecker, I. Imaz, D. Maspoch*, N. Vogel**

SUPPORTING INFORMATION

Experimental Procedures

Materials. Zirconium (IV) chloride (ZrCl_4), cetyltrimethylammonium bromide (CTAB), terephthalic acid (1,4-BDC), oxalylchloride, tetrahydrofurane, trimethylamine, O,O-bis(2-aminopropyl) polypropylene glycol-block-polyethylene glycol-*block*-polypropylene glycol 900 (Jeffamine D-900) and polyvinylpyrrolidone (Mw 10000) were purchased from Sigma Aldrich. Glacial acetic acid and *N,N*-dimethylformamide (DMF) were purchased from Fisher Chemical. 2-methylimidazole (2-MiM), zinc acetate dihydrate ($\text{Zn}(\text{CH}_3\text{COO})_2 \cdot 2\text{H}_2\text{O}$) and zinc nitrate hexahydrate ($\text{Zn}(\text{NO}_3)_2 \cdot 6\text{H}_2\text{O}$) were purchased from TCI Chemical. Krytox 157 FSH and HFE 7100 were purchased from Dupont and 3M company, respectively. Lutensol (TO 8) was kindly provided by BASF. All chemical reagents and solvents were used as received without further purification. De-ionized (DI) water was obtained from a Milli-Q water purification system.

Characterization. Field-emission Scanning Electron Microscopy images were collected on SEM FEI Magellan 400L XHR at an acceleration voltage of 2.0 kV and on a Zeiss Gemini 500 SEM with the SE2 detector and an acceleration voltage of 1kV. The average size distribution of each synthesized MOF particle was statistically estimated from FESEM images by counting the sizes of 200 particles at different areas from each sample. X-ray Powder diffraction (PXRD) diagrams were collected on a Panalytical X'pert diffractometer with monochromatic Cu-K α radiation ($\lambda_{\text{Cu}} = 1.5406 \text{ \AA}$). Zeta potential (ζ) was measured using a Malvern Zetasizer (Malvern Instruments, UK).

Synthesis of cubic C-ZIF-8 particles. In a typical synthesis, $\text{Zn}(\text{NO}_3)_2 \cdot 6\text{H}_2\text{O}$ (140 mg) dissolved in 8 mL of water was added to 24 mL of an aqueous solution containing 2-MiM (1920 mg) and 4 mL of 0.85 mg mL^{-1} CTAB solution. After standing for 5 h, the resulting ZIF-8 particles were washed with deionized water (10 mL) upon centrifugation at 9000 rpm in 50-mL Falcon tubes. The zeta potential of the resulting cubic ZIF-8 particles was approximately +30 mV.

Synthesis of truncated rhombic dodecahedral TRD-ZIF-8 particles with truncation $t = 0.68$. TRD-ZIF-8 particles were produced by following the protocol reported in a previous work.^[1] Typically, $\text{Zn}(\text{CH}_3\text{COO})_2 \cdot 2\text{H}_2\text{O}$ (300 mg) dissolved in 5 mL of water was added to 5 mL of an aqueous solution containing 2-MiM (2.72 M) and CTAB (0.54 mM) with gentle stirring. The mixture was left at room temperature for 2 h, and the resulting TRD-ZIF-8 particles with a size of $181 \pm 9 \text{ nm}$ were washed with deionized water (10 mL) upon centrifugation at 9000 rpm in 50-mL Falcon tubes. The zeta potential of the resulting TRD-ZIF-8 particles was approximately +30 mV. The conditions used for the synthesis of the other TRD ZIF-8 particles were as follows: for $198 \pm 10 \text{ nm}$, $[2\text{-MiM}] = 2.58 \text{ M}$ and $[\text{CTAB}] = 0.54 \text{ mM}$; for $229 \pm 9 \text{ nm}$, $[2\text{-MiM}] = 2.72 \text{ M}$ and $[\text{CTAB}] = 0.44 \text{ mM}$; and for $247 \pm 10 \text{ nm}$, $[2\text{-MiM}] = 2.72 \text{ M}$ and $[\text{CTAB}] = 0.54 \text{ mM}$.

SUPPORTING INFORMATION

Synthesis of rhombic dodecahedral RD-ZIF-8 particles. An aqueous solution (5 mL) of $\text{Zn}(\text{CH}_3\text{COO})_2 \cdot 2\text{H}_2\text{O}$ (334 mg) was added to 5 mL of an aqueous solution of 2-MiM (1.30 g) with gentle stirring. Then, the mixture was left at room temperature for 2 h. The resulting RD-ZIF-8 particles with a size of 293 ± 13 nm were washed with deionized water (10 mL) upon centrifugation at 9000 rpm in 50-mL Falcon tubes. The zeta potential of the resulting RD ZIF-8 particles was approximately + 30 mV. The conditions used for the synthesis of the other RD ZIF-8 particles were as follows: for 246 ± 12 nm, the mass of 2-MiM was 1.34 g; and for 267 ± 12 nm, the mass of 2-MiM was 1.32 g.

Synthesis of octahedral O-UiO-66 particles. O-UiO-66 particles were produced by following the protocol reported in a previous work.^[1] Typically, ZrCl_4 (34.9 mg) and 1,4-BDC (24.9 mg) were dissolved in 10 mL of DMF containing 2.1 M acetic acid and transferred to a scintillation vial. This mixture was heated at 120 °C for 12 h. Afterwards, the synthesized particles with an edge size of 238 ± 13 nm were washed twice with DMF (10 mL) and twice with methanol (10 mL) upon centrifugation at 9000 rpm in 50-mL Falcon tubes. The zeta potential of the resulting octahedral UiO-66 particles was approximately +45 mV. The conditions used for the synthesis of the other O-UiO-66 particles were as follows: for 194 ± 12 nm, the ZrCl_4 was dried in the oven for 2 hours; and for 247 ± 13 nm, a concentration of 2.45 M of acetic acid was used.

Synthesis of the perfluorosurfactant.

The synthesis protocol followed the literature.^[2,3] In short, 10 g of Krytox 157 FSH was dissolved in 30 mL of HFE 7100. The solution was placed in ice bath. 2.1 mL of oxalylchloride was injected into the solution, followed by a drop of DMF. The mixture was stirred for 2 h until no gas development. After evaporation of the solution, the reaction mixture was redissolved in 30 mL of HFE 7100 oil. 1.6 g of Jeffamine D-900 was dissolved in 30 mL of anhydrous tetrahydrofuran, followed by 1.7 mL of triethylamine. The HFE 7100 solution was then injected into the THF solution while stirring overnight in open atmosphere. At inert conditions, the reaction yielded Krytox-PEG surfactant. In open atmosphere, the reaction yielded Krytox-ammonium salt. After synthesis, the reaction mixture was evaporated, leaving whitish honey-like viscous fluid, which was purified by dissolution in a mixture of HFE 7100 and methanol. The mixture was centrifuged at 11000 rpm for 20 min, and the supernatant was removed. The purification step was repeated four times. The remaining fluid was vacuum dried to obtain the pure surfactant.

Assembly of MOF supraparticles.

Initially, 0.5 wt% non-ionic alcohol ethoxylate surfactant (Lutensol TO-8, BASF) and polyvinylpyrrolidone were added into separate dispersions of the ZIF-8 and O-UiO-66 particles, respectively, to improve their colloidal stability. This was followed by three centrifuge cycles to remove residual reagents, including any excess surfactant. Next, each aqueous MOF particle dispersion was emulsified in perfluorinated oil (HFE 7500), either by vigorous shaking or by droplet-based microfluidics.

For the first case, water-in-oil droplets were obtained by pipetting 10 μL of MOF aqueous colloid dispersion into 200 μL HFE 7500 oil (containing 1 wt% perfluorosurfactant) directly in a 1.5 mL glass vial. After sealing the vial with a cap, the vial was shaken vigorously by hand. After emulsification, the cap was removed to allow droplet

SUPPORTING INFORMATION

evaporation at room temperature overnight. After droplet drying, the consolidated MOF supraparticles were suspended in the remaining oil phase. With ~40 mg/mL MOF particle concentration, this procedure produces 2 mg/mL supraparticle concentration in HFE 7500 oil. Note that such supraparticles can exhibit a broad size distribution with supraparticle sizes between ~10 μm and ~50 μm , caused by the inhomogeneous droplet formation process. Nevertheless, this method is valuable as a simple procedure to screen for formation efficiencies of supraparticles, provide sufficient material for macroscopic characterization and to produce polydisperse sample to study the influence of supraparticle size on the reflected color intensity.

For the supraparticles synthesized through droplet-based microfluidics, the MOF colloidal particle dispersion and the perfluorinated oil HFE 7500 (containing 1 wt% perfluorosurfactant) were pumped into PDMS microfluidic through HDPE tube at 50 $\mu\text{L/hr}$ and 300 $\mu\text{L/hr}$ rate. Droplets were collected by inserting 1 mL pipette tip at the microfluidic outlet and subsequently transferred to 1.5 mL glass vial for storage and drying at room temperature overnight. After droplet drying, the consolidated MOF supraparticles were suspended in the remaining oil phase. Supraparticles formed by droplet-based microfluidics exhibited superior uniformity, with relative polydispersity below 5%. The size of the resultant supraparticles can be adjusted by changing the flow rates, the concentration of the colloidal dispersions, and the channel widths of the chip. These variations allow fabrication of uniform supraparticles between approximately 10 μm and 50 μm . Samples produced by microfluidics were used for the detailed investigation of the optical properties of individual supraparticles.

X-ray image of MOF supraparticles.

A droplet of MOF supraparticle suspension was casted on a TEM grid. The grid containing the dried MOF supraparticles was mounted on a sample holder clip and inserted into the X-ray microscope (Zeiss Xradia 810 Ultra, 5.4 keV X-rays). The MOF supraparticles were imaged in high resolution Zernike phase contrast mode with a spatial resolution of 50 nm, field of view of 16 μm x 16 μm and an illumination time of 200 s. The images were reference corrected.

Focused-ion beam (FIB) milling of MOF supraparticles.

A 3 μL droplet of oil containing the MOF supraparticles was casted onto a sticky carbon pad on the SEM stub. 20 nm carbon was deposited on top of the MOF supraparticles as a protection layer before inserting the sample into SEM/FIB. FIB cross sectioning of the particles and subsequent SEM imaging was performed on a Helios NanoLab 660 DualBeam SEM/FIB instrument. FIB milling was performed using Ga⁺ ions at 30 kV acceleration voltage and beam currents of 0.8 - 2.5 nA. Cross sectional imaging was performed using the backscattered electron signal at 1 - 2 kV acceleration voltage and 25 - 100 pA beam current in 38° inclined view with respect to the cross section with the image tilt correction being enabled.

Optical characterization of MOF supraparticles.

Microscopic reflection spectra of individual MOF supraparticle: A 3 μL droplet of oil containing the MOF supraparticles was casted onto clean glass substrate. After oil evaporation, isolated MOF supraparticles were successfully deposited on the substrate. Microscopic images were taken via a custom-modified (A.S. & Co.) Zeiss Axio Imager. Z2 in reflection mode using a Zeiss Epiplan 100x/NA0.75 and a CMOS camera (Zeiss Axiocam 208

SUPPORTING INFORMATION

color) with the field diaphragm partially closed and the aperture completely closed to the minimum opening. Spectra were measured by coupling light out via an optical fiber to a CCD spectrometer (Zeiss MCS CCD/UV-NIR). The outcoupling resulted in a measurement spot with an approximate diameter of 18 μm . Spectra were recorded by taking the average of 20 individual spectra integrated for around 150 μs ; all with respect to a silver mirror as a 100% reflection reference.

Macroscopic reflection spectra of MOF supraparticles in suspension: For the angle-dependent reflection spectra measurements, a tungsten halogen light source (HL-2000-FSHA, ocean optics) was used for illumination. MOF supraparticles were suspended in 600 μL HFE 7500 oil in a 1.5 mL clear glass vial. The incident light was focused in an area (2mm in diameter) normal to the glass vial below the oil-air interface to illuminate the samples of MOF supraparticles in dispersion. The scattered light was collected using a collimator (2 mm spotsize) connected via class fibre to a Flame-T-VIS-NR-ES spectrometer (ocean optics). While the direction of the light source is fixed, both the sample and the collimator are mounted on a rotational stage. A clear glass vial containing the same amount of HFE 7500 oil without supraparticles was measured and used as a reference. Angle-dependent measurement was performed by rotating the stage from 30°, 45°, 60°, 75° to 90°. As the MOF supraparticles have lower density than the HFE 7500 oil, the samples constantly rise up to the oil-air interface. The vial is shaken to redistribute the samples homogeneously and inserted onto the stage immediately before each measurement. This dynamically changing concentration prevents the direct and quantitative comparison of the reflected light intensity.

Photograph of MOF supraparticles in suspension: Angle-depended photographs of MOF supraparticle suspension in glass vials were taken using a Sony A6400 with a Laowa 65 mm f/2.8 2:1 Ultra Makro. The samples were illuminated by a photo flash (Godox V1), with a snoot (Godox AK-R1) attached. The illumination-angle was further restricted by a custom-made snoot-elongation.

Simulation of hard polyhedral particles in spherical confinement:

MOF particles were simulated with a Monte Carlo algorithm as hard polyhedra with excluded volume interactions. The four shapes are cube, truncated rhombic (truncation parameter t) dodecahedron, (perfect, i.e. $t = 0$) rhombic dodecahedron, and octahedron. Overlaps were checked with the Gilbert-Johnson-Keerthi algorithm.^[4,5] Spherical confinement was realized by rejecting translations and rotations of polyhedra that moved one or more vertices outside of the confining sphere. Because the shapes studied here are convex, it is sufficient to test the vertices. 2000 hard polyhedra were placed in the spherical confinement. Simulations were set up at low density (10%) and then compressed up to target density (53%) for 10^7 Monte Carlo cycles. Snapshots were created using ambient occlusion shading in Injavis.^[6]

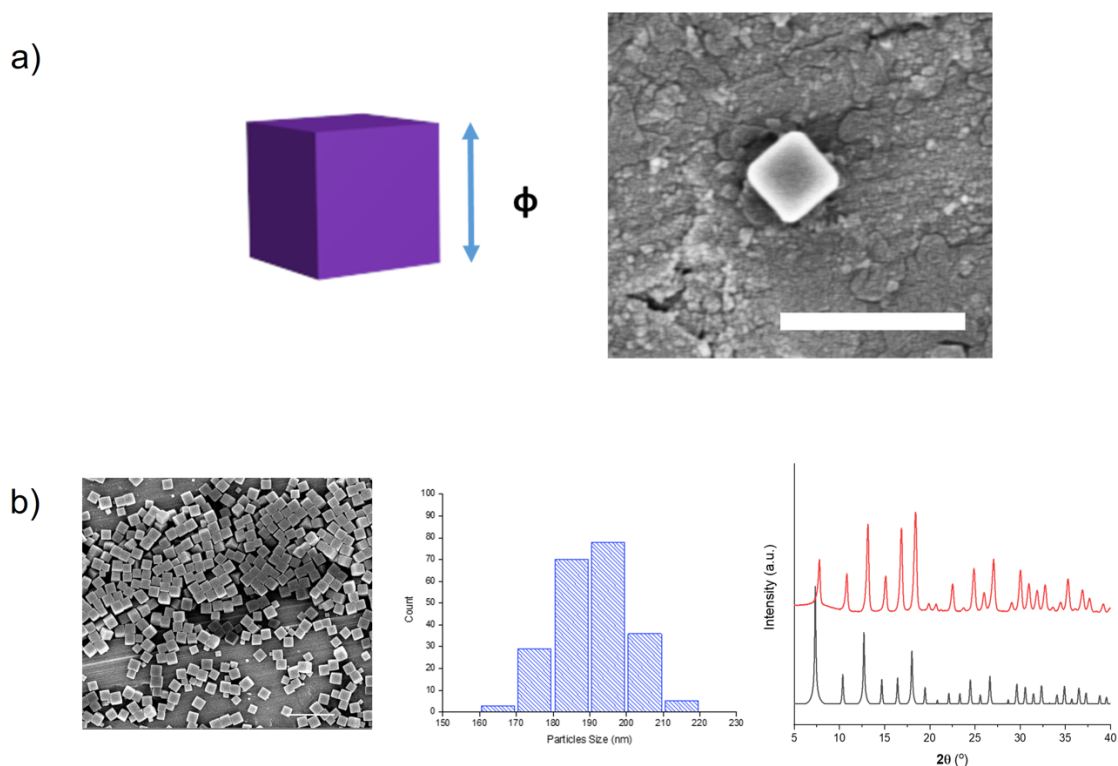


Figure S1. (a) Scheme and FESEM image of an as-synthesized C-ZIF-8 particle, highlighting the edge length (ϕ). Scale bar: 500 nm. (b) Left: Representative FE-SEM image of C-ZIF-8 particles. Scale bar: 1 μm . Middle: Size-distribution histogram of as-synthesized C-ZIF-8 particles with a mean ϕ of 191 ± 9 nm. Right: PXRD patterns of simulated (black) and as-synthesized C-ZIF-8 particles (red).

SUPPORTING INFORMATION

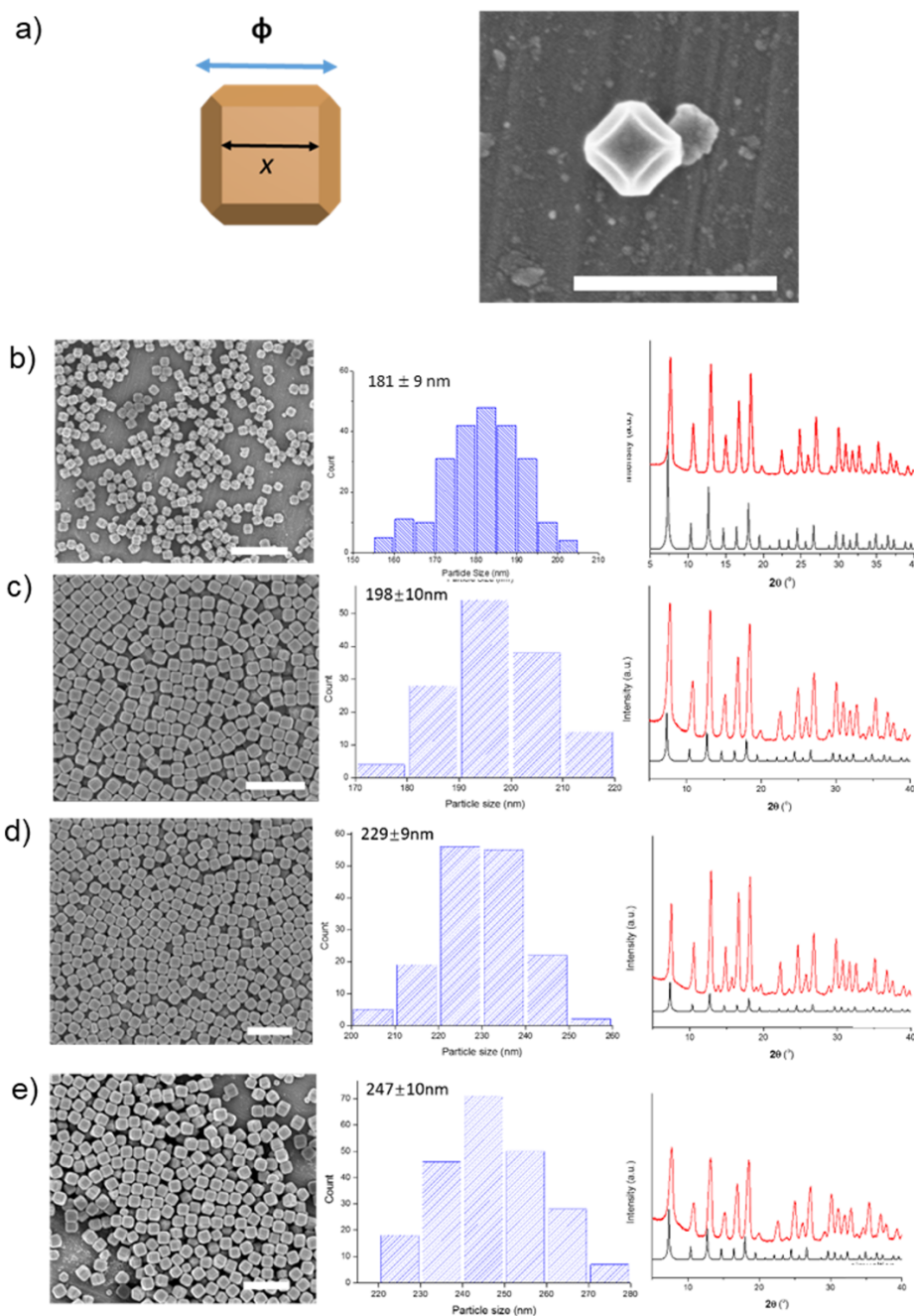


Figure S2. (a) Scheme and FESEM image of an as-synthesized TRD-ZIF-8 particle, highlighting the particle size (ϕ) and edge length (x). Scale bar: 500 nm. (b-e) TRD ZIF-8 particles ($t = 0.68$) with a mean ϕ of 181 ± 9 nm (b), 198 ± 10 nm (c), 229 ± 9 nm (d) and 247 ± 10 nm (e). Left: Representative FE-SEM images; Middle: Size-distribution histograms; and Right: PXRD patterns of simulated (black) and as-synthesized TRD-ZIF-8 particles (red).

SUPPORTING INFORMATION

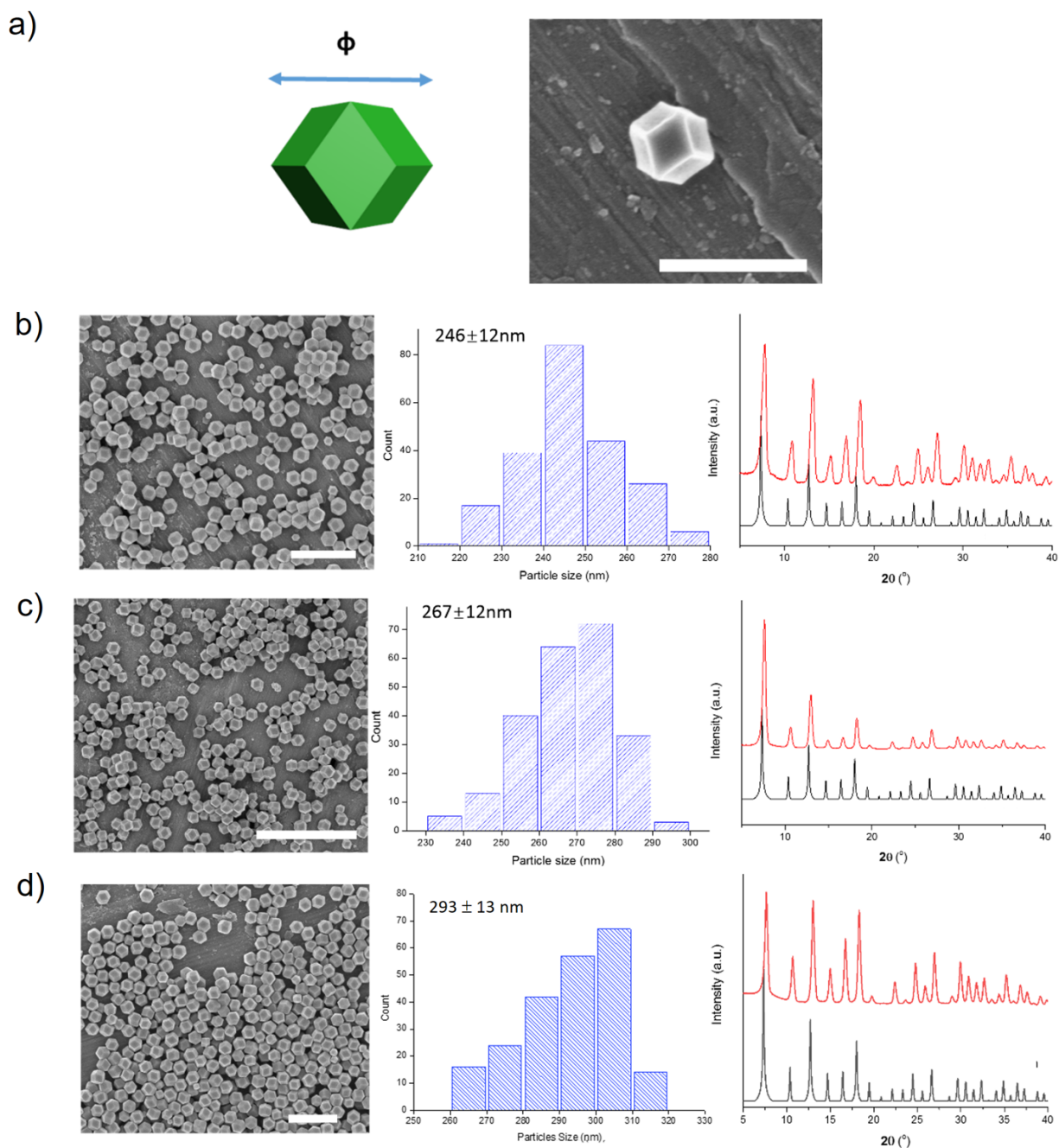


Figure S3. (a) Scheme and FESEM image of an as-synthesized RD-ZIF-8 particle, highlighting the particle size (ϕ). Scale bar: 500 nm. (b-e) RD ZIF-8 particles with a mean ϕ of 246 ± 12 nm (b), 267 ± 12 nm (c), and 293 ± 13 nm (d). Left: Representative FE-SEM images; Middle: Size-distribution histograms; and Right: PXRD patterns of simulated (black) and as-synthesized RD-ZIF-8 particles (red).

SUPPORTING INFORMATION

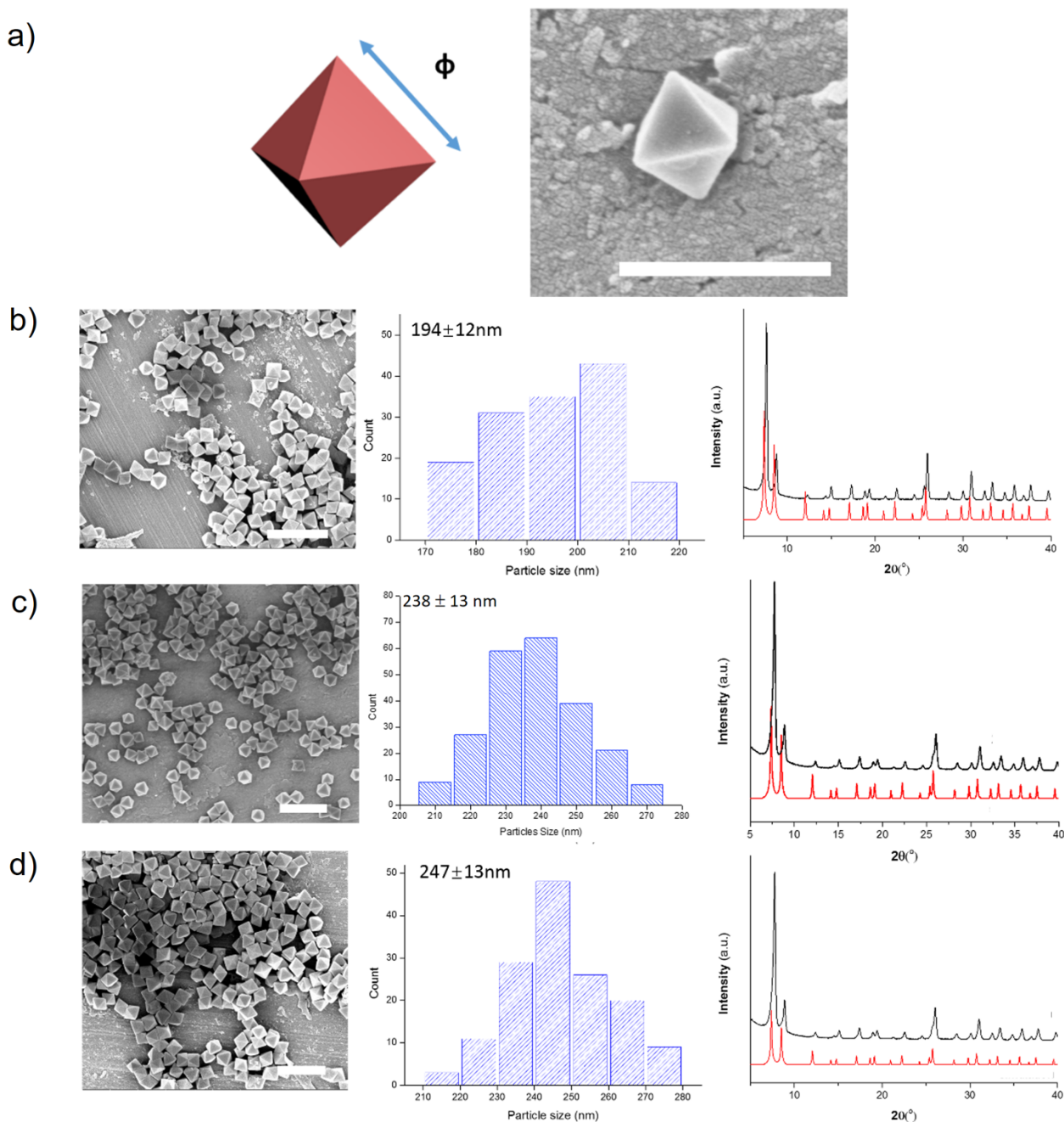


Figure S4. (a) Scheme and FESEM image of an as-synthesized O-UiO-66 particle, highlighting the edge length of particles (ϕ). Scale bar: 500 nm. O-UiO-66 particles a mean ϕ of 194 ± 12 nm (b), 238 ± 13 nm (c), and 247 ± 13 nm (d). Left: Representative FE-SEM images; Middle: Size-distribution histograms; and Right: PXRD patterns of simulated (black) and as-synthesized RD-ZIF-8 particles (red).

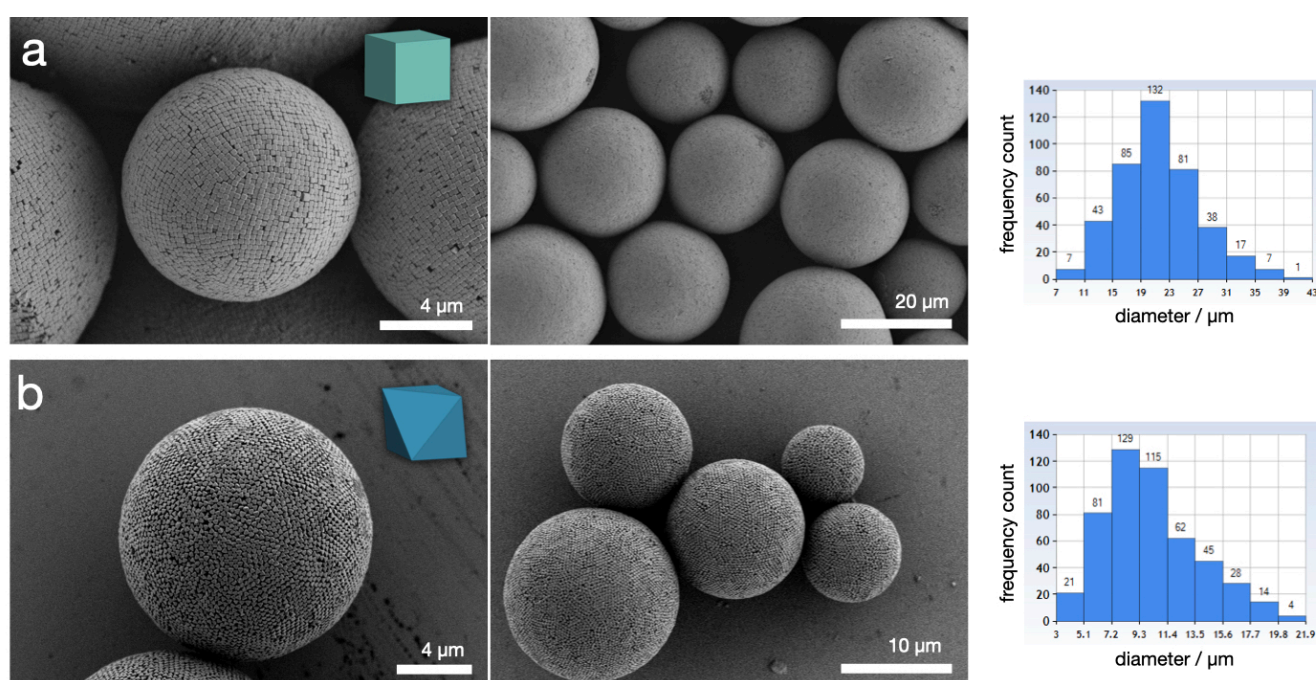


Figure S5. Representative FESEM images of polydisperse C-ZIF-8 (a) and O-Uio-66 (b) supraparticles prepared by shaking emulsifying, with a size of $21 \pm 5.6 \mu\text{m}$ (26% polydispersity) and $9.9 \pm 3.4 \mu\text{m}$ (34% polydispersity, approximately 500 counts), respectively. The dimensions of the produced supraparticles depends on the time duration and power input of the emulsification. Details of emulsification is described in the Experimental Procedure section.

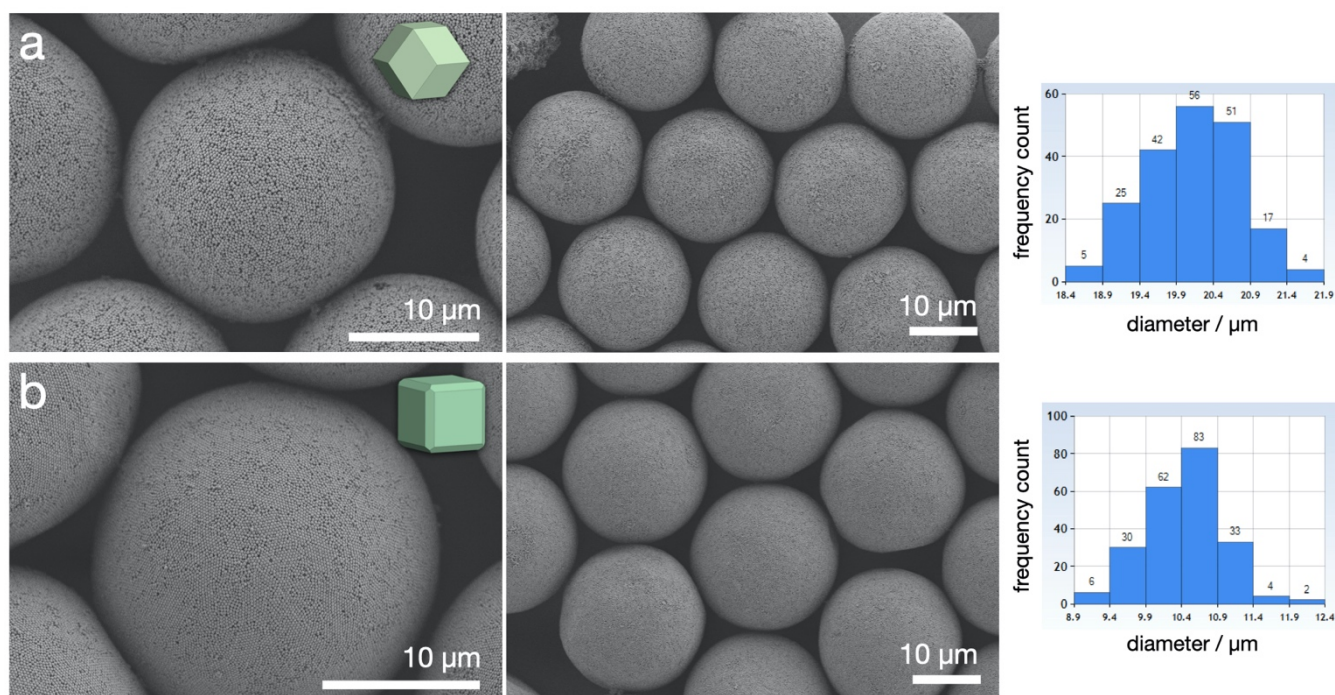


Figure S6. Representative FESEM images of monodispersed RD-ZIF-8 (a) and TRD-ZIF-8 (b) supraparticles prepared using a droplet-based microfluidic device, with a size of $20.1 \pm 0.6 \mu\text{m}$ (3% polydispersity) and $10.4 \pm 0.5 \mu\text{m}$ (5% polydispersity, approximately 200 counts), respectively. The size can be controlled by varying flow rates in the microfluidic device. Details of the emulsification is described in Experimental Procedure section.

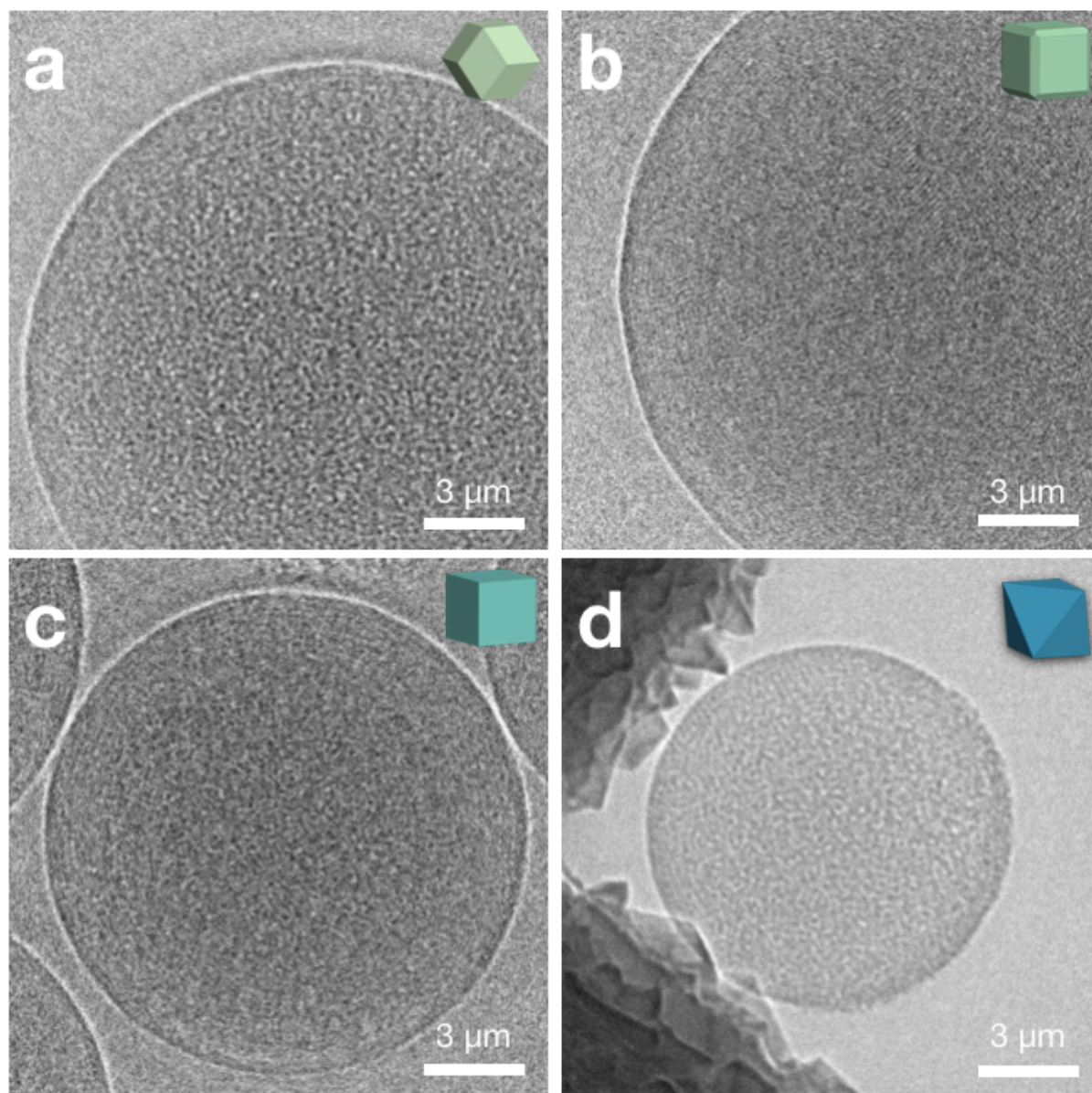


Figure S7. Transmissive X-ray image of MOF supraparticles of a) RD-ZIF-8, showing few onion-like layers near the surface; b) TRD-ZIF-8, showing thick onion-like layers, as well as some lattice fringes; c) C-ZIF-8, showing thick onion-like layers, as well as some lattice fringes; and d) O-UiO-66 particles, showing only little onion-like layer structures.

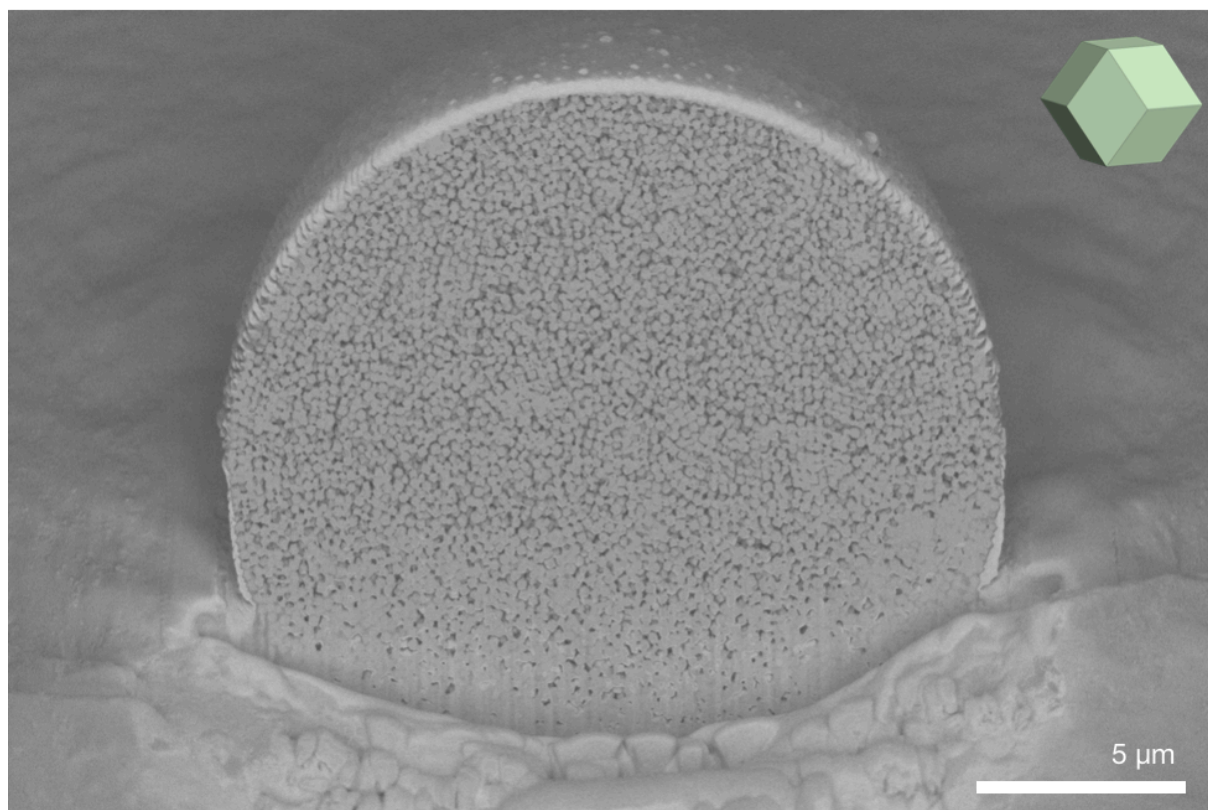


Figure S8. Cross-section of RD-ZIF-8 supraparticles revealed by focused-ion beam milling.

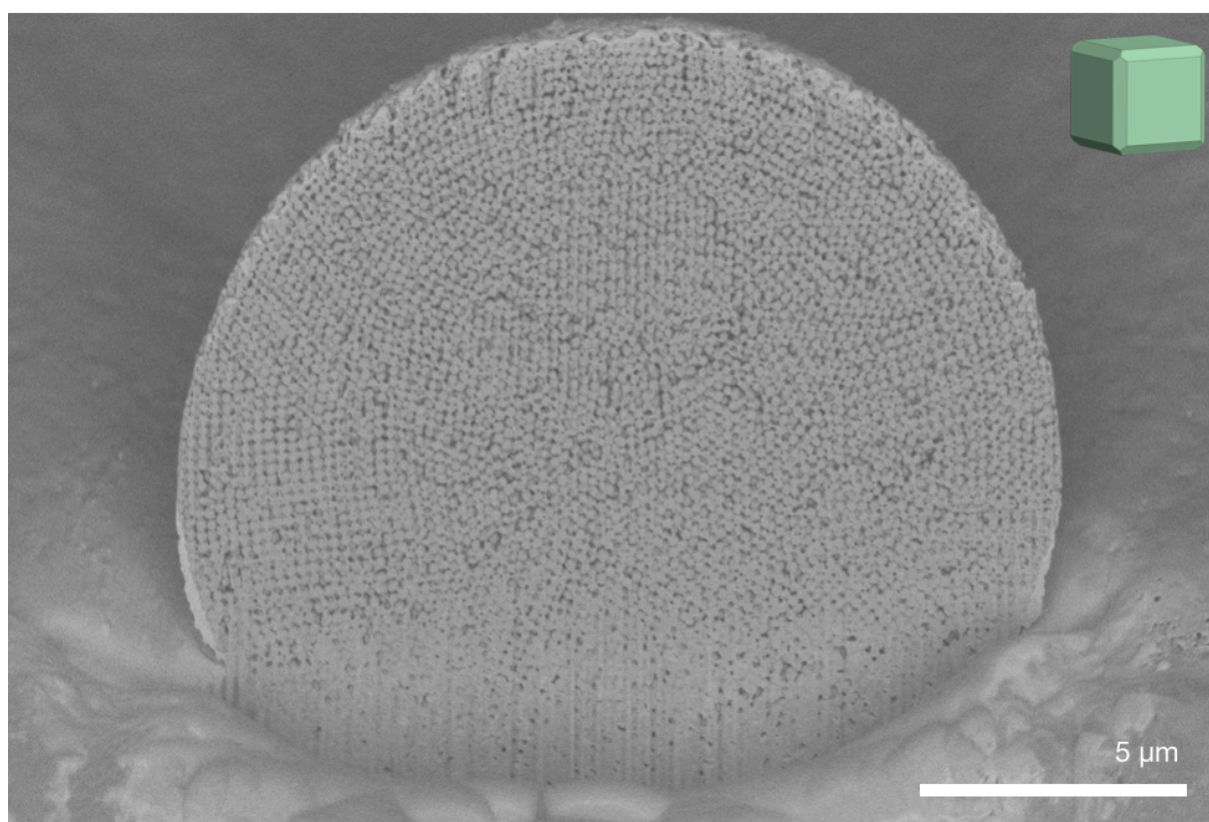


Figure S9. Cross-section of TRD-ZIF-8 supraparticles revealed by focused-ion beam milling.

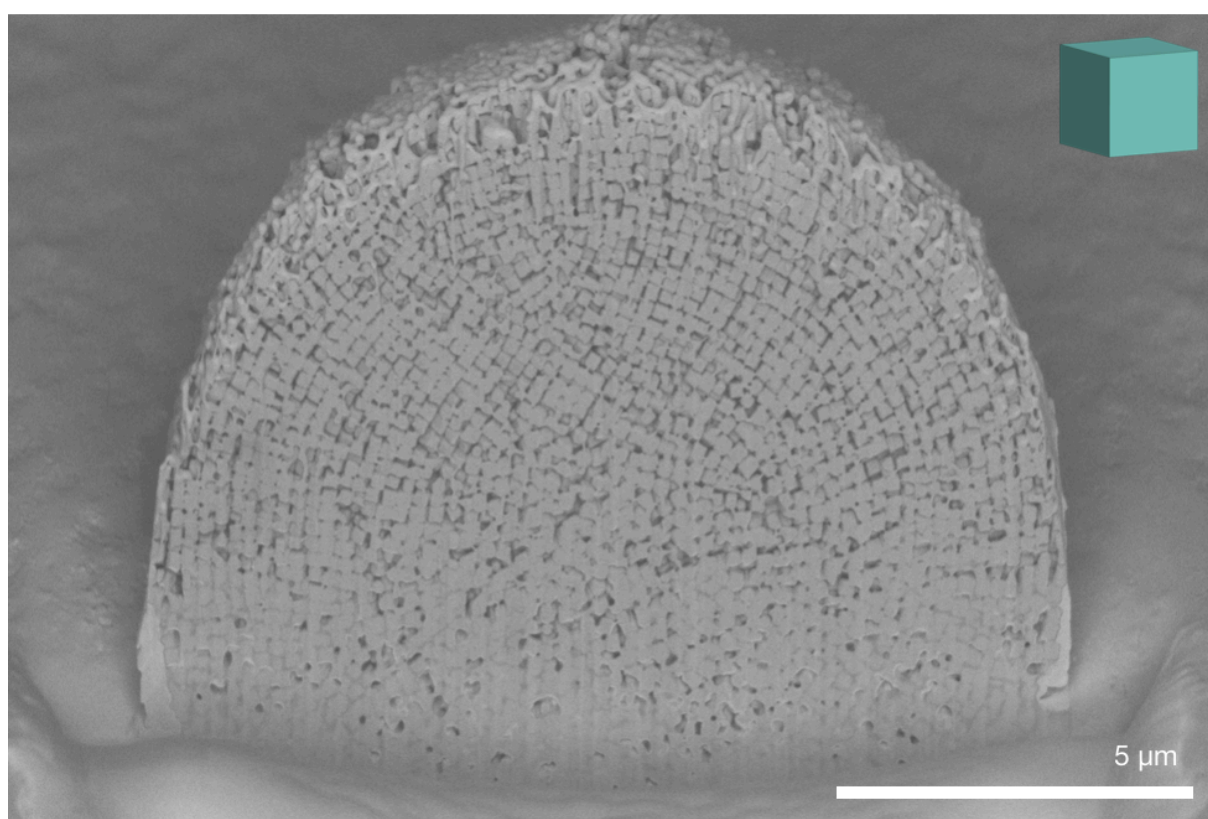


Figure S10. Cross-section of C-ZIF-8 supraparticles revealed by focused-ion beam milling.

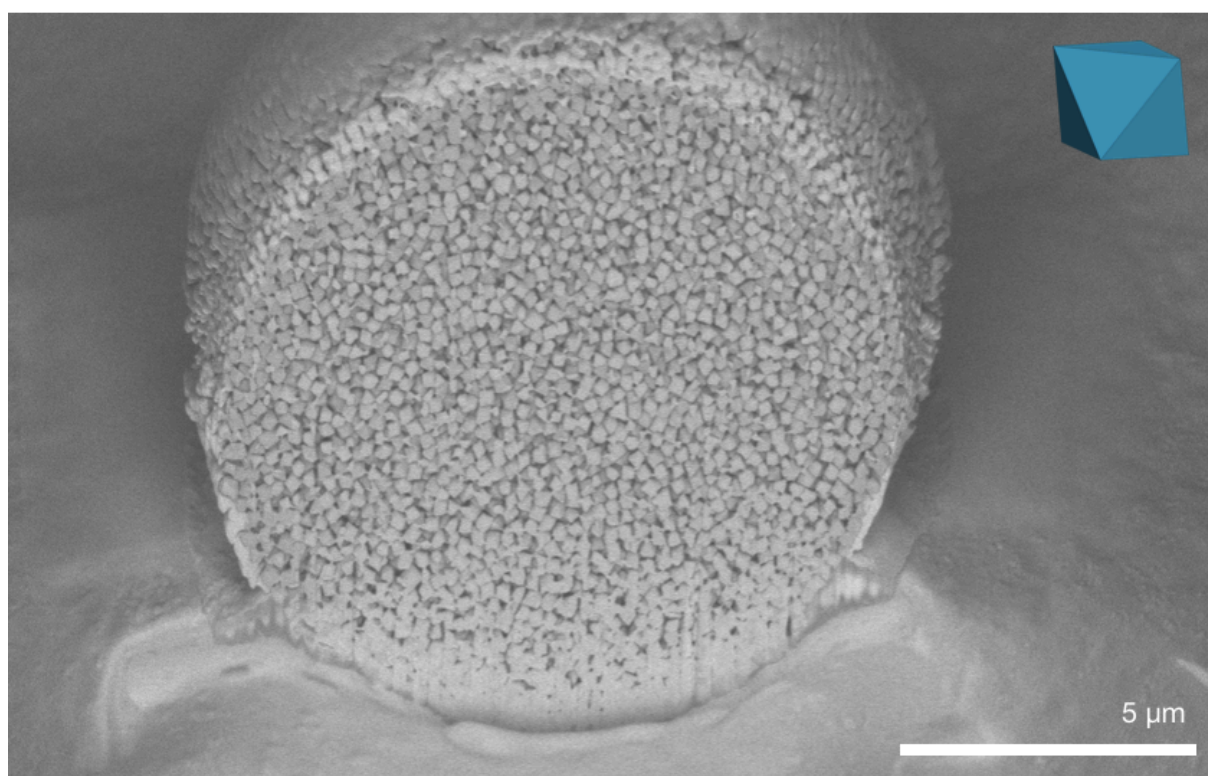


Figure S11. Cross-section of O-UiO-66 supraparticles revealed by focused-ion beam milling.

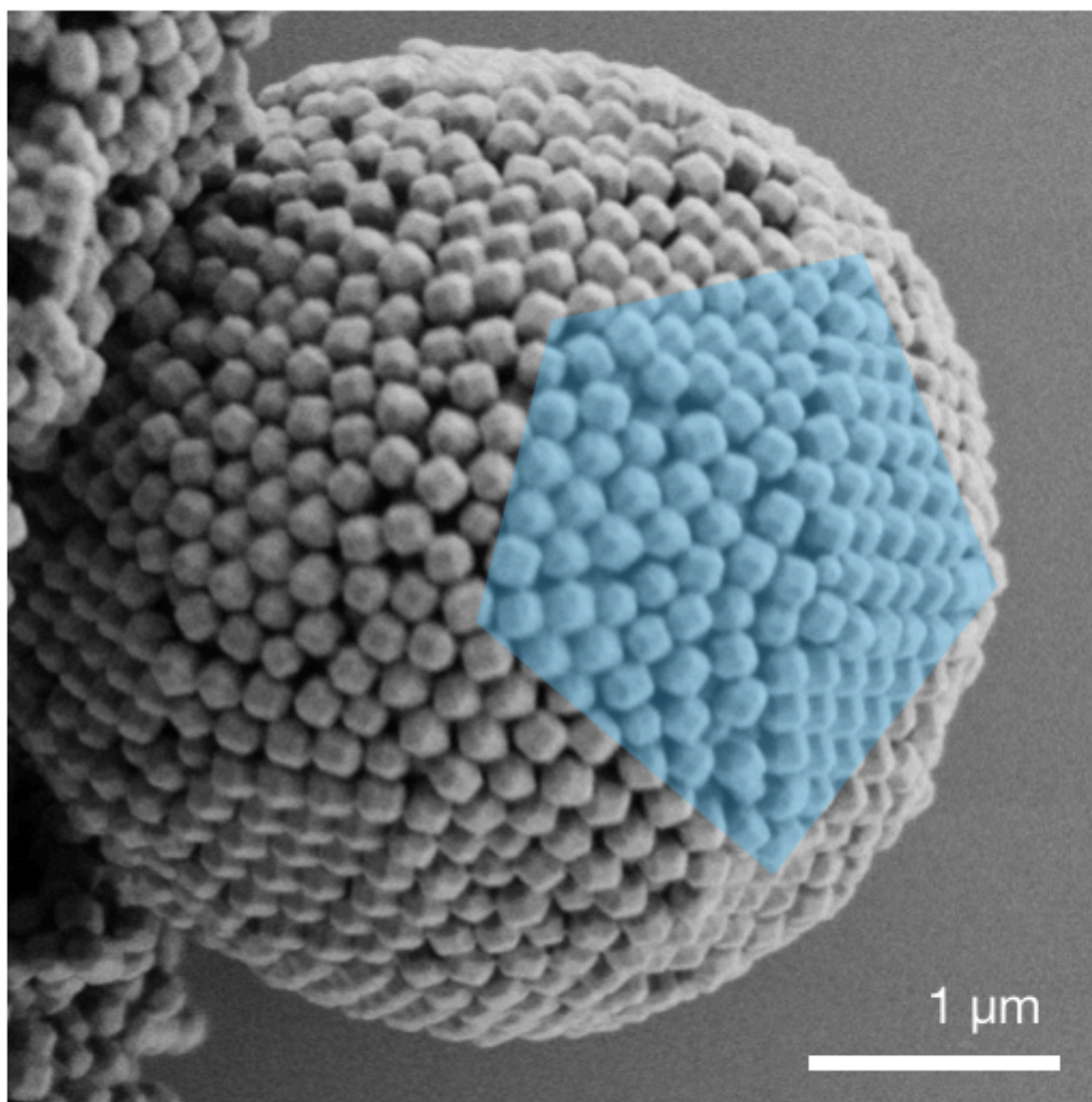


Figure S12. A TRD-ZIF-8 supraparticle exhibiting local five-fold symmetric surface pattern, marked with blue colour.

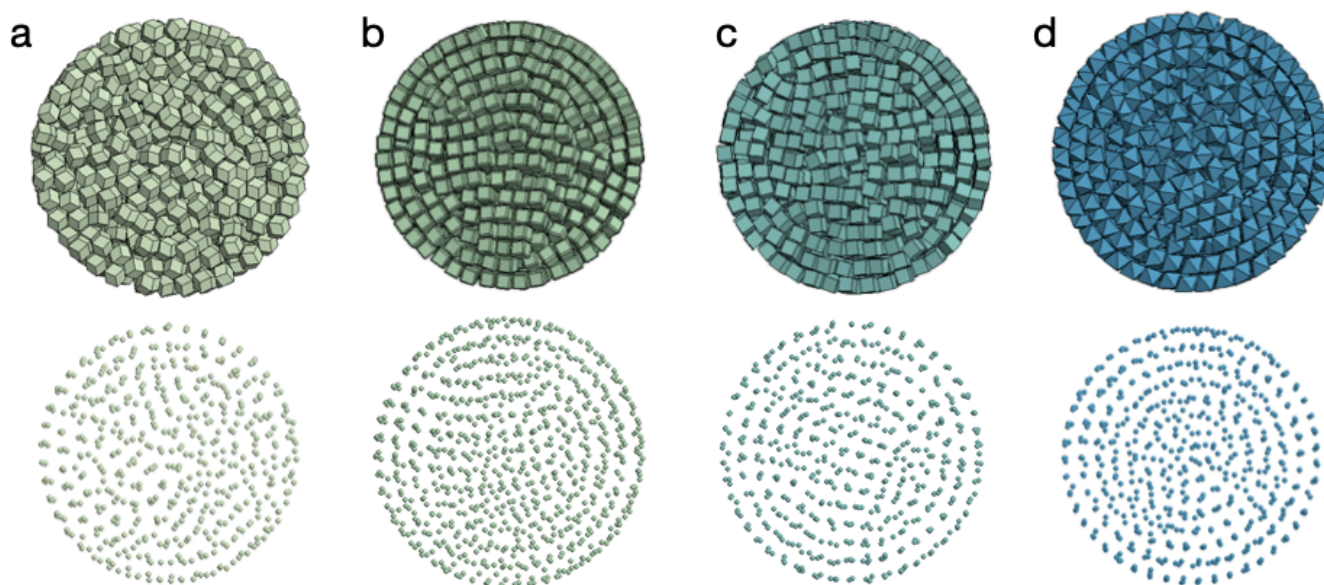


Figure S13. Cross-sectional images of simulated supraparticles of hard polyhedra in spherical confinement. All shapes (rhombic dodecahedron **(a)**, truncated rhombic dodecahedron **(b)**, cube **(c)**, octahedron **(d)**) form three to four onion-like layers near the confinement surface (upper row: rendering of particle at the cross-section, lower row: particles in the cross-sectional regions, each dot represents the geometric center of a particle). Cube particles form body-center cubic lattice in the interior. Octahedron particles form the thickest onion layers. The contrast to experimental observation suggests that the MOF particles in droplets in our experiments cannot be approximated as hard polyhedral-like particles.



Figure S14. Photograph of the self-assembled superstructures resulting from the centrifugation of different aqueous colloidal MOF particles (from left to right: RD-ZIF-8, TRD-ZIF-8, C-ZIF-8 and O-UiO-66). Strong iridescence is observed for TRD-ZIF-8 sample. Weak iridescence is observed for C-ZIF-8 sample. No color is observed for RD-ZIF-8 and O-UiO-66 samples.

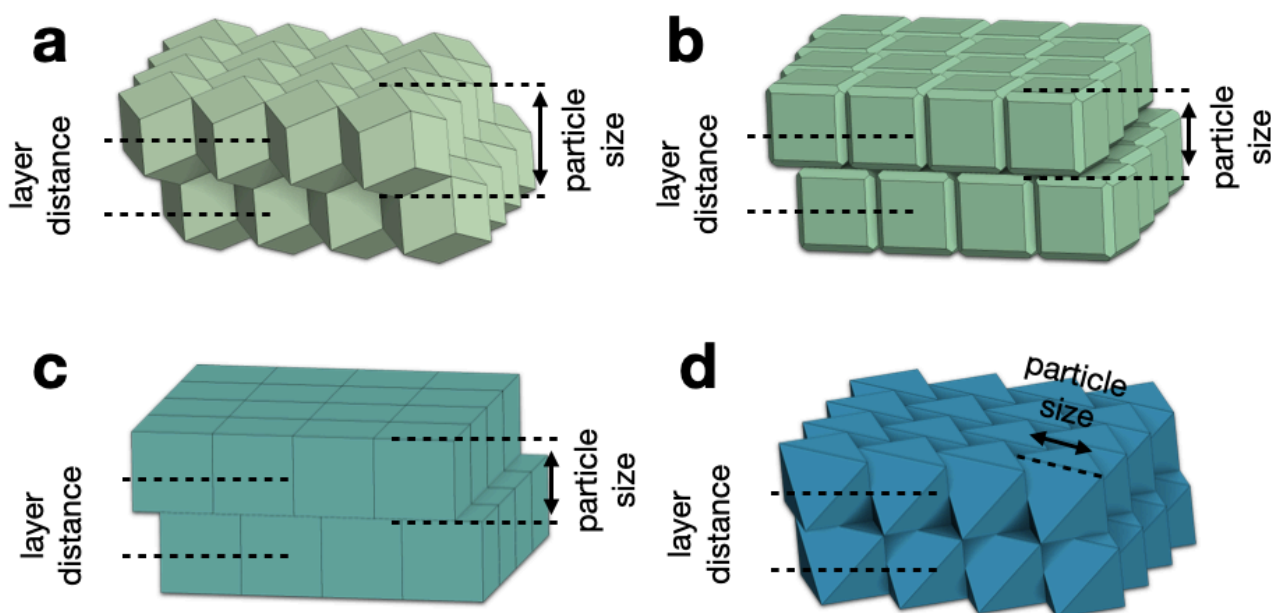


Figure S15. Relationship between MOF particle size of different shapes and layer distance. For RD-ZIF-8 particles, the protrusion and indentation on the surface of the close-packed layer can register with neighboring layer and bring them closer than the size of the particle (**a**). For TRD- and C-ZIF-8 particles, the close-packed layer has a “flat” surface, the layer distance equals to the particle size (**b,c**). For O-UiO-66 particles, the layer distance equals to the distance between two parallel faces of the octahedron, which is approximately 0.8 of the particle size (edge length of octahedron, **d**). The definition of sizes for polyhedral MOF particles follows the tradition to provide reference in the MOF community. It is in general difficult to have a simple yet consistent definition. Measuring TRD-ZIF-8 edge length results in large deviation due to the small truncation in the SEM image, the farthest vertex distance (used in RD-ZIF-8) is difficult to measure for O-UiO-66 particles.

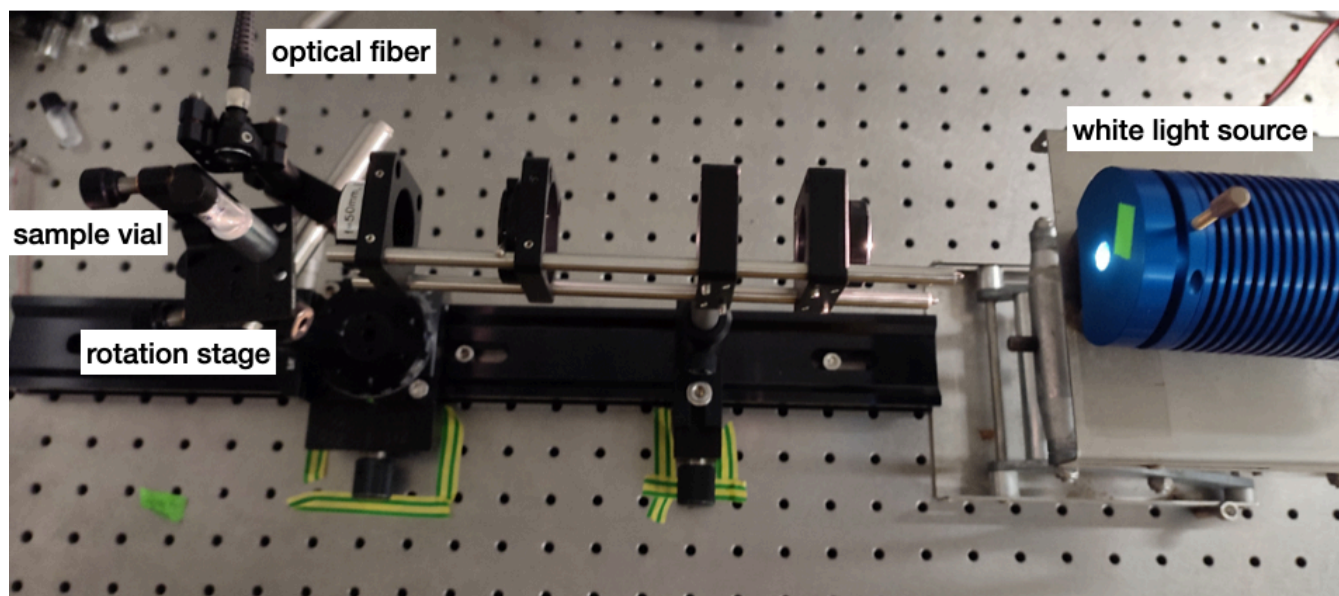


Figure S16. Optical setup to measure reflectance spectra directly from MOF supraparticles suspended in liquid in a glass vial. This enables the angle-dependent optical characterization of a large number of supraparticles at once, and directly in dispersion.

SUPPORTING INFORMATION

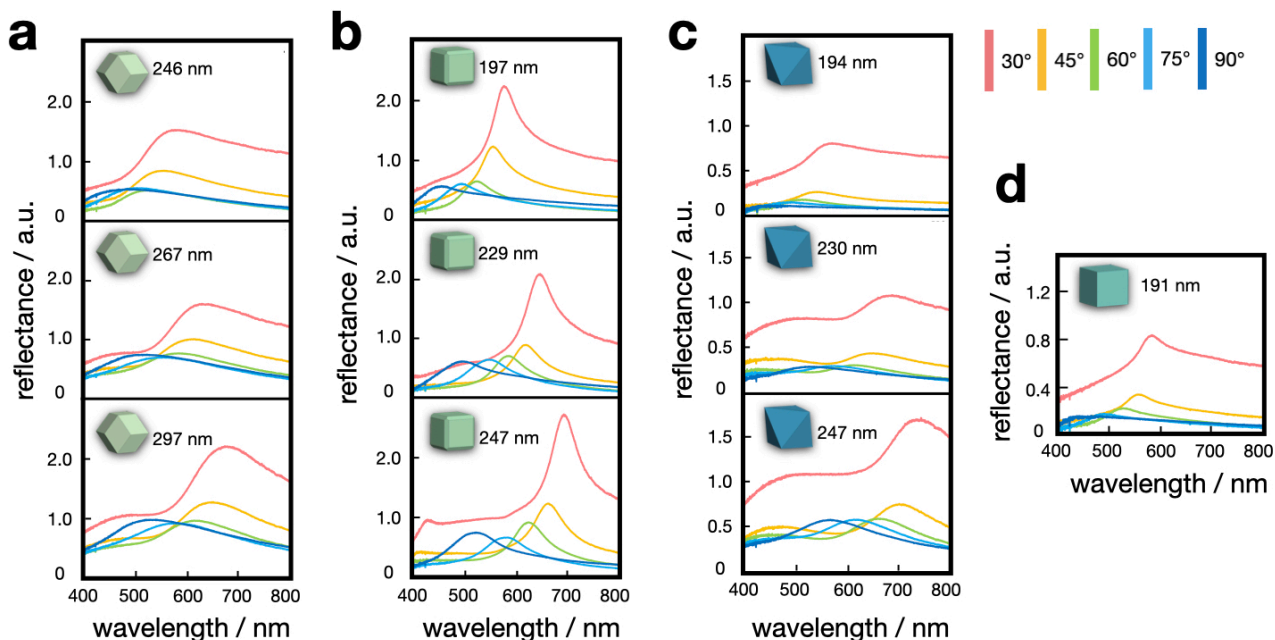


Figure S17. Angle-dependent reflection spectra of four types of MOF supraparticles measured directly from liquid suspension. For all samples, the reflection peaks move towards larger wavelengths with increasing particle sizes, and towards lower wavelength with larger angles between incident light and observation.

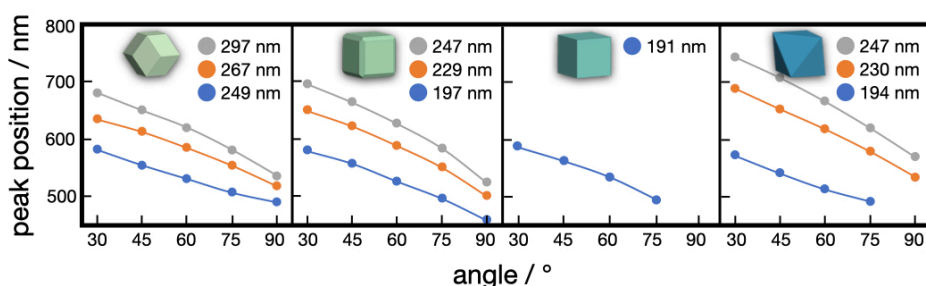


Figure S18. Shift of the reflectance peak with increasing viewing angle for four types of MOF supraparticles. Particle size, shape and material type do not show a discernable influence on the peak shift.

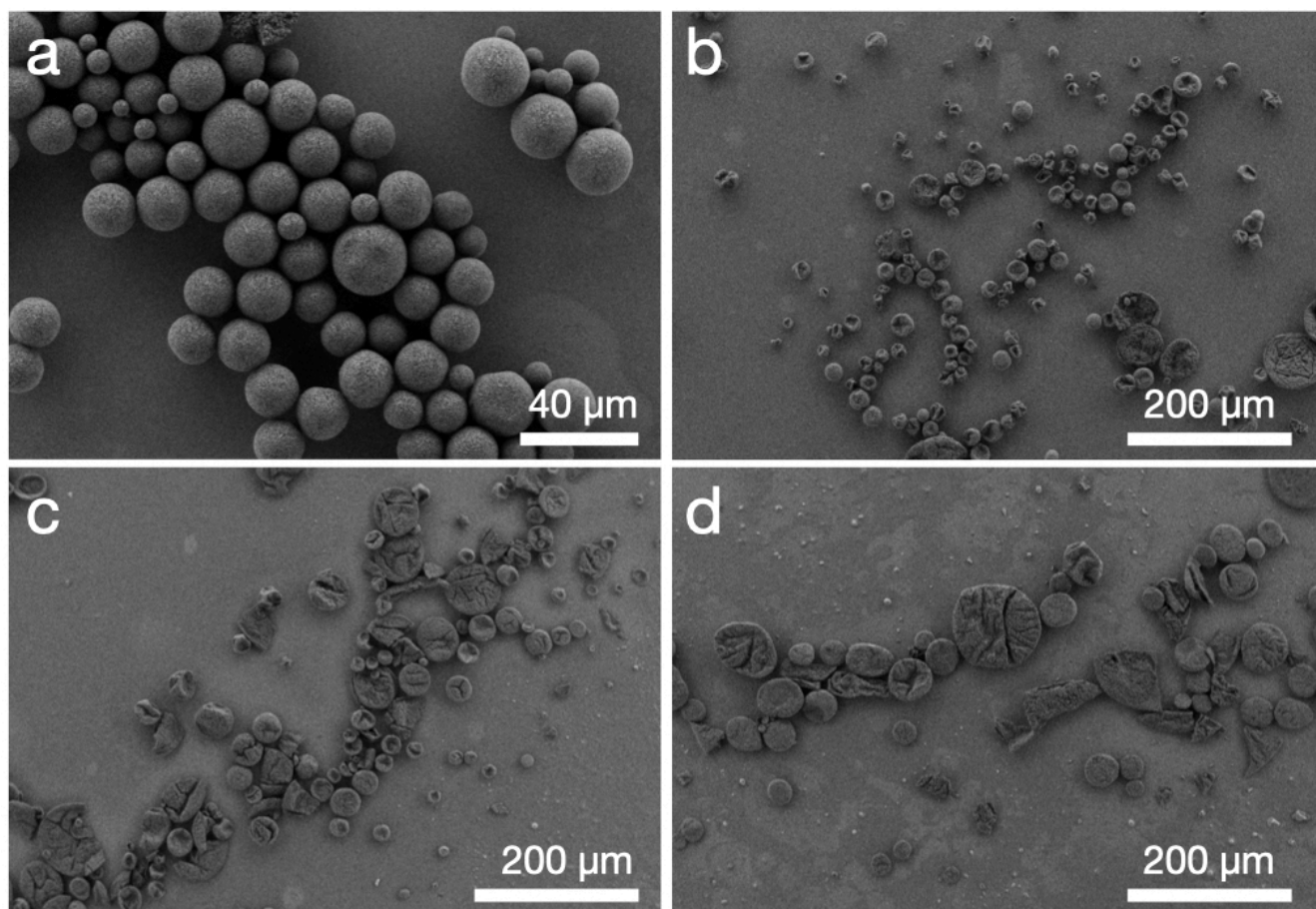


Figure S19. Buckled RD-ZIF-8 supraparticles. 1.0 mL 1 wt% Lutensol TO8 surfactant is added to 0.5 mL 2 wt% RD-ZIF-8 particle dispersion. The dispersion is centrifuged four times. After each centrifuge cycle, 10 μ L of particle dispersion is emulsified in 200 μ L of HFE 7500 oil containing 1 wt% perfluorinated surfactant for subsequent drying into MOF supraparticles. Spherical supraparticles are formed after one centrifuge cycle (a), buckled supraparticles are formed after two, three and four centrifuge cycles (b,c,d). We note that influence of surfactant on the self-assembly of MOF particles in droplet is complex. For a combination of 0.5 mL 1 wt% Lutensol TO8 and 1.0 mL 2 wt% RD-ZIF-8 (synthesized in the same batch), all four centrifuge cycles resulted in spherical supraparticles. The tendency to buckle also depends on the shape of particles, TRD-ZIF-8 particles formed spherical supraparticles even without the addition of surfactant.

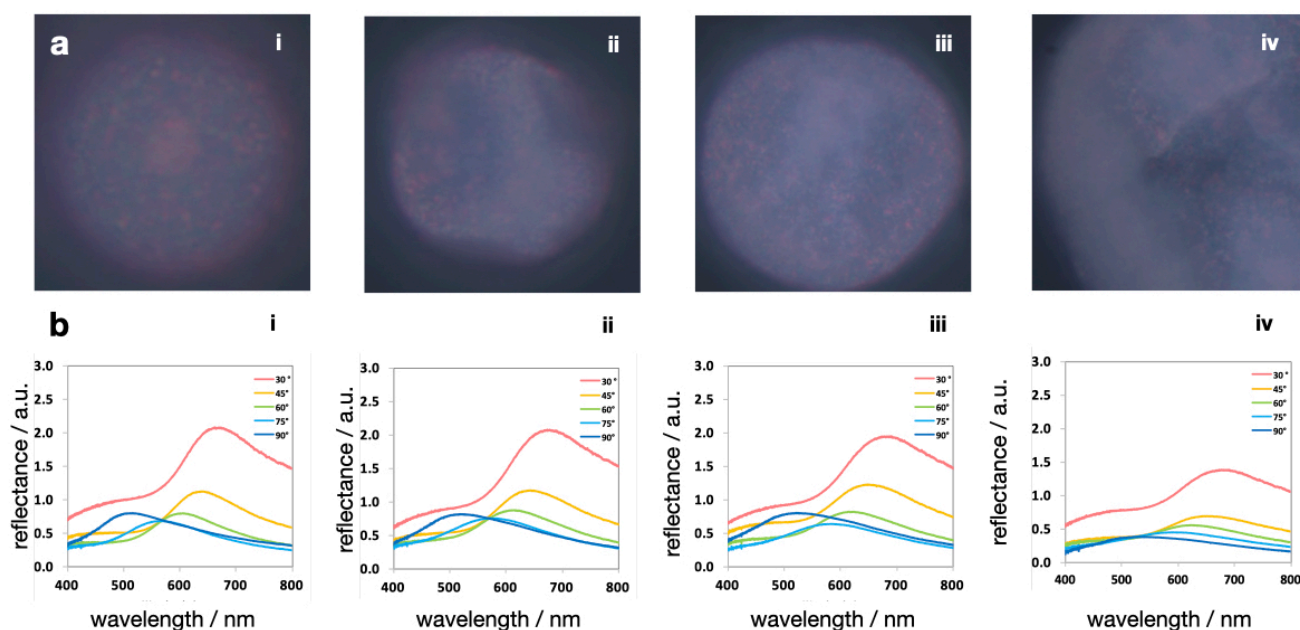


Figure S20. Angle-dependent reflection spectra of buckled MOF supraparticles measured directly from suspension. Supraparticles with increasing deviations from spherical geometry and more buckling are produced from RD-ZIF-8 MOF primary particles (**a**, from i to iv) by increasing centrifugation cycles to remove the surfactant. Note that all samples exhibit macroscopic, angle-dependent structural color (bottom row) even though the observable microscopic coloration at the single particle level is reduced (top row).

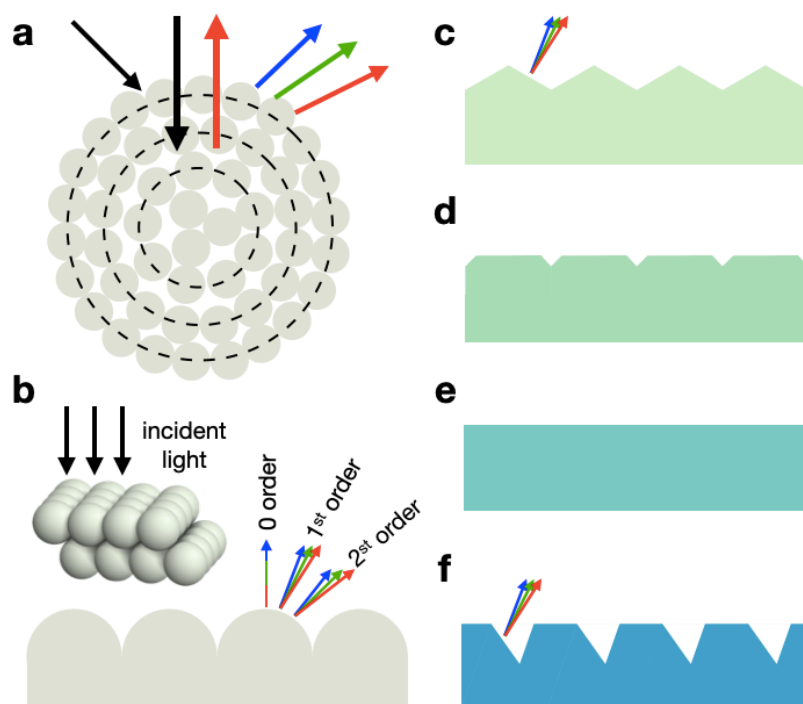


Figure S21. Hypothesized surface grating effects of MOF supraparticles. Typical spherical supraparticles consisting of spherical particles form concentric onion-like layers (**a**), which creates alternating refractive index that produces color by Bragg reflection at the onion-like layers. In addition, parts of the incident light are also diffracted from the supraparticle surface, where the ordered particles form a nanostructured surface grating. Layers consisting of spherical particles resembles a grating with sinusoidal groove, which disperse light into several diffraction orders at different angles (**b**). Polyhedral particles can create surfaces with sharp protrusion of large inclination angles, which resembles a blazed grating (**c** for RD-ZIF-8, **d** for TRD-ZIF-8, **f** for O-UiO-66 particles). The blazed grating is known to have higher diffraction efficiency at non-zero diffraction order. Cubic shape creates surfaces with little to no grooves (**e** for C-ZIF-8 particles).

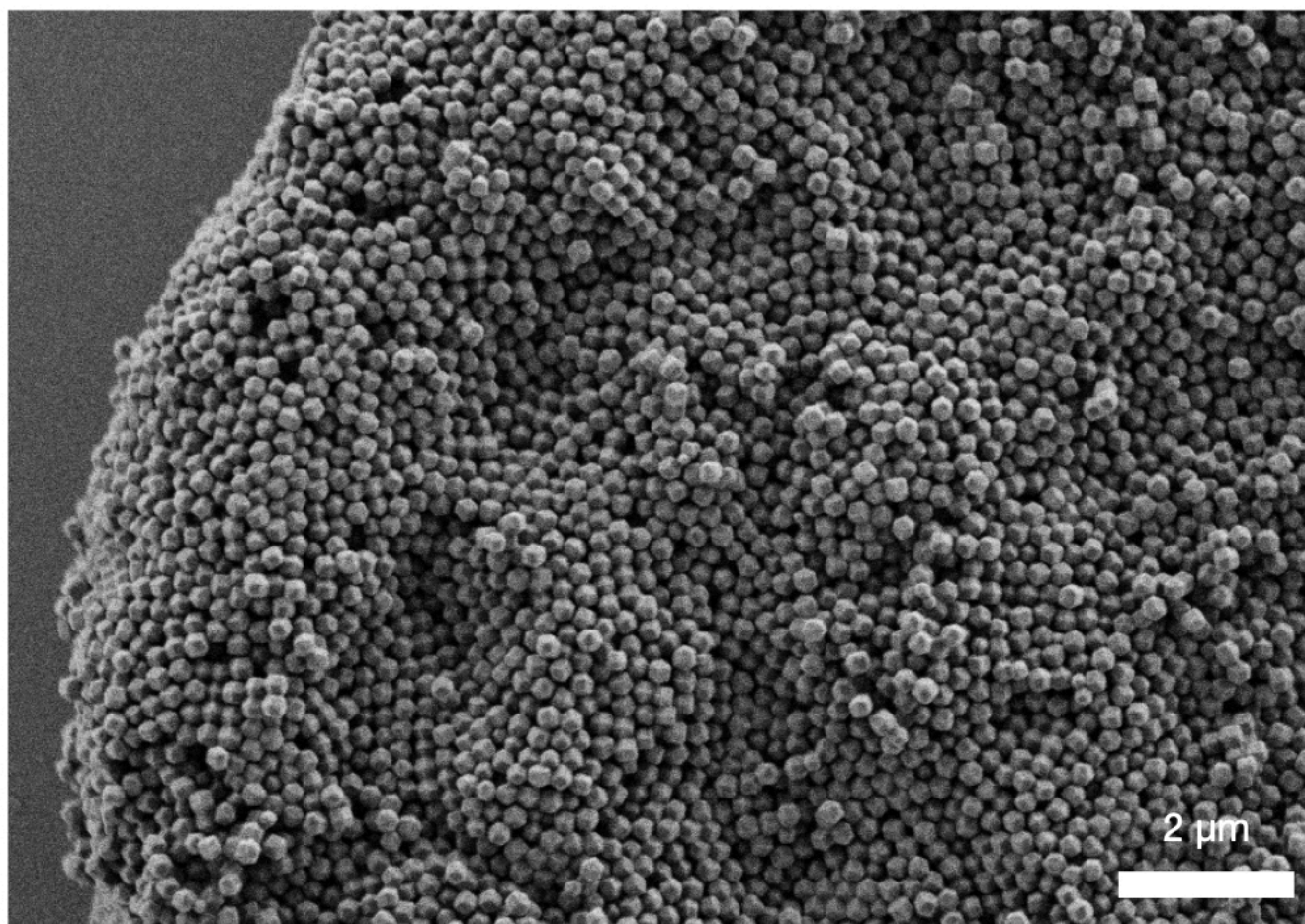


Figure S22. Buckled RD-ZIF-8 supraparticles exhibit ordered surface features, visualized in scanning electron microscopy.

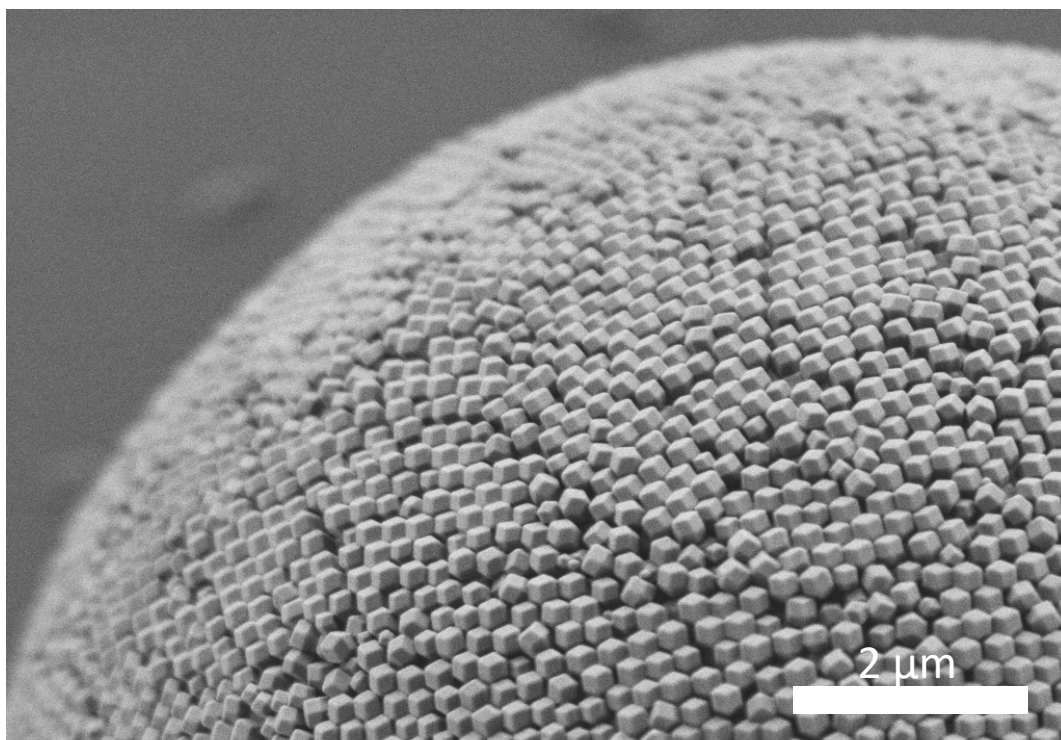


Figure S23. The surface packing of RD ZIF-8 supraparticles shows a sawtooth groove profile, as seen in scanning electron microscopy

References

- [1] C. Avci, I. Imaz, A. Carné-Sánchez, J. A. Pariente, N. Tasios, J. Pérez-Carvajal, M. I. Alonso, A. Blanco, M. Dijkstra, C. López, D. Maspoch, *Nat. Chem.* **2018**, *10*, 78.
- [2] R. Scanga, L. Chrasteka, R. Mohammad, A. Meadows, P.L. Quan, E. Brouzes, *RSC Adv*, **2018**, *8*, 12960.
- [3] R. Birte, PhD thesis. Georg-August-Universität Göttingen (Germany), **2015**.
- [4] E.G. Gilbert, D.W. Johnson, S.S. Keerthi, *IEEE J Robot Autom.* **1988**; *4*, 193- 203.
- [5] P. F. Damasceno, M. Engel, S. C. Glotzer, *ACS Nano* **2012**, *6*, 609.
- [6] M. Engel; 2021; INJAVIS - INteractive JAva VISualization; doi: 10.5281/zenodo.4639570.